

Zwitterionic materials for biomedical applications

Pol Cabanach Xifró

<http://hdl.handle.net/10803/671831>

ADVERTIMENT. L'accés als continguts d'aquesta tesi doctoral i la seva utilització ha de respectar els drets de la persona autora. Pot ser utilitzada per a consulta o estudi personal, així com en activitats o materials d'investigació i docència en els termes establerts a l'art. 32 del Text Refós de la Llei de Propietat Intel·lectual (RDL 1/1996). Per altres utilitzacions es requereix l'autorització prèvia i expressa de la persona autora. En qualsevol cas, en la utilització dels seus continguts caldrà indicar de forma clara el nom i cognoms de la persona autora i el títol de la tesi doctoral. No s'autoritza la seva reproducció o altres formes d'explotació efectuades amb finalitats de lucre ni la seva comunicació pública des d'un lloc aliè al servei TDX. Tampoc s'autoritza la presentació del seu contingut en una finestra o marc aliè a TDX (framing). Aquesta reserva de drets afecta tant als continguts de la tesi com als seus resums i índexs.

ADVERTENCIA. El acceso a los contenidos de esta tesis doctoral y su utilización debe respetar los derechos de la persona autora. Puede ser utilizada para consulta o estudio personal, así como en actividades o materiales de investigación y docencia en los términos establecidos en el art. 32 del Texto Refundido de la Ley de Propiedad Intelectual (RDL 1/1996). Para otros usos se requiere la autorización previa y expresa de la persona autora. En cualquier caso, en la utilización de sus contenidos se deberá indicar de forma clara el nombre y apellidos de la persona autora y el título de la tesis doctoral. No se autoriza su reproducción u otras formas de explotación efectuadas con fines lucrativos ni su comunicación pública desde un sitio ajeno al servicio TDR. Tampoco se autoriza la presentación de su contenido en una ventana o marco ajeno a TDR (framing). Esta reserva de derechos afecta tanto al contenido de la tesis como a sus resúmenes e índices.

WARNING. The access to the contents of this doctoral thesis and its use must respect the rights of the author. It can be used for reference or private study, as well as research and learning activities or materials in the terms established by the 32nd article of the Spanish Consolidated Copyright Act (RDL 1/1996). Express and previous authorization of the author is required for any other uses. In any case, when using its content, full name of the author and title of the thesis must be clearly indicated. Reproduction or other forms of for profit use or public communication from outside TDX service is not allowed. Presentation of its content in a window or frame external to TDX (framing) is not authorized either. These rights affect both the content of the thesis and its abstracts and indexes.

DOCTORAL THESIS

Title Zwitterionic Materials for Biomedical Applications

Presented by Pol Cabanach Xifró

Centre IQS School of Engineering

Department Bioengineering

Directed by Dr. Salvador Borrós Gómez
Dr. Abdon Pena Francesch

Als meus pares

*The most exciting phrase to hear in science,
the one that heralds new discoveries, is not "Eureka"
but "That's funny..."* **Isaac Asimov**

Agraïments – Acknowledgements

“La vida d’un no cap en la vida d’un, sinó en la de molts.” Feliu Ventura.

Si hagués de triar l’aspecte més positiu de realitzar aquesta tesi doctoral diria, sens dubte, que ha sigut poder conèixer i aprendre de tantes persones que s’han creuat en el meu camí durant aquests últims quatre anys. La tesi doctoral suposa el final de un llarg procés de formació acadèmica però, sobretot, suposa un procés de maduració personal que, en gran part, es deu a totes les persones que surten aquí esmentades.

I no podria començar agraint a ningú altre que qui em va donar la oportunitat de realitzar aquest camí, el dr. (o millor dit, director) Salvador Borrós. Moltes gràcies per confiar en mi des d’un bon principi. M’has donat llibertat durant el transcurs de tota la tesi i, en comptes de donar-me directament solucions als problemes, m’has donat una cosa encara més important, les eines per trobar-les jo mateix. La teva visió de com afrontar els problemes, de concebre com ha de ser la ciència i la investigació i de tractar amb els teus estudiants ajuda molt a que tothom a GEMAT hi estigui a gust i, en conseqüència, que tothom surti content i agrait després de realitzar una tesi aquí. Per totes aquestes coses i moltes altres més, moltes gràcies Salvador!

Abdon, ja fa dos anys que vaig aterrar a Stuttgart per primera vegada i d’aquell dinar al King’s Palace. Dos anys en els quals has tingut una gran presència en la meua vida com a mentor, però sobretot com a amic. He après tant de tu que no sé ni per on començar i ha sigut molt inspirador poder veure en directe tot el teu camí fins arribar a on has arribat. Gràcies per totes les hores de converses mentre em feies de taxi , per introduir-me a la cultura heavy (“666, the number of the beast!!”), per recórrer junts tots els garitos de Stuttgart buscant les millors alitas i la millor cervesa i, en general, per aquest sentiment de nostàlgia que se’m genera sempre que penso en el meu temps a Stuttgart. Molta sort en la teua nova aventura a Michigan (espero que ja tinguis la ruta plantejada per quan vingui a fer alguna visita).

I would also like to thank director Metin Sitti from the Physical Intelligence group in the Max Planck Institute for Intelligent Systems for allowing me to be in his group during almost one year and giving me the opportunity to work on the exciting field of microrobotics.

També vull donar les gràcies al dr. Xavier Fernàndez Busquets i al dr. Arnau Biosca per la col·laboració amb el projecte de malària. Ha sigut molt interessant treballar i saber més sobre aquesta malaltia que encara ara causa tant patiment arreu del món.

Gràcies Xevi per estar sempre disposat a ajudar-me en un projecte que va començar casi com a un "hobby". Al final sembla que ha agafat forma... També has sigut un gran suport durant tota la meva època de representant dels doctorands. El teu entusiasme i suport per organitzar diverses activitats són molt importants pel nostre col·lectiu.

No em vull oblidar del gran nombre de persones que m'han ajudat en els diversos projectes durant aquest 4 anys. Gràcies Victor Ramos per tota l'ajuda que em vas donar al principi, explicant-me una i altre vegada com realitzar la síntesi RAFT i també per estar sempre disponible per a qualsevol dubte que em sorgís. També gràcies Cristina Fornaguera per tota la ajuda durant la tesi, sobretot al principi, on em vas introduir en la caracterització de nanopartícules. Gracias Miguel Ángel por ser una ayuda constante durante todos esos años de síntesis. Siempre tenías una solución para todo, con una gran cantidad de truquillos que aún conservo. Aún recuerdo las discusiones químicas y cinematográficas que animaban los días más largos. I gràcies Marta Guerra per els últims mesos d'ajuda amb els *in vivos*. Ha sigut molt agradable treballar amb tu. Gràcies també al Marc, Laura i Dario per haver decidit venir a realitzar les vostres tesi de màster i grau en aquests projectes. El vostre esforç i les vostres ganes d'aprendre han sigut molt valuoses per aquesta tesi.

I ara toca el torn de GEMAT. Compartir el dia a dia durant tants d'anys amb tots vosaltres ha sigut tota una aventura. Robert, crec que tu ets la essència de GEMAT. Ja no me'l sabria imaginar sense tu. És curiós perquè ets la persona que costa més convèncer per a fer qualsevol cosa, però al mateix temps deus ser amb qui he fet més coses durant la meva estada al grup. Potser per això ets tant especial. Jocs de taula, puros i gintònics, xerrades filosòfiques, la visita a Stuttgart, col·laboracions... i, sobretot, el "micro-bullying" diari. Fins i tot has tingut temps per "solucionar-me la p*** vida". Són tantes les coses que hem compartit que ets de lo primer que em ve al cap quan penso en aquests últims 4 anys. I si això ho dic pel Robert, també ho podria dir per l'Anna (potser canviant els jocs de taules per nits de copes). Companya de la posverdad i del bacon-queso, dels jagers a l'Arena i dels whiskies japonesos, la gran quantitat de moments divertits i de converses interessants són inesborrables. Gràcies per confiar en mi per ser el teu "delfín", pel teu humor "incorrecte", per lluitar per mantenir el

contacte i per estar sempre present. Joan, l'últim membre del triumvirat, tot i que ets fins i tot més difícil d'arrossegar que el Robert (la teva "espantada" del taxi al sopar GEMAT queda per la història) et fas estimar. Els cafès de després de dinar a la cantonada Tractivus no haguessin sigut el mateix sense els teus "speech". Gràcies per tots els moments viscuts, per les leccions de "entrepreneur" al bar esmorzant i per ser el meu (i de gairebé tothom) suport tècnic d'Apple. Germaaaaaaan, tu representes l'alegria de la saleta. La teva positivitat es transmet, i feia que el dia a dia fos més divertit. M'ho he passat molt bé sent el teu compi de taula durant aquests anys. Gràcies per tots els moments i, també, per "el calvo de Menorca", la contrasenya que obre moltes portes a la Barcelona nocturna. Laura, la única del grup amb qui podia rajar del Bartorossellisme, riure amb els tweets de @JaumeTorres14 o comentar l'actualitat basquetbolística, ha sigut molt guay compartir tota la tesi amb tu. El mateix dic per tu, Nunu! Has sigut la nostre font de plans hipsters i alternatius. Qui ens diria quan vam començar el màster ja fa gairebé 7 anys que acabariem fent la tesi junts! Cris, empezamos juntos y terminamos juntos. Gracias por esa fuerza e iniciativa que tienes, por estar siempre dispuesta a ayudar y por todas las horas que has pasado contando colonias por mi culpa. Titooo, ¿que decir de ti? Has sido fuente de grandes momentos (las clases de boxeo con German, tu impecable negociación para comprar 20 rosas por 15 euros y muchos otros). ¡Con German formabais el mejor tándem de calvos nunca visto! Alba, Mire, vosotras erais la base de la torreta. Cuántas horas de momentos divertidos pasamos allí. Gracias por estar siempre, por esa alegría, ganas de hacer cosas y capacidad para convencer a los más indecisos para que se unieran al grupo. Vuestra presencia en el grupo hizo que hacer la tesis fuera mucho más divertido. Tampoc em puc oblidar de tu, Peri. Vas ser molt important al meu inici (fins i tot em vas ajudar a trobar pis!) i les escapades a Cal Xena per provar la millor sopa de ceba del món quedaran sempre al meu record. ¡Mario, el rey de los jueves por la tarde (y a veces noche)!. Gracias por mostrarnos dónde bailar salsa o cantar flamenquito en Barcelona. Siempre que apareces (aunque sea en cuentagotas) la diversión está asegurada. Tony, aunque empezases tímido te hemos acabado descubriendo. Tus comentarios alegraban las comidas y horas del café. Y Patri, gracias por ser la artista de nuestro grupo. Pau, tot i no compartir molt laborator amb tu, sempre era molt interessant escoltar la teva visió de la ciència. I arriba el torn de la nova guardia. Coral, mi "padawan", espero que estos polímeros no te vuelvan loca y que no me echas en cara todos los marrones en los que te he metido. Roberta y Elena, aunque no hayamos podido coincidir mucho tiempo juntos, gracias por vuestro trato amable siempre que hemos coincidido en la salita. I Glòria, Laura i Mònica, les recents incorporacions, molta

sort en el que us queda per endavant. Gràcies Irene i Elena, per oferir-vos a donar un cop de mà sempre que ho necessitava. I, finalment, gràcies Núria i Marina. Sou l'engranatge que fa que tot funcioni. Gràcies per la vostra ajuda i el vostre bon tracte cap a mi!

I would also like to thank all the people from the Physical Intelligence group of the MPI. You integrated me in the group since the first day and I felt really comfortable in it. First of all, thanks to Ugur, Devin and Oncay for being part of the project. I think we made an amazing team together. You always offered your help when we needed it and you were indispensable for the final success of the project. I enjoyed a lot working and learning with you, guys! Thank you Hamed and Amir for all the lunches, tea times, bowling games and many more plans we did together. You always counted on me for everything, and I really appreciate that. Utku, despite at the start you don't wanted me in the office, I think that at the end you enjoyed it. It was really fun to discover your sense of humour. I passed a lot of good and funny moments with you in that office. Donghoon, Martin, Yunusa and Berk, it was fun to discover the Stuttgart nightlife with you. You showed me a lot of cool places where we enjoyed good moments together. Ville, Josh, Varun and Jack, colleagues of the "Chicken Thursday", thanks for all the interesting talks during lunchtimes. And Dirk, thank you for your kindness, for inviting me to your house and, the most important, to show me how a true Schwabavian serves the Hefeweizen. Thanks Alp, Birgul, and Ceren for being always so kind to me! And also thanks Nagarash and Anita for all the help you gave me in the Nanoscribe.

Gaurav (or Garup?) what should I say about you? Thank you for all the nights in the PhD room watching movies or playing boardgames, all the Ping Pong games and, in summary, to be always available to pass time with me. Gonçalo, I still remember the Insektburger of the first time we met in the Guesthouse, or the visit with Gaurav to the Hohenzollern Castle (or should I say Winterfell castle?). Pietro and Mateo, the Italian twins. Together with Gaurav and Gonçalo you were the hard core of the group. We passed a lot of good moments together that I will always remember. Also thank you Lina, Efe, Charlotte and Karla. A lot of good memories come to my mind when I remember the time spent with you in that PhD room.

Wiltons, encara que fora del lloc de treball heu sigut vitals en aquests darrers 4 anys. Munic, Manchester, Colònia i Stuttgart (menció especial al porter del Schoken) han sigut pit-stops necessaris que m'ajudaven a recargar energies i tornar amb més ganes (tot i que els dilluns

post-viatge eren durs...). Gràcies per la vostra amistat i per estar sempre allà. I Mireia, Ramon, Judit, Iker i Alberto, gràcies també per la vostra amistat i per tots els moments viscuts.

Pascu, són ja 10 anys a IQS, i sobretot aquest dos últims han sigut intensos. A principi d'any vam viure "els millors moments de la nostra vida" junts fins que el virus ens va retirar. Però en quin moment estàvem! Gràcies per la infinitat de moments viscuts, per les converses on salvàvem el Barça o Catalunya (en 20 anys ja parlem per presentar-nos a algo), per ser un digne rival del FIFA i per ensenyar-me el camí a través del gurú General Fórceps.

I acabo amb el cercle més pròxim. Papes, gràcies per el suport incondicional, per deixar-me fer sempre el que m'ha semblat i per la educació que m'heu donat, sense la qual segur que no hagués arribat on sóc ara mateix. Gràcies també Marta, veure't forta en les situacions que t'ha tocat viure ha sigut també una font d'inspiració per lluitar per aquesta tesi. I Mireia, què puc dir que no sàpigues? Gràcies per aguantar-me quatre anys més, per aportar-me alegria dia rere dia i, en definitiva, per ser com ets i estimar-me tal com sóc.

Pol Cabanach Xifró, 3 de Març de 2021

This thesis has been done thanks to the fellowship grant of personal novice investigator (FI) SUR funded by the DEC of the Government of Catalonia and the European Social Fund.

Credentials:

2017 FI_B 00642

2018 FI_B1 00172

2019 FI_B2 00165



This thesis has also received fund from Max Planck Gesellschaft Stipend.



MAX-PLANCK-GESELLSCHAFT

Abstract

Body response to biomaterials suppose a major roadblock for the effectiveness of multiple biomaterial-based therapies. Via unspecific absorption of biomolecules, barriers such as immune system or mucosal surfaces clear foreign materials from the body, preventing them to reach their target and perform their function. Zwitterionic materials have emerged in the last years as promising antifouling materials to overcome the mentioned barriers. Although many systems have used zwitterionic materials as coatings, the unique properties of superhydrophilicity and chemical versatility suggest multiple benefits of using zwitterionic polymers as bulk materials.

Here, two different systems based on zwitterionic materials are presented. In first place, an antifouling drug delivery platform based on zwitterionic amphiphilic polymers (ABC) is developed. Zwitterionic ABCs are synthesized and optimized to self-assemble in zwitterionic nanoparticles. The antifouling properties of zwitterionic nanoparticles are proved, together with their potential to become an oral drug delivery system. Next, the system is used as a drug carrier for antimalarial and anticancer drugs. Nanoparticles show internalization in Plasmodium infected erythrocytes, and curcumin-loaded nanoparticles prove their antimalarial efficacy *in vitro*. Oral absorption of polymer and curcumin is also observed *in vivo* using mice model, indicating the potential of this system to become oral therapy against malaria. When optimizing the system for anticancer therapy, Paclitaxel-loaded nanoparticles exhibit anticancer activity in *in vitro* cancer cell models.

Second, non-immunogenic stealth zwitterionic microrobots that avoid recognition from immune cells are introduced. Zwitterionic photoresist are developed for the 3D microprinting of zwitterionic hydrogel microrobots through 2-photon polymerization with ample functionalization: tunable mechanical properties, anti-biofouling and non-immunogenic properties, functionalization for magnetic actuation, encapsulation of biomolecules, and surface functionalization for drug delivery. Stealth microrobots avoid detection by macrophage cells of the innate immune system after exhaustive inspection (> 90 h), which has not been achieved in any microrobotic platform to date. These versatile zwitterionic materials eliminate a major roadblock in the development of biocompatible microrobots, and will serve as a toolbox of non-immunogenic materials for medical microrobot and other device technologies for bioengineering and biomedical applications.

Table of Contents

<i>Agraïments – Acknowledgements</i>	<i>I</i>
<i>Abstract</i>	<i>IX</i>
<i>Table of Contents</i>	<i>XI</i>
<i>List of Figures</i>	<i>XV</i>
<i>List of Tables</i>	<i>XIX</i>
<i>Table of Abbreviations</i>	<i>XXI</i>
<i>Chapter 1: Motivation and Aims</i>	<i>3</i>
<i>Chapter 2: Synthesis and Characterization of Zwitterionic Amphiphilic Polymers</i>	<i>13</i>
<i>2.1. Introduction</i>	<i>13</i>
<i>2.2. Results and Discussion</i>	<i>21</i>
2.2.1. Selection of the Synthesis pathway	<i>21</i>
2.2.2. Synthesis of PBMA- <i>b</i> -PSBMA copolymers	<i>25</i>
2.2.3. Characterization of the ability of PBMA- <i>b</i> -PSBMA to form Amphiphilic Nanoparticles: UCST and Salt Responsiveness.....	<i>28</i>
2.2.4. Overcoming the UCST: Synthesis and characterization of PBMA- <i>b</i> -PMESBMA polymers	<i>39</i>
2.2.5. Synthesis and Characterization of PBMA- <i>b</i> -PCBMA polymers	<i>47</i>
<i>2.3. Concluding Remarks</i>	<i>52</i>
<i>Chapter 3: Applications of Zwitterionic Amphiphilic Block Copolymers</i>	<i>55</i>
<i>3.1. Introduction</i>	<i>55</i>
<i>3.2. Results and Discussion</i>	<i>60</i>
3.2.1. Characterization of the interaction between BSA and zwitterionic nanoparticles.....	<i>60</i>
3.2.2. Internalization of the zwitterionic nanoparticles in a gastrointestinal epithelium model	<i>63</i>
3.2.3. Capacity of zwitterionic nanoparticles to pass through the mucus.....	<i>66</i>

3.2.4. Curcumin encapsulation for antimalarial applications	68
3.2.5. Antimalarial characterization of curcumin-loaded zwitterionic nanoparticles	73
3.2.6. Zwitterionic nanoparticles against cancer	83
3.3. Concluding Remarks	90
Chapter 4: Zwitterionic Stealth Microrobots	95
4.1. Introduction	95
4.2. Results and Discussion.....	99
4.2.1. Development of a zwitterionic photoresist	99
4.2.2. 2-Photon Polymerization 3D microprinting of zwitterionic photoresists	102
4.2.3. Bio-adhesion characterization of the zwitterionic microrobots	106
4.2.4. Zwitterionic non-immunogenic microrobots.....	109
4.2.5. Magnetically actuated zwitterionic microrobots.....	114
4.2.6. Biomolecule encapsulation.....	116
4.2.7. Surface functionalization of the zwitterionic microrobots	118
4.3. Concluding Remarks	121
Chapter 5: Conclusions.....	125
Chapter 6: Materials and Methods	131
6.1. Methods of Chapter 2.....	131
6.1.1. Synthesis of Poly(Butyl methacrylate-b-sulfobetaine methacrylate) (PBMA-b-SBMA).....	131
6.1.2. Synthesis of Poly(Butyl methacrylate-b-sulfobetainized morpholinoethyl methacrylate) (PBMA-b-MESBMA)	131
6.1.3. Synthesis of Poly(Butyl methacrylate-b-carboxybetaine methacrylate) (PBMA-b-CBMA)	132
6.1.4. Formation of zwitterionic nanoparticles	132
6.1.5. DLS Characterization.....	132
6.1.6. Cryogenic Transmission Electron Microscopy (Cryo-TEM) analysis.....	133
6.2. Methods of Chapter 3.....	133
6.2.1. Differential Scanning Calorimetry (DSC) analysis	133
6.2.2. Modification of Zwitterionic polymers with Cy3	133
6.2.3. Caco-2 cell culture	134
6.2.4. Caco-2 internalization experiment	134
6.2.5. Multiple particle tracking (MPT) analysis	134

6.2.6. Curcumin encapsulation	136
6.2.7. P. falciparum cultures and in vitro growth inhibition assays	136
6.2.8. Targeting analysis	137
6.2.9. Body weight loss analysis.....	137
6.2.10. Hemolysis tests	138
6.2.11. In vivo antimalarial assays	138
6.2.12. In vivo determination of polymers in pRBCs after oral administration	138
6.2.13. Paclitaxel (PTX) encapsulation	139
6.2.14. HeLa cell line culture.....	139
6.2.15. Incucyte [®] live-cell analysis.....	139
6.2.16. MTT toxicity assay.....	140
6.2.17. Introduction of S12 targetting peptide.....	140
6.2.18. U87 cell culture	140
6.2.19. S12 targetting evaluation	141
6.3. Methods of Chapter 4	141
6.3.1. Synthesis of carboxybetaine methacrylate (CB)	141
6.3.2. Synthesis of sulfobetaine methacrylate (SB)	141
6.3.3. Synthesis of carboxybetaine dimethacrylate (CBX)	141
6.3.4. Synthesis of sulfobetaine dimethacrylate (SBX)	142
6.3.5. UV photopolymerization of zwitterionic photoresists.....	143
6.3.6. 3D microprinting (two-photon polymerization)	143
6.3.7. J774A.1 and THP-1 cell culture conditions.....	144
6.3.8. J774A.1 Cell Culture	144
6.3.9. THP-1 Cell Culture	144
6.3.10. Murine Spleen Isolation/Harvest.....	144
6.3.11. Cell viability of ZW hydrogels.....	145
6.3.12. Cell adhesion on ZW hydrogels.....	146
6.3.13. Protein adsorption on ZW microrobots	146
6.3.14. Cell inspection of microrobots.....	146
6.3.15. Scanning Electron Microscopy.....	147
6.3.16. Magnetic actuation of microrobots	147
6.3.17. Biomolecule encapsulation in 3D-printed zwitterionic microstructures	147
6.3.18. Microrobot functionalization for light-triggered controlled drug release.....	148
Chapter 7: Bibliography.....	151

List of Figures

Figure 1.1 Schematic of the stages of Foreign Body Response (FBR) for nano-micro scale materials and macroscale.	5
Figure 1.2 Natural zwitterions and zwitterionic polymers	8
Figure 2.1. Self-assembly of Amphiphilic polymers.....	14
Figure 2.2 (a) Chemical structure of Chain Transfer Agent (CTA), (b) reversible addition/fragmentation Transfer of the CTA, (c) Chain equilibration/propagation in RAFT polymerization and (c) creation of block copolymers by the reactivation of the macro-CTA and addition of new monomers.	19
Figure 2.3 Synthesis route of Zwitterionic Amphiphilic Block Copolymers.....	22
Figure 2.4 H^1 - NMR of (a) PBMA (in $CdCl_3$), (b) PBMA- <i>b</i> -PDMAEMA (in $CdCl_3$) and (c) PBMA- <i>b</i> -PSBMA (in TFA- <i>d</i>).....	26
Figure 2.5 Antipolyelectrolyte effect in polyzwitterions.....	29
Figure 2.6 Translucid aspect of SB1.1 polymer (0.8 mg/ml) after 12h of steering in NaCl 1M.	30
Figure 2.7 Extrusion process to produce nanoparticles.....	31
Figure 2.8 Graphical representation of the Table 2.2 data ($n=3$).....	32
Figure 2.9 Stability measurements of SB1 ($n=3$).	35
Figure 2.10 Cryo-TEM images of SB1 nanoparticles and histogram of the size count. Histograms have been made by counting 100 nanoparticles.	36
Figure 2.11 Cryo-TEM images of Poly(ethylene glycol)-co-poly(butadiene) polymersomes [91] in which it can be clearly observed the polymer bilayer of the polymersomes.....	37
Figure 2.12 Our hypothesis about the nanoparticle type of SB1. Before extrusion, we have aggregated micelles (due to antipolyelectrolyte effect). After extrusion, these aggregates are broken, forming smaller aggregated micelles of nanometer size.....	38
Figure 2.13 Study of Laschewsky and coworkers on the UCST of different sulfobetaine homopolymers [85].....	40
Figure 2.14 Introduction of a voluminous pendant group in the quaternary amine in order to avoid collapse.	41
Figure 2.15 H^1 - NMR of (a) PBMA (in $CdCl_3$), (b) PBMA- <i>b</i> -PMEMA (in $CdCl_3$) and (c) PBMA- <i>b</i> -PMESBMA (in $CdCl_3$).....	42
Figure 2.16 Z-Potential of the different PBMA- <i>b</i> -PMESBMA nanoparticles ($n=3$).	46
Figure 2.17 Cryo-TEM analysis of the three PBMA- <i>b</i> -PMESBMA samples. Histograms have been done by counting 100 nanoparticles.	47
Figure 2.18 Synthesis of PBMA- <i>b</i> -PCBMA polymers.	48

Figure 2.19 H^1 -NMR spectra of (a) PBMA (in $CdCl_3$), (b) PBMA- <i>b</i> -PDMAEMA (in $CdCl_3$) and (c) PBMA- <i>b</i> -PCBMA (in $CdCl_3$), the different steps in the synthesis of PBMA- <i>b</i> -PCBMA.	49
Figure 2.20 Z-Potential of PBMA- <i>b</i> -PCBMA nanoparticles ($n=3$).	51
Figure 3.1 Role of nanoparticle's surface chemistry in the interaction with the mucus.	57
Figure 3.2 DSC thermograms used to characterize the interaction between nanoparticles and BSA.	61
Figure 3.3 Trithiocarbonate aminolysis used to include the Cy3 fluorophore molecule to the polymers produced.	64
Figure 3.4 Fluorescence microscopy images of Caco-2 cells incubated 6 hours with the different zwitterionic nanoparticles (488/532 laser line.).....	65
Figure 3.5 MPT analysis of the different zwitterionic nanoparticles in mucus.....	67
Figure 3.6 Curcumin encapsulation in the different zwitterionic nanoparticles.	70
Figure 3.7 Encapsulation of Curcumin..	72
Figure 3.8 Flow cytometry analysis of the interaction between Cy3-labeled zwitterionic nanoparticles and pRBC (which DNA was labeled with Hoescht).	74
Figure 3.9 Confocal Microscopy of the samples containing pRBC and Cy3-labeled zwitterionic nanoparticles. (A) Images of the different microscopy lines for 2 positions of each polymer. (B) time-lapse of S1 polymer.	75
Figure 3.10 Cytometry assay of the curcumin-loaded zwitterionic particles in contact with pRBCs... ..	77
Figure 3.11 <i>P. falciparum</i> Growth Inhibition Assay (GIA) of curcumin-loaded zwitterionic polymers.	78
Figure 3.12 Body weight change of mice injected with different sulfobetaine nanoparticles. ($n=4$).. ..	79
Figure 3.13 Hemolysis test for the different sulfobetaine polymers ($n=3$).	80
Figure 3.14 Survival of the different groups of <i>P. yoelii</i> -infected mice after the administration of curcumin ($n=4$).	81
Figure 3.15 Confocal fluorescence microscopy analysis of the presence of orally administered Cy3-PBMA-MESBMA in pRBCs of a <i>P. yoelii</i> -infected mouse.	82
Figure 3.16 Characterization of the antitumoral activity of PTX-loaded zwitterionic nanoparticles using Incucyte® Live cell analysis..	85
Figure 3.17 MTT of HeLa cells treated with PTX-loaded NPs.....	87
Figure 3.18 Targetting of C1 nanoparticles. (A) introduction of the targetting moiety by NHS/EDC coupling of the carboxylic group from the carboxybetaine. (B) Evaluation of the targetting capacity of the modified NPs using U87 cell line.	89
Figure 4.1 (A) Challenges for Medical microrobots [178] and (B) some strategies of locomotion and control [162].	96
Figure 4.2 Synthesis of (A) Zwitterionic monomers and (B) crosslinkers. (C) H^1 -NMR of the CB and SB monomers. (D) H^1 -NMR of CBX and SBX crosslinkers.....	100
Figure 4.3 Photorheological characterization of the polymerization of the different photoresists. .	101

Figure 4.4 *Difference in the printing area between 1-photon polymerization and 2-photon polymerization (absorption image was obtained from www.microlight.fr).* 103

Figure 4.5 *2PP printing of the Zwitterionic photoresists.* 105

Figure 4.6 *Viability assay performed with the different zwitterionic photoresists (n=3). (A) WST-8 assay (B) Live/Dead staining and J774A.1 murine macrophages.* 106

Figure 4.7 *J774A.1 murine macrophage adhesion to zwitterionic photoresists.* 107

Figure 4.8 *Fluorescence microscope images of the different microrobots incubated with Cy5-BSA.* 108

Figure 4.9 *Zwitterionic Stealth Microrobots.* 110

Figure 4.10 *SEM images of the interaction between macrophages and the S30 and PEG microrobots.* 111

Figure 4.11 *SEM images of (a) LPS-stimulated macrophages and (b) non-stimulated macrophages.* 112

Figure 4.12 *S30 microrobot arrays co-cultured with macrophages, monocytes and splenocytes for 24h.* 113

Figure 4.13 *Magnetic actuation of the zwitterionic helical microrobots.* 115

Figure 4.14 *Drug and biomolecule encapsulation in zwitterionic 3D printed microhydrogels.* 117

Figure 4.15 *Fluorescence microscope images of Cy5-amine modified C30 microrobots and bare C30 microrobots.* 118

Figure 4.16 *On-demand light-triggered release of Doxorubicin.* 119

List of Tables

Table 2.1 PBMA-b-PSBMA polymers synthesized.	27
Table 2.2 Results of DLS of the samples prepared by extruding the dispersed polymer solutions through a filter of 200 μm (n=3).	32
Table 2.3 PBMA-b-PMESBMA polymers synthesized.	43
Table 2.4 Results of DLS of the samples prepared by different methods (n=3). Centrifugation of M1 sample was performed at 6000 g and extrusion was performed with a pore size of 100 μm	44
Table 2.5 PBMA-b-PCBMA synthesized.....	50
Table 2.6 Hydrodynamic Size of PBMA-b-PCBMA nanoparticles (n=3).....	50
Table 3.1 T_m of BSA in a native form and in contact with the two nanoparticles tested (with zwitterionic and cationic surface).	63
Table 3.2 Data from the MPT analysis.....	67
Table 3.3 Data of the curcumin encapsulation in the different zwitterionic nanoparticles produced. (native curcumin solubility in PBS is taken from [144]).....	71
Table 3.4 Encapsulation of PTX in the different zwitterionic nanoparticles (*[Polymer] =10 mg/ml).	84

Table of Abbreviations

(H¹)-NMR	(proton) Nuclear Magnetic Resonance
1,3-PS	1,3-PropaneSultone
2PA	2-Photon Absorption
2PP	2-Photon Polymerization
ABC	Amphiphilic Block Copolymer
ATRP	Atom Transfer Radical Polymerization
BMA	Butyl MethaAcrylate
BSA	Bovine Serum Albumin
C-6	Coumarin-6
CB	CarboxyBetaine
CBMA	CarboxyBetaine MethAcrylate
CMC	Critical Micelle Concentration
CRP	Controlled Radical Polymerizations
CTA	Chain Transfer Agent
DDS	Drug Delivery System(s)
DLS	Dynamic Light Scattering
DMAEMA	<i>N,N</i>-DiMethyl(AminoEthyl) MethAcrylate
DOX	DOXorubicin
DSC	Differential Scanning Calorimetry
EPR	Enhanced Permeability and Retention
EPR	Enhanced Permeation and Retention
FDA	Food and Drug Administration
GB	Glycine Betaine
GIA	Growth Inhibition Assay
GIT	GastroIntestinal Tract
HFIP	HexaFluoroIsoPropanol
LAP	Lithium phenyl-2,4,6-trimethylbenzoylphosphinate
MESBMA	Morpholino Ethyl Sulfobetaine Methacrylate
MPC	2-Methacryloyloxyethyl PhosphorylCholine
MPS	Mononuclear Phagocyte System

MPT	Multiple Particle Tracking
MSD	Mean Square Displacement
MTT	3-(4,5-diMethylThiazol-2-yl)-2,5-diphenylTetrazolium bromide
NMP	Nitroxide-Mediated radical Polymerization
NP	NanoParticle
P-NIPAAm	Poly-N-IsopropylAcrylAmide
PBS	Phosphate Buffer Saline
PEG	Poly(Ethylene Glycol)
PEGDA	Poly(Ethylene Glycol) DiAcrylate
PMPC	Poly(2-Methacryloyloxyethyl PhosphorylCholine)
pRBC	Parasitized Red Blood Cell(s)
PTX	PacliTaxel
QDMAEMA	Quaternized DiMethyl(AminoEthyl) MethAcrylate
RAFT	Reversible Addition-Fragmentation Transfer
SB	SulfoBetaine
SBMA	SulfoBetaine MethAcrylate
SPION	Small Paramagnetic Iron Oxide Nanoparticle
TEM	Transmission Electron Microscopy
TFA	TriFluoroAcetic acid
TFE	TriFluoroEthanol
Tm	Thermal Transition Midpoint
TMAO	TriMethylAmine N-Oxide
UCST	Upper Critical Solution Temperature

Chapter 1: Motivation and Aims

Chapter 1: Motivation and Aims

The use of materials for medical applications has been present through all humankind history. It began in ancient times, with the use of natural materials such as wood to replace injured parts of the body and evolved in the 1940s, when pioneer physicians started using non-medical oriented synthetic materials that replaced the natural ones. That brought scientists to ask themselves if the physical and chemical properties of these materials determined the body response to them, which led to the birth of Biomaterial Science in 1970s [1–3]. Since then, the biomaterials field has experienced an exponential growth, converging with other disciplines such as engineering, physics, molecular biology or genomics to become a +\$300-billion market that saves thousands of lives every year and improves our quality of live [4,5].

The biomaterials field has been characterized for having a high scientific output over all its history (nowadays, more than 10,000 publications are published every year and a high number of patents are requested [3]). All this research resulted in an evolution of biomaterial's designs, functions and applications. The first biomaterials were designed to be bioinert (not interact with body tissues) and to have a mechanical function (i.e. knee/hip prosthesis). But, with the molecular biology revolution in 1970s and genomics/proteomics in 1990s, a second generation of bioactive materials appeared, in which the paradigm changed and materials were designed to interact with the body in order to induce a therapeutic effect. Drug eluting medical devices, drug delivery systems and biodegradable implants were developed during this second generation of biomaterials, enabling a wide spectrum of applications for treating diseases that were uncurable until then. And recently, a third generation of biomaterials is arising, trying to develop materials that, when placed in the body, interact with the surrounding tissue and recruit cells to perform an active function in our body. If achieved, these materials would suppose a revolution in the medical field.

Although one could think that this evolution would have an immediate effect on the impact of biomaterials in clinics, the reality is that we are still far from this scenario. Most of the current biomaterials used in medicine are not so different to the ones created in the 1970s [5], meaning that all the work and money comprised in the hundreds of thousands of publications during the last decades has a limited impact in the current standards of clinical medicine.

Although there are multiple logistic factors that have influence on the inability of medical devices to reach the market (a strong regulation on medical devices and drugs, the absence of proper disease models or the lack of communication between scientists and doctors), the body response to external materials supposes a major scientific challenge to solve in order to achieve a better translation of biomaterials from the laboratory to clinics. This body response, normally produced due to the stimulation of the immune system of our body by the biomaterial, supposes the fall of a large number of biomaterials in the clinical trials in which they are neutralized and loss their efficiency or produce immune reactions. Therefore, the study of the body response to biomaterials and the development of immune evasive materials is crucial to overcome this major roadblock of the biomaterials field.

During millions of years of evolution, mammals have developed a complex immune system optimized to identify and destroy any harmful organism/cell/material present inside their body. This immune system is also helped by different barriers such as epithelia, gastrointestinal mucus barrier or blood brain barrier that prevents the pass of potentially harmful materials to different sensible parts of it [6]. All these defenses sort the harmful materials from the non-dangerous ones by surface effects. When a material is placed in the body, a layer of proteins is formed instantly in the surface of it, producing the so-called protein corona [6–8]. The corona is formed due to interactions between the material's surface and the proteins found in plasma and, therefore, the chemistry on the surface of the materials will determine the size and composition of it. Macrophages, immune system cells specialized to remove harmful materials from the body, can recognize the protein's corona composition and, if detected as dangerous (proteins are denaturalized or strongly attached), they proceed to phagocytize the material [9]. When the material is small enough (e.g. nanoparticles, microparticles), the macrophage phagocytize it and the material is removed from blood and eliminated [10]. But if the macrophages cannot phagocytize a material due of its size, a capsule surrounding the material is formed, isolating it from the tissues. This phenomena is called the foreign body response (FBR, **Figure 1.1**) [8].

In the first generation of biomaterials (in which a mechanical function and bioinert properties were desired), the recognition of biomaterials by the immune system was not seen as a problem but as something positive. The formation of FBR was considered a favorable reaction, because the existence of the capsule prevented possible toxicity or reverse effects of

the materials to the surrounding tissues. But with the appearance of biomaterials with more complex functions (second and third generation), the interaction of the biomaterial with cells and/or environment is needed. And this interaction cannot occur if the material is neutralized by the immune system. This fact explains the problems that complex biomaterials such as drug delivery systems, biosensors or cardiovascular implants are experiencing to reach the clinical use.

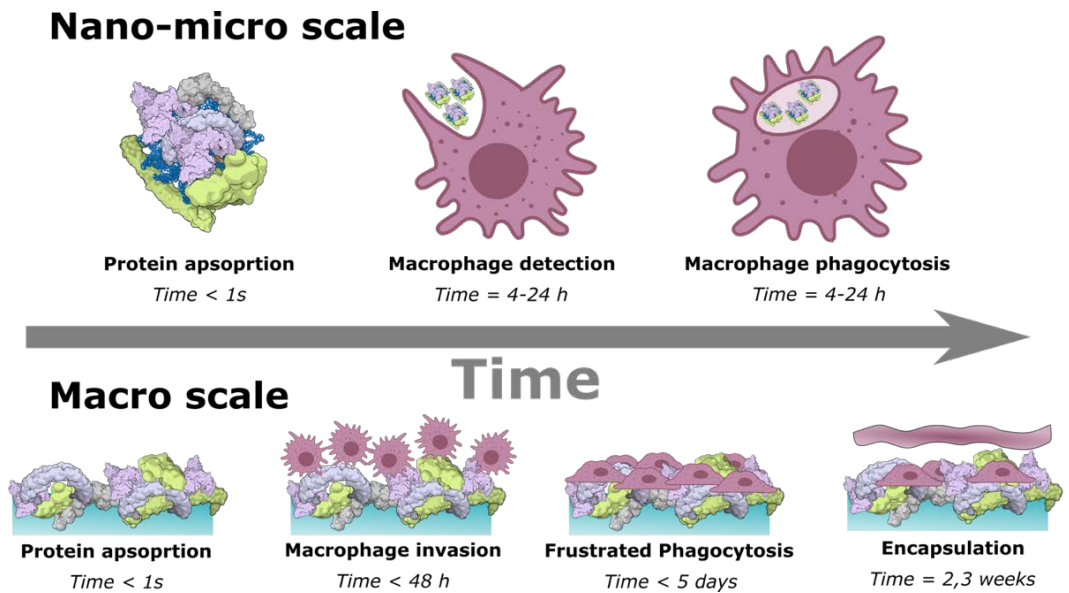


Figure 1.1 Schematic of the stages of Foreign Body Response (FBR) for nano-micro scale materials and macroscale.

For all the reasons commented above, scientists have focused on the design of materials that can bypass the immune system and, therefore, perform complex functions in the body. And the main strategy that has been used to prevent the neutralization of a material by the immune system has been to avoid the immune detection. Thus, antifouling materials with the capacity to resist the protein adsorption and consequently the immune detection have drawn the attention of the biomedical field during the past decades [2,3,11].

The first antifouling materials were found through an experimental observation, by trial and error or serendipity. But a systematic analysis was necessary to understand how materials interacted with proteins. This analysis was performed by Whitesides' group in 2001

[12], when they analyzed up to 60 known non-fouling surfaces and determined 3 common properties that all the antifouling materials shared: (i) they were hydrophilic (polar), (ii) they had zero net-charge and (iii) they contained H-bond acceptors groups but not H-bond donor groups .

With these three rules, some light was shed on the interaction protein-material. If the material presents a hydrophobic surface, host proteins denaturalize and aggregate in the surface due to hydrophobic effect [13]. If the surface is charged, there are interactions with oppositely charged regions of proteins [14]. Then, an antifouling surface has to be hydrophilic and neutrally charged to avoid interactions with proteins. But other than only the surface properties, Whitesides empathized in the interactions with the material surface and water (the rule about the H-bonds). The more water interacts with the surface of the material, less proteins will be absorbed into it.

Among all the surfaces studied in Whitesides' work, poly(ethylene glycol) (PEG) outshined as the most promising antifouling. The non-fouling properties of this polymer were discovered in 1983 [15,16] and gained great notoriety in the field in 1990, when the first PEGylated protein (Pegadamas) for the treatment of severe combined immune-deficiency (SCID) was developed [17]. In 1995, the interest for these polymers increased even more when it was used in the first FDA approved Drug Delivery System, Doxil® (Doxorubicin loaded PEGylated liposomes for the treatment of Kaposi's Sarcoma) [18]. Since then, PEGylation has been the "gold standard" to provide non-fouling properties to surfaces and avoiding its immunogenicity [19–22].

PEG's antifouling properties comes from its non-charged hydrophilic nature and the presence of repetitive ether bonds (H-bond acceptors) that generate a stable hydration layer around the polymer. Also, it has been proved that part of the antifouling of PEG comes from the mobility of their chains, that prevents the approximation of biomolecules to the surface and increases its hydration [23]. However, in the last years there have appeared some drawbacks regarding PEGylation in clinics. Although early preliminary results showed the absence of immune response to PEGylated drugs, PEG-induced immune response and anti-PEG antibodies have been reported in the last years [24–28]. These results can be explained by the recent claims that PEG is not a hydrophilic polymer but an amphiphilic one (they have

repeated units of an hydrophilic ether group and two hydrophobic methylene groups), proved by its solubility on organic solvents such as acetonitrile or chloroform apart from water [24,29]. The amphiphilicity of PEG also generates problems in the stability of the systems, such as the decrease of activity of some PEGylated proteins [30] and the destabilization of liposomes [31].

These evidences make necessary the search for new antifouling surfaces with a better performance of PEG, as they are needed not only to bring new therapeutics and medical devices to clinics, but also they may be needed in the near future for these approved PEGylated therapies in case that more issues with PEG allergies appear. In this scenario, zwitterionic polymers have emerged as one of the most promising strategies to become the substitute of PEG as gold standard for antifouling surfaces [32]. These polymers consist in polymer chains that contain both positive and negative charges at equal ratio. By having these repeated charges, the polymer has a high charge density, but at the same time they do not present net charge. This fact is important because they can strongly interact with water, as the ion-dipole interaction is stronger than the dipole-dipole interaction (they show a 8-fold increase in the water molecules bonded in comparison to PEG [33,34]). But they are at the same time neutral, preventing possible interactions with charged host proteins.

Zwitterions are abundantly present in nature, normally having functions related to proteins. Amino acids, the building block of proteins, are zwitterionic molecules at neutral pH, as they have a positive charge in the amine and a negative in the carboxylic acid. Simple zwitterionic molecules such as glycine betaine (GB) and Trimethylamine N-oxide (TMAO) (**Figure 1.2**) are present in plants and animals acting as osmolytes. Their function is to regulate osmotic pressure and to avoid protein denaturalization due to extreme conditions in heat, salt concentration or pressure [35,36]. For example, TMAO is used by different organisms to counteract the effect of urea in the denaturalization of proteins [37]. It has also been proved that the exposed residues of proteins have a high abundance of lysin, glutamate and aspartate, generating a pseudo-zwitterionic surface with equal positive and negative charges on it. These amino acids are more present in chaperones and blood proteins, which are characterized by being in protein-rich environment, where they have to avoid aggregation and denaturalization (in the case of chaperones, their function is to refold misfolded proteins) [38,39]. Finally, phosphocholine groups are present in the cell membrane of animals. All the

functions of these natural zwitterions show how they have an active role in avoiding protein denaturalization and, therefore, that zwitterionic polymers are interesting candidates for generating bioinspired antifouling materials.

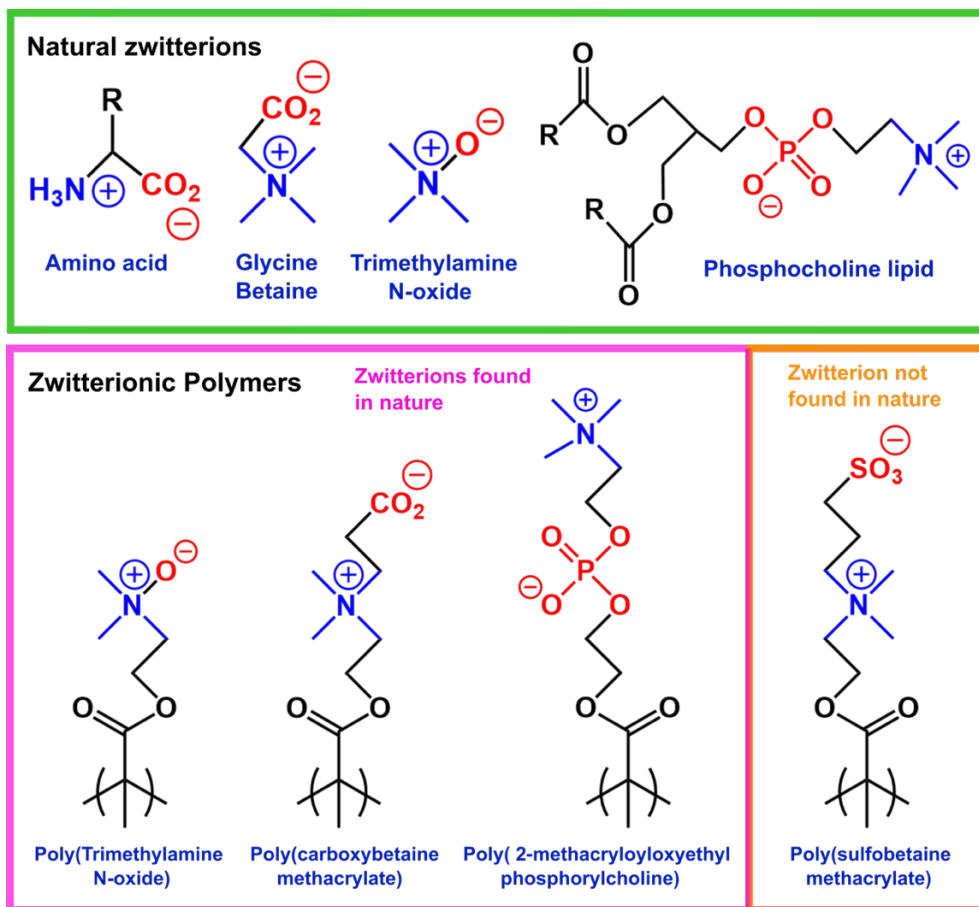


Figure 1.2 Natural zwitterions and zwitterionic polymers

It has been proved that zwitterionic polymers can avoid protein absorption, achieving <0.3 ng/cm² of protein adhesion in single protein solution and complex media [40–42]. And some zwitterionic polymers have showed the same capacity that osmolytes for stabilization of proteins and prevention of aggregation [43,44].

The first synthetic zwitterionic polymer used in the biomedical field was Poly(2-methacryloyloxyethyl phosphorylcholine) (Poly(MPC)), synthesized by Nakabayashi's group

in 1976 [45]. Back then, the term “zwitterionic polymer” was not invented yet. By observing the cell membrane, Nakabayashi thought that if a non-thrombogenic material was desired, the surface of the material should be as similar as possible to cell membranes. They synthesized a polymerizable monomer mimicking the phosphocholine group of cell membranes. During a decade, the synthesis of MPC was not efficient enough to fully test its performance as non-fouling material. In 1990, Ishihara and Nakabayashi optimized the synthesis [46] and allowed the scalation to industrial production in Japan in 1999. Nowadays the factory is still working, producing 40 tons of MPC every year that are being used in cardiovascular and ophthalmological devices [47].

Since then, the interest in zwitterionic polymers have increased and new zwitterionic polymers have been described. Together with MPC, two other groups have become the most used zwitterions in the recent years. Their development was motivated by the difficult and expensive synthesis of MPC and for the search of other functionalities [48]. These two zwitterionic groups are sulfobetaine and carboxybetaine (**Figure 1.2**). Sulfobetaines are zwitterions not present in nature, and are composed of a quaternary ammonium cation and a sulfonate anion. They have been proved to be more stable than the phosphocholine and carboxybetaine group [48]. Polysulfobetaines have also attracted attention by their upper critical solution temperature (UCST) around physiological temperature (35-45 °C), which makes them attractive for designing temperature responsive materials. On the other hand, polycarboxybetaines are inspired in glycine betaine, and have a quaternary ammonium as cation and a carboxylic acid as anion. They are the most hydrophilic zwitterion and has the advantage that can be easily to functionalize through activation of the carboxylic acid [42]. Also, in the last year, a new type of zwitterionic polymers inspired in TMAO has been developed by Jiang’s group, and its antifouling and biocompatibility properties have been proved [49].

This development of new zwitterionic polymers together with the understanding of their mechanism has resulted in a growing interest in these polymers for biomedical applications. They are being used as antifouling materials in multiple cases, such as medical device coatings, biosensors, drug delivery systems or soft tissue implants [32,50]. In the vast majority of these applications, zwitterionic polymers are used as coatings. They are synthesized in a way that they can be attached (covalently or physically) to a biomaterial to form a zwitterionic

layer in its surface. This layer prevents the protein absorption and, therefore, the immune response generated by the biomaterial. Although this technology is widely used, it presents some drawbacks that prevents their use in some other applications. It supposes an extra step in the development of the material, it needs to be uniform in all the material surface and it can be degraded or damaged during its use, among others.

Trying to enlarge the range of application of zwitterionic polymers, in this thesis we want to provide of zwitterionic bulk biomaterials to the biomedical field. These materials would have an intrinsically antifouling properties, without the need of coatings or other treatments, fact that would make them suitable to a bigger number of applications. Specifically, in this thesis we have focused on two fields in which their antifouling properties are strongly demanded: the drug delivery field and the microrobotics field. Then, the objectives that we have set for this thesis are the following:

- To synthesize zwitterionic block copolymers and evaluate their capacity to form self-assembled nanoparticles to become a zwitterionic drug delivery platform (**Chapter 2**).
- To evaluate the antifouling properties of the different drug delivery systems produced and optimize them to cross the gastrointestinal barrier and to encapsulate hydrophobic drugs in order to create antimalarial and anticancer therapies (**Chapter 3**).
- To develop a zwitterionic photoresist suitable for advanced microprinting manufacturing of “stealth” non-immunogenic zwitterionic microrobots with multiple functionalities (**Chapter 4**).

Chapter 2: Synthesis and Characterization of Zwitterionic Amphiphilic Polymers

Part of this chapter has been published in:

A.Biosca*, P.Cabanach*, M. Abdulkarim, M. Gumbleton, C.Gómez-Canela, M. Ramírez, I. Bouzón-Arnáiz, Y. Avalos-Padilla, S. Borrós, X. Fernández-Busquets “Zwitterionic self-assembled nanoparticles as carriers for Plasmodium targeting in malaria oral treatment” **Journal of Controlled Release** (2021),331,364-375.

Chapter 2: Synthesis and Characterization of Zwitterionic Amphiphilic Polymers

2.1. Introduction

The majority of biomedical applications require of antifouling and immune-evasive materials. Among them, the development of drug delivery systems (DDS) with antifouling surface arouses special interest, since the immune system is still an unsurmountable barrier for this type of systems. In this chapter we have addressed this problem by using antifouling zwitterionic materials to create zwitterionic DDS based on amphiphilic block copolymers.

Amphiphilic block polymers have attracted the attention of the drug delivery field during the last three decades for their ability to self-assemble in aqueous solution similarly as surfactants do [51–53]. They present a unique structure, in which at least two blocks with different chemical properties (hydrophilic and hydrophobic) are bonded covalently, creating a resulting molecule composed of regions with different affinity to water (**Figure 2.1a**). The composition of these regions, as well as their length and the proportion between themselves, give to ABCs a structural versatility that is translated to a capacity to form different structures when dispersed in water, such as micelles and polymersomes, with different properties and potential applications.

Block copolymer micelles are formed by the agglomeration of the hydrophobic part of the ABC in the center, with the hydrophilic part forming a hydrated corona in contact with the aqueous media (**Figure 2.1b**). Depending on the ABC composition, micelles can show different thermodynamical behavior, being classified in two subtypes: dynamic micelles (**Figure 2.1d**), in which ABCs are in an equilibrium between their unimer state (in solution) and micelle state and frozen micelles (**Figure 2.1e**), in which this equilibrium does not exist and the micelle formation is not thermodynamically reversible. The structure of the micelles allows them to solubilize hydrophobic drugs (in the hydrophobic region of the micelle), protecting them from enzymatic degradation. And their chemical versatility make them tunable in terms of morphology, biological activity and stability, allowing the design of multiple systems with different features [54,55]. For these reasons, micelles are one of the most widely used drug delivery systems for hydrophobic drug delivery.

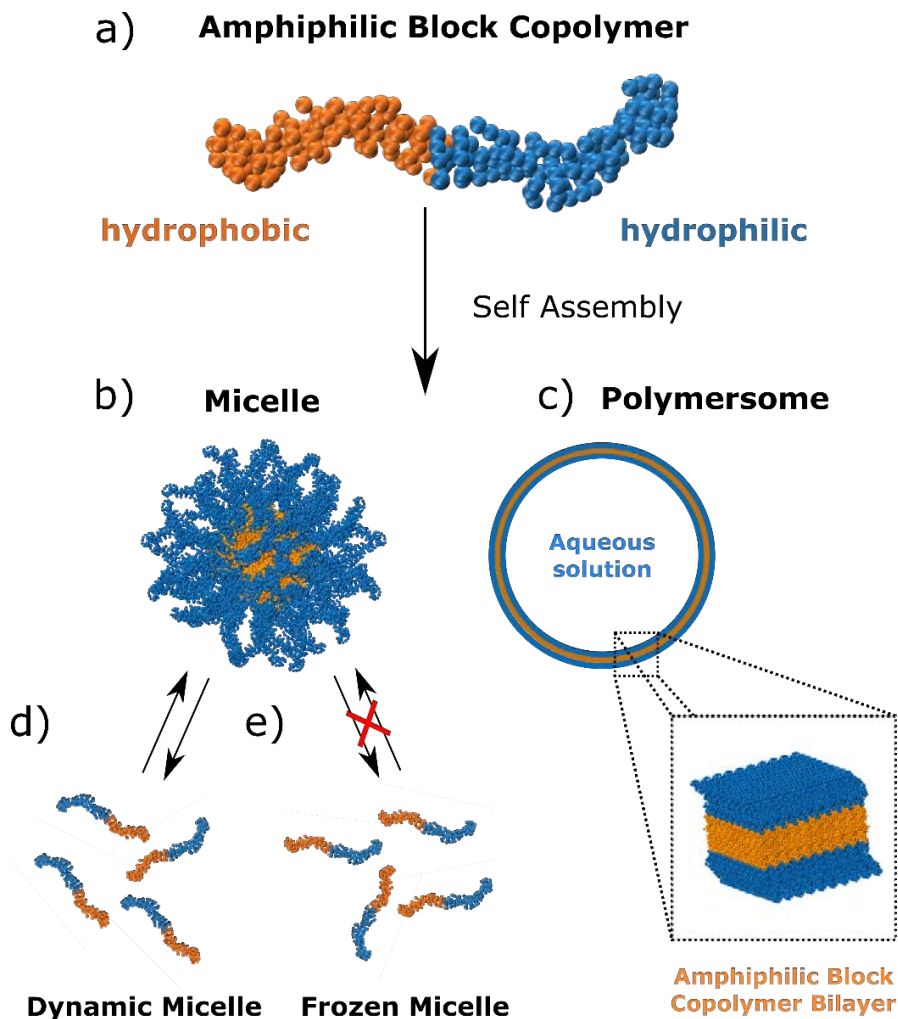


Figure 2.1. Self-assembly of Amphiphilic polymers. (a) amphiphilic polymers can self-assemble in (b) micelles or (c) polymersomes. Micelles are classified as (d) dynamic micelles or (e) frozen micelles depending if there exist a thermodynamic equilibrium between unimers and micelles.

On the other side, polymersomes are hollow vesicles formed by a bilayer of amphiphilic polymer (**Figure 2.1c**) with a similar structure than liposomes, but that outperform them in terms of stability and chemical versatility. They are interesting due to their capability of not only incorporate hydrophobic molecules in the membrane, but also hydrophilic molecules can be placed in the aqueous environment in the center of the polymersome, protecting them from the biological environment [56,57].

Apart from modulating the self-assembly of the ABCs, the control of the chemical properties of each block allows the introduction of multiple functionalities to this type of polymers. Some examples are the use of thermo-responsive (or pH-responsive) blocks that can be used for on-demand release of drugs [58–60] or the introduction of antibodies or other targeting molecules to target specific cells [61,62].

As any other drug delivery system, the objective of ABCs is to deliver a therapeutic cargo (small molecule, protein, genetic material, etc.) to a specific site. To perform this function, the DDS has to be stable until it reaches the desired site. Moreover, in the case of cancer treatment (the disease for which more DDS are designed), a long stability of the nanoparticle also enhances the therapy efficacy due to the Enhanced Permeation and Retention effect (EPR effect). This effect is derived from the need of vascularization of solid tumors, that generate abnormal blood vessels that are more permeable and that lack of lymphatic drainage. These two factors combined produce that nanoparticles can permeate in the tumor regions and be retained there, increasing the concentration of drug in the tumor with respect to the rest of the body [63]. Thus, if the blood residence time of the DDS allows the pass of nanoparticles through the tumor site multiple times, this effect is maximized [64].

The time that ABC nanoparticles can remain in blood without losing its drug load is determined by multiple factors, being the physical/chemical stability and the interaction with the immune system the two main factors. When the nanoparticles enter in the body fluid/tissue, they face a sharp change of conditions that compromises their stability. The body is at a certain temperature and salt concentration and it contains different host biomolecules such as proteins, lipids and hormones. If the nanoparticles were sensible to these conditions, their effectivity would be compromised. Therefore, when designing a DDS, it is important to assure that the system is stable at body's temperature and salinity, as well as avoiding aggregation and interaction with the host biomolecules. In the case of dynamic micelles, the final concentration of the polymers in the body is also critical, as above a Critical Micelle Concentration (CMC) the equilibrium is displaced to the unimer form, resulting in the disassembly of the micelles and the release of the payload [65].

Although these many factors affecting the stability of the nanoparticles, DDSs that are stable inside the body have been developed in the last years. But the design of systems that can

completely avoid the immune system response is still a challenge that has not been solved. As has been commented in Chapter I, when a material (in this case, nanomaterial) is introduced in the body/bloodstream, protein opsonization occurs, creating a layer of proteins called protein corona. These absorbed proteins are recognized by macrophages, immune cells present in all body tissues (and specially in the lung and spleen) that are in lookout for pathogens. When recognized as a foreign treat, the macrophages phagocyte the nanoparticles removing them from the bloodstream, preventing its capability to deliver the drug to the target site [66–68]. The immune detection of the nanoparticles starts with the protein absorption (that is later detected by the macrophages). This protein absorption depends on the chemical and physical properties of the nanoparticles' surface. Therefore, the engineering of the surface of the nanoparticles to avoid the protein absorption that leads to the immune clearance is still a big topic in the drug delivery field.

The search for polymers that can avoid the undesired protein absorption (antifouling polymers) has been the main strategy to create long-circulating drug delivery systems. It has been explored in multiple drug delivery system types, including the amphiphilic block copolymers. As in the majority of biomaterials, the introduction of poly(ethylene glycol) (PEG), the current antifouling “gold” standard, has been a widely used strategy for ABCs. Its first use was in 1989 by Kabanov et. al. [69], when amphiphilic Poly(ethylene glycol)-co-poly(propylene glycol)-co-poly(ethylene glycol), referred with the commercial name of Pluronic®, was used to encapsulate haloperidol (a neuroleptic agent). And, since then, a big number of DDS have been developed using PEG as the hydrophilic part of amphiphilic polymers [20]. In all these cases, when the nanoparticles are formed, it is produced a PEG corona in contact with water, reducing protein adsorption.

But the appearance of cases of hypersensitivity and immunological response to PEG is compromising the effectiveness of PEGylated therapies [25,26,28,70] and generate concern about their use as the benchmark antifouling polymer for drug delivery systems. These problems have motivated scientist to search for other hydrophilic polymers to be used in ABCs [71], such as poly-oxazolines [72,73] or Poly(hydroxypropyl methacrylate) [74] among others. But, although multiple systems have been developed, there is still not a clear substitute to PEG in amphiphilic block copolymer-based drug delivery systems.

By using zwitterionic polymers as the hydrophilic part of ABCs, in this thesis we want to translate the unique properties of these polymers to the field. As has been commented in Chapter I, the two principal features of zwitterionic polymers are its superhydrophilicity and antifouling behavior. By being superhydrophilic, when introduced in an ABC the change of polarity between the hydrophilic part and the hydrophobic part is bigger than the ones containing PEG or other hydrophilic polymers. This change of polarity is the driving force that produces the self-assembly to form nanoparticles and, if it is bigger, the resulting nanoparticle will be more stable. Also, in these self-assembled structures, the zwitterionic moieties are found in the surface, giving antifouling and anti-immunogenic properties to the system. These two properties combined make zwitterionic polymers promising for overcoming the barriers that prevent a long circulation of ABC nanoparticles and produce DDS with more therapeutic efficiency than current ones. And, for this reason, in this chapter, we broach the synthesis and characterization of amphiphilic block copolymers containing a zwitterionic block.

The strategy we have followed to obtain these polymers is to synthesize them by Reversible Addition-Fragmentation Transfer (RAFT) Polymerization. RAFT polymerization is a type of radical polymerization encompassed in the family of living radical polymerizations (or controlled radical polymerizations (CRP)). This type of polymerizations, in which they are also found the Atom Transfer Radical Polymerization (ATRP) and the Nitroxide-Mediated radical Polymerization (NMP), are polymerizations that pursue a high control over the polymerizing chains. This degree of control is achieved by three factors: all chains are initiated at the start of the reaction (i); the growth of the chains is homogenous (ii); and transfer/termination reactions are avoided (iii) [75].

The mechanism of RAFT polymerization is based on the presence of one compound, named RAFT agent or Chain Transfer Agent (CTA) (**Figure 2.2a**) that has a thiocarbonylthio group (such as dithioesters, dithiocarbamates and xanthates) capable of reversibly deactivate the propagating chains. This fact produces a situation in which most of the living chains are in a dormant form and only few of them are active. There is a rapid equilibrium between the active form and the dormant form, resulting in a similar propagation of all the chains. This equilibrium (**Figure 2.2b**) takes place due to the capability of the reactive double bond (C=S) to react with a radical ($R'\bullet$) producing a stable free radical in the dithiocarbamates structure.

Due to this radical formation, a weak double bond (S-R) can be homolytically cleaved producing the radical R•. As is shown in **Figure 2.2a**, the selection of the CTA (R and Z groups) has importance in the constants of this equilibrium and, therefore, in the final result of the controlled polymerization. The R group has to be stable enough to favor the transfer of the CTA to an active chain but also unstable enough to react with a monomer to start a new active chain (R-M•). On the other side, the Z group has influence on the stability of the CTA agent and the CTA-Polymer. So, it will determine the transfer rate of the CTA from one polymer chain to another polymer chain.

To perform the RAFT polymerization, we will need the CTA together with the two typical elements of any radical polymerization (the initiator (I) and the monomer (M)). The polymerization starts as any other radical polymerization: a radical in the initiator (I•) is formed due to an external input (normally temperature). These radicals start propagating by adding monomer units and forming growing chains ($I\bullet \rightarrow IMMM\bullet \rightarrow P_m\bullet$). And, at some point, they add a CTA instead of a Monomer. When this happens, the growing chain becomes dormant, and the R unit of the CTA is released as a radical (R•) and starts forming a growing chain ($R\bullet \rightarrow RMMM\bullet \rightarrow P_n\bullet$). Due to the reversible character of all these reactions, the RAFT polymerization enters in an equilibrium phase (called chain equilibration/propagation) (**Figure 2.2c**) in which the CTA jumps from a growing chain to another, activating and deactivating these chains.

The ratio of growing/dormant chains can be adapted depending on the proportion of CTA/M/I added in the reaction, and, normally, it is selected to be a low ratio of growing chains to dormant chains. So, the majority of chains are in a dormant state, while few are actively growing. But, at the same time, the kinetics of the CTA transfer from a chain to another chain are fast. The combination of the low number of active chains and the fast transfer of CTA from one chain to another chain produces that active chains only adds few monomers before being deactivated. This feature of RAFT polymerization is important because it prevents the excessive growing of some chains, consuming the totality of the monomer in the solution and stopping the polymerization with a big dispersity of chain lengths (phenomenon occurred in the simple radical polymerization). Therefore, in RAFT polymerization all chains grow at the same rate, creating a population with low polydispersity.

This low ratio of growing/dormant chains also produces that, when monomer concentration starts to fall, there is a low number of dead chains (chains that have lost the radical). This is a key fact for our purpose of producing ABCs, as it allows to reinitiate the polymerization by adding more monomer and initiator and create a block copolymer (**Figure 2.2d**).

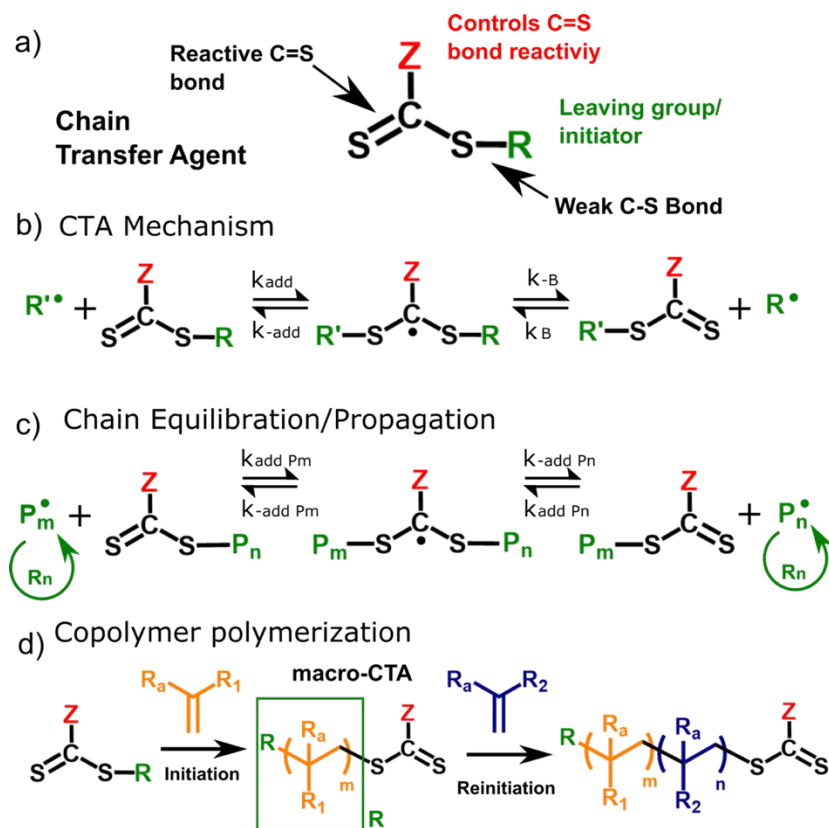


Figure 2.2 (a) Chemical structure of Chain Transfer Agent (CTA), (b) reversible addition/fragmentation Transfer of the CTA, (c) Chain equilibration/propagation in RAFT polymerization and (c) creation of block copolymers by the reactivation of the macro-CTA and addition of new monomers.

And also, the fact that the R group and the thiocarbonylthio groups in the edges of the polymer allows the post-polymerization modification of the polymers produced [76–79]. This possibility has important utility for the application of ABCs in drug delivery, as by these post-polymerization modifications of the polymers there can be added different functional groups to add functionalities (such as targeting or on-demand delivery) to the system.

Knowing the potential of the zwitterionic polymers as antifouling polymers and the advantages that RAFT polymerization offers to produce amphiphilic block copolymers, in this Chapter we have developed zwitterionic amphiphilic block copolymers. With them, we want to provide alternatives to the current PEG-based antifouling drug delivery systems, that have been recently proved to generate immune response and that have limitations of chemical versatility and stability.

We have used RAFT polymerization, to produce well-defined zwitterionic block copolymers. Thanks to the control over the polymer structure that this polymerization offers, we have been able to explore the influence of different factors such as the zwitterionic type or polymer architecture in their self-assembly of the polymers produced. And we have also determined which advantages and drawbacks do these polymers present as possible drug delivery systems, in order to be able to rationally design optimized zwitterionic ABCs for possible future applications, that will be explained in next Chapters.

2.2. Results and Discussion

RAFT polymerization offers a high degree of control over the structure of the polymer. By using this type of polymerization, we can choose the chemical nature of each block as well as the length of the block, factor that will also determine the proportion between blocks in case of diblock copolymers. All these variables offer the possibility to create a broad spectrum of polymers sharing some similarities but also with small structural differences that can suppose an important change in their behavior as drug delivery systems.

Since the objective of this part of the thesis was more focused in developing zwitterionic DDS than in exploring all the possible combinations of block types and length, we followed the strategy of starting from few initial polymers and then, after characterizing them, redesign the design of the polymers in order to improve their performance as DDS. So, we explain the results of this chapter in a chronological way, in order to make easier to understand the selection of the polymers used.

2.2.1. Selection of the Synthesis pathway

Poly(butyl methacrylate)-*b*-Poly(Sulfobetaine methacrylate) (PBMA-*b*-PSBMA) was the first amphiphilic block copolymer that we decided to produce. We selected PBMA as the hydrophobic block as it is a highly used monomer in biomedical applications due to its availability, chemical stability and versatility. As has been previously commented, the hydrophobic block of the ABC will try to hide from the water, producing the self-assembly in core-shell structures (micelles) or in polymeric bilayer (polymersomes). Thus, the PBMA block will influence in the stability, formation and self-assembly of the structure, but will not determine the interaction of the DDS with the environment.

This is the function of the hydrophilic block, for which we selected PSBMA. This type of zwitterionic polymer is one of the most widely used zwitterionic polymer (together with poly(carboxybetaine methacrylate) (PCBMA) and poly(2-Methacryloyloxyethyl phosphorylcholine) (PMPC)), and stands out in terms of pH stability and synthesis conditions.

In order to synthesize the desired ABCs, first we had to design a polymerization and purification route. And, due to the special solubilization properties of ABCs, doing such experimental design forced us to resolve two challenges (**Figure 2.3a**).

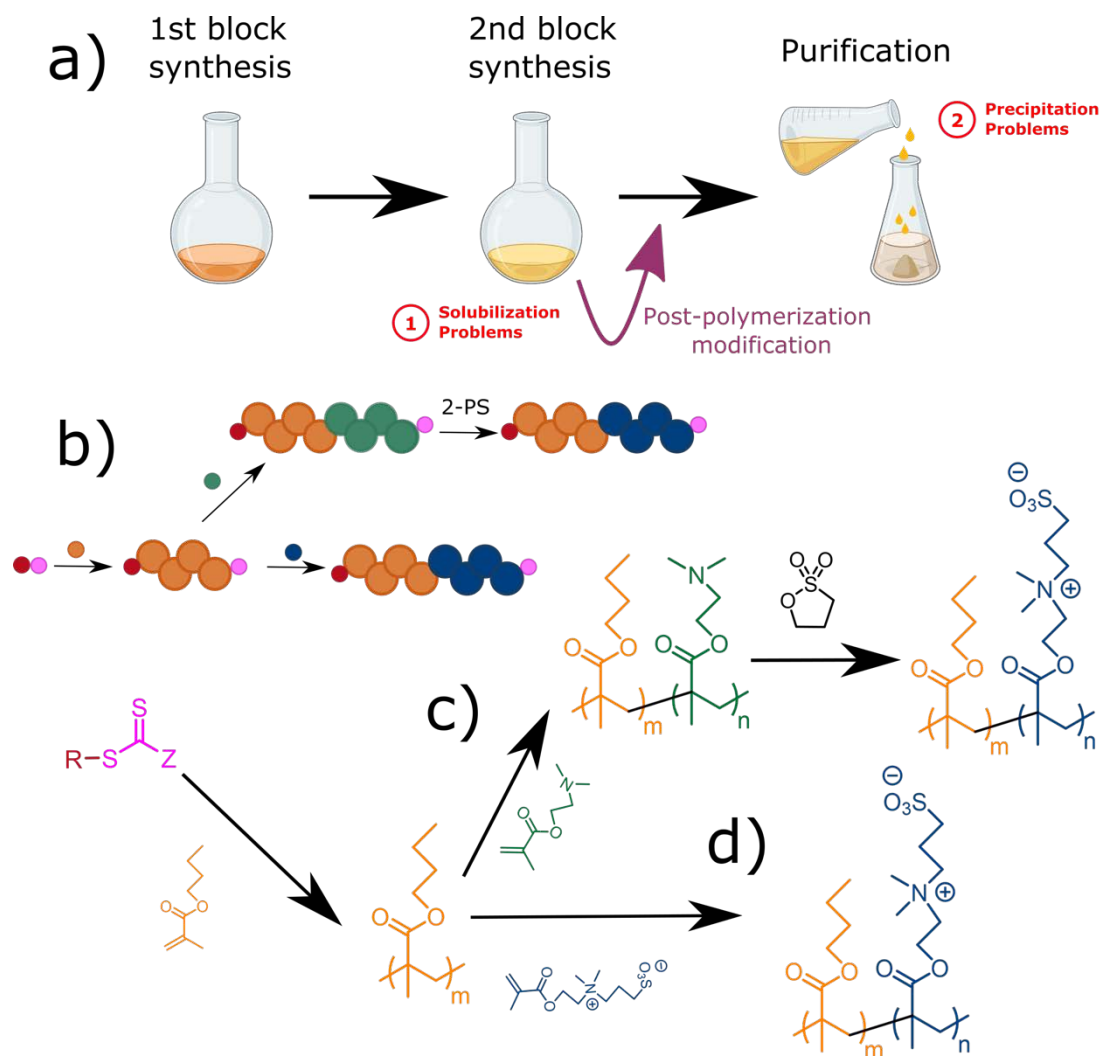


Figure 2.3 Synthesis route of Zwitterionic Amphiphilic Block Copolymers. (a) Schematic representation of the experimental procedure to produce the polymers, indicating its two main challenges. (b) Schematic representation of the two synthesis routes to produce a zwitterionic amphiphilic block copolymer. These routes are: (c) synthesis of a zwitterionic polymer via a post-polymerization modification of a precursor block. (d) direct polymerization of a zwitterionic block using zwitterionic monomers.

The first challenge consisted in solubilizing all the precursors of the polymerization (CTA, initiator and monomer) in a common solvent. We solved this problem in the synthesis of the first block of the ABC by selecting an initiator and RAFT agent with similar polarity than the monomer. But we had to deal with solubility problems when synthesizing the second block. One of the precursors was the macro-CTA (the first block), and the other precursor (apart from the initiator) was the precursor of the second block. By definition, an ABC contains two (or more blocks) with a sharp change of polarity. Therefore, we had to find a solvent in which the hydrophobic block and hydrophilic monomer (or vice versa) were soluble. This challenge was even harder in the case of zwitterionic ABCs due to their insolubility in the vast majority of organic solvents.

If a common solvent cannot be found, there is the alternative of performing an emulsion RAFT polymerization. In this type of the polymerization, an emulsion between two solvents (one of the solvents may be the monomer itself) is formed, and the chain growth takes place in the interface between the two phases [80,81]. Although this type of polymerization has been done successfully many times, it needs very controlled conditions, and only some monomers, CTA and initiators can be used. So, we thought that this loss of versatility would not be desirable for our design and, therefore, we preferred to avoid this type of polymerization. Therefore, we needed to achieve polymerization conditions in which all the precursors were soluble in the reaction solvent.

We had to deal with the second challenge in the purification step. In there, we had an amphiphilic polymer soluble in a cosolvent (a solvent that can solubilize both blocks). But also, there were unreacted monomers of the first block, dead polymeric chains, unreacted initiator and other impurities that have to be removed before having the final ABC. Precipitation into a non-solvent (a solvent in which the desired specie is not soluble) is typically the preferred form of purification because it is a facile and fast process. But, in our case, a solvent in which the final ABC was insoluble, but the precursors were soluble had to be found. Due to the special solubility properties of zwitterionic ABCs, this step was not trivial. Moreover, this process could be affected by the block ratio of the polymer, as it defines its hydrophilic/hydrophobic ratio, which has a high influence in the solubility properties of the ABC.

Trying to overcome these challenges, we came up with two possible ways to synthesize this first zwitterionic ABC (**Figure 2.3b**). In both pathways, we decided to synthesize first the hydrophobic block (PBMA) for then adding the zwitterionic block to produce the final copolymer. One of the possibilities (**Figure 2.3c**) consisted in polymerizing a block from a monomer that could be modified after the polymerization to become a zwitterionic block. This zwitterionic precursor is *N,N*-dimethyl(aminoethyl) methacrylate (DMAEMA), and had the advantage that, although having some degree of hydrophilicity, is soluble in most of the organic solvents, even once polymerized. Then, we would perform the polymerization and purification of PBMA-*b*-DMAEMA and then modify it with the quaternizing agent 1,3-Propanesultone (1,3-PS), that would create the sulfobetaine. The purification of the unreacted 1,3-PS would be simple due to the insolubility of the sulfobetaine block in organic solvents. The second possible strategy that we evaluated to produce PBMA-*b*-PSBMA was the direct polymerization of SBMA monomer to create the PSBMA block (**Figure 2.3d**). In there, we would polymerize the PBMA macro-CTA and the SBMA monomer in a fluorinated solvent, like trifluoroethanol (TFE) or hexafluoroisopropanol (HFIP), that are the only organic solvent that can solubilize the zwitterionic blocks.

The first strategy (polymerization of the precursor and modification) had the drawback of a possible incomplete sulfobetainization, resulting in the presence of some free tertiary amines in the polymer. In contrast, the second strategy had the problem of the purification step, as it was difficult to remove the unreacted SBMA monomers from the sulfobetainized polymer. We decided to first explore the strategy consisting in the synthesis of PBMA-*b*-PDMAEMA and then the post-polymerization modification to PBMA-*b*-PSBMA (**Figure 2.3c**). The selection was based in the fact that both PBMA and PDMAEMA are polymers widely used in RAFT polymerization. Therefore, we reduced the risk of problems during the polymerization, characterization and purification, having then the only critical step of the post-polymerization modification. We assumed the possible risk of a non-complete modification, knowing that the reaction between the PDMAEMA and 1,3-PS has been performed previously in other studies without compromising the antifouling properties of the zwitterionic polymers [82,83]. On another hand, performing the direct polymerization of PBMA-*b*-PSBMA (**Figure 2.3d**) would force us to design a method of purification and characterization of the polymer, without having too much information in the literature and, therefore, taking more time than the other option.

2.2.2. Synthesis of PBMA-*b*-PSBMA copolymers

Once decided the polymerization route that we had to do to produce PBMA-*b*-PSBMA, the polymerizations were performed. We started with low molecular weight polymers (30-60 monomers), easier to handle.

As shown in **Figure 2.3c**, the steps to produce the final polymer are: i) RAFT polymerization of PBMA, ii) reinitiation of the RAFT polymerization with DMAEMA to produce PBMA-*b*-PDMAEMA and iii) post-polymerization modification of the PDMAEMA block into PSBMA block. The characterization of the different polymerization steps was performed by H^1 -NMR (proton nuclear magnetic resonance) analysis (**Figure 2.4** shows an example of H^1 -NMR characterization of a polymer comprised of 25 monomers of PBMA and 35 monomers of PSBMA).

Analyzing the PBMA block NMR (**Figure 2.4a**) we could determine the success in the polymerization and purification (absence of the methacrylate signals at 5.5-6.0 ppm). Due to the small size of the polymers produced (less than 100 monomers), we could determine the polymer length by comparing the signals of the 8 methylene groups of the RAFT agent (at 1.25 nm; α -methylene and β -methylene of the trithiocarbonate group are not included in this signal) with the signal corresponding to the methylene group of the ester bond of each BMA moiety (appearing around 4.1-4.2 nm) (**Figure 2.4**).

$$l_{PBMA} = \frac{\frac{\int CH_{2PBMA}}{2}}{\frac{\int (CH_2)_{8CTA}}{16}} = \frac{16 \int CH_{2PBMA}}{2 \int (CH_2)_{8CTA}} = 8 \frac{\int CH_{2PBMA}}{\int (CH_2)_{8CTA}}$$

Equation 2.1 Determination of the block length of PBMA.

In the NMR of PBMA-*b*-DMAEMA (**Figure 2.4b**) we also saw the absence of the methacrylate signals (confirming successful polymerization and purification). We also could determine the length of the second block by comparing the signals of the methylene groups connected to the ester (**Equation 2.2**).

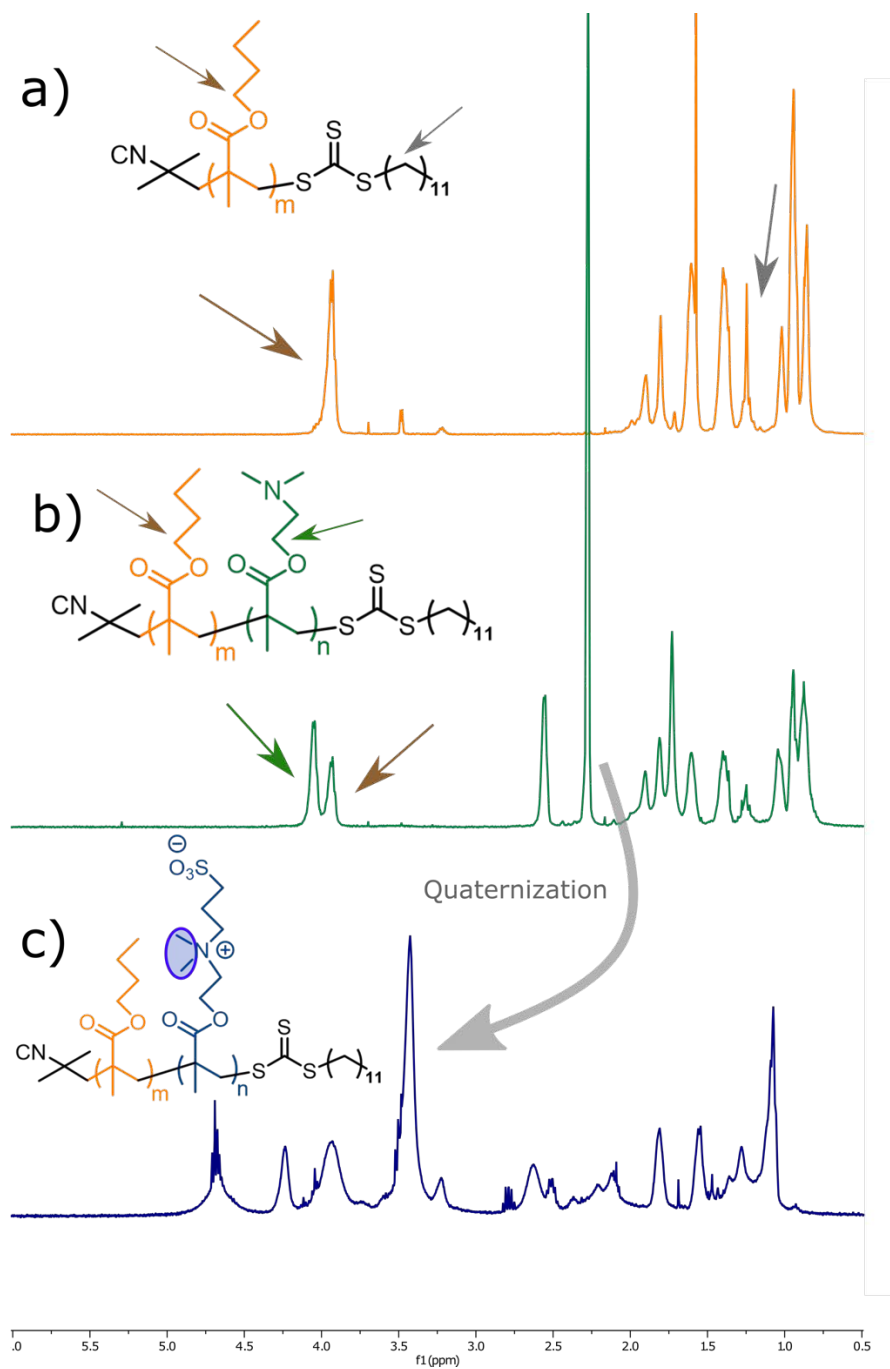


Figure 2.4 $^1\text{H-NMR}$ of (a) PBMA (in CdCl_2), (b) PBMA-*b*-PDMAEMA (in CdCl_2) and (c) PBMA-*b*-PSBMA (in TFA-*d*).

$$l_{PDMAEMA} = \frac{\int CH_{2DMAEMA}}{\int CH_{2DMAEMA}} = l_{PBMA} \frac{\int CH_{2DMAEMA}}{\int CH_{2DMAEMA}}$$

Equation 2.2 Determination of the block length of PDMAEMA.

Finally, in the analysis of PBMA-*b*-SBMA (**Figure 2.4c**) we were not analyzing a polymerization step but a derivatization step. We had to use a different solvent (deuterated TFA) due to the solubilization problems of the zwitterionic amphiphilic polymer (producing some shifts in the signals). Although this fact, we could check the success on the derivatization of the tertiary amine by the shift of the signals of the two methyls bonded to the amine. The singlet on 2.2 ppm in **Figure 2.4b** disappears in **Figure 2.4c**, but it appears another singlet at 3.5 ppm. This shift corresponds to the quaternization of the amine, confirming a successful reaction.

Aside from the NMR, another fact that indicated the success of the reaction is the precipitation of the polymer (that is soluble on THF before of the reaction occurs) during the reaction, converting the reaction solution in a gel.

	length PBMA	length PSBMA	Ratio PBMA/PSBMA	MW (KDa)
S1	25	35	0.71	13.6
S2	18	25	0.72	9.8
S3	18	12	1.5	6.4
S4	20	21	0.95	9.0

Table 2.1 PBMA-*b*-PSBMA polymers synthesized.

We decided to produce different types of PBMA-*b*-PSBMA polymers using this procedure (summarized in **Table 2.1**). We selected this polymer structures, in first place, because they were short length polymers and, as has been commented, they have an easy polymerization and characterization by NMR. Then, we decided to produce polymers with a different PBMA/PSBMA ratio and with different Molecular Weight, trying to check if one of the conditions had a better performance than the others.

2.2.3. Characterization of the ability of PBMA-*b*-PSBMA to form Amphiphilic Nanoparticles: UCST and Salt Responsiveness.

Once the zwitterionic amphiphilic polymers were produced, we started the optimization of the process to produce zwitterionic amphiphilic nanoparticles out of them. There are many methods described in the bibliography to produce nanoparticles with ABCs [51], being the most common the thin film rehydration and the nanoprecipitation. For both of these techniques, the selection of an organic solvent in which the amphiphilic is soluble into is really important, and, in the case of PBMA-*b*-PSBMA, the only organic solvents in which we could dissolve them was TFE and HFIP. We tried both techniques, characterizing the results using Dynamic Light Scattering (DLS) to know the hydrodynamical size and the polydispersity of the nanoparticles produced.

Although both techniques typically work in most of amphiphilic copolymer systems, we could not obtain self-assembled nanoparticles using PBMA-*b*-PSBMA. These results were surprising, as our system was formed by two blocks with a sharper change of polarity than most of the ABCs, fact that should induce to the formation of stable self-assembled nanoparticles. We found a possible explanation of this phenomenon in the Antipolyelectrolyte effect (**Figure 2.5**). This effect receives the name from the polyelectrolyte effect, an effect for which charged polymers (polyelectrolytes) collapse due to the addition of salts (ions) in the system [84]. Polysulfobetaines show the opposite behaviour: in absence of a counterion and below a determined temperature (Upper Critical Solution Temperature (UCST)), their charges collapse and became insoluble [48,85–87]. This phenomenon only occurs in polysulfobetaine homopolymers of more than 50 monomers (our system has less). Therefore, the presence of the hydrophobic block affects this phenomenon. At the time this thesis is written, this phenomenon has still not been fully characterized by the scientific community [88–90].

Antipolyelectrolyte effect

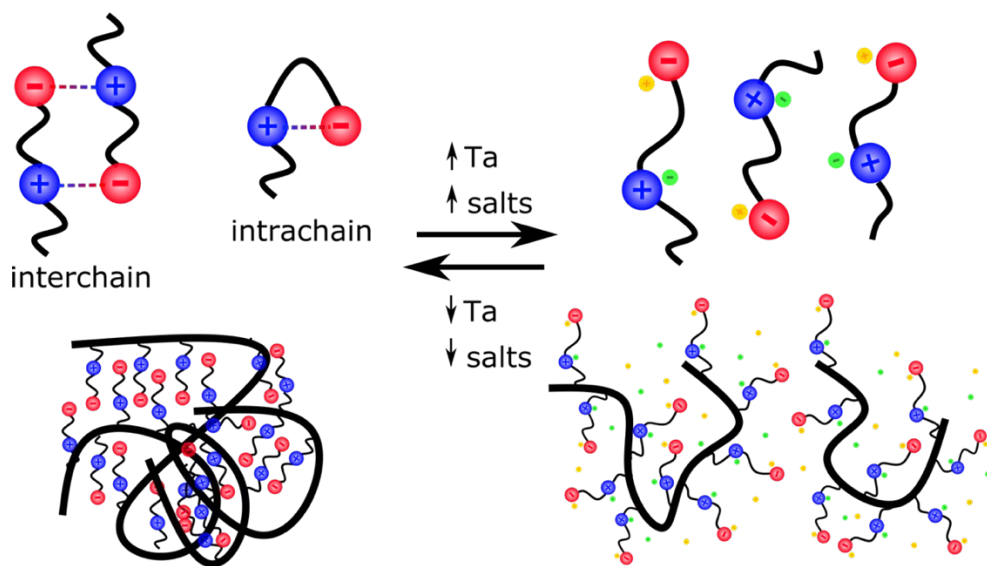


Figure 2.5 Antipolyelectrolyte effect in polyzwitterions.

Although the observed phenomenon would be interesting for future studies, we prioritized to continue with our efforts to produce zwitterionic amphiphilic nanoparticles. Thus, we had to find a way in which the self-assembly of the zwitterionic ABCs could be possible. We knew that temperature and salt concentration had influence on the hydrophilicity of sulfobetaines. But if these nanoparticles had to be used for real therapies, the temperature and salt conditions should be the ones in the body (around 37 °C and around 150 mM of salt in the blood).

Working at 37°C during all the production process would suppose a challenge and would difficult the production and storage in a real scenario. Thus, we decided to fix the temperature at room temperature and try to determine if the change of salt molarity would affect the self-assembly of our system. To do so, we chose the conditions 1M NaCl and Phosphate Buffer Saline (PBS). The condition of 1M of NaCl, although being much higher than the concentration in blood, would be useful to know if we could produce nanoparticles out of a certain polymer. And, with the condition of PBS, we would know which nanoparticles were stable at the salt concentration of the body.

We tried nanoprecipitation and thin film rehydration techniques with the synthesized polymers using 1M NaCl and PBS as the aqueous phase. The DLS results showed how the samples were not in the nanometre size but, by looking to the samples, we observed a significant difference. While in the first case (water) we obtained a non-translucid solution with observable aggregates, in the case of 1M NaCl and PBS samples (of some of the polymers) we observed how the solution started becoming more translucid with the pass of the time, and no aggregates were observed. Although this solution was not a dispersion of nanoparticles (DLS results showed a population higher of 1 μm), this behaviour in the salt solutions conduced us to think that our hypothesis was correct and was a difference in the hydration of the sulfobetaine block.

At this point, we hypothesized that the hydration process of the sulfobetaine block was time dependent and, therefore, that more time of hydration was needed in order to obtain the nanoparticles. To check if the time was an important variable to produce nanoparticles, we directly dispersed polymer powder on NaCl 1M and PBS (with a polymer concentration of 0.8 mg/ml) and left the solution steering overnight. So, the samples were being hydrated during more than 12 h. After this time, the solution presented the same translucid aspect (**Figure 2.6**) than in the case of thin film rehydration.

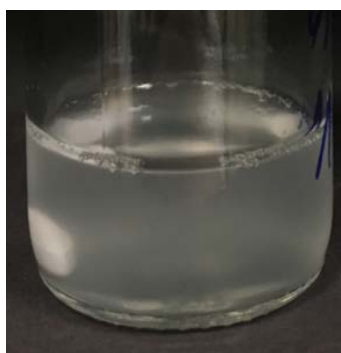


Figure 2.6 *Translucid aspect of SB1.1 polymer (0.8 mg/ml) after 12h of steering in NaCl 1M.*

These results proved that the sulfobetaine nanoparticles did not form spontaneously nanoparticles at any of the tested conditions. Therefore, we needed a method in which we gave energy to the system to form the nanoparticles. We decided that this method would be extrusion process (**Figure 2.7**).

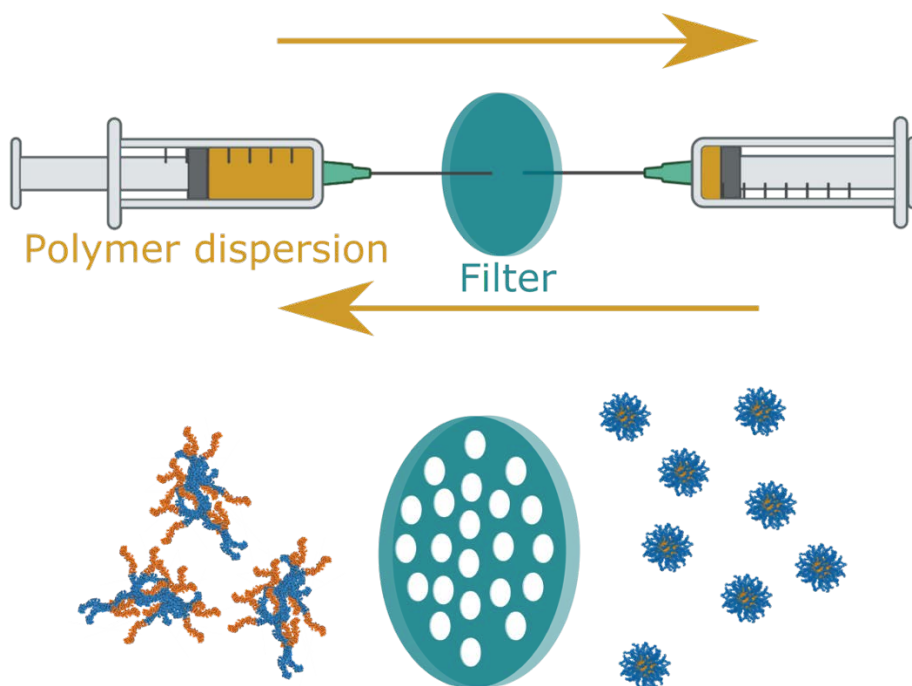


Figure 2.7 *Extrusion process to produce nanoparticles.*

The method consists in repeatedly passing the polymer solution through a filter with a nanometric pore size that forces it to self-assemble in a nanometre size structure. This is a method mostly used to produce liposomes, as it converts big multilamellar phospholipid structures in unilamellar liposomes. So, we thought that, as liposomes are also amphiphilic molecules, it could exist some analogy that could make extrusion a valid method for producing our zwitterionic ABC nanoparticles. We used this method with all the polymer produced dispersed in solutions of NaCl 1M and PBS, and we observed how, in some compositions, we finally could obtain samples with a population of nanoparticles (**Table 2.2** and **Figure 2.8**).

DLS results showed the successful production of zwitterionic amphiphilic nanoparticles using the extrusion method. They also showed different behaviours of the different polymers produced (meaning that the block size had influence in the self-assembly of the polymers).

	Solution	Hydration Time	Size (Mean \pm SD)	PDI (Mean \pm SD)
S1	NaCl 1M	6h	211 \pm 2	0.317 \pm 0.005
		24h	221 \pm 6	0.18 \pm 0.04
	PBS	6h	>1000	1.0
		24h	184 \pm 3	0.18 \pm 0.02
S2	Nanoparticles could not be obtained in any condition			
S3	NaCl 1M	6h	>1000	1.0
		24h	212 \pm 28	0.25 \pm 0.06
	PBS	6h	>1000	1.0
		24h	495 \pm 56	0.45 \pm 0.11
S4	Nanoparticles could not be obtained in any condition			

Table 2.2 Results of DLS of the samples prepared by extruding the dispersed polymer solutions through a filter of 200 μm (n=3).

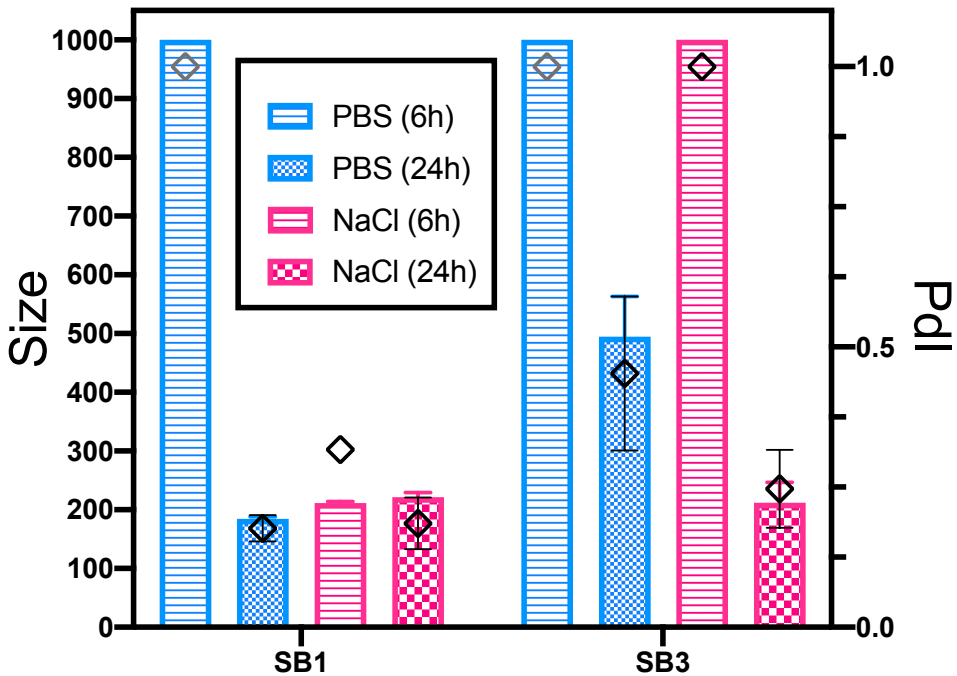


Figure 2.8 Graphical representation of the Table 2.2 data (n=3).

SB1 and SB3 polymers formed nanoparticles, while SB2 and SB4 polymers did not. Comparing SB1 and SB2 polymers, we saw that the ratio PBMA/PSBMA was the same. Therefore, the polymer length was a factor in the self-assembly of the polymer. But SB3, a polymer with lower chain length but a lower PBMA/PSBMA ratio did also form nanoparticles (indicating that the ratio hydrophobicity/hydrophilicity was also influencing the process). These non-intuitive results indicated that, although in some polymers the addition of salts solved the problem, the antipolyelectrolyte effect was not completely avoided in all the polymers tested.

To have more information about the influence of the antipolyelectrolyte effect in the produced polymers, we compared the two polymers forming nanoparticles (**Figure 2.8**). There were some differences between SB1 and SB3 polymers depending on the conditions. In the case of SB1 polymers, we could clearly see the relation between the salt concentration and the hydration time needed. When using 1M NaCl (a highly concentrated salt solution), the hydration of the hydrophilic part takes place faster. Therefore, with this concentration we could produce nanoparticles with only 6 h of hydration (the time starts at the time that the polymer powder is added to the solution). On the other hand, when using PBS (a solution with a lower salt concentration, that corresponds to the salinity of the body), we could not produce nanoparticles when we extruded the sample after 6 hours of incubation. But, when we did the same process after 24 hours of incubation, we obtained nanoparticles with a similar diameter than the ones produced with 1M NaCl. Thus, with these results we could conclude that the salt concentration played a key role in the hydration kinetics of the sulfobetaine polymers.

The same behaviour was observed for SB3 polymer. In this case, the polymer needed 24 hours of incubation independently of the salinity of the solution. But the influence of the salinity on this polymer was reflected in the size and polydispersity of the samples. While in the case of 1M NaCl the size and polydispersity were similar to the ones on SB1 nanoparticles, when we dispersed the particles in PBS we obtained a higher size and PDI, indicating a more heterogenous and agglomerated population. Therefore, these results suggested that when using PBS, the salt concentration is not enough to prevent all SBMA interactions, resulting in the formation of aggregates that are still in the nanometre scale.

Finally, we tried to deduce the nanoparticle type using these results. As has been commented in the introduction of this chapter (**Figure 2.1**), there are multiple ways in which amphiphilic block copolymers can self-assemble. And the different structures have different peculiarities and also different behaviours. Therefore, to know the nanoparticle type of our polymers was important in order to use them in future applications. As has been also commented, the extrusion process is normally used to produce liposomes and, therefore, we first thought that the nanoparticles produced would be polymersomes (hollow vesicles). But, to confirm this hypothesis, we needed to perform more characterization to obtain more data that could support the hypothesis.

We decided that, to continue characterizing the polymers, we would use SB1 polymer. The selection of this polymer over SB3 was done in basis of the formation of nanoparticles in the PBS medium. As has been commented, PBS is a medium with approximately the same salinity than the blood and, therefore, if the nanoparticles were stable in this solution, the salinity would not be a destabilizing factor for the nanoparticles in *in vitro* and *in vivo* experiments. We can see in **Figure 2.8** how, in PBS, the nanoparticles produced by SB3 polymer have a bigger size and higher PDI than in NaCl 1M, indicating a relation between the nanoparticle morphology and the salt concentration. And, therefore, this could affect its performance in future applications.

The next step in the characterization process was to know the stability of the nanoparticles over time. And we used DLS technique to do so. Nanoparticle size and polydispersity were analysed in different times after the extrusion process. We obtained positive results out of this experiment (**Figure 2.9**). We saw how nanoparticles were stable up to 89 hours after extrusion (no size nor PDI change was observed). Therefore, nanoparticles had the potential to be prepared up to 4 days before their final use and still remain in the same conditions than they were after the extrusion.

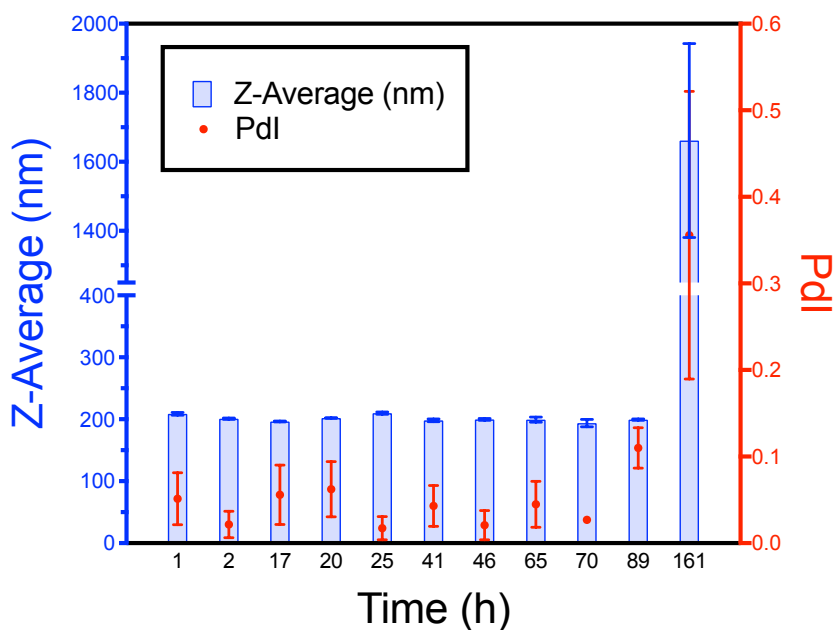


Figure 2.9 Stability measurements of SB1 ($n=3$).

We then decided to perform a Cryo- Transmission Electron Microscopy (Cryo-TEM) analysis of SB1 nanoparticles to have more information about their morphology. As has been commented, the nanoparticle size was first characterized by DLS. With this technique, we could rapidly and easily analyse a sample with a high count (statistically representative). But it has the drawbacks that it cannot detect multiple populations in a same sample and that it does not indicate the morphology of the sample. Also, the technique gives a hydrodynamic diameter, formed by the nanoparticle and all the water molecules that interact with it. By Cryo-TEM, although not being able to analyse a big number of nanoparticle (and, therefore, taking the risk of analysing a region of the sample that is not statistically representative), we can observe the nanoparticle morphology and, in the case that two or more populations were present in a sample, we can observe and differentiate them.

The first conclusion that we could make after observing the images in **Figure 2.10** was that SB1 nanoparticles presented a spherical morphology. We also determined the presence of one single population of nanoparticles with a mean size of 110 nm (as shown in the histogram in **Figure 2.10d**, obtained by manually measuring the size of each nanoparticle in the images). This size did not match with the nanoparticle size obtained by DLS (184 nm on the solution

of PBS, the same solution used to produce the nanoparticles that were characterized with Cryo-TEM).

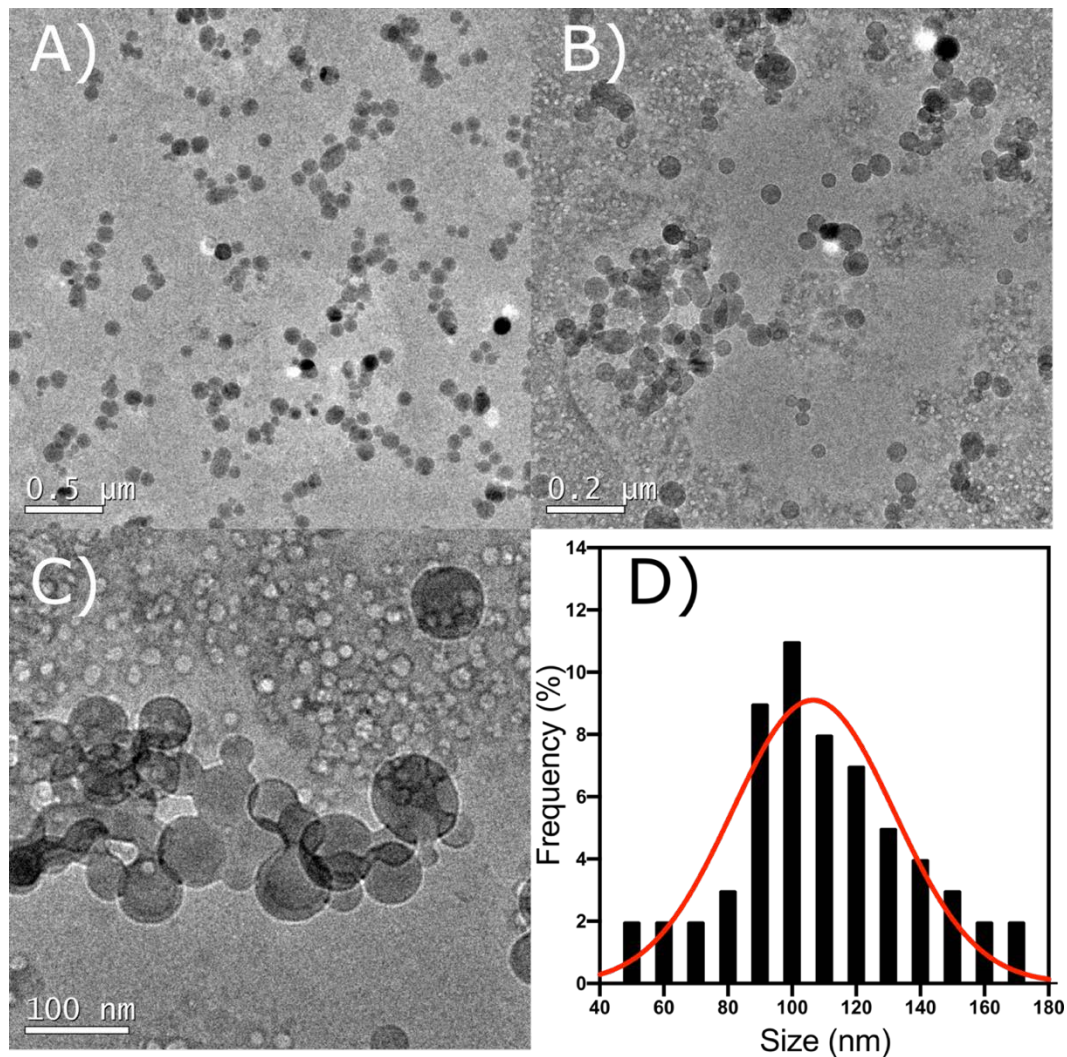


Figure 2.10 Cryo-TEM images of SB1 nanoparticles and histogram of the size count. Histograms have been made by counting 100 nanoparticles.

The difference between the Cryo-TEM analysis and DLS analysis can be explained by the hydration layer. DLS measures the hydrodynamical radius of the nanoparticles (the nanoparticle with the water molecules that also moves when the nanoparticle moves). While in the Cryo-TEM it is only observed the nanoparticle itself (without the water molecules). We

know that PSBMA is a superhydrophilic polymer, forming a big hydration layer. Therefore, this decrease of size observed was not considered as a strange phenomenon and we considered it normal.

After analysing the size distribution and the morphology of the nanoparticles, we proceeded to try to deduce the nanoparticle type that SB1 polymer formed. But, in this case, the analysis was not obvious. First of all, the nanoparticle size indicated that the nanoparticles were not simple micelles. The polymer length of the polymer was small and, therefore, a micelle of these polymers could not have a size of more than 50 nm.

As has been previously commented, the production procedure of the nanoparticles could indicate that they would be polymersomes. But, normally, when polymersomes are analysed by Cryo-TEM it can be observed clearly the polymer bilayer (**Figure 2.11**). And, when observing the images of Cryo-TEM in **Figure 2.10**, the bilayer could not be observed in any nanoparticle. Moreover, we could observe, especially in **Figure 2.10c**, how SB1 nanoparticles seemed to fuse to form bigger particles. And membrane fusion it is not a phenomenon normally observed in polymer bilayers.

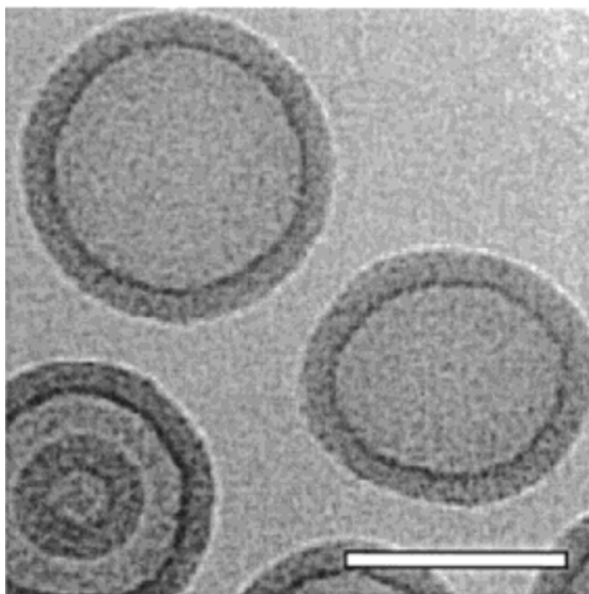


Figure 2.11 Cryo-TEM images of Poly(ethylene glycol)-co-poly(butadiene) polymersomes [91] in which it can be clearly observed the polymer bilayer of the polymersomes.

We could not validate our hypothesis with the Cryo-TEM images. Therefore, we had to think about another nanoparticle type that could explain a nanoparticle size bigger than a micelle but a structure that is not a polymersome. The explanation that we found after analysing all the data from DLS and Cryo-TEM was that the SB1 polymer self-assembles in micelles. But, due to the interactions between sulfobetaine chains, these micelles form aggregates bigger 1 μm (so, they cannot be analysed with DLS). After passing these micelles aggregates through a nanometre sized filter during the extrusion process, the big aggregates break creating nanometre sized aggregates, that are the ones observed in Cryo-TEM and DLS (**Figure 2.12**). These structures would explain the nanoparticle size (they are small micelles aggregated forming bigger structures) and also the fusion of the nanoparticles (two aggregates can form bigger aggregates due to the interactions of sulfobetaine chains).

As has been commented in the previous lines, there is not too much literature about the behaviour of zwitterionic amphiphilic block copolymers and their behaviour when self-assembling and forming particles. Therefore, all these phenomena should be studied deepest to understand with certainty which type of nanoparticles form and which behaviour these polymers have in solution.

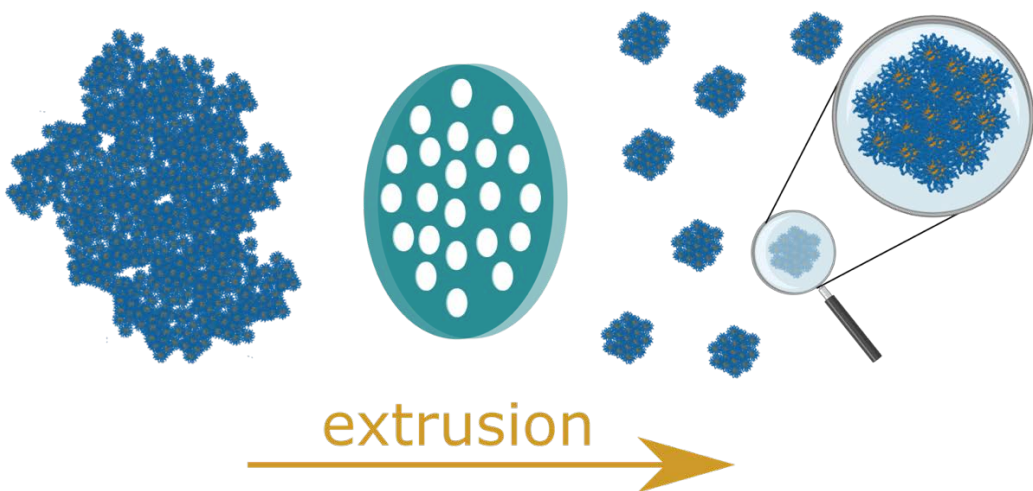


Figure 2.12 Our hypothesis about the nanoparticle type of SB1. Before extrusion, we have aggregated micelles (due to antipolyelectrolyte effect). After extrusion, these aggregates are broken, forming smaller aggregated micelles of nanometer size.

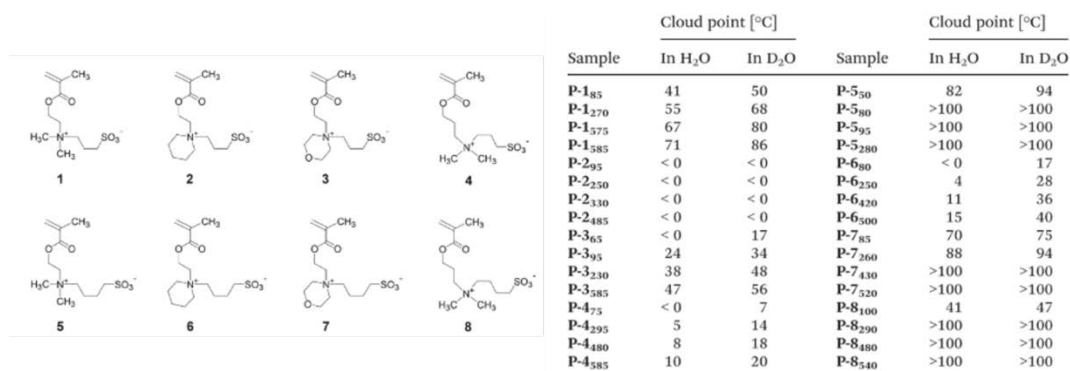
Although the analysis of this phenomenon would be interesting to better understand the behaviour of antipolyelectrolyte effect, we preferred to follow the objective of focusing in the final application (developing a drug delivery system with capability of carry different drugs and characterizing its behaviour *in vitro* and *in vivo*) rather than put effort in performing a full study of the system.

2.2.4. Overcoming the UCST: Synthesis and characterization of PBMA-*b*-PMESBMA polymers

With the PBMA-*b*-PSBMA nanoparticles produced previously, we proved that we could produce zwitterionic amphiphilic nanoparticles. But the antipolyelectrolyte effect could hinder the effectivity of these nanoparticles in certain applications. To solve this problem, we tried to design another zwitterionic ABC that could prevent the effect. Moreover, producing nanoparticles without the antipolyelectrolyte effect could also help us in understanding the behaviour of the PBMA-*b*-PSBMA nanoparticles.

We decided that this second zwitterionic ABC type would have the same hydrophobic block (BMA) as it was not the source of the phenomena observed in the PBMA-*b*-PSBMA. Therefore, we had to change the zwitterionic block. We had two options to perform this change. The first one consisted in the use of another type of zwitterion (carboxybetaine or phosphocholine). And the second one consisted in the use of a sulfobetaine that did not present the antipolyelectrolyte effect. We decided to search for another sulfobetaine in order to produce a polymer as similar as possible to the one produced previously. Thus, we needed to find the sulfobetaine type that prevents the antipolyelectrolyte effect.

For this search, we used a work from Laschewsky and coworkers [85] in which they studied the influence of the sulfobetaine type and the polymer length in the UCST of sulfobetaine homopolymers (**Figure 2.13**). They synthesized 8 sulfobetaine monomers and analysed the influence of polymer type and length in the UCST. Of all the sulfobetaines tested, **2, 3, 4** and **6** presented low UCSTs.



The figure shows eight chemical structures of sulfobetaine homopolymers, labeled 1 through 8. Each structure consists of a methacrylate backbone with a zwitterionic pendant group. The pendant groups vary in the size and nature of the hydrophobic group attached to the nitrogen atom of the sulfobetaine moiety. Structures 1-4 have different hydrophobic groups, while 5-8 have different quaternary ammonium counterions (methyl, ethyl, propyl, butyl).

Sample	Cloud point [°C]		Sample	Cloud point [°C]	
	In H ₂ O	In D ₂ O		In H ₂ O	In D ₂ O
P-1 ₈₅	41	50	P-5 ₅₀	82	94
P-1 ₂₇₀	55	68	P-5 ₈₀	>100	>100
P-1 ₃₇₅	67	80	P-5 ₉₅	>100	>100
P-1 ₃₈₅	71	86	P-5 ₂₈₀	>100	>100
P-2 ₉₅	< 0	< 0	P-6 ₈₀	< 0	17
P-2 ₂₅₀	< 0	< 0	P-6 ₂₅₀	4	28
P-2 ₃₃₀	< 0	< 0	P-6 ₄₂₀	11	36
P-2 ₄₈₅	< 0	< 0	P-6 ₅₀₀	15	40
P-3 ₆₅	< 0	17	P-7 ₈₅	70	75
P-3 ₉₅	24	34	P-7 ₂₆₀	88	94
P-3 ₂₃₀	38	48	P-7 ₄₃₀	>100	>100
P-3 ₃₈₅	47	56	P-7 ₅₂₀	>100	>100
P-4 ₇₅	< 0	7	P-8 ₁₀₀	41	47
P-4 ₂₉₅	5	14	P-8 ₂₉₀	>100	>100
P-4 ₄₈₀	8	18	P-8 ₄₈₀	>100	>100
P-4 ₅₈₅	10	20	P-8 ₅₄₀	>100	>100

Figure 2.13 Study of Laschewsky and coworkers on the UCST of different sulfobetaine homopolymers [85].

We decided to use Poly(sulfobetainized 2-morpholinoethyl methacrylate) (MESBMA) to produce our polymers. This decision was taken for two reasons: i) it was the only commercially available monomer and ii) the voluminous group pendant to the amine was a morpholino group with an oxygen, while in the other cases were hydrophobic groups. And we considered that a big hydrophobic group could affect the self-assembly of the resultant polymer. Thus, Poly(butyl methacrylate)-*b*-poly(sulfobetainized 2-morpholinoethyl methacrylate) (PBMA-PMESBMA) was the next zwitterionic ABC candidate.

We expected that, with the change on the quaternary amine pendant group, the opposite charges of the sulfobetaine group would not collapse due to steric impedance **Figure 2.14**. Without this collapse, the sulfobetaine group would not lose its hydrophilicity and would not need the addition of salts to the system to interact with the water molecules. And all these facts should result in an ABC with improved tendency to form spontaneously self-assembled nanoparticles with a zwitterionic corona, the main objective of this Chapter.

To synthesize the PBMA-*b*-PMESBMA we decided to follow the same strategy used for the synthesis of PBMA-*b*-PSBMA (showed in **Figure 2.3**). We first would synthesize the PBMA block for then synthesize the 2-morpholinoethyl methacrylate block (precursor of the sulfobetaine); and finally, we would add 1,3-propanesultone to the polymer to form the quaternary amine and the sulfonic acid. As commented above, the risk of this strategy is the possible incomplete derivatization of all the amines present in the polymers. And this risk was higher with this polymer as the 2-morpholinoethyl methacrylate amine is less accessible

for the 1,3-propanesultone and, therefore, the reaction takes place with slower kinetics and requires more energy.

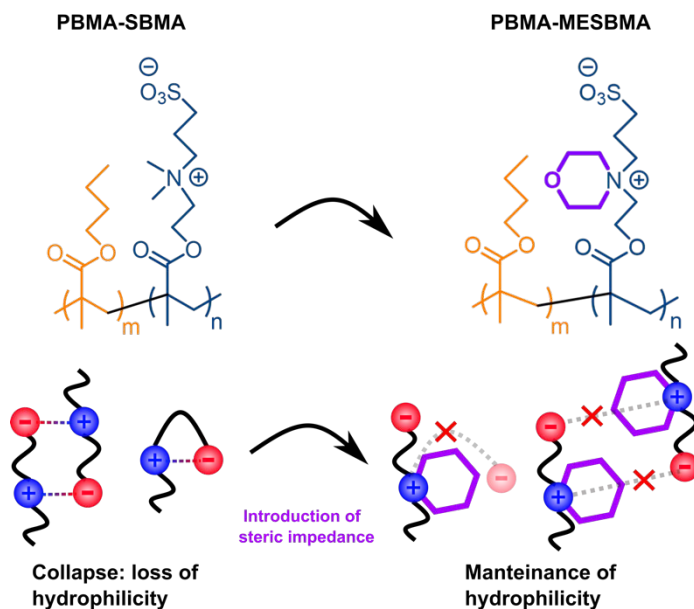


Figure 2.14 Introduction of a voluminous pendant group in the quaternary amine in order to avoid collapse.

The synthesis of the polymer was done without any complication, and the characterization of the polymer was performed using again $^1\text{H-NMR}$. In **Figure 2.15** there is an example of the $^1\text{H-NMR}$ of the different steps in the PBMA-*b*-PMESBMA polymer synthesis. In there we checked that the synthesis of the MESBMA block was performed and that the length of the blocks was the one expected (in the case of the PBMA step, this fact was confirmed in the synthesis of PBMA-*b*-PSBMA).

We observed how the signals of the hydrophilic block did not appear in this $^1\text{H-NMR}$ (there is only one signal around 4.1-4.3 ppm). This signal corresponds to the methylene group next to the ester and, therefore is not affected by the quaternization reaction.

The conditions of the modification reaction were not aggressive enough to cleave an ester bond, thus the possible explanation that we found of this phenomenon was that, when dissolved in CdCl_2 , the polymer only exposes the hydrophobic groups to the solvent and, therefore, the signals corresponding to the hydrophilic groups are not showed in the spectra.

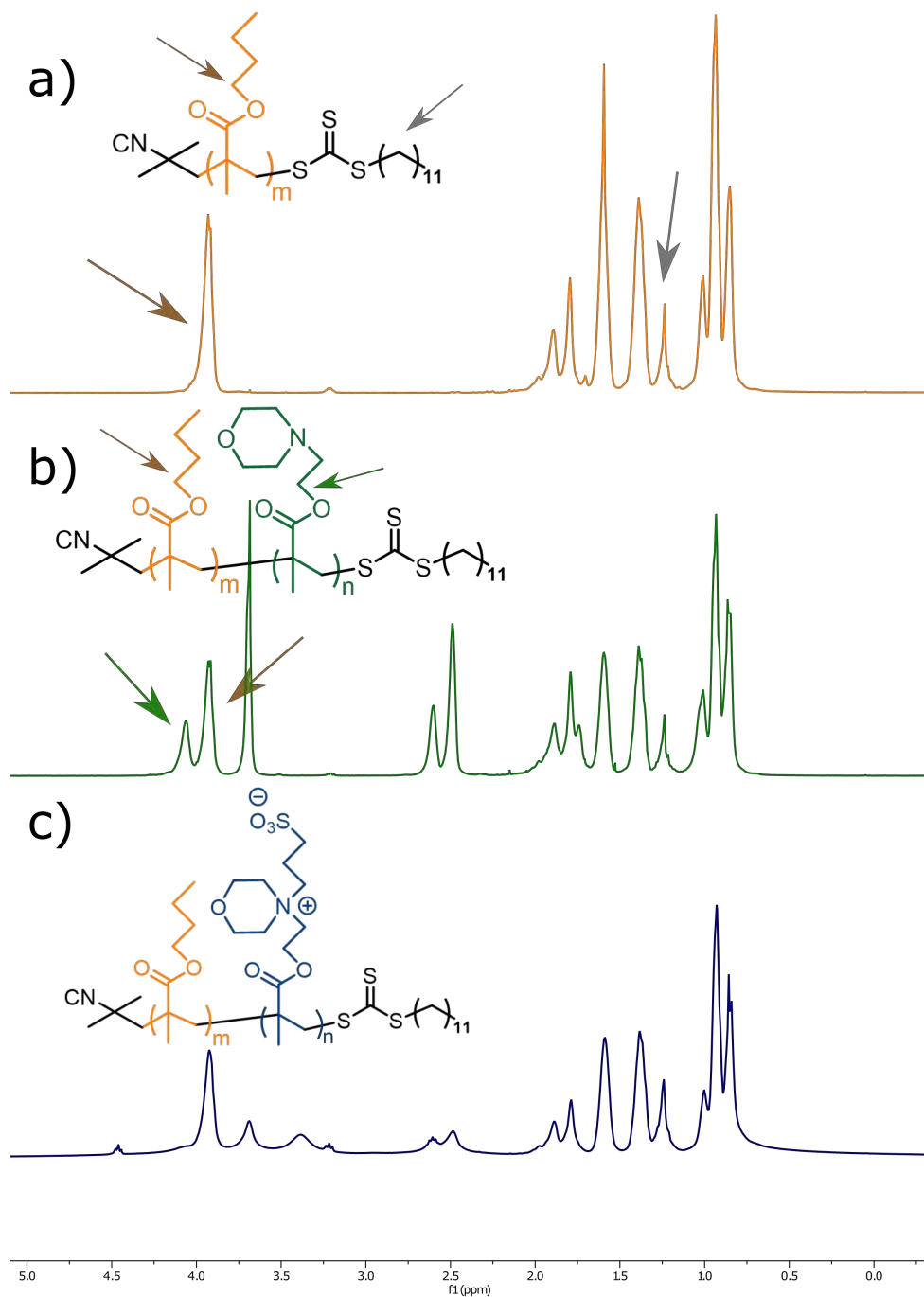


Figure 2.15 $^1\text{H-NMR}$ of (a) PBMA (in CdCl_3), (b) PBMA-b-PMEMA (in CdCl_3) and (c) PBMA-b-PMESBMA (in CdCl_3).

This hypothesis would also explain why, at lower ppm (0-2 ppm; corresponding to the hydrophobic parts of the polymer), the signals are almost identical in both spectra, while at higher ppm (2.2-5 ppm) the intensity of all signals decrease (except the signal corresponding to the methylene of the ester group of PBMA). All these $^1\text{H-NMR}$ problems were expected for zwitterionic ABCs, as they sharp change of polarity in the same polymer structure makes almost impossible to solubilize both blocks in one solvent. Therefore, the appearance of these problems confirmed the quaternization of the amines from PMEMA, as only a zwitterionic ABC could explain these solubilization problems. In the same $^1\text{H-NMR}$, we also observed signals at 3.75 and 2.5 ppm. These signals could indicate that some of the PMEMA amines were not modified; but, due to the above-mentioned problems of this $^1\text{H-NMR}$, this fact could not be characterized nor quantified. Although that there could be some of these non-quaternized amines in the polymer, their percentage would be low (there is a big decrease in the intensity of these signals between **Figure 2.15b** and **Figure 2.15c**). Moreover, the morpholino group is basic (the pK_a of the conjugated acid is 4.9 [92]) and would remain in a deprotonated form at physiological pH, fact that would not compromise the antifouling properties of the polymer.

Following this synthesis route and characterization procedure, we developed 4 different PBMA-*b*-PMESBMA polymers with different length and block ratio (**Table 2.3**). The first polymer (**M1**) was selected in order to compare its behaviour with the polymer **S1**, characterized previously. And, with the polymers **M2**, **M3** and **M4** we wanted to study if the hydrophobic/hydrophilic ratio and the length of the hydrophilic ratio had an influence in the behaviour of the nanoparticle.

	length PBMA	length PMESBMA	PBMA/PMESBMA	Mw (KDa)
M1	25	35	0.71	14.7
M2	40	10	4.00	8.8
M3	40	20	2.00	12.0
M4	70	20	3.50	16.2

Table 2.3 PBMA-*b*-PMESBMA polymers synthesized.

To explore this self-assembly, we started using the same protocol that worked in the case of PBMA-*b*-PSBMA. We dispersed the polymer directly in MiliQ water (these polymers

should avoid the antipolyelectrolyte effect) and stirred overnight in order to promote the hydration of the sulfobetaine. We observed different behaviors depending on the polymer. In the case of polymer M1, the solution was almost translucent with small little white particles in suspension. In the case of polymers M2 and M3, the solution was completely translucent and, finally, in the case of M4 polymer, big aggregates could be observed in the solution, that was not translucent. These results indicated that we had success in overcoming the problems with the antipolyelectrolyte effect by adding the morpholino group. M2 and M3 samples could self-assemble without further processes, while M1 polymer, had a partial self-assembly, as some polymer aggregates could be observed in the solution. Finally, M4 polymer block ratio did not allow the formation of nanoparticles, possibly due to an excessive hydrophobic part that could not be solubilized by the zwitterionic one.

To get more information, we proceeded to perform DLS analysis of the samples (**Table 2.4**). To be able to analyze M1 nanoparticles, we decided to remove the aggregates by 2 strategies. In the first one, we centrifuged the sample to remove these aggregates. And, in the second one, we performed the extrusion process (just like we did in PBMA-*b*-PSBMA polymers) to break these aggregates and form more nanoparticles. We can observe in **Table 2.4** that we obtained nanoparticles using both procedures. By these two procedures we could know that, in first place, the major part of the polymer can self-assemble spontaneously forming nanoparticles and, if some energy is given to the process (extrusion), these small aggregates can break and form nanoparticles.

	Preparation	Size (Mean \pm SD)	PDI (Mean \pm SD)
M1	Centrifugation	63 \pm 6	0.295 \pm 0.045
	Extrusion	88 \pm 1	0.181 \pm 0.005
M2	Direct Dissolution	52 \pm 1	0.216 \pm 0.004
M3	Direct Dissolution	96 \pm 1	0.384 \pm 0.006
M4	Did not form nanoparticles		

Table 2.4 Results of DLS of the samples prepared by different methods ($n=3$). Centrifugation of M1 sample was performed at 6000 g and extrusion was performed with a pore size of 100 μm .

Analyzing M1 samples we could also determine that extrusion process generate slightly bigger nanoparticles with a lower PDI. This lower PDI can be explained by the homogenization of the population by the extrusion process. And the change in size can be explained by the appearance of new particles with a similar size than the pore size, increasing the mean size of the population. M2 and M3 polymers formed nanoparticles with different size and PDI. M2 nanoparticles were smaller and with a lower PDI, while M3 nanoparticles had a slightly bigger size and a higher PDI. The difference between both polymers was the length of the zwitterionic part (M2 had 10 monomers and M3 had 20). Therefore, we considered normal that M3 nanoparticles were bigger. With M4 polymer it was impossible to obtain nanoparticles by any method, indicating that the polymer composition was not favorable for the self-assembly.

When preparing the different samples, we also realized that there was another important difference between the PBMA-*b*-PMESBMA samples and the PBMA-*b*-PSBMA samples. This difference consisted in the maximum polymer concentration. When we prepared samples of PBMA-*b*-PSBMA polymers, the maximum polymer concentration that allowed extrusion was 1 mg/ml. But, when using PBMA-*b*-PMESBMA polymers, this concentration could be raised to 20 mg/ml. This 20-fold increase can be explained also by the antipolyelectrolyte effect, as the interaction between the polymers increase with the polymer concentration. PBMA-*b*-PMESBMA samples do not show this effect and, consequently, they do not aggregate when the concentration increase. This difference is also important for future applications, in which concentrated samples may be needed in order to increase the effectivity of the DDS.

Continuing with the characterization of this set of polymers, we analyzed the Z-potential of the nanoparticles. This parameter gives information about the surface charge of the nanoparticles in the sample. In PBMA-*b*-PSBMA samples we could not analyze this parameter due to the presence of salts in the sample (the method is incompatible with a high concentration of salts). But with PBMA-*b*-PMESBMA we did not need to use salts to produce nanoparticles and, therefore, we could analyze them. Z-potential results (**Figure 2.16**) showed similar behavior for all three samples. The Z-potential values were influenced by the pH, showing positive Z-potential at acidic pH, slightly negative Z-potential at neutral pH and a negative Z-potential at basic pH. This type of behavior is common in all Z-potential analysis [93,94] due to the interaction of the protons and hydroxides with the nanoparticle surface.

Finally, the neutral Z-potential at neutral pHs indicated the zwitterionic surface of the nanoparticles [95,96]

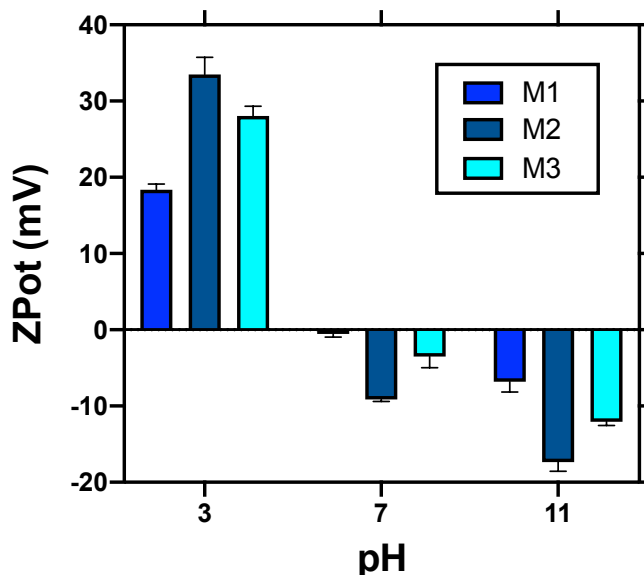


Figure 2.16 Z-Potential of the different PBMA-*b*-PMESBMA nanoparticles ($n=3$).

Finally, we finished our characterization of PBMA-*b*-PMESBMA nanoparticles with the analysis by Cryo-TEM (**Figure 2.17**). The results for M1 and M2 polymers were just like we expected. We observed a uniform population of nanoparticles with around 20 nm of diameter. Again, as happened with PBMA-*b*-PSBMA nanoparticles, these sizes were different from the ones obtained with DLS technique (due to the hydration layer). Therefore, with this technique we could have the certainty that these systems were micelles.

On the other hand, M3 samples (**Figure 2.17**) presented an unexpected morphology. They presented a structure of interconnected tubular polymeric structures with some spherical particles on it. This structure did not match with the macroscopical aspect of the sample, as it should be a gel and it was a solution. Therefore, we assumed that during the sample preparation (cooling) the sample suffered a transformation and self-assembled in these structures. Although they were unexpected, having such structures could be useful in different applications and, therefore, it would be interesting to characterize this behavior in future works.

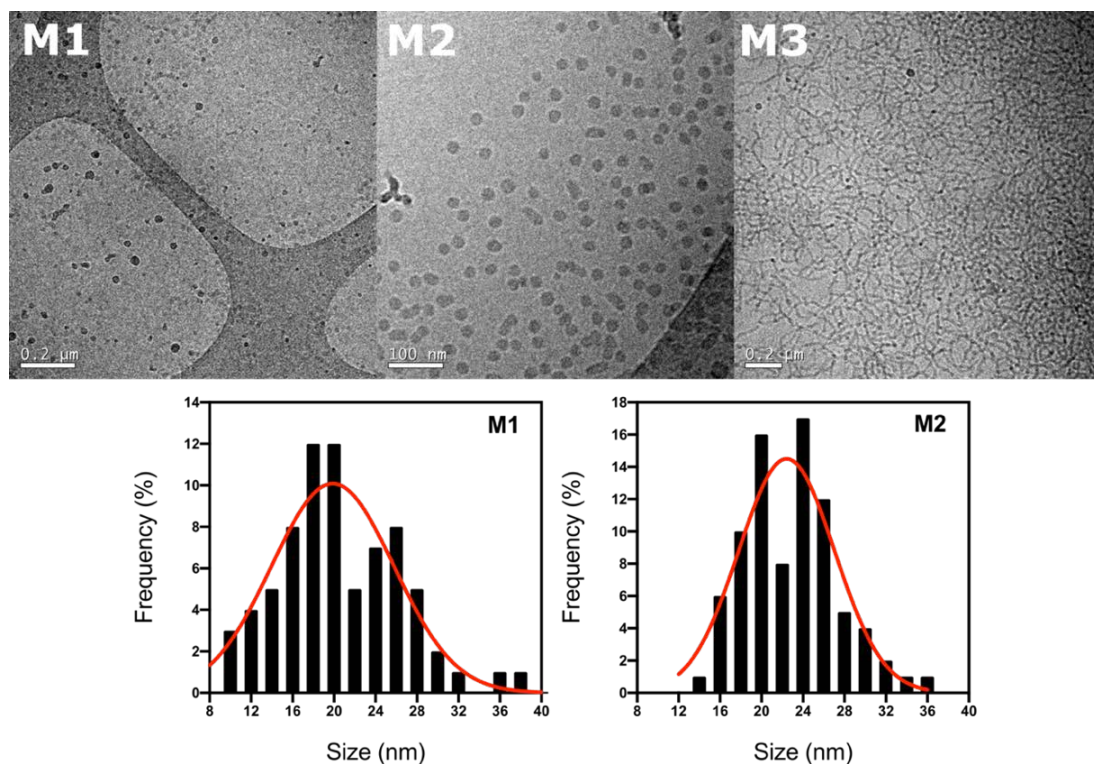


Figure 2.17 Cryo-TEM analysis of the three PBMA-*b*-PMESBMA samples. Histograms have been done by counting 100 nanoparticles.

After the characterization of PBMA-*b*-PMESBMA polymers, they showed the capability to self-assemble in micelles at a high concentration (up to 20 mg/ml) regardless of salt concentration. These properties, together with their zwitterionic surface, converted them in attractive polymers to be used in different applications.

2.2.5. Synthesis and Characterization of PBMA-*b*-PCBMA polymers

Although PBMA-*b*-PMESBMA nanoparticles showed to be stable zwitterionic nanoparticles that could be further used, we decided to produce another type of zwitterionic ABCs by changing the zwitterionic type to carboxybetaine. This zwitterionic type, in contrast with sulfobetaines, contain a carboxylic acid instead of a sulfonic acid, changing some properties. This type of zwitterions are described as the ones with lower protein absorption [29,42,95], they do not present UCST and they are pH sensitive (carboxylic acid can be

protonated). Moreover, the presence of the carboxylic group of the carboxybetaine allows the postpolymerization modification in order to add more functionality to the polymer.

To synthesize this polymer, we followed the same method than the one used for sulfobetaines. We first synthesized the PBMA block, then the PDMAEMA block and, finally, we quaternized the amine with acrylic acid obtaining the quaternary amine and the carboxylic group (**Figure 2.18**). Acrylic acid was used to quaternize the amine because it is an accessible and easy to work reactant that is suitable for the nucleophilic attack of the amine (the presence of the acid in beta of the alkene increases the electrophilic behaviour of the alkene, allowing the reaction).

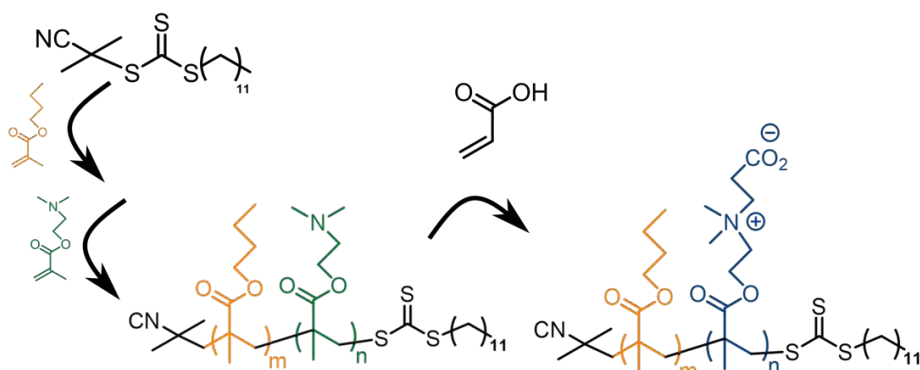


Figure 2.18 Synthesis of PBMA-*b*-PCBMA polymers.

And, as we did in the previous synthesis, we checked the different steps using H¹-NMR analysis (**Figure 2.19**).

The synthesis of PBMA-*b*-PDMAEMA had been previously done to produce PBMA-*b*-PSBMA. Then, we only had to analyze the modification of the PDMAEMA block into PCBMA. The H¹-NMR in **Figure 2.19c** presents the same problems previously observed for PBMA-*b*-PMESBMA: some signals corresponding to protons in the zwitterionic block do not appear or appear with less intensity (this behavior is, itself, a prove that the reaction has been produced). As has been commented, this phenomenon can be explained by the low affinity that the hydrophilic block has with the CdCl₃ solvent and that may produce this decrease in the intensity of its signals. Even so, the appearance of the signal at 3.2 ppm (methyls in the quaternary amine) proves that the modification had been successful.

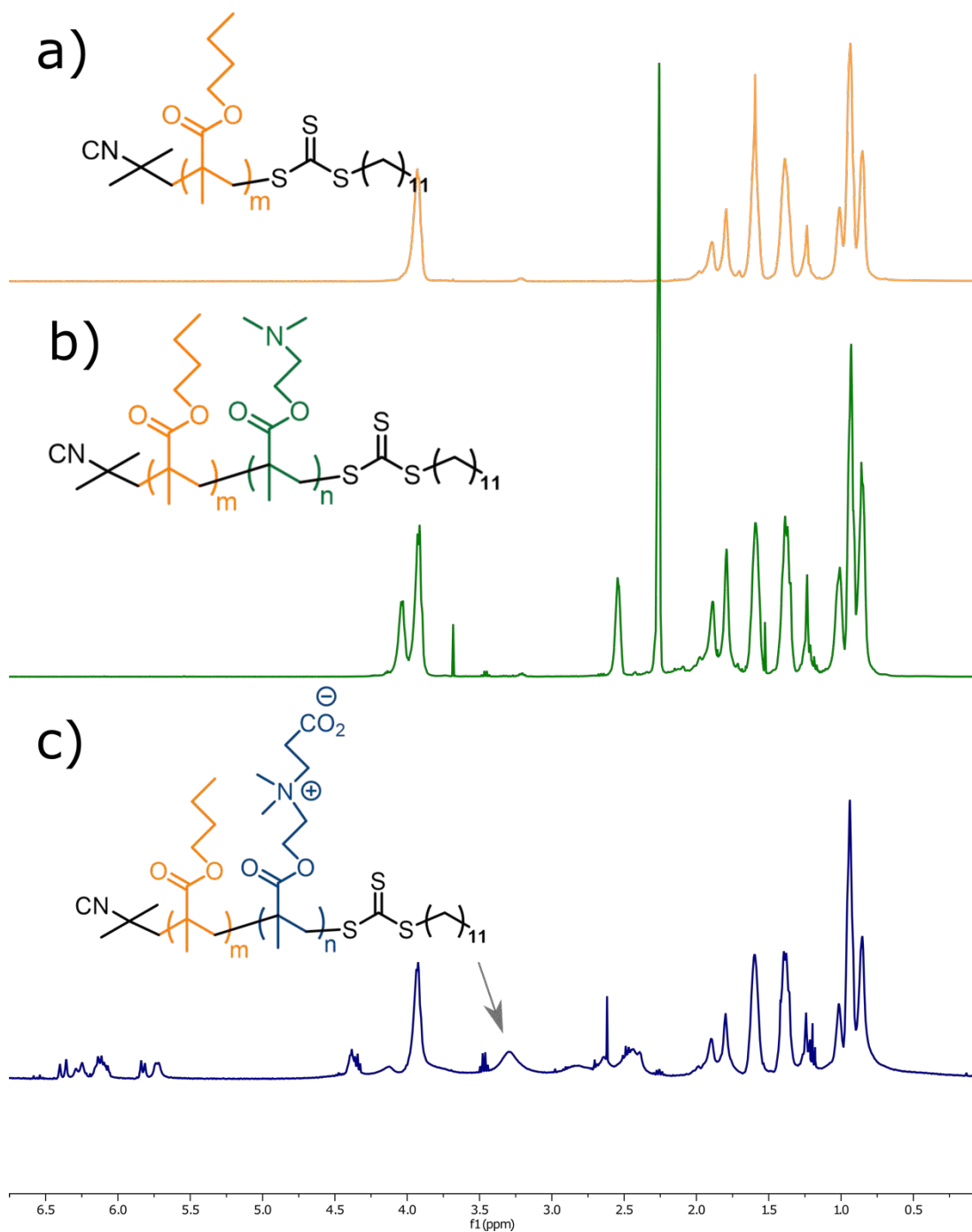


Figure 2.19 $^1\text{H-NMR}$ spectra of (a) PBMA (in CdCl_2), (b) PBMA-b-PDMAEMA (in CdCl_2) and (c) PBMA-b-PCBMA (in CdCl_2), the different steps in the synthesis of PBMA-b-PCBMA.

Traces of unreacted acrylic acid (5.5-6.5 ppm) were also detected in in **Figure 2.19c**. Their presence was produced by the inability to completely eliminate the unreacted acrylic acid due to the complex that it forms with the betaine moiety. We decided to accept these impurities as they were not abundant.

We produced 2 PBMA-*b*-PCBMA polymers (**C1** and **C2**) in which we decided to maintain a common hydrophilic block of 20 monomers and change the hydrophobic block length (the hydrophobic block length has importance in the loading of hydrophobic molecules, aspect that will be addressed in chapter 2) (**Table 2.5**). These two polymers had the same block ratio than the PBMA-*b*-PMESBMA **M3** and **M4** (showed in **Table 2.3**), fact that allowed us to compare the influence of the zwitterionic block on the self-assembly (M3 could do nanoparticles, but M4 did not).

	length PBMA	length PMESBMA	PBMA/PMESBMA	Mw (KDa)
C1	40	20	2	10.1
C2	70	20	3.50	14.2

Table 2.5 PBMA-*b*-PCBMA synthesized.

When dissolving these two polymers in pure water for 24 hours, we observed how both polymer dispersions became completely transparent without any aggregate. We also were able, in the case of **C1**, increase the polymer concentration up to 20 mg/ml without the appearance of aggregates (in the case of **C2**, the maximum concentration was 10 mg/ml). This behavior confirmed that carboxybetaines do not present UCST and, therefore, the self-assembly of the amphiphilic polymer takes place without any problem.

Polymer	Preparation	Size (Mean \pm SD)	PDI (Mean \pm SD)
C1	Direct Dissolution	46 \pm 1	0.227 \pm 0.005
C2	Direct Dissolution	97 \pm 1	0.266 \pm 0.007

Table 2.6 Hydrodynamic Size of PBMA-*b*-PCBMA nanoparticles ($n=3$).

We analyzed both samples in the DLS, obtaining the results showed in **Table 2.6**. The results obtained were similar to the ones obtained for PBMA-*b*-PMESBMA nanoparticles. Both **C1**

and C2 nanoparticles presented a hydrodynamical size suggesting a micelle structure. Therefore, we could conclude that, when we used a zwitterionic block without UCST behavior in an ABC, the polymer self-assembled in a structure of micelle.

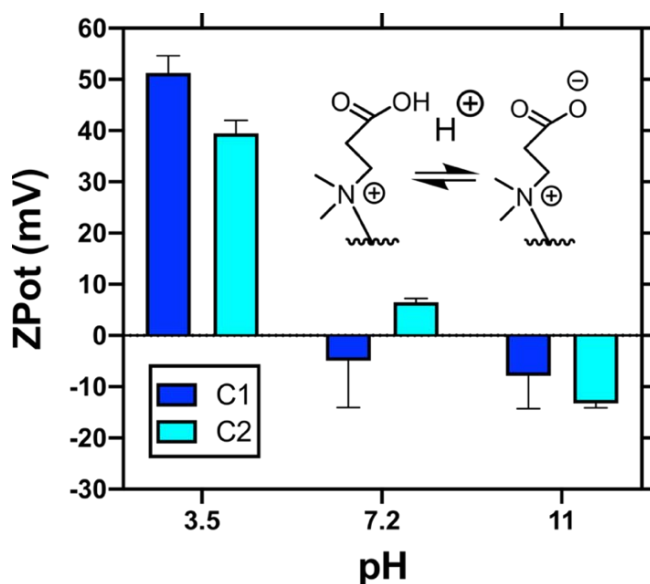


Figure 2.20 Z-Potential of PBMA-*b*-PCBMA nanoparticles ($n=3$).

Finally, to end the characterization of the PBMA-*b*-PCBMA polymers, we performed a Z-potential analysis of the samples (Figure 2.20). The results were similar to the ones in PBMA-*b*-PMESBMA nanoparticles with a difference in the acidic pH. The PCBMA pH sensitivity produces that, above certain pHs, the carboxylic acid from the carboxybetaine protonates. This protonation produces that the carboxylic group loses its charge and the carboxybetaine becomes positive (it only contains the charge of the quaternary ammonium). This pH-sensitivity of the PCBMA can be a drawback for some applications but can also be useful in other applications. Positively charged particles are characterized by a high cell internalization, as well as for good levels of DNA entrapment. Therefore, PBMA-*b*-PCBMA offers possibilities that are not possible with the sulfobetaine copolymers produced before.

After this characterization of PBMA-*b*-PCBMA, we decided that we had enough versatility in the chemical structure of the zwitterionic amphiphilic polymers to adapt to the requirements of future applications. Therefore, we proceeded to start the optimization and

characterization of these nanoparticles for different applications in which their properties were demanded

2.3. Concluding Remarks

In this Chapter, we have developed different zwitterionic amphiphilic block copolymers with the intention to create drug delivery systems with antifouling surfaces. In first place, we have proved that RAFT polymerization followed by a post-polymerization modification is an effective method to produce zwitterionic amphiphilic block copolymers. Then, we have demonstrated the capacity of these polymers to self-assemble in stable nanoparticles, accomplishing the first objective of this thesis. This self-assembly can be modulated by changing the polymer length as well as the hydrophilic/hydrophobic ratio and zwitterionic polymer.

By producing different families of polymers, we have generated ABCs with different properties. PBMA-*b*-PSBMA polymers have shown to be sensible at changes in salinity due to the inner interactions of their charges, fact that can compromise their future applications. To overcome this problem, we have generated another sulfobetaine ABC containing a morpholino group connected to the amine (PBMA-*b*-PMESBMA). These polymers have shown their ability to self-assemble in stable micelles in low salinity solutions. Finally, we have produced carboxybetaine ABCs (PBMA-*b*-PCBMA) that also formed stable micelles. The carboxybetaine moiety convert these nanoparticles into pH-sensible (their surface change from zwitterionic to cationic at low pHs) and also offers different possibilities of post-polymerization modification to the systems.

Overall, the work done in this Chapter has resulted in a catalog of different zwitterionic ABCs that have the ability to form nanoparticles with a zwitterionic surface but with different self-assembly and surface properties. Therefore, they will offer a versatile solution for the development of antifouling and non-immunogenic drug delivery systems, that will be important to achieve the different objectives set in the next Chapter.

Chapter 3: Application of Zwitterionic Amphiphilic Block Copolymers

Part of this chapter has been published in:

A.Biosca*, P.Cabanach*, M. Abdulkarim, M. Gumbleton, C.Gómez-Canela, M. Ramírez, I. Bouzón-Arnáiz, Y. Avalos-Padilla, S. Borrós, X. Fernàndez-Busquets “Zwitterionic self-assembled nanoparticles as carriers for Plasmodium targeting in malaria oral treatment”
Journal of Controlled Release (2021),331,364-375.

Chapter 3: Applications of Zwitterionic Amphiphilic Block Copolymers

3.1. Introduction

In the previous Chapter, we developed different families of zwitterionic amphiphilic block copolymers that showed capacity to form different type of stable nanoparticles with a zwitterionic surface. This zwitterionic surface is interesting for its superhydrophilicity, that is translated in outstanding antifouling properties [32,40–42]. With these properties, the zwitterionic nanoparticles had potential to be used to solve different problems that are currently limiting the application of drug delivery systems in the clinics.

The first of these problems, consist in the fast clearance of nanoparticles from the body. When injected in the blood, most of the drug delivery systems are detected by immune cells as a threat through the detection of protein opsonization [9,97–99]. These cells remove the nanoparticles from the circulation and accumulate them in the spleen, the liver, lymphatic nodes and the lungs, in where they are removed from the body [98]. Moreover, the adaptative immune system (responsible of the immune memory) generate specific antibodies and trained T-cells that specifically recognize the detected material. These antibodies and cells remain in the body for certain time, and generate a faster response to the material if it is administrated again [97]. This immune response to nanoparticles hinders their clinical application, drastically reducing its efficacy. Antifouling materials, such as zwitterionic polymers, have arisen as a possible solution to reduce the immune clearance by avoiding the absorption of proteins around the nanoparticles [100]. Therefore, in this chapter we have explored the capacity of the zwitterionic nanoparticles produced to avoid the protein opsonization and, consequently, increase the efficacy of current drug delivery systems, as has been stated in previous chapters.

The second problem of drug delivery systems in which we evaluated the zwitterionic nanoparticles was their oral drug delivery capacity. This is an important topic for the effectivity of any therapy, as oral delivery is the preferred route of drug administration. But many therapeutic molecules (and DDS) in the market are not suitable to be taken orally. Furthermore, in the recent years, the development of poorly-water-soluble molecules with

low bioavailability but with high potential is emerging [101]. These molecules often have problems of solubility, poor stability in the gastrointestinal tract (GIT) or bad permeation through the intestinal epithelium and have to be injected to improve their bioavailability [102]. This type of administration increases the effectiveness of the drug, but at the same time it supposes a decrease in the life quality of the patient and can lead to a disease mismanagement, especially in chronic patients (such as diabetic patients) [103]. For these reasons, the development of oral drug delivery systems would be a breakthrough in the field. However, the drug delivery field is struggling in developing nanomaterials that can permeate through the mucosa and gastrointestinal epithelium [104].

When a drug delivery system or a therapeutic reaches the GIT, it faces the mucosal membrane, one of the natural barriers that has our body. Mucosal membranes are the mechanism that have our body to protect from hazardous external agents. It is composed by mucosal epithelium cells that excrete mucus. Mucus is a viscoelastic material composed majorly by mucin, long flexible peptide chains densely coated with short glycans, most of which containing a negative charge (carboxyl or sulfate groups). These glycosylated and highly hydrophilic regions are separated by non-coated relatively hydrophobic regions of the protein that fold into somewhat hydrophobic globules or “beads”, that are stabilized by multiple internal disulfide bonds [105]. These long peptide chains assemble in a matrix optimized to allow the exchange of nutrients, water, gases, odorants, hormones, and gametes while preventing the pass of pathogens and other external agents, including most nanoparticles. Size and chemical nature are the two main aspects that determine if a particle can pass through the mucus. It has been demonstrated that small particles can diffuse over the mucin matrix, but large particles do not [105]. In the case of the chemical nature, negative surfaces will be repelled by the negatively charged groups of the mucin, while positive and hydrophobic surfaces will stick to the negative charges and the hydrophobic domains respectively and will diffuse depending on their size. If their diffusion rate is not higher enough, the mucus will be shed before they reach the bloodstream (**Figure 3.1**).

Therefore, to be able cross this barrier, particles have to avoid the repulsion by the mucus but, at the same time, prevent being strongly attached to it. Antifouling polymers have been highlighted as a possible solution to this important problem. As has been commented, their

surface is normally neutral and hydrophilic. Therefore, they do not interact neither with the negative charged mucin nor with the hydrophobic beads.

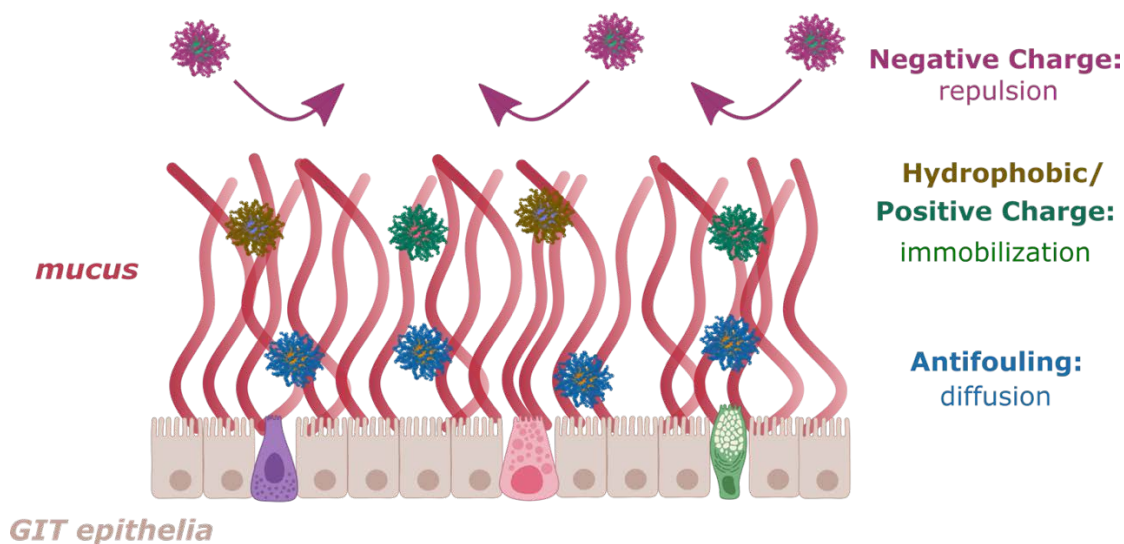


Figure 3.1 Role of nanoparticle's surface chemistry in the interaction with the mucus.

PEGylation of nanoparticles is the current procedure to design oral drug delivery systems (as the current “gold standard” antifouling surfaces) [106–108]. But, despite they improve the nanoparticle diffusion in mucus, current oral drug delivery systems don't achieve good levels of absorption and biodisponibility [109]. Thus, new materials need to be found in order to increase these absorption values and achiever and efficient oral drug delivery system [110].

Olmsted et al. (2001) [111] and Saltzman et al. (1994) [112] respectively discovered how Norwalk virus with a size of 38 nm and human papilloma virus (HPV) with a size of 55nm diffused in human mucus as rapidly as they do in water. These viruses have a surface with positive and negative charges separated with an average of 0.5 nm. Moreover, these type of neutral surfaces are also present in hydrophilic proteins, such as Bovin Serum Albumin or antibodies, that can also diffuse through the mucus [112]. The opposite charges placed so close will neither be repelled nor attracted to the negatively charged glycan domains of mucins; and, also, prevent the interaction to the hydrophobic regions.

Zwitterionic surfaces mimic these hydrophilic surfaces from biomolecules, offering a bioinspired strategy to create oral drug delivery systems. Recent work by Cao et al. [113] (published during the writing of this thesis) shows the success of zwitterionic micelles in crossing both the mucus and the epithelium tissue. Moreover, they proved their efficacy *in vivo* using insulin loaded zwitterionic micelles to treat diabetic mice. Thus, the nanoparticles produced in this thesis have potential to become efficient oral drug delivery systems. Furthermore, their structural versatility can be an advantage in order to be adaptable to different therapies that require an oral administration.

Finally, the last challenge that we addressed with the zwitterionic amphiphilic copolymers developed in Chapter 1 was the solubilization of hydrophobic drugs. As above-mentioned, a big number of hydrophobic molecules have been discovered to have promising therapeutic uses. But their solubility problems hinder their potential, preventing them to reach the market or diminishing their effectivity [101]. This problem has motivated scientists to create drug delivery systems with the capability solubilize them, increasing their biodisponibility [114–117]. Block copolymer micelles are one of the best alternatives to solubilize these drugs due to their core-shell structure that mimics surfactants [55,116–118]. When an hydrophobic drug is added to a solution of a amphiphilic block copolymer, it will be encapsulated in the core of the micelles due to the hydrophobic effect [119]. This effect describes how systems try to reduce the contact between hydrophobic surfaces with water molecules, promoting the encapsulation of the hydrophobic molecule inside of the hydrophobic core of the nanoparticle (this effect is also the responsible of the self-assembly of ABCs).

This capacity of micelles to solubilize hydrophobic drugs have motivated many scientists to develop different micelle systems. Efforts have been putted in optimizing micelles in order to increase its performance *in vivo*. And, of all of micelle properties, those affecting the distribution in the body and the drug loading have been the two that have generated more interest [118]. The distribution of a micelle in the body depends on two factors. In first place, the circulation time that the system can be in the blood without being cleared. And then, if the micelle has targeting properties that direct them to some tissue. Otherwise, the drug loading of a micelle depends on its self-assembly and the change of polarity between the hydrophobic and hydrophilic part.

The zwitterionic amphiphilic block copolymers synthesized in Chapter 2 had potential in both aspects. As has been broadly commented previously, the zwitterionic surface gives them stealth properties for long circulation time. And the polymer structure also converts these micelles in candidates for having good drug loading values. The superhydrophilicity of the zwitterionic part contrasts with the hydrophobicity of the PBMA block. And this sharp change of polarity promotes a strong self-assembly that, at the same time, should allow a high drug payload inside the micelles without destabilizing them.

Overall, in this Chapter we explored the possibilities that the zwitterionic amphiphilic copolymers synthesized offer to solve these three big barriers that prevent the efficacy of the vast majority of drug delivery systems. Then, we optimized their design and drug loading to provide a long-circulating, oral administrated drug delivery system for malaria and cancer treatment, two of the current most devastating diseases that require of optimized systems to improve their current treatment.

3.2. Results and Discussion

3.2.1. Characterization of the interaction between BSA and zwitterionic nanoparticles

Antifouling behaviour was the first property of the zwitterionic nanoparticles that we characterized. As has been broadly commented, preventing the absorption and denaturalization of the proteins in the nanoparticle surface is a key fact to avoid immune response.

We used albumin as a protein model, as it is the most abundant protein in the blood and one of the most important proteins of the protein corona. Moreover, it has been recently discovered that its denaturation in the surface of the nanoparticles results in an increase of the immune response and, therefore, in the reduction of residence time in nanoparticles [120]. And we characterized the interaction between this protein and the zwitterionic nanoparticles using Differential Scanning Calorimetry (DSC). This is a technique widely used in our group to determine the interaction between proteins and nanoparticles. It can determine the thermal Transition midpoint (T_m) between different states of the protein (the temperature in which a protein change its state). Therefore, by using this technique, we could determine if there is a change in the states of the protein due to the presence of nanoparticles [121].

We decided to use PBMA-*b*-PCBMA as the zwitterionic polymer model to perform this analysis. But we also needed a polymer without antifouling properties in order to see if there was a difference with the antifouling zwitterionic one. For this reason, we synthesized poly(butyl methacrylate)-*b*-poly(quaternized dimethyl aminoethyl methacrylate) (PBMA-*b*-PQDMAEMA). This polymer was selected because it comes from the same precursor (PBMA-PDMAEMA) than the zwitterionic polymers, but it has a cationic charge instead of a zwitterionic one.

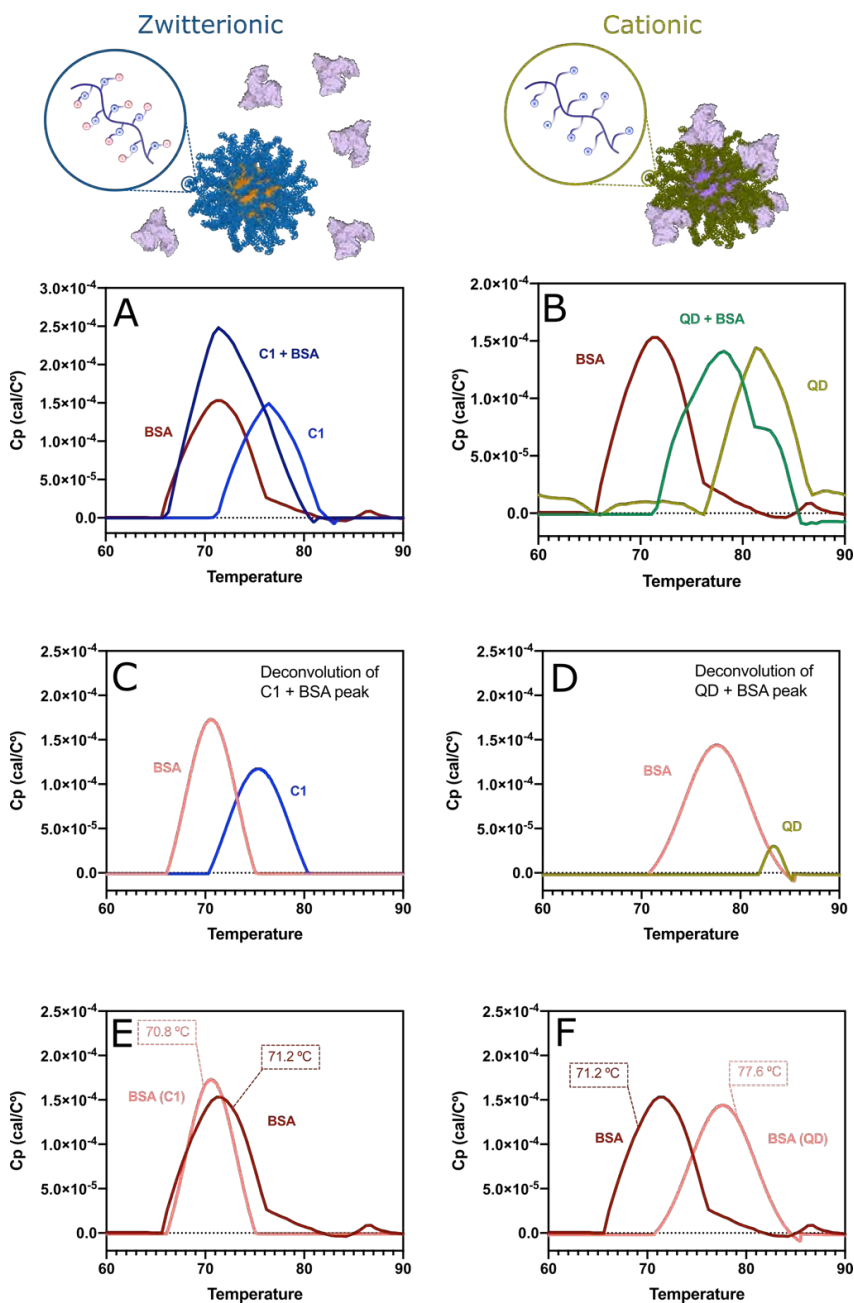


Figure 3.2 DSC thermograms used to characterize the interaction between nanoparticles and BSA. (A,B) Thermograms of BSA, polymer (C1 in A and QD in B) and polymer + BSA. (C,D) Deconvolution of the polymer + BSA peak. (E,F) Comparison between the BSA peak and the deconvoluted BSA peak from the polymer + BSA sample.

The results of the DSC analysis are shown in **Figure 3.2**. We used the different thermograms obtained to compare if there was a shift in the BSA peak when it was in contact with the different nanoparticles. A change in the peak of the BSA would suppose a change in their conformational states, indicating some sort of interaction between the nanoparticle and the protein.

In **Figure 3.2A** and **Figure 3.2B** there are represented the thermograms of a BSA sample, a polymer sample and a sample in which polymer and BSA were incubated for 1 hour. In the case of **Figure 3.2A**, we could observe how the native BSA had a T_m around 70 °C (corresponding to the denaturation of the protein) while the C1 nanoparticles had a T_m around 76 °C that corresponds to the change in the self-assembly of the nanoparticles. Then, in the case of the C1:BSA sample we saw how the peak had not a normal distribution (due to the presence of two species with different T_m). On the other hand, in **Figure 3.2B** we saw that the QDMAEMA nanoparticles had a T_m around 80, and that QD:BSA sample presented also a peak without normal distribution.

To continue the analysis, we took the peaks of the polymer:BSA samples and deconvoluted them with the *Multiple peak fit* function of *Origin®* software. These results are showed in **Figure 3.2C** and **Figure 3.2D**. In the case of the polymer C1, we saw how this deconvolution gave two peaks, that we assigned to the BSA and the nanoparticles. For the polymer QD, we also obtained two peaks, but this time with different integrals. We assigned the bigger peak to the BSA and the small one to the nanoparticles.

With the data obtained from the deconvolution, we could compare the T_m of BSA when it was in a native state and when it was in contact with the zwitterionic and cationic nanoparticles (**Table 3.1**). These results clearly indicated that while the BSA in contact with the zwitterionic nanoparticles presented almost the same T_m than in the native state (70.8 °C vs 71.2 °C), the BSA in contact with the cationic nanoparticles suffered a change in the T_m (70.8 °C vs 77.6 °C). This change in the T_m indicates a change in the conformation of the BSA when it is in contact with the cationic nanoparticles, possibly due to a partial denaturalization and absorption on the nanoparticle surface.

Samples	T _m
BSA (native)	70.8 °C
BSA (ZW surface)	71.2 °C
BSA (positive surface)	77.6 °C

Table 3.1 *T_m of BSA in a native form and in contact with the two nanoparticles tested (with zwitterionic and cationic surface).*

These results indicated the inert effect of zwitterionic surfaces towards a the BSA protein model, produced by the strong hydration of such surfaces that avoid the interaction with the biomolecules present in the media. Although more experiments with different proteins would be needed to have a big picture of the protein corona around the zwitterionic nanoparticle, these results indicated that the most common protein in the plasma did not interact with the zwitterionic nanoparticles. These results were in line with the results published about this issue in the bibliography and were also complemented by the work presented in the next chapter. Therefore, these results were used to prove that the self-assembly of the zwitterionic ABC resulted in zwitterionic nanoparticles with a zwitterionic surface. And that this zwitterionic surface presented antifouling properties.

3.2.2. Internalization of the zwitterionic nanoparticles in a gastrointestinal epithelium model

We continued the characterization of the nanoparticles by analysing their capacity to cross the gastrointestinal barrier. As has been previously commented, achieving an oral drug delivery system is a complicated task due to the double barrier consisting in the mucus and the epithelium layer. Although diffusing over the mucus has been the aspect that has generated more scientific interest, crossing through the epithelia is just as important. If nanoparticles diffuse over mucus but cannot cross the epithelia, they will be removed from the body and will not reach the bloodstream. For example, PEG has exhibited some diffusion over the mucus, but it has low internalization into the cells, compromising its performance in oral drug delivery systems [110].

We started testing the internalization of the nanoparticles into gastrointestinal epithelium cells. But to be able to perform this analysis, we needed a way to track the polymer inside the cells. We decided to introduce a fluorescent molecule in the structure of our polymer using the trithiocarbonate end group that they had from the RAFT Agent. This trithiocarbonate group can be cleaved by a nucleophile attack from an amine giving a reactive free thiol. Then, this thiol can be modified through the different options that the thiol chemistry offers [122]. Thus, we cleaved the trithiocarbonate with cyclohexylamine and used a Cy3-maleimide (the maleimide group effectively reacts with the free thiols by the thiol-ene reaction) to attach this fluorophore to our polymer **Figure 3.3**).

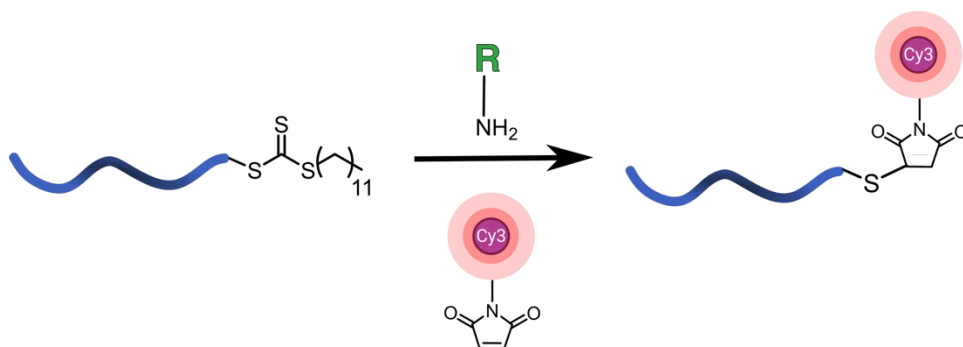


Figure 3.3 Trithiocarbonate aminolysis used to include the Cy3 fluorophore molecule to the polymers produced.

Once we had marked the polymer, we characterized the internalization of the different zwitterionic nanoparticles into gastrointestinal epithelial cells. We used Caco-2 cells to perform this analysis, as they are a well described cell line broadly used as a gastrointestinal barrier model [123]. The different marked zwitterionic nanoparticles were incubated during 6 hours with Caco-2 cells. After this time, the medium of the cells was changed and the fluorescence of the samples was analysed with fluorescence microscopy. Therefore, we could observe the fluorescence of the nanoparticles that internalized into the cells (while the non-internalized nanoparticles were removed with the change of media).

We observed a successful internalization of all the different nanoparticles into Caco-2 cell model (**Figure 3.4**). These results were important because, in first place, they showed the success of nanoparticles to cross the Caco-2 cell membrane and indicated potential to pass-

through the gastrointestinal cell barrier. And they also showed that the internalization occurred with the three type of zwitterionic nanoparticles, indicating that this phenomenon took place due to the surface charge of the nanoparticles and not due to the surface type.

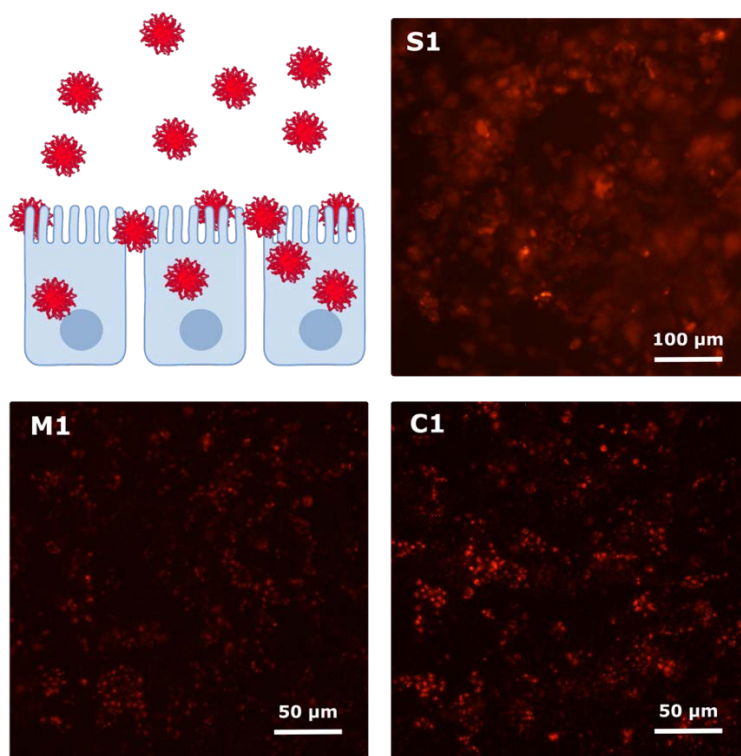


Figure 3.4 Fluorescence microscopy images of Caco-2 cells incubated 6 hours with the different zwitterionic nanoparticles (488/532 laser line.)

The internalization of the zwitterionic nanoparticles into Caco-2 cells was an important milestone to achieve our goal. A big number of mucus penetrating materials fail in crossing the gastrointestinal epithelium (PEG, for example [110]). Therefore, proving that zwitterionic polymers can internalize in Caco-2 cells shows their capability to cross this barrier. This capability of zwitterionic materials to internalize into Caco-2 cells have been recently investigated by Cao et al. [113] in a work where they showed that this internalization is due to the similarity of zwitterionic surfaces with betaine (an important zwitterionic osmolyte found in many foods). Then, the bioinspired design of zwitterionic polymers is a key fact in their capability to cross the gastrointestinal barrier.

3.2.3. Capacity of zwitterionic nanoparticles to pass through the mucus

Once proved that the nanoparticles could enter into the epithelium cells, we characterized their capacity to penetrate through the mucus in order to prove their potential to become an oral drug delivery system. To do so, we performed a Multiple Particle Tracking (MPT) of the different samples (we performed these experiments in collaboration with Prof. Gumbleton group in Cardiff University).

The MPT technique is used in multiple fields due to its ability to track fluorescent particles in different biofluids [124]. In our case, we tracked the marked zwitterionic particles in mucus in order to know their diffusion in this fluid (directly related with the interactions between the mucus mesh and the nanoparticles).

We again analysed the 3 zwitterionic nanoparticles with different zwitterionic surfaces (sulfobetaine, sulfobetainized morpholinoethyl and carboxybetaine) in order to know if there were differences in the performance of the nanoparticles depending on the zwitterionic type (**Figure 3.5** and **Table 3.2**)

In **Figure 3.5a** there are represented diffusion distribution for the different polymers. In there, we observed how SB1 nanoparticles were the nanoparticles that presented a higher diffusion over the mucus, followed by M1 nanoparticles and finally by C1 nanoparticles. S1 and M1 nanoparticles had similar diffusion distribution (slightly higher diffusion for S1) while C1 nanoparticles clearly showed less diffusion. It is also interesting the difference between the 10th percentile of the C1 and the rest of percentiles was bigger than for M1 and S1 polymers (meaning a higher degree of heterogeneity). This difference in the diffusion is clearly shown in **Figure 3.5b**, in which we represented the mean diffusion of the three polymers depending on their size. This representation was important because size can have a role in the diffusion of the nanoparticles through the mucus (as the mucus is a mesh). We determined that the size was not the main factor affecting the diffusivity of the nanoparticles, as C1 and M1 nanoparticles showed a different size and the diffusion of M1 was 2-fold times the diffusion of C1. In this graph we could also clearly see the difference of diffusivity between the sulfobetaine and carboxybetaine zwitterionic types of nanoparticles.

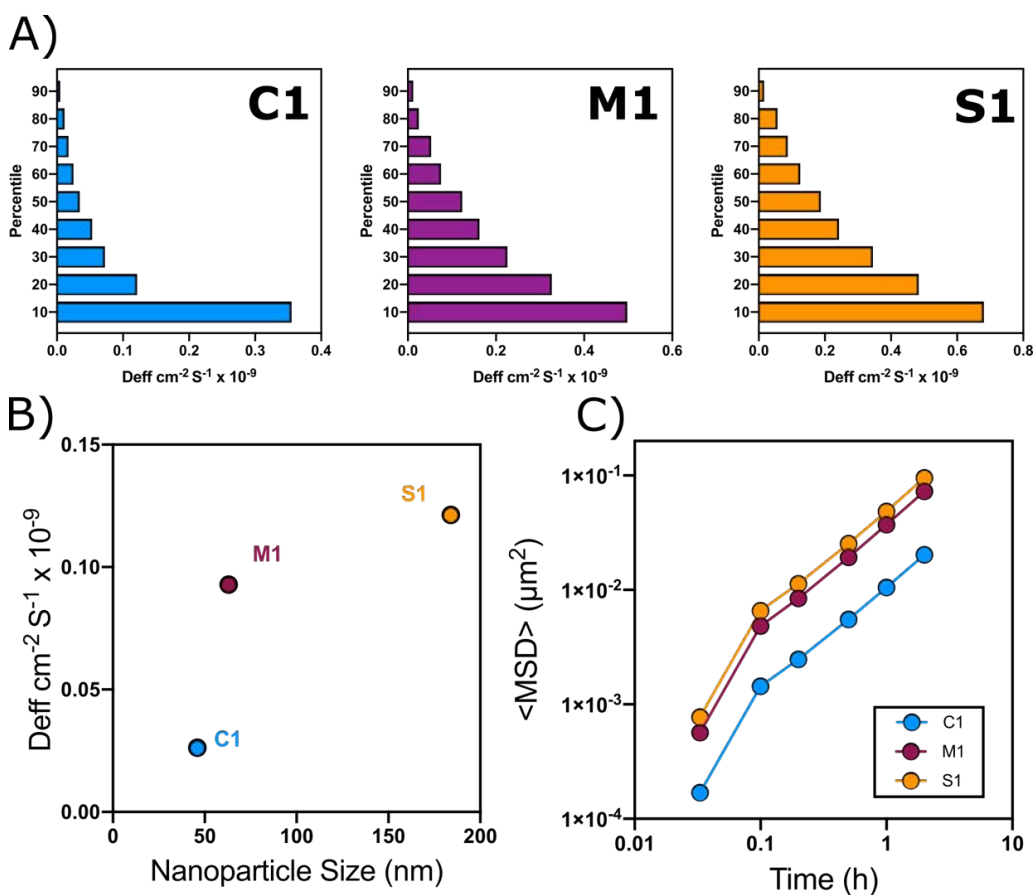


Figure 3.5 MPT analysis of the different zwitterionic nanoparticles in mucus. (A) Heterogeneity of the nanoparticle movement ($n=360$). The percentile shows the D_{eff} value below which a percentage of the D_{eff} observations may be found. (B) D_{eff} of the particles depending on their size. (C) Ensemble-averaged geometric mean squared displacement (MSD) as a function of time scale for the different zwitterionic nanoparticles.

Nanoparticle size (nm)	D^0 water ($\text{cm}^2 \times \text{S}^{-1} \times 10^{-9}$)	$\langle D_{eff} \rangle$ (mucus) ($\text{cm}^2 \times \text{S}^{-1} \times 10^{-9}$)	% Ratio Muc/W	
C1	46	83.4	0.026	0.0314%
M1	63	59.8	0.093	0.1553 %
S1	184	22.9	0.121	0.529 %

Table 3.2 Data from the MPT analysis.

Finally, in **Figure 3.5c** it is represented the ensemble average Mean Square Displacement (MSD) of the different nanoparticles. With this graph we could get an idea about the penetration of the nanoparticles into the mucus mesh and the interaction with it. We observed a change in the slope of the MSD at $t \approx 0.1$ s. This change of slope can be attributed to the interaction of the nanoparticles with the mucus mesh. But although this interaction, the slope of the MSD at $t > 0.1$ s is still positive, indicating that the nanoparticles diffuse through the mucus and do not strongly attach to it.

The Caco-2 internalization experiment together with the MPT analysis showed that the zwitterionic nanoparticles produced could cross both of the barriers to achieve an oral administration. While in the case of internalization into Caco-2 cells all nanoparticle types succeeded, sulfobetaine nanoparticles outperformed carboxybetaine nanoparticles in the diffusion over the mucus. Therefore, sulfobetaine nanoparticles proved to be the best candidates for oral administration.

3.2.4. Curcumin encapsulation for antimalarial applications

At this point of the thesis, we had characterized the antifouling properties of the zwitterionic nanoparticles and their capacity to pass through the gastrointestinal tract barrier. They had been proved to be a promising strategy for both of these big drug delivery challenges. Therefore, the incorporation of therapeutic molecules into them was the next necessary step. To become a drug delivery system, our nanoparticles had to be able to load drugs inside them. And as has been explained in the introduction of this chapter, we considered that hydrophobic drugs were the type of drugs that more fitted in our system.

In this scenario, we decided to characterize the capacity of the zwitterionic nanoparticles to encapsulate the hydrophobic drug curcumin and become an antimalarial drug delivery system. Malaria is the most devastating parasitic disease of all humankind history. It is caused by a protozoan parasite of the genus *Plasmodium* and is transmitted by female mosquitos of the genus *Anopheles*. Nowadays, its impact is concentrated in the sub-saharian regions, representing an important health and economic burden for the developing of these underdeveloped countries [125–127]. Although in the last decades there have been many efforts to eradicate the disease that have resulted in the reduction of its impact (mainly through chemotherapy and insecticide-treated nets) [128], the appearance of drug-resistant

strains is a big roadblock for the eradication of the disease [129]. Therefore, new forms of chemotherapy are necessary to achieve this objective [130]. The possibility of using curcumin against malaria would give a new tool, especially for the most affected zones, to fight this disease. Curcumin is a polyphenolic compound that has been used as a food colorant since ancient times in Asia and Africa (i.e., it is a component of the curry). But in the last century this molecule has also generated interest for its potential therapeutic applications. It has been proved to be antioxidant, anti-inflammatory, anticarcinogenic and, also, antimalarial [131–137]. Although these properties, the use of curcumin in clinics is limited due to bioavailability problems. Its oral absorption is poor and, if injected in blood, it is rapidly cleaned from the circulation [138]. Thus, multiple curcumin drug delivery strategies have been proposed in the recent years [133,139–142]. Following this line, we thought that our zwitterionic polymeric nanoparticles were interesting to encapsulate this hydrophobic drug due to their potential to be a long-circulating system and also the possibility to administrate them orally.

This second property is of vital importance for a successful anti-malarial treatment in the most affected zones. These zones are mainly underdeveloped and lack of a proper logistic system. And the difference of logistics needed between oral and intravenously administration make the first option more prone to have a success in the medication campaign than the second one. Curcumin is a hydrophobic drug and, therefore, its encapsulation into amphiphilic nanoparticles is entropically favourable (due to the hydrophobic effect). The encapsulation of hydrophobic drugs into amphiphilic nanoparticles is entropically favourable, due to the hydrophobic effect. Therefore, when added curcumin to the system, the system itself should tend to incorporate the curcumin into the core of the nanoparticles.

With this hypothesis, we produced curcumin loaded nanoparticles by following the same procedure used in the production of non-loaded nanoparticles but adding a curcumin solution in DMSO at a certain moment of the process. In the case of PBMA-*b*-PSBMA nanoparticles in which an extrusion process is needed to form the nanoparticles, curcumin was added after the overnight stirring, followed by 30 minutes of incubation and extrusion. In the case of PBMA-*b*-PMESBMA and PBMA-*b*-PCBMA, curcumin was added directly after the overnight stirring. We observed clear differences between the curcumin samples and the curcumin-loaded nanoparticles (**Figure 3.6**).

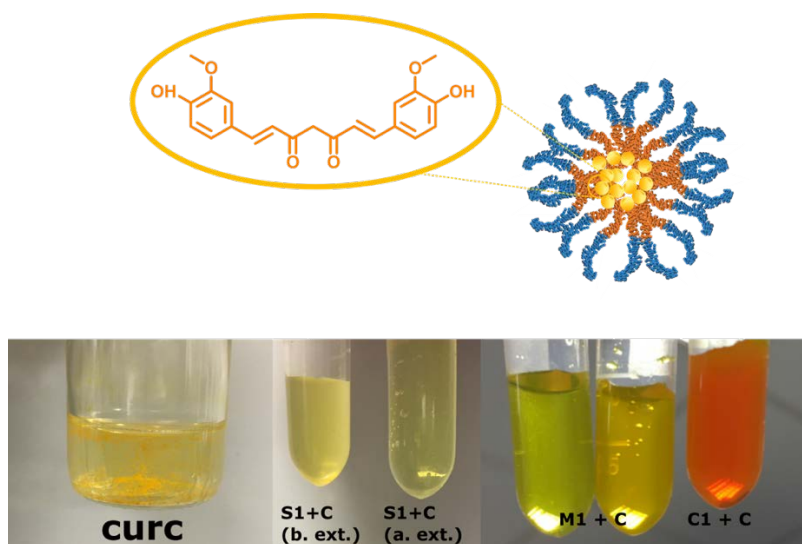


Figure 3.6 Curcumin encapsulation in the different zwitterionic nanoparticles.

When we added curcumin (dissolved in DMSO) to a water solution, a yellow precipitate appeared, proving the low solubility of curcumin in water. On the other hand, when we added curcumin to a solution containing the zwitterionic amphiphilic copolymers, we observed a complete dissolution of the curcumin, without forming any type of precipitate.

In order to determine the maximum amount of curcumin that we could load in our nanoparticles, we gradually increased the curcumin added until a non-transparent solution was obtained (meaning that there was unencapsulated curcumin). The results of maximum curcumin concentration are showed in **Table 3.3**.

With these results, we first confirmed the capacity of our nanoparticles to encapsulate a hydrophobic drug. Moreover, the curcumin concentrations and the drug loading efficiency that the zwitterionic nanoparticles showed (specially the PBMA-*b*-PMESBMA and PBMA-*b*-PCBMA polymers) had a similar efficiency or even outperformed the different curcumin nanoformulations [143]. Therefore, the prediction done at the start of this thesis was correct (the sharp change of polarity of the polymers enhances the encapsulation of the nanoparticles).

	PBMA-ZW block	[Polymer] (mg/ml)	[Curcumin] (mg/ml)	Solubility increase [144]	Drug loading (w C / w Total)
S1	25-35	0.6	0.04	20-fold	6.3 %
M1	25-35	10.0	1.5	750-fold	13.0 %
M2	40-10	10.0	3.0	1500-fold	23.1 %
M3	40-20	10.0	3.0	1500-fold	23.1 %
C1	40-20	10.0	4.0	2000-fold	28.6 %
C2	70-20	10.0	5.0	2500-fold	33.3 %

Table 3.3 Data of the curcumin encapsulation in the different zwitterionic nanoparticles produced. (native curcumin solubility in PBS is taken from [144]).

These results also showed that polymers with a higher proportion of hydrophobicity had better drug loading (M2, M3, C1 and C2 polymers). In the case of S1 polymer we supposed that the UCST problems that this polymer presented, and that limited the maximum polymer concentration, hindered the encapsulation of curcumin in the hydrophobic parts, resulting in a limited encapsulation.

After proving the encapsulation of curcumin in the nanoparticles, we characterized the size of these nanoparticles to see if there was a difference between the empty nanoparticles and the curcumin-loaded ones. We performed DLS analysis of the different curcumin-loaded nanoparticles (**Figure 3.7A**) and we obtained similar size results than the ones of empty nanoparticles. We also performed Cryo-TEM images of S1, M1 and M3 nanoparticles (**Figure 3.7B**, **Figure 3.7C** and **Figure 3.7D**). In these images, we saw some interesting phenomena. In first place, in S1 polymer we could see the presence of two populations. One of 200 nm approximately (in the Cryo-TEM images of empty nanoparticles, the size of the particles was around 100 nm (**Figure 2.10**)) and another smaller population around 50 nm). This phenomenon is interesting, as it seems to show the formation of small micelles but also bigger aggregates (further characterization on the interaction of an hydrophobic molecule in the UCST of these polymers would be interesting). In the case of M1 polymer, there was not change between the empty and loaded nanoparticles (as the polymer directly formed micelles without a hydrophobic drug).

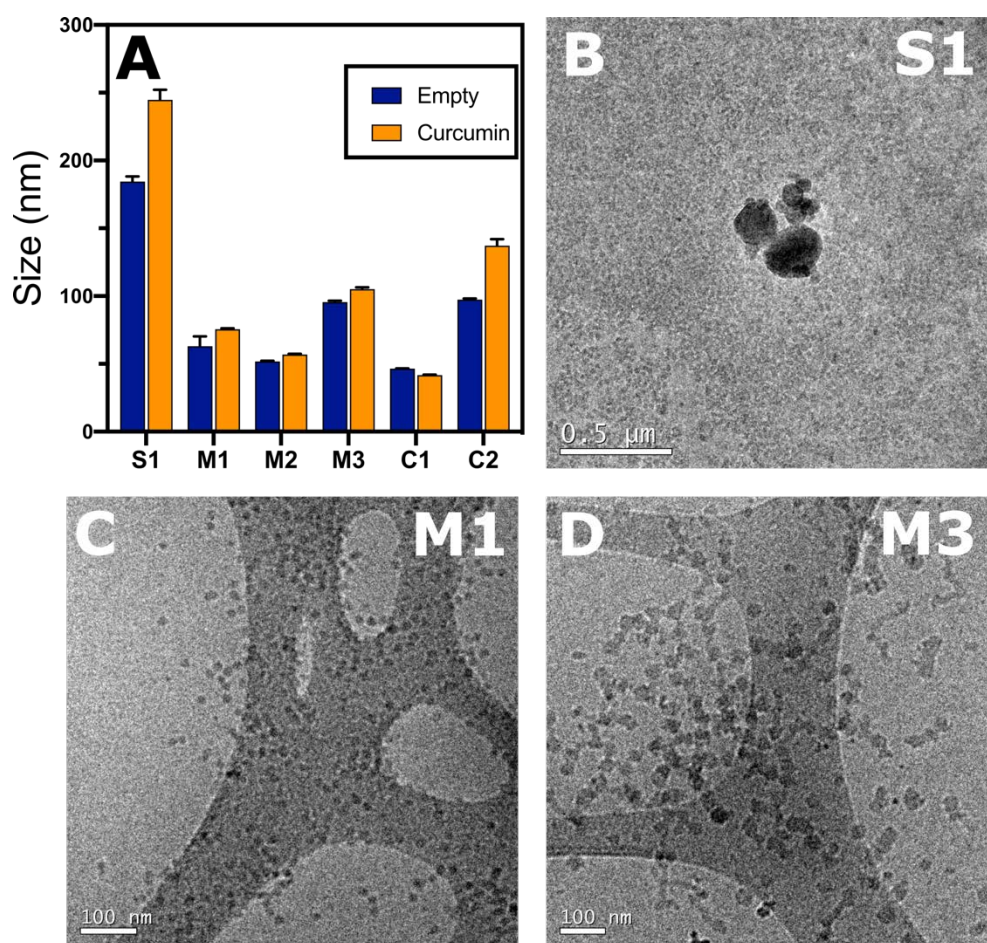


Figure 3.7 Encapsulation of Curcumin. (A) DLS measured size of curcumin-loaded NPs compared to Empty NPs ($n=3$). (B,C,D) Cryo-TEM images of curcumin-loaded S1 (B), M1 (C) and M2 (D) polymers.

Finally, in M3 nanoparticles we observed a complete change of morphology. While in the empty nanoparticles (Figure 2.17) we observed nanotubular structures, in the curcumin-loaded the structure was spherical. We could also observe the interaction between these nanoparticles, as there were multiple particles with fused membranes in the images. This change of morphology produced by curcumin could be explained by the enhancement of the micellar self-assembly produced by hydrophobic molecules. By the hydrophobic effect, the hydrophobic molecule tends to move to the most hydrophobic environment (where the contact with water is minimum). And when interacting with the hydrophobic segments of the polymer, it can change its conformation. As has been commented in the previous chapter,

this behavior is interesting for further investigation (but in the case of this thesis, we preferred to continue with our main objective rather than focusing at this part).

3.2.5. Antimalarial characterization of curcumin-loaded zwitterionic nanoparticles

At this point, we had proved that our zwitterionic nanoparticles could encapsulate a hydrophobic drug model (curcumin) with high levels of drug loading and achieving concentrations up to 5 mg/ml. This encapsulation values were enough to start characterizing the effect that these nanoparticles had in malaria models. We collaborated with the *Nanomalaria* group from the IBEC/ISGlobal (directed by Dr. Xavier Fernández-Busquets) to perform the characterization of the curcumin-loaded nanoparticles in malaria models.

We first tried to evaluate the capacity of our sulfobetaine nanoparticles to interact with *P. falciparum* parasitized red blood cells (pRBC). To perform this evaluation, we used the previously produced Cy3-labeled sulfobetaine polymers (S1 and M1) and we added them to a culture of infected blood in which the DNA of the *P. falciparum* was labeled with Hoescht 33342 (RBC do not have DNA, so they are not labeled). Then, we analyzed the samples using flow cytometry (**Figure 3.8**) and confocal microscopy (**Figure 3.9**). For flow cytometry assay, samples were analyzed directly (without washing) and after a washing in cell culture media. The results of this analysis were promising, as we observed accumulation of the nanoparticles in the intraerythrocytic form of the plasmodium falciparum while there was not observed any accumulation in the non-infected RBC (<0.8 %). We observed a slightly better performance of the M1 polymer compared to the S1 polymer, especially after the washing (74.8% over 41.2%). While the percentage of the pRBC containing M1 nanoparticles do not change with the washing, in the S1 polymer there is a decrease of 36.7 % of pRBC with nanoparticles. This decrease could be derived from the washing of loosely bound nanoparticles.

Complementary to the flow cytometry assay, we decided to perform confocal microscopy to have a more visual idea of the interaction of the zwitterionic nanoparticles and the pRBC (**Figure 3.9**).

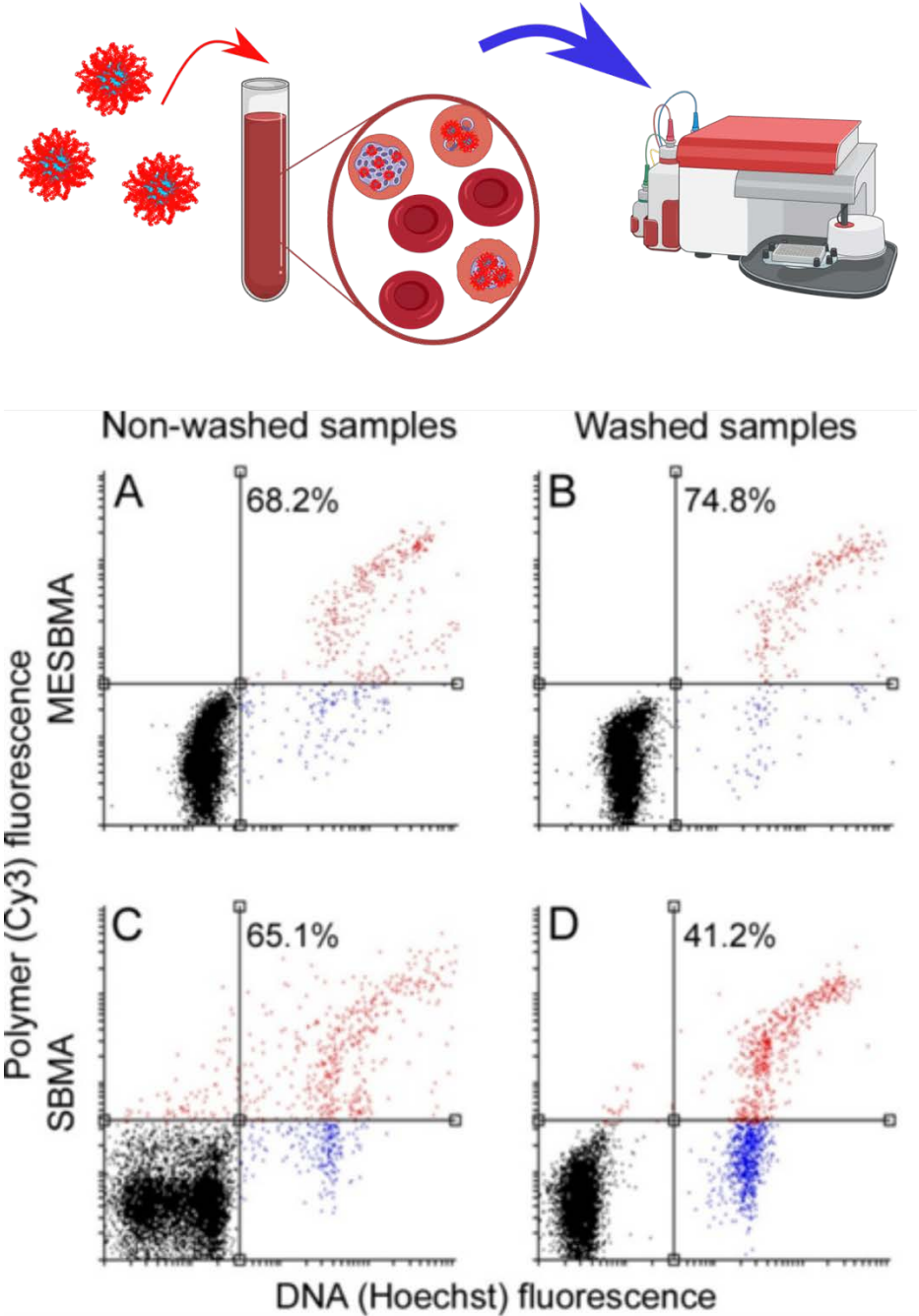


Figure 3.8 Flow cytometry analysis of the interaction between Cy3-labeled zwitterionic nanoparticles and pRBC (which DNA was labeled with Hoescht).

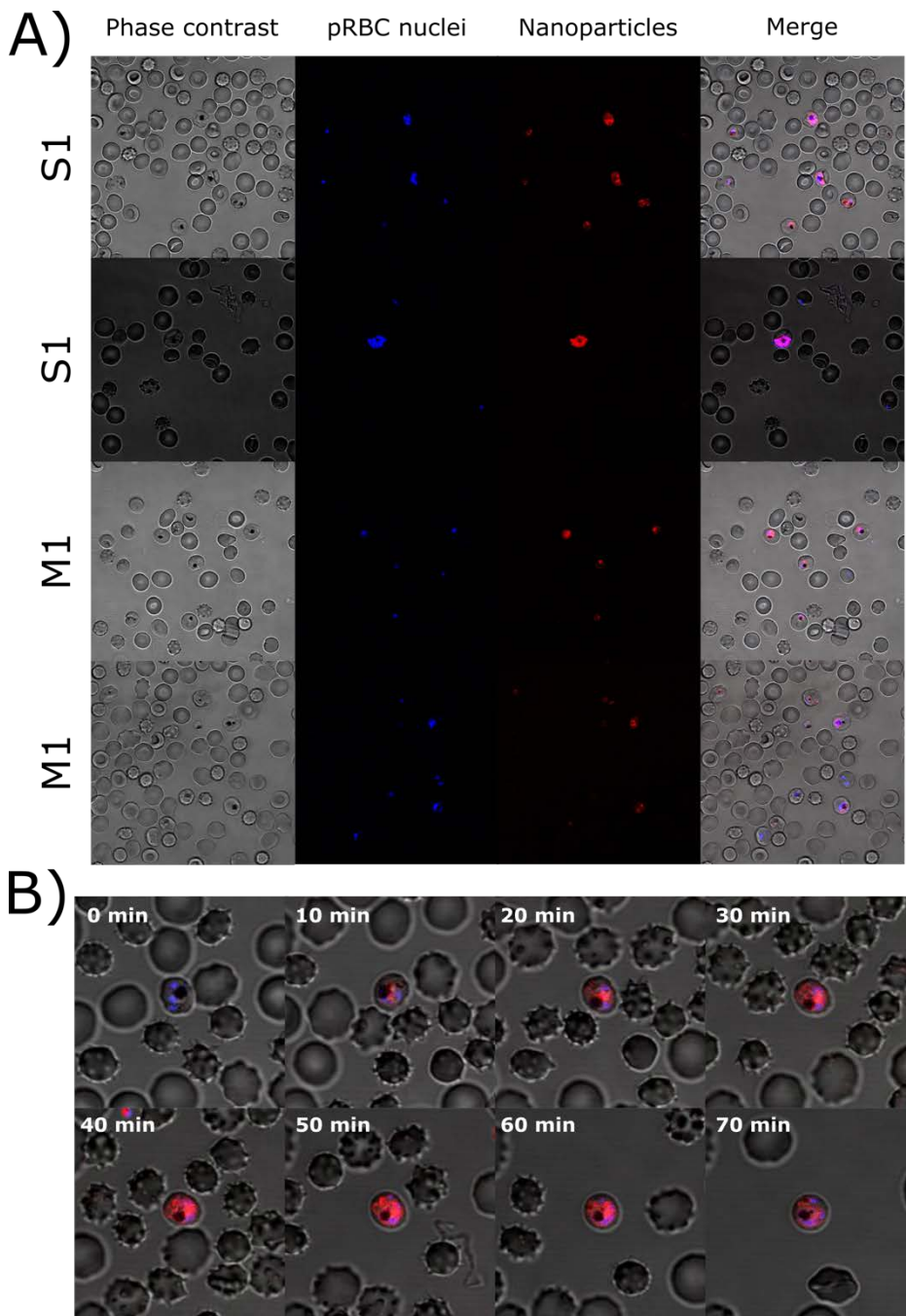


Figure 3.9 Confocal Microscopy of the samples containing pRBC and Cy3-labeled zwitterionic nanoparticles. (A) Images of the different microscopy lines for 2 positions of each polymer. (B) time-lapse of S1 polymer.

In **Figure 3.9A** there are showed the different excitation lines (and the merge of the different lines) for a same image (2 images for M1 and 2 images for S1). In there, we could see the total colocalization of polymer signals with the parasite signal for both polymers. This fact is really interesting, because even in the pRBCs, the polymer is only found inside the parasite and not in the cytosol of the pRBC. The polymers used had not any active targeting to the parasite. Thus, to explain the accumulation of the nanoparticles in the parasite we hypothesized that the nanoparticles could diffuse over the erythrocyte and parasite membranes freely but, once they enter in the parasite, they interacted with it and loss their ability to diffuse again.

Another interesting fact that we observed in these images was that the polymer could enter in all the stages of the parasite, even in the ring stages (typically the most inaccessible stage of the parasite life-circle). By entering to the different stages of the parasite, the zwitterionic nanoparticles became more interesting for the malaria treatment, as they had the potential to deliver drug to all the parasites of a patient and, therefore, they could eliminate a big number of pRBCs.

In **Figure 3.9B** it is showed a time-lapse experiment that we performed to know how the system evolved when nanoparticles were added to it. In there, we saw that in few minutes (10 minutes) the polymer started concentrating in the parasite, reaching a maximum signal at 40 minutes. Then, the signal started to decrease (possibly due to the degradation of the fluorophore by the parasite metabolism). With these results we confirmed the affinity that our polymers had for the parasite. We also could know that the internalization occurred in few minutes, fact that could be important in a *in vivo* experiment (if the particles can accumulate fast into the parasite, the circulation time would not be a critical factor).

Once proved the excellent performance of the zwitterionic nanoparticles when placed in contact with pRBCs, we characterized by flow cytometry the performance of the curcumin-loaded nanoparticles (**Figure 3.10**).

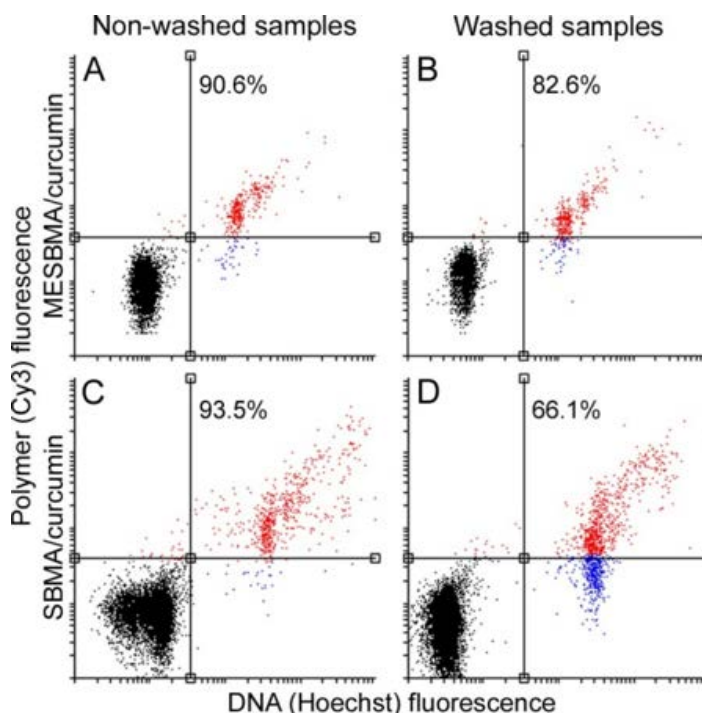


Figure 3.10 Cytometry assay of the curcumin-loaded zwitterionic particles in contact with pRBCs.

Curcumin-loaded nanoparticles presented an improved internalization into the pRBCs compared with the empty nanoparticles. This improvement could be explained by the stabilization of the nanoparticle for the curcumin load, that leads to a better performance. We also observed the same tendency than observed in the previous experiment. While the internalization of M1 nanoparticles was not heavily affected by the washing step, the S1 nanoparticles suffered an important reduction of the internalization after this step.

These results showed that the addition of curcumin into the nanoparticles did not only not reduce the internalization of the nanoparticles but slightly increase it. Thus, we were ready to characterize the antimalarial activity of these nanoparticles. This evaluation was performed by adding different amounts of curcumin-loaded nanoparticles (and curcumin as a control) and observing the decrease in the pRBC population of the samples (**Figure 3.11**).

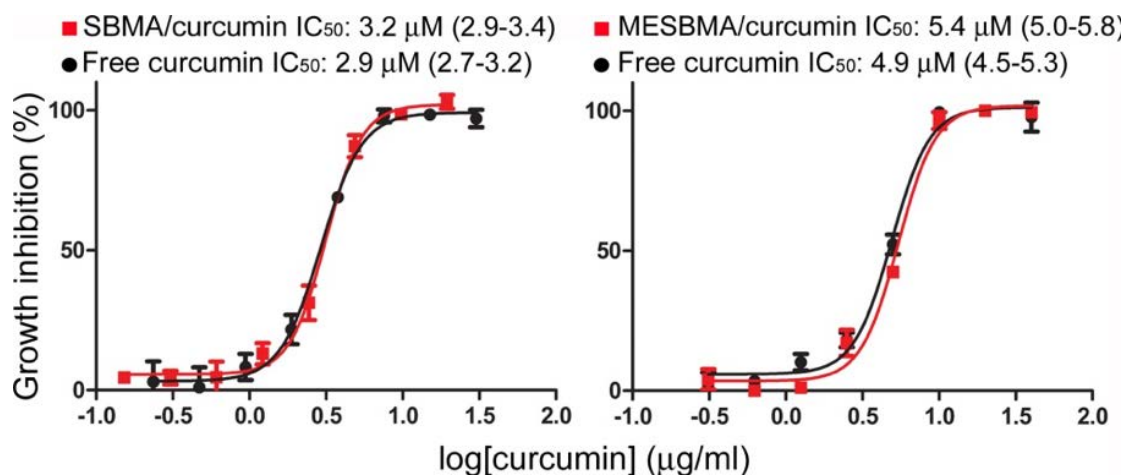


Figure 3.11 *P. falciparum* Growth Inhibition Assay (GIA) of curcumin-loaded zwitterionic polymers.

The results of the Growth Inhibition Assay (GIA) showed a similar behavior of the curcumin loaded nanoparticles versus curcumin free drug. Although there was not an improvement in the antimalarial effect of curcumin, neither was a decrease. The antimalarial activity of curcumin has been vastly proved, and to have this activity has to enter into the parasite. Thus, the limited current use of curcumin as antimalarial is not limited by its capacity to enter into the parasite but for its low solubility, low bioavailability and fast metabolism. These results showed that the curcumin-loaded nanoparticles did not lose the antimalarial activity while being inside a polymeric nanoparticle. And the loading of curcumin in the nanoparticles increase dramatically its solubility (as shown in **Table 3.3**) and should also increase its bioavailability while decreasing its metabolism.

For all these reasons, the results obtained from the GIA were also promising. Thus, the next steps for testing the antimalarial activity was to try their performance *in vivo*. But before, we had to determine the possible toxicity of the samples.

To determine the possible toxic effects of the zwitterionic nanoparticles *in vivo*, we performed two type of analysis. In first place, we injected the different concentrations of the polymers to mice and monitored its weight over days (**Figure 3.12**). The body weight loss is one of the most obvious symptoms of a toxic treatment. Thus, if this phenomenon was observed would have indicated that the nanoparticles were toxic.

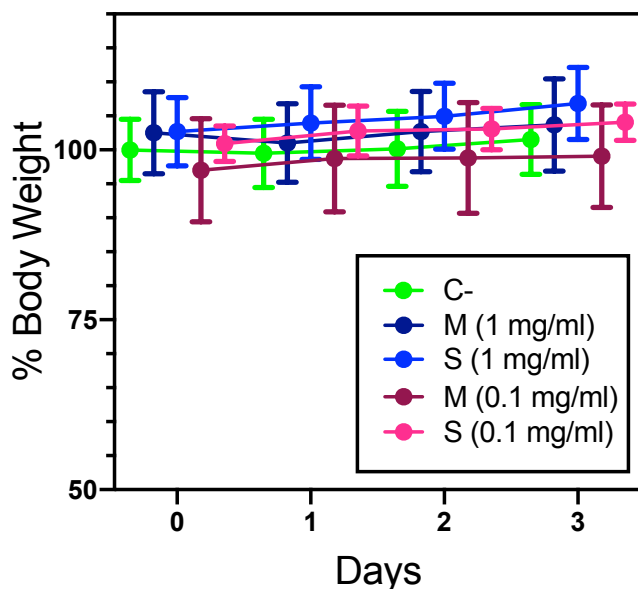


Figure 3.12 Body weight change of mice injected with different sulfobetaine nanoparticles. ($n=4$)

The results showed that even at high concentrations of polymer (1 mg/ml) there was not any decrease in the body weight of the mice. Therefore, we did not observe any toxicity in this experiment. We also checked the hemolysis produced for the polymers. In this case, fresh harvested mice blood was added to the polymer solutions to see if there was a lysis in the RBC. We did not observe any toxic effect of any nanoparticle at any concentration (**Figure 3.13**). Even the higher concentrations of M1 polymer (10mg/ml) and S1 polymer (1 mg/ml) did not produce any level of hemolysis. With these two results, we knew that the toxicity levels of our sulfobetaine nanoparticles were low and, therefore, that they could be used *in vivo* to test their antimalarial effect.

After the *in vitro* characterization, we knew that the different zwitterionic nanoparticles could encapsulate curcumin with high efficiency, drastically increasing its solubility in aqueous media. Moreover, we proved that these nanoparticles not only could enter to the infected RBC but that there was occurring some sort of passive targeting inside the parasites. And finally, we proved that the antimalarial efficacy of curcumin-loaded nanoparticles was not reduced in comparison to free curcumin.

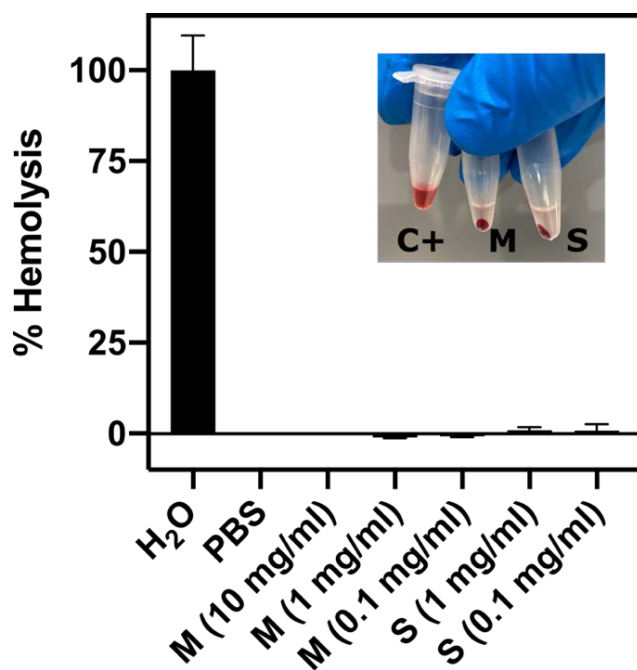


Figure 3.13 Hemolysis test for the different sulfobetaine polymers ($n=3$).

These exceptional results of the zwitterionic nanoparticles encouraged us to evaluate if the use of curcumin-loaded nanoparticles could improve enough the bioavailability of curcumin (when administrated orally) to become a viable strategy for an antimalarial treatment.

To do this evaluation, we performed an *in vivo* with *P. yoelii*-infected mice. Infected mice were orally administered free curcumin and curcumin-loaded M1 nanoparticles at a curcumin dose of 100 mg/Kg. We used only M1 nanoparticles due to their capability to encapsulate higher quantities of curcumin. It is also important to remark that in the case of curcumin, it is administrated as a suspension (due to its low solubility in water). The results of the *in vivo* (**Figure 3.14**) did not show an improvement of the survival of infected mice with the curcumin-loaded nanoparticles. The blood curcumin concentration achieved was not enough to kill the parasites in the mouse blood and improve its survival. These results could be explained by different factors: (i) a low permeation of the nanoparticles through the mucus and epithelial barrier, (ii) the loss of the curcumin payload and the rapid metabolization of it or (iii) the elimination of the nanoparticles of the body before they could reach the infected erythrocytes.

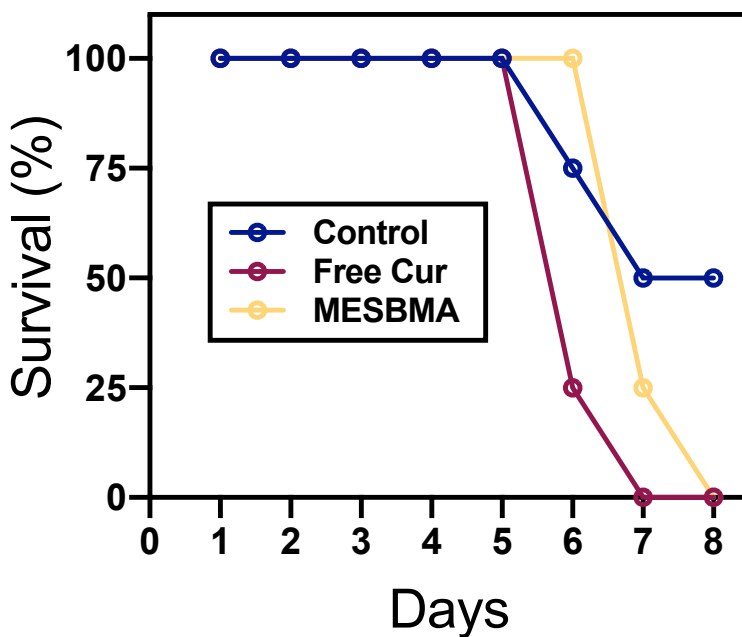


Figure 3.14 Survival of the different groups of *P. yoelii*-infected mice after the administration of curcumin ($n=4$).

The results of the *in vivo* did not show an improvement of the survival of infected mice with the curcumin-loaded nanoparticles. The blood curcumin concentration achieved was not enough to kill the parasites in the mouse blood and improve its survival. These results could be explained by different factors: (i) a low permeation of the nanoparticles through the mucus and epithelial barrier, (ii) the loss of the curcumin payload and the rapid metabolism of it or (iii) the elimination of the nanoparticles from the body before they could reach the infected erythrocytes.

Then, to obtain more information about the capability of the nanoparticles to be administered orally, we performed another *in vivo* in which, instead of evaluating the survival of infected mice, we used marked nanoparticles and tracked them inside the blood of infected mice using confocal microscopy (**Figure 3.15**)

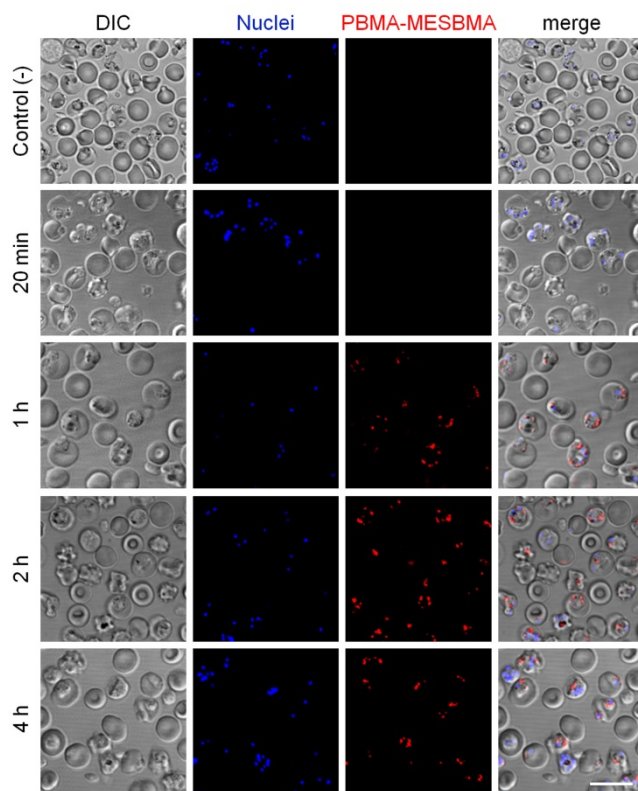


Figure 3.15 Confocal fluorescence microscopy analysis of the presence of orally administered Cy3-PBMA-MESBMA in pRBCs of a *P. yoelii*-infected mouse. After blood removal at the indicated times, *Plasmodium* nuclei were stained with Hoechst 33342 before proceeding to microscopic observation. The negative control was a blood sample taken just before polymer administration. DIC: differential interference contrast. Scale bar: 10 μm .

In the confocal images we observed the appearance of fluorescence corresponding to PBMA-PMESBMA 1 hour after the oral administration. Moreover, these nanoparticles accumulated in the infected erythrocytes, as we also observed in the *in vitro* experiments. These results indicated that the nanoparticles could cross the mucus and epithelial barrier and reach the bloodstream. Then, the results in **Figure 3.14** (in which there was not observed any increase in the survival of the infected mice when treated with curcumin-loaded nanoparticles) are not consequence of a bad permeation of the nanoparticles in the gastrointestinal barrier but due to the insufficient amount of curcumin that reaches the malaria parasites. This problem can be addressed in the future by changing the antimalarial

drug to another with more toxicity towards the parasite (curcumin IC_{50} for *Plasmodium* is 5-20 μ M [145]) or by increasing the drug dosage. Overall, zwitterionic nanoparticles have been proved to have potential to serve for a future oral therapy against malaria, as they can reach the bloodstream and accumulate in the parasites after being orally administrated.

3.2.6. Zwitterionic nanoparticles against cancer

The results of encapsulation of curcumin in zwitterionic nanoparticles motivated us to research for other hydrophobic molecules that had therapeutic interest for other diseases. In this search we came up with paclitaxel (PTX), one of the most used molecules to fight cancer.

Paclitaxel is a hydrophobic drug (with a solubility around 1 μ g/ml) approved by the FDA for the treatment of ovarian, breast and lung cancer as well as Kaposi's sarcoma, and it is also used off-label for gastroesophageal, endometrial, cervical, prostate, and head and neck cancers, in addition to sarcoma, lymphoma, and leukaemia. It was discovered in 1971 [146] during a program of the National Cancer Institute to find possible anticancer candidates and got the scientific community attention due to its impressive antitumoral activity [147,148]. And was after the success of its chemical synthesis in 1994 [149–151] and its FDA approval in 1993, that the paclitaxel use grew exponentially, creating a 1.5\$ billion dollar market in 2000.

Although its proven efficacy, it faces problems in the clinics due to its insolubility. Excipients have to be used in order to improve its solubility. Currently, the use of Cremophore EL to solubilize paclitaxel (having only 1% paclitaxel) is the standard for its clinical use (Taxol®), with some associated drawbacks such as side effects or bad pharmacokinetics [152,153].

Recently, a formulation that uses albumin to solubilize paclitaxel (Abraxane®) has improved the solubility of paclitaxel to reach a 10% drug content [154]. But there is still a considerable room for improvement. Achieving systems in which paclitaxel can be solubilized, protected from the immune system removal and directed to the cancer therapy has been a big goal for the nanomedicine field [155]. Thus, trying to encapsulate PTX in the zwitterionic nanoparticles could fit all the previously commented demands.

To encapsulate PTX, we used the same procedure that the one used with curcumin. Paclitaxel was dissolved in DMSO and added to the nanoparticle solution, that spontaneously encapsulate the hydrophobic drug due to the hydrophobic effect.

	Hydrophobic- ZW block	[PTX] (mg/ml)	Increase respect native PTX	Drug loading (w PTX / w Total)*
M1	25-35	1.0	1000-fold	9.1 %
M2	40-10	2.0	2000-fold	16.6 %
M3	40-20	2.0	2000-fold	16.6 %
C1	40-20	2.0	2000-fold	16.6 %
C2	70-20	3.0	3000-fold	23.1 %

Table 3.4 Encapsulation of PTX in the different zwitterionic nanoparticles (*[Polymer]=10 mg/ml).

The encapsulation of PTX into the zwitterionic nanoparticles was slightly smaller than in the case of curcumin (**Table 3.4**), possibly to the lower water solubility of paclitaxel. But the results were also promising. The encapsulation levels of paclitaxel were up to 23.1 % w/w, outperforming the currently used systems. These encapsulation results also proved the versatility of our nanoparticles, that were able to encapsulate different hydrophobic drugs with similar efficiencies.

Once proved the encapsulation of the PTX inside the zwitterionic nanoparticles, we tested if the encapsulated PTX had the same antitumoral activity than the free drug. Incucyte® Live-Cell Analysis platform was used to evaluate the antitumoral activity of PBMA-*b*-PMESBMA polymer. With this platform, we analysed the cell death using the cell morphology (the cells change from an elongated morphology to a round morphology when they die), with the advantage of being able of monitoring it in a live mode. We used HeLa cell line as a cancer cell model, and we monitored its growth when the different PTX formulation were added.

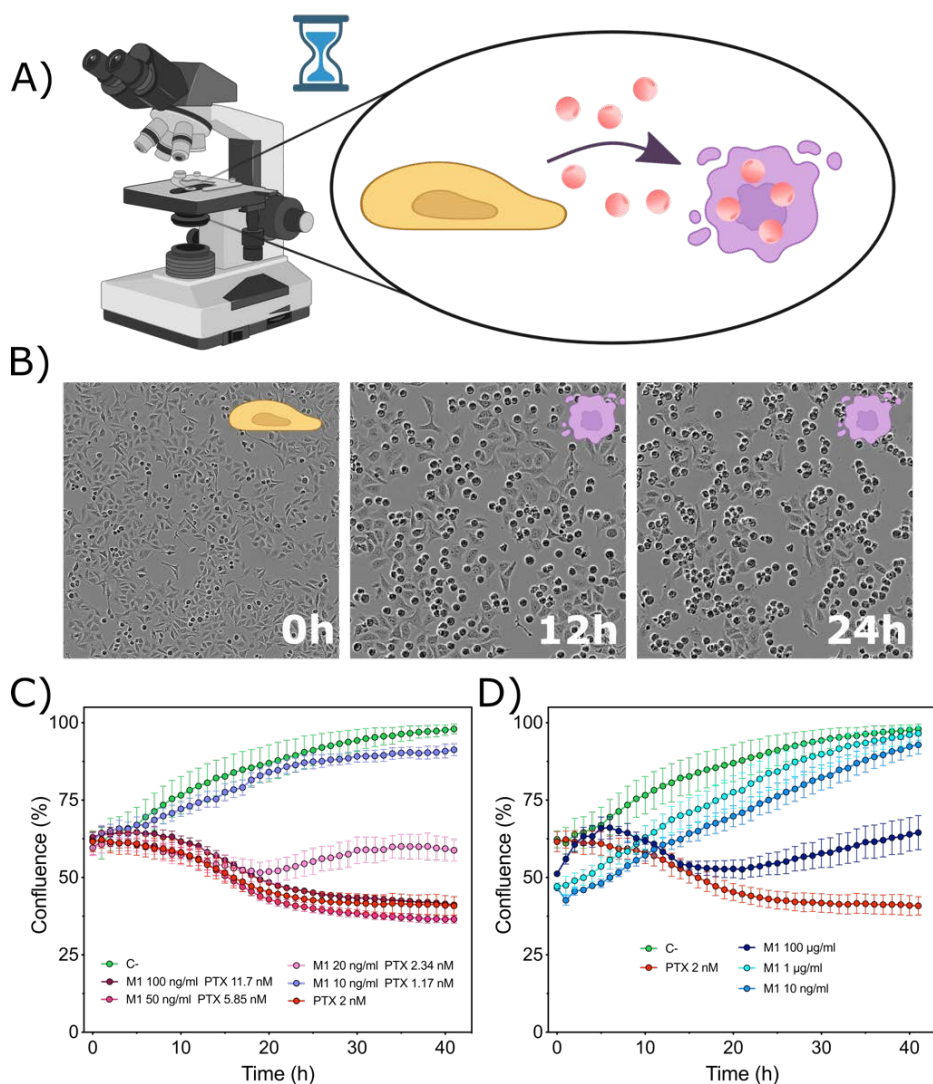


Figure 3.16 Characterization of the antitumoral activity of PTX-loaded zwitterionic nanoparticles using Incucyte® Live cell analysis. (A) Monitoring of the morphology change of the cells. (B) Example of images taken by Incucyte® at different times of the treatment with PTX. (C) Comparison of PTX-loaded nanoparticles with free PTX. (D) Toxicity of polymers.

When we compared the antitumoral effect of the PTX-loaded nanoparticles with the free PTX (**Figure 3.16C**), we saw a slight decrease in the activity. While PTX at a concentration of 2 mM completely flattened the growth curve, PTX-loaded NPs at a PTX concentration of 2.34 nM did not completely stop the cell growth. It was needed a PTX concentration of 5.85 nM to

achieve this complete inhibition. This small change in the antitumoral activity can be produced by many factors, such a progressive or non-complete release of the drug. But as it did not change dramatically the activity (less than 1 order of magnitude) we did not considered it as a major concern.

We also used the Incucyte® technology to know the effect of the polymer concentration in the growth of the cells (**Figure 3.16D**). We saw that polymer did not have any effect in the growth of cells up to 1 µg/ml (higher concentrations than the ones used in the previous experiment). Therefore, we determined that the antitumoral activity observed in the PTX-loaded NPs was completely produced by the drug and not by the polymer.

We also characterized the antitumoral effect of the PTX-loaded PBMA-*b*-PCBMA nanoparticles using the MTT 3-(4,5-dimethylthiazol-2-yl)-2,5-diphenyltetrazolium bromide (MTT) method. HeLa cells were incubated with the PTX-loaded nanoparticles and the mitochondrial activity was measured using MTT. These results were similar to the ones obtained using Incucyte® and PBMA-*b*-PMESBMA nanoparticles. The antitumoral activity of PTX was slightly lower when encapsulated, especially if the samples were not washed. In the case of the samples washed (the media is changed at 4h after the addition of the drug), the results were almost identical. This difference between washed and non-washed samples could be produced by difference in the kinetics of internalization and release of the drug in its free state or encapsulated in the zwitterionic nanoparticles.

Both experiments (Incucyte® and MTT) confirmed that PTX could be encapsulated into the zwitterionic nanoparticles without compromising its efficacy *in vitro*. These results, together with the experiments done with curcumin, indicated that the nanoparticles produced during this thesis were suitable for encapsulating hydrophobic molecules and dramatically increase its solubility while not affecting its efficacy. In the case of PTX and cancer, the high solubility of PTX achieved using these nanoparticles outperforms the currently used technologies. Moreover, the stealth effect of these nanoparticles should also improve its pharmacokinetics *in vivo*.

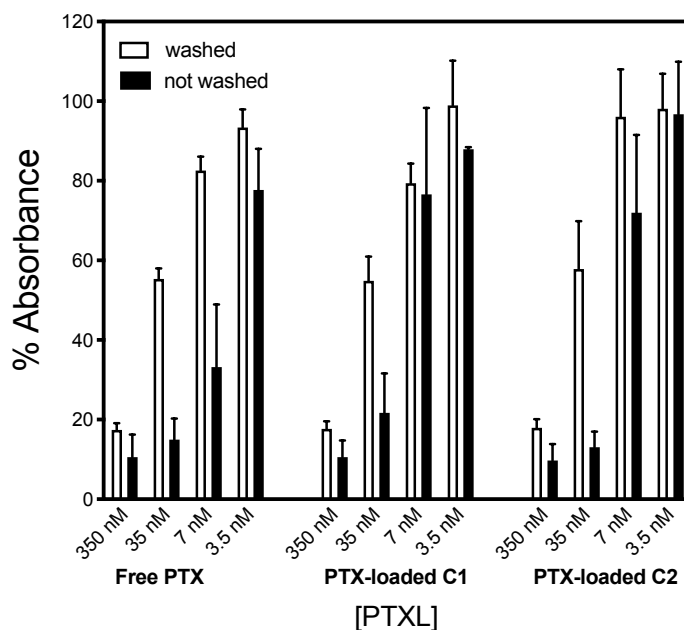


Figure 3.17 MTT of HeLa cells treated with PTX-loaded NPs

To further improve the efficacy of the nanoparticles developed, we decided to include an active targeting to the PBMA-*b*-CBMA nanoparticles. One of the advantages of CBMA zwitterionic polymer is its capacity to be modified in an easy way (it contains a carboxylic group that can be modified through an EDC/NHS coupling to produce an amide with any free amine) (Figure 3.18A). This modification does not need organic solvents or extreme conditions. Therefore, the modification can be done directly to the nanoparticle in mild conditions.

Introducing targeting moieties in the zwitterionic nanoparticles was interesting for various reasons. In first place, due to the antifouling properties of the zwitterionic surface, any targeting molecule introduced should have improved performance than if used in fouling surfaces. By avoiding the absorption of proteins, the zwitterionic surface allows the total exposure of the targeting moieties, increasing its detection by the targeted biomolecule [156].

Moreover, including active targeting to the zwitterionic nanoparticles would be interesting due to their long circulation lifetime. The antifouling properties of the zwitterionic surface prevents its rapid clearance, increasing the time that the nanoparticles are 'operative'.

Therefore, if the nanoparticles include a targeting, it will have more time to interact with the target, increasing its effectivity if compared with other nanoparticle types.

We modified the C1 nanoparticles with a targeting peptide widely used in our group (S12 peptide) that has been proved to increase the accumulation of nanoparticles in glioblastoma models.

We coupled the peptide in our nanoparticle by using a terminal cysteine, that was modified with N-(2-aminoethyl)maleimide to introduce a free amine that then was bonded to the carboxybetaine carboxylic acid through EDC/NHS coupling. Then we tested the internalization of the nanoparticles in the glioblastoma human cell model U87 (**Figure 3.18B**). We used Coumarin-6 ((C-6) a hydrophobic fluorophore) and Cy3 modified polymer to be able to track the drug-payload and the polymer.

We observed that the non-modified polymer could internalize inside the U87 cells, slightly increasing the drug concentration compared to the free drug. But, when the nanoparticles were modified, the internalization was even higher as can be observed in the Coumarin-6 and Cy3 lines. In the bright field images, we also observed that the cells treated with S12 modified NPs had a different morphology than the ones treated with C-6 and un-modified nanoparticles. This change of the morphology, consisting in the appearance of vesicles around the cells, could be induced by the S12 peptide and be the responsible of the higher internalization of the modified nanoparticles.

With these results we knew that the unmodified nanoparticles have the ability to internalize in this hard-to-penetrate cell line. And that if these nanoparticles are modified, their internalization ratio increases, proving the effectiveness of the modification of the polymer and the targeting efficiency of the S12 peptide. Therefore, we had proved that the zwitterionic PBMA-*b*-PCBMA nanoparticles are suitable for the inclusion of targeting moieties in an easy process. This property can be useful in multiple applications, increasing the potential of this type of nanoparticles for the use in drug delivery therapies.

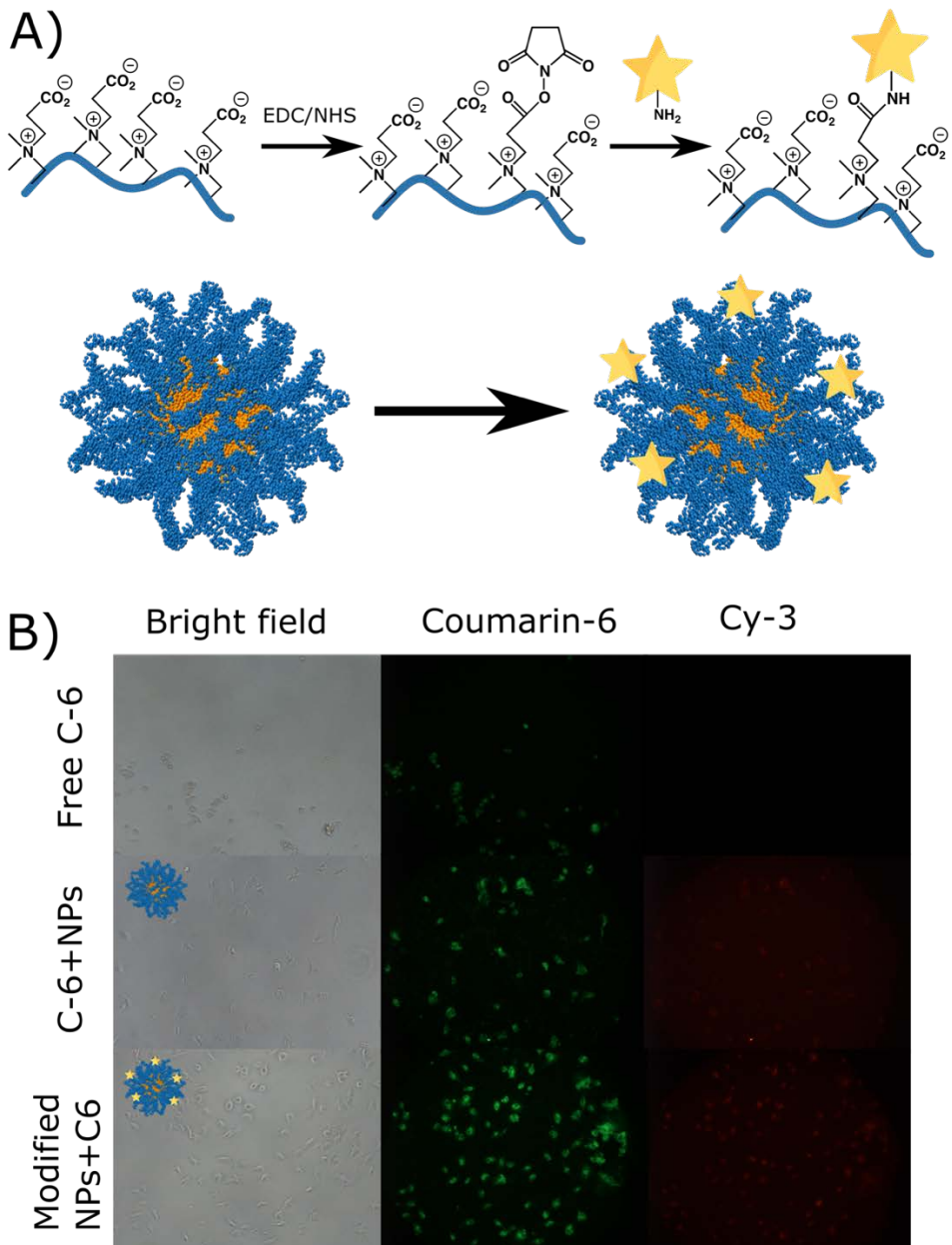


Figure 3.18 Targetting of C1 nanoparticles. (A) introduction of the targetting moiety by NHS/EDC coupling of the carboxylic group from the carboxybetaine. (B) Evaluation of the targetting capacity of the modified NPs using U87 cell line.

3.3. Concluding Remarks

In this chapter we have evaluated and optimized the zwitterionic polymers previously synthesized to convert them drug delivery systems with the potential overcome some of the current roadblocks of the field. First, we have proved the antifouling surface of the zwitterionic amphiphilic nanoparticles using BSA as a protein model. These antifouling properties suggest a “stealth” and anti-immunogenic behaviour in future *in vitro* and *in vivo* applications (as will be shown in the next chapter), one of the objectives set in this thesis. We have also proved the capability of the zwitterionic nanoparticles to internalize in epithelial gastrointestinal cell model and show levels of diffusion in mucus comparable to the current “state of the art” oral drug delivery systems, another of the objectives of this chapter.

Finally, to prove their potential for the use in different treatments, we have encapsulated curcumin and paclitaxel with high efficiency, outperforming the current formulations for the use of these drugs. The curcumin-loaded nanoparticles have been tested in malaria *in vitro* models, showing a passive targeting to infected erythrocytes that results in antimalarial activity. The *in vivo* experiments have shown polymers in the mice blood after oral administration, proving the capacity of the polymers to pass through the gastrointestinal barrier. Although there has not been an increase in the survival of infected mice, these results suggest that, with more optimization, it is possible to obtain an efficient oral drug delivery system for malaria treatment. Paclitaxel-loaded nanoparticles have shown anticancer activity in cancer cell model, and the successful modification of the nanoparticle surface to introduce targeting moieties have been also proved.

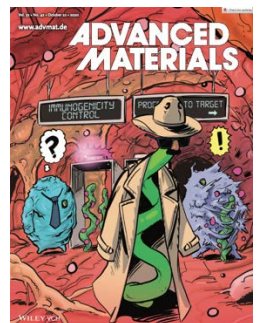
On balance, after the work performed on this chapter (and Chapter I), we have accomplished the objective to create different zwitterionic drug delivery systems based in zwitterionic amphiphilic block copolymers. The superhydrophilic character of zwitterionic polymers allow the encapsulation of hydrophobic drugs with high encapsulation efficiency, while providing the necessary antifouling and “stealth” properties that are demanded to reach the clinics. For all these reasons, these drug delivery systems contain potential to be used in multiple fields in which the encapsulation of hydrophobic drugs are needed.

Chapter 4: Zwitterionic Stealth Microrobots

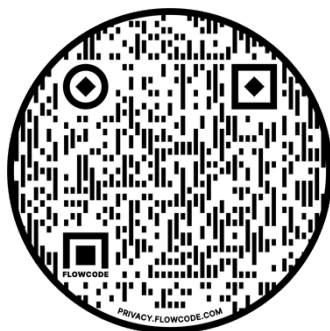
Originally published as:

P. Cabanach*, A. Pena-Francesch, D. Sheehan, U. Bozuyuk, O. Yasa, S. Borros, M. Sitti
“Zwitterionic 3D-Printed Non-Immunogenic Stealth Microrobots”
Advanced Materials (2021), 32, 2003013.

Selected as front
cover page:



This Chapter contains Supplementary Videos that are found in the following QR code link:



Chapter 4: Zwitterionic Stealth Microrobots

4.1. Introduction

After developing zwitterionic-based drug delivery systems and exploring their potential in different applications, we had the opportunity to use zwitterionic materials in another field in which the antifouling properties of these materials are of special interest: the microrobotics field.

Robotic systems were primarily used in industry to automate routine and dangerous manufacturing tasks. But with the advances in motors, control theory, materials and medical imaging, as well as the patient/surgeon acceptance, they started to be used in medical applications [157–159]. This transition required the miniaturization of parts and the inclusion of smart materials for complex and precise operations in the human body. These medical robotic systems have decreased the degree of invasiveness of some surgeries, reducing the appearance of complications during the surgery and accelerating the recovery of the patient. Some examples are the *Da Vinci Surgical System* [160] or robotic capsules for gastrointestinal endoscopies [161], among others. However, although they offer solutions to perform some minimally invasive surgeries, the size of current medical robots is a problem for a wide spectrum of applications, in which the robot should pass through narrow conducts into hard-to-reach zones of the body. For this reason, the use of robots in the micrometer size that could reach this zones would be a breakthrough solution for non-invasive procedures of surgery, diagnosis or drug delivery [159,162–164].

The advances in nanotechnology and materials science, together with the demands of the biomedical community, have pushed scientists to research in this direction. And the idea of having a microrobot that could enter inside our body and perform medical operations is no longer a sci-fi movie plot, but a real goal for the scientific community.

Many challenges appear when designing an untethered (wireless) microscale robot for medical applications (**Figure 4.1A**). Locomotion and control represent the first challenge. In the miniaturization of a robot to the microscale, traditional power supplies (like batteries) cannot be incorporated, neither control systems, due to the impossibility to fabricate these

components in such a small size. Therefore, the microrobotics community put many efforts in designing locomotion and control systems in the microscale. A myriad of microscale mobile robots has been developed in recent years, with different actuation strategies, including magnetic [165,166], electric [167], acoustic [168,169], photo [170,171], thermal [172,173], biological [174], and chemical [173,175–177] actuation (**Figure 4.1B**).

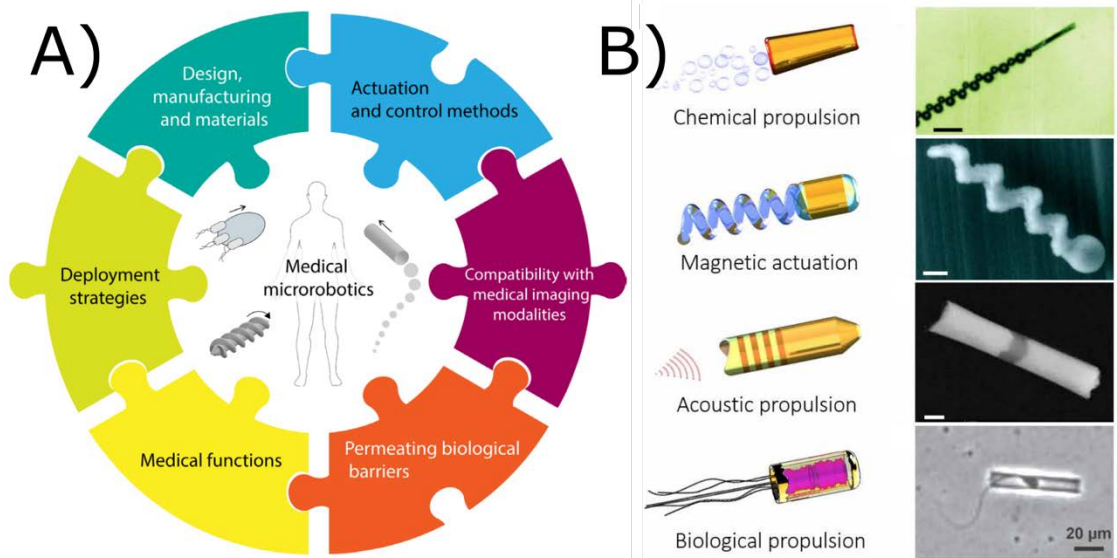


Figure 4.1 (A) Challenges for Medical microrobots [178] and (B) some strategies of locomotion and control [162].

Functionality has been also another aspect in which there has been an evolution in the recent years. Macroscale sized robots normally have multiple components in which each component performs a function. But when designing a microscale robot, the incorporation of multiple components becomes a challenge due to the reduced space. Then, functionality has to be included in the robot body itself, together with the control and the locomotion. Drug loading (inserting a drug payload inside the robot), remote sensing (robot functionalization with bioreceptors) and minimally invasive surgery (drilling and gripping functions) have been some of the medical functionalities successfully incorporated in microscale robots [162,178].

Although the advances in locomotion, control and functionality of the microrobots, there is still a long way to go until such technologies reach clinical applications. Improved locomotion

in biological fluids, penetration of biological barriers, biocompatibility or biodegradation are some of the challenges that the field is facing nowadays. Among them, the interaction of the robot with the immune system remains a big concern poorly addressed. As any other biomaterial, microrobots will have to face the immune system when introduced in the body and, if detected as harmful, will be neutralized. Therefore, this is a crucial problem to be solved before the application of these promising technologies in the clinics.

As has been commented in the previous chapters, when the microrobot (as any other material) is placed inside the body, it will be rapidly coated by a surrounding layer of proteins via nonspecific adsorption [3,8,179,180]. This protein absorption will trigger the response of macrophages, that are on the lookout for pathogens and recognize these nonspecifically protein-coated materials as foreign threats [3]. Then, as the microrobots are in the microscale range, they will phagocytose them and eliminate them from the system (disabling their functions and eventually digesting them) [9,181,182]. Therefore, the immune system is the first barrier to entry and a major roadblock to developing functional micro/nanorobots that can operate in the body.

Compared to nanoparticles, microrobots have a bigger size (10-200 μm) and a diversity of shapes. But although it has been showed that the size and shape of microparticles [183–185] and microrobots [186] have a role in the kinetics of its internalization by the macrophages, this influence comes from the difficulty of macrophages to engulf the particle and not from an non-detection of the particle. If, for example, we have a long and narrow particle, the macrophage will have more difficulty to phagocyte it than a round shape; but in both cases the macrophage will detect the material and try to phagocyte it. This detection is a problem for a future use of the robots *in vivo*. Even if these robots are not phagocytosed, the macrophages will attach to it, changing its form and making impossible its locomotion and control.

Therefore, microrobots that can pass under the radar of macrophages and avoid any type of recognition are needed to reach the clinic. And, to achieve this objective, microrobot materials are of crucial importance. There has been small research in the use of antifouling materials for microrobots. The production of microrobots is challenging, as it requires precise microfabrication normally by 3D printing. And only few materials have been optimized for these procedures. PEG, the current “Gold Standard” in antifouling materials, requires the

mobility of chains in order to be antifouling. And this chain mobility can only be obtained by surface coating. This process is not suitable for most of the current robots, as they are made of non-functionalizable materials. Moreover, the recent concerns about PEG immunogenicity [25,27] could also affect the efficacy of the robots *in vivo*.

Differently to PEG, that has an antifouling behavior due to its chain mobility, zwitterionic materials are intrinsically antifouling due to their superhydrophilicity. They also have shown better immune-evasive behavior, as well as more chemical versatility. All these properties make zwitterionic materials good candidates to become materials for the fabrication of microrobots. But although all these advantages, they are still not used in the microrobotics field.

Trying to develop the first zwitterionic microrobots, in this chapter we collaborated with prof. Metin Sitti, director of the Max Planck Institute for Intelligent Systems of Stuttgart, and prof. Abdon Pena-Francesch (former postdoc in the same group and now professor in University of Michigan) to design a zwitterionic photoresist suitable for the fabrication of zwitterionic microrobots. By using this strategy, the zwitterionic material would be the robot material itself, resulting in a full zwitterionic microrobot that would be completely antifouling. Moreover, the development of a zwitterionic photoresist suitable for microfabrication would serve as a toolbox of non-immunogenic materials for medical microrobot and other device technologies for bioengineering and biomedical applications.

4.2. Results and Discussion

4.2.1. Development of a zwitterionic photoresist

As has been commented in previous lines, the strategy that we took to fabricate zwitterionic microrobots was to develop a zwitterionic photoresist suitable for microfabrication. We decided that this photoresist would be composed of acrylic monomers and crosslinkers.

In the previous chapters, we synthesized zwitterionic nanoparticles via post-polymerization modification (**Figure 2.3b**). But to produce this photoresist we decided to use directly the zwitterionic acrylates and diacrylates. This decision was made in order to directly obtain a zwitterionic material after printing, avoiding further steps and achieving a 100% presence of zwitterionic groups in the robot. Therefore, we had to produce the zwitterionic monomers and crosslinkers. We used sulfobetaine (SB) and carboxybetaine (CB) zwitterions to produce the photoresists. This decision was taken because they are two of the most used zwitterionic moieties (with low non-specific protein adsorption from blood serum and plasma [187]), as well as for their described and accessible monomer and crosslinker synthesis.

We synthesized both SB and CB monomers using DMAEMA as precursor. In the case of SB monomer, the synthesis is described elsewhere using 1,3-propanesultone as precursor. For CB, we used acrylic acid as precursor, as described in the work of Jiang et al. [188] (**Figure 4.2a**) Both monomers were obtained without important impurities, as shown in **Figure 4.2c**. For the synthesis of CBX and SBX, we adapted the protocols of Lácik et al. [189] and Jiang et al. [190] respectively (**Figure 4.2b**). We used diethanolamine as the starting material, followed by an esterification using methacrylic acid under acid catalysis. Then, to produce the SBX, we modified the difunctional tertiary amine with propanesultone, generating the sulfobetaine. And in the case of CBX, we quaternized the amine using a protected bromoacetic acid followed by an acid deprotection to obtain the final difunctional carboxybetaine. We followed the different steps using H^1 -NMR and we confirmed the structure and purity of the zwitterionic crosslinkers (**Figure 4.2d**).

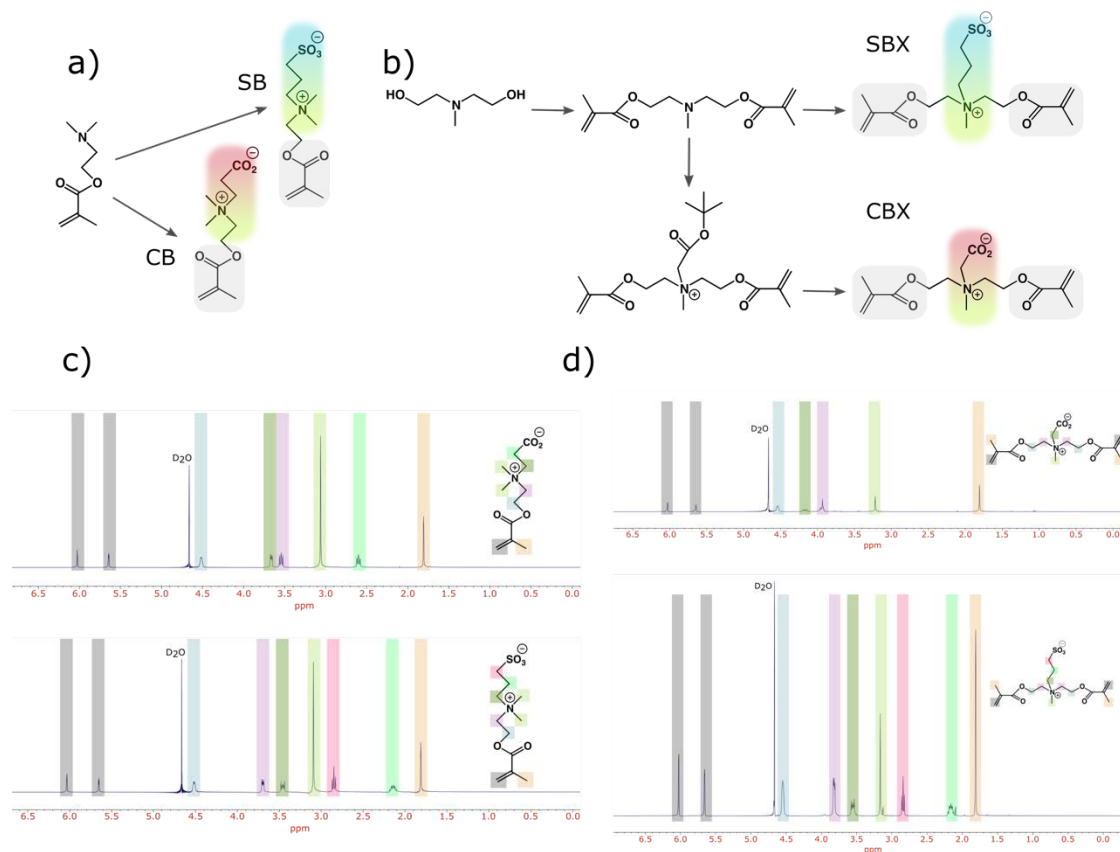


Figure 4.2 Synthesis of (A) Zwitterionic monomers and (B) crosslinkers. (C) $^1\text{H-NMR}$ of the CB and SB monomers. (D) $^1\text{H-NMR}$ of CBX and SBX crosslinkers.

Having both zwitterionic monomers (CB & SB) and zwitterionic crosslinkers (CBX & SBX) allowed us to formulate hydrogel photoresists with varying crosslinking ratios without losing the zwitterionic properties (all-zwitterionic hydrogels), which gave us a broad design space for tuning the mechanical properties and photopolymerization kinetics of our materials. Then, we performed a photopolymerization characterization using rheology in order to determine the influence of the photoresist composition in its photopolymerization kinetics (Figure 4.3a).

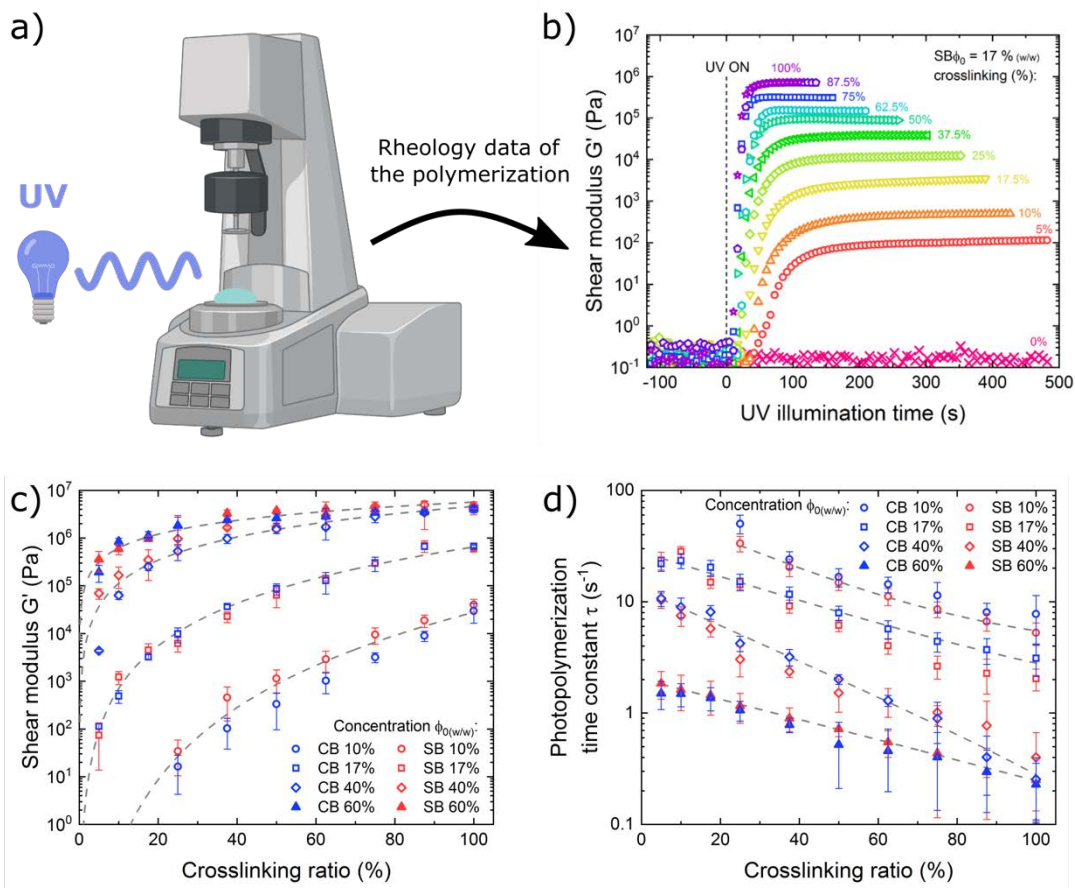


Figure 4.3 Photorheological characterization of the polymerization of the different photoresists. (A) The different photoresists were placed in a rheometer equipped with a UV light. (B) Example of a photorheological graph. (C) Shear modulus depending on the crosslinking ratio of SB and CB photoresists. (D) Polymerization kinetics depending on the crosslinking ratio of SB and CB photoresists.

We analyzed CB-based and SB-based photoresists with crosslinking ratios from 5% to 100% (CBX and SBX, respectively) by photorheological characterization (**Figure 4.3b**). Due to the superhydrophilic nature of the zwitterionic monomers and crosslinkers and their high solubility in water, we achieved high concentrations (up to 70% w/w) in our water-based zwitterionic photoresists that are not possible in other water-based photoresists due to their low solubility limits. We performed the analysis using pure SB and CB photoresists (for further works, they could be formulated using mixtures of SB and CB) and using Igracure 2959, a widely used water-soluble photoinitiator, as photoinitiator.

By adjusting the crosslinking ratio and concentration, we could tailor the elastic moduli of CB- and SB-based hydrogels from soft (0.1 kPa) to hard (10 MPa) (**Figure 4.3c**), matching the moduli of a wide range of biological tissues. We also observed faster polymerization with increasing crosslinking ratio and overall concentration, which is expected due to a higher concentration of methacrylate reactive groups (**Figure 4.3d**). We note that these data are *in situ* shear measurements during photopolymerization, and might slightly differ from other reports on crosslinked hydrogel moduli measured *a posteriori* by other methods [190].

4.2.2. 2-Photon Polymerization 3D microprinting of zwitterionic photoresists

With the photorheological characterization, we proved that the photoresists developed were suitable for 3D polymerization and versatile in terms of physical properties. But to be able to produce microrobots, we had to optimize the zwitterionic photoresist for 3D microprinting.

We decided to use the 2-photon polymerization (2PP) technique as the 3D microprinting technique to produce the microrobots. This is an emerging nanofabrication technique that enables 3D complex polymeric structures with down to 100 nm resolution and has found broad applications in fabricating photonic crystals, metamaterials, cell scaffolds, microfluidic devices, and microrobots [165,191,192]. It is based in the 2 Photon Absorption (2PA), phenomena predicted in theory by Goeppert–Mayer in the 1930s and demonstrated in experiment by Kaiser in 1961 after the invention of the laser. The phenomenon consists in the absorption of two photons by a molecule to reach its excited state. It scales with the square of incident light intensity and the maximum absorption occurs at the focal point of light (more information about this phenomenon can be found in [193–196]).

2-photon polymerization introduces initiators that present 2PA in the photoresist. Then, this photoresist is illuminated with focused femtosecond laser pulses with a wavelength two times the excitation wavelength of the initiator. Through the 2PA phenomenon, in the focal point of the laser pulses (and only in the focal point) the initiator will absorb 2 photons from the laser and generate the radical that will start the polymerization. Therefore, the polymerization only occurs on the confined nanoscale voxel illuminated by the focal point of the laser pulses (**Figure 4.4**). Then, by moving the focal point of the laser pulses following

complex computer-aided design (CAD) files, photopolymerized nanoscale complex 3D structures can be produced [197].

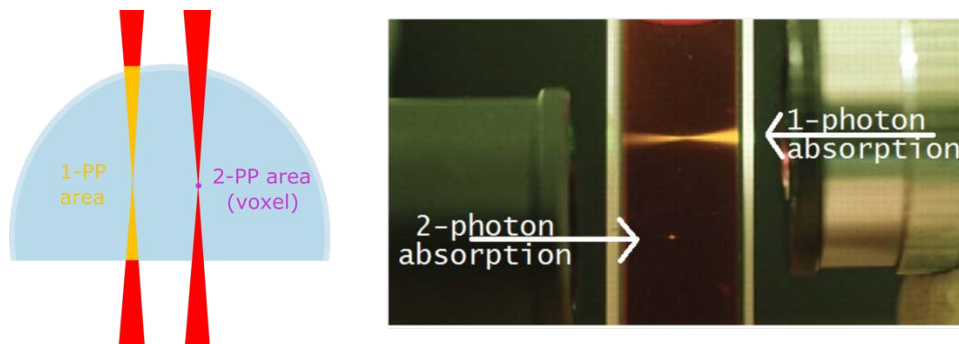


Figure 4.4 *Difference in the printing area between 1-photon polymerization and 2-photon polymerization (absorption image was obtained from www.microlight.fr).*

Current commercially available photoresists for 2PP lack chemical versatility, and significant research efforts are being made in the development of new functional photoresists [191,192]. Our zwitterionic photoresists presented multiple advantages over the state-of-the-art natural and synthetic materials for 2PP: (i) CB, SB, SBX, and CBX are highly soluble in water, and therefore, they do not require organic solvents and can be polymerized with water-soluble photoinitiators, which are less toxic [192]. Furthermore, water-only-compatible materials, such as biomolecules or cells, can be integrated into a single printing step. (ii) Natural polymers, including gelatin, chitosan, hyaluronic acid, alginate, *etc.*, have limited methacrylation of functional groups (adjusted by reaction time), which restricts the crosslinking density available to such hydrogels. On the other hand, zwitterionic photoresists have a high density of methacrylate groups, which offers tunable control over the hydrogel chemistry and network density, tunable mechanical properties (from soft to hard), and enhanced printing resolution (hydrogels are more stable and preserve their shape, allowing for smaller structural features). (iii) Synthetic hydrogels typically use PEG-based or bisacrylamide-based crosslinkers that have limited solubility in water, and therefore restrict the crosslinking density and the hydrogel mechanical properties. In contrast, CBX and SBX crosslinkers have high solubility in water, which allows for high crosslinking ratios and fabrication of stiffer hydrogels without compromising the zwitterionic properties. (iv) CB and CBX are directly functionalizable through their carboxylic groups which, together with their

(v) non-fouling properties, make them a superior alternative to natural and synthetic materials for bioengineering applications, such as drug functionalization and specific targeting.

We adapted the previously formulated zwitterionic photoresists (**Figure 4.3**) for 2PP by changing the Igracure 2959 initiator for Lithium phenyl-2,4,6-trimethylbenzoylphosphinate (LAP), a 2PP suitable initiator. Both photoresists formulated (SB and CB) could be printed (at certain concentration and crosslink percentage) with 2PP, becoming the first reported zwitterionic materials printed using this method. Moreover, the resolution of the printed structures had a high degree of accuracy (**Figure 4.5a**, **Movie S1**). This proves that zwitterionic materials can be printed through 2PP opens new doors in the application of zwitterionic materials in fields such as microrobotics or microfluidics. Producing microscale 3D structures with their antifouling and superhydrophilic properties may be useful in a wide range of applications.

In order to further characterize the printing properties of the photoresists, we analyzed a range of concentrations and crosslinking ratios of the photoresist, generating a matrix indicating at which concentrations and crosslink percentages there was obtained a high-resolution printing (**Figure 4.5b**). We achieved high printing resolution and full structural reproducibility from CAD files at high concentrations and crosslinking ratios due to an increase concentration of reactive species (methacrylate groups) and faster polymerization kinetics, while less concentrated and crosslinked photoresists exhibited lower resolution and structural stability or even the absence of printing.

As has been commented in previous lines, this was the first reported 2PP printing of zwitterionic materials. Therefore, we focused on proving the printability of the zwitterionic photoresists and the generation of zwitterionic microrobots. However, it could be further modified by incorporating high molecular weight zwitterionic prepolymers, thickeners, fillers, other photoinitiators, and different laser parameters (power, scan speed, *etc.*) in order to reduce the concentration of the photoresists.

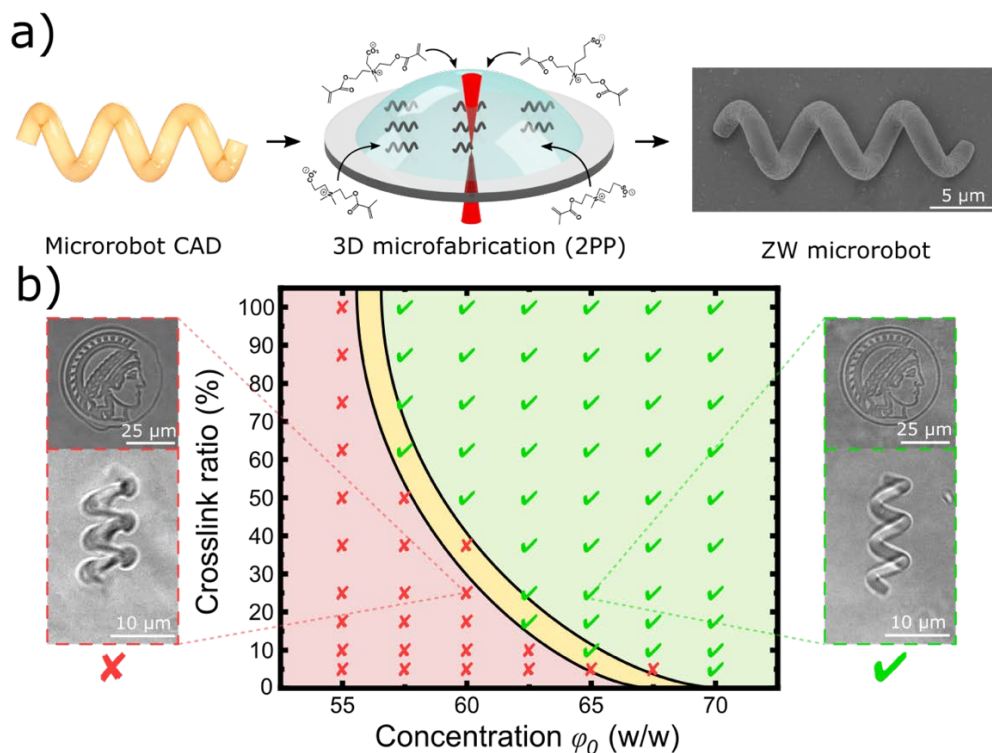


Figure 4.5 2PP printing of the Zwitterionic photoresists. (a) Zwitterionic photoresists (containing zwitterionic monomers, zwitterionic crosslinkers, and photoinitiators) were printed into 3D complex microstructures (including helical microrobots) via two-photon polymerization (2PP). (b) Printing diagram for optimized resolution as a function of concentration and crosslink ratio. Insets show printed microstructures with sub-optimal resolution (left, red) and optimal resolution for full structural reproducibility (right, green).

Different structures were printed using the zwitterionic photoresists (see Max Planck Institute Minerva symbol and helical microrobot in **Figure 4.5**). Of all of them, we focused on the printing resolution of helical microrobots as it was the microrobot chosen to be used in all further experiments. Helical microrobot design inspired in the flagella of *E.coli* was developed by Nelson's group in 2007 and it is one of the most used designs for microrobots and is widely characterized [198,199]. This deep understanding of how the helical microrobot works made us chose it, as we were not focused on improving any microrobot type, but in produce a new biomaterial with which anti-immunogenic robots could be printed. The zwitterionic photoresists developed presented a high degree of resolution and high structural reproducibility (**Figure 4.5a**). Thus, we had proved that they were suitable for 2-photon

polymerization, becoming the first reported zwitterionic material printed using this advanced manufacturing technique. We then moved to the next step of the characterization of the zwitterionic printed materials, consisting in the analysis of their interaction with proteins and cells.

4.2.3. Bio-adhesion characterization of the zwitterionic microrobots

To characterize the biological properties of the zwitterionic microrobots produced, we first had to select at which crosslink percentage we wanted to work. As shown in **Figure 4.3**, there was a big difference between the mechanical properties of different crosslink concentrations. And these mechanical properties could also have a role in the biological properties of the material. We chose to work with a crosslink concentration of 30% and 100% (referred as S30/C30 and S100/C100). We chose the 100% concentration because is the stiffer one, while 30% was an intermediate crosslink concentration. We also selected Poly(ethylene glycol) diacrylate (PEGDA) as the control material to compare our zwitterionic ones.

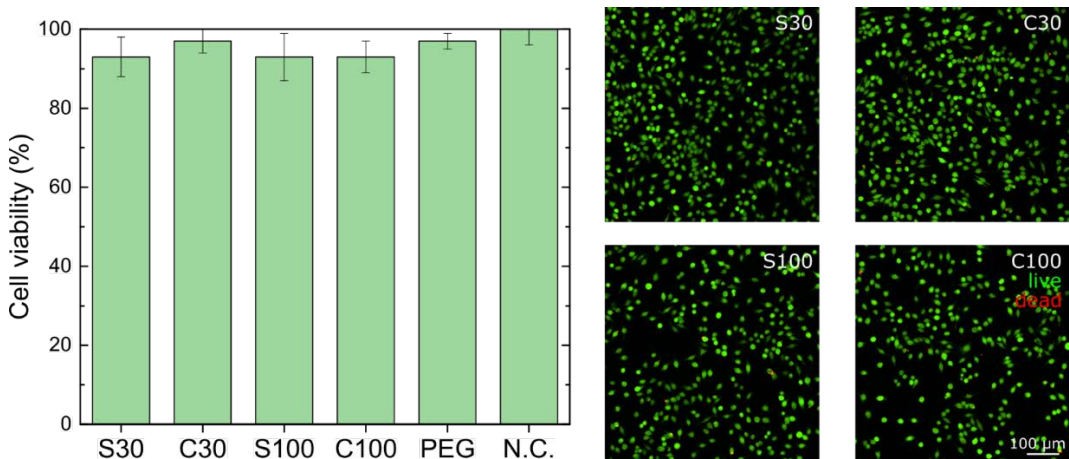


Figure 4.6 Viability assay performed with the different zwitterionic photoresists ($n=3$). (A) WST-8 assay (B) Live/Dead staining and J774A.1 murine macrophages.

We first wanted to characterize the toxicity of the printed structures. Depending on the photoresist composition and the printing parameters, there could be a leakage of precursors that led to cell death. We printed 5 mm disks with the different zwitterionic photoresists, washed them and incubated with cells, performing a live/dead staining and a WST-8 viability

assay to determine the possible toxicity (**Figure 4.6**). In all the samples there was not observed any anomalous behavior or cell death, confirming that the printed zwitterionic structures were biocompatible and non-toxic. Therefore, they were suitable to be used with cellular cultures.

Then, we performed a cell-adhesion analysis by culturing macrophages in the top of the different hydrogel disks (**Figure 4.7**). Cells did not attach in the S30, S100 and C30 samples, while they did in the C100 samples and the PEGDA control. In here, we saw the first difference between the PEGDA control and the zwitterionic photoresists. The zwitterionic hydrogels have an antifouling surface, that prevents the adhesion of the macrophages. But these attach in the PEGDA sample, as their surface is not antifouling enough. The only zwitterionic sample that showed some cell adhesion was C100. There was not a rational explanation about this phenomenon, as cells did not attach to S100 and C30 samples, with the same degree of crosslink and the same zwitterion type respectively. Therefore, some phenomenon was happening at high degrees of crosslink of carboxybetaine hydrogels.

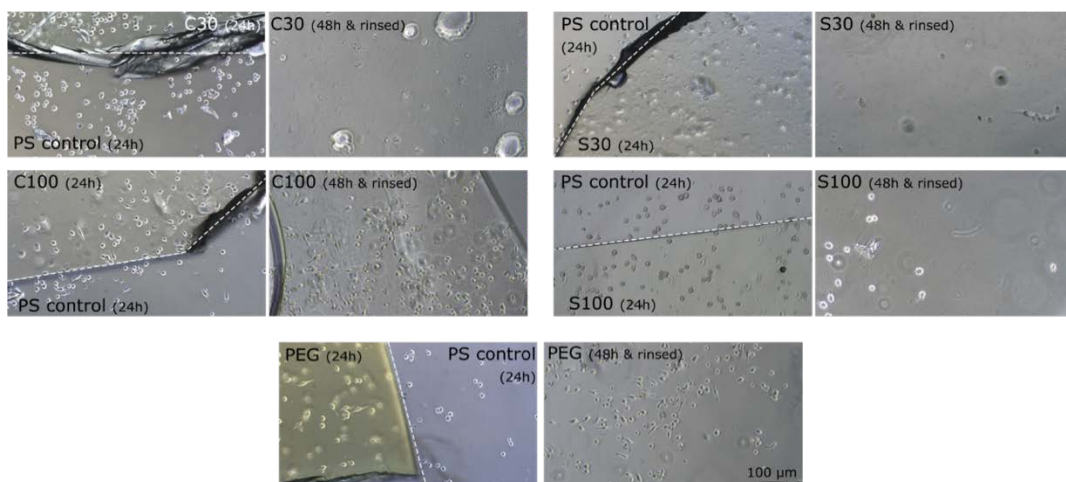


Figure 4.7 J774A.1 murine macrophage adhesion to zwitterionic photoresists.

We further characterized the antifouling behavior of the zwitterionic printed structures using BSA as a model. As has been commented in the previous chapter, BSA is the most abundant protein in the blood [200] and one of the main components of the protein corona. We printed microrobots using 2PP with the different zwitterionic photoresists and also with

PEGDA and IP-S (a commercial photoresist from the 2PP equipment supplier recommended for biological use). Then, we incubated the different microrobots with a fluorescent-labeled BSA solution, washed them and observed the fluorescence of the sample using fluorescence microscopy (**Figure 4.8**).

We observed that PEGDA and IP-S had a high fluorescence intensity, while there was no visible fluorescence in the zwitterionic microrobots. These results were in the line with the results of cell adhesion showed in **Figure 4.7**. Again, the antifouling behavior of the zwitterionic materials was proved, as they prevented proteins to attach in their surface. On the other hand, the two controls presented fluorescence corresponding to absorbed protein. C100 samples did not present protein absorption, in contrast with the cell adhesion experiments.

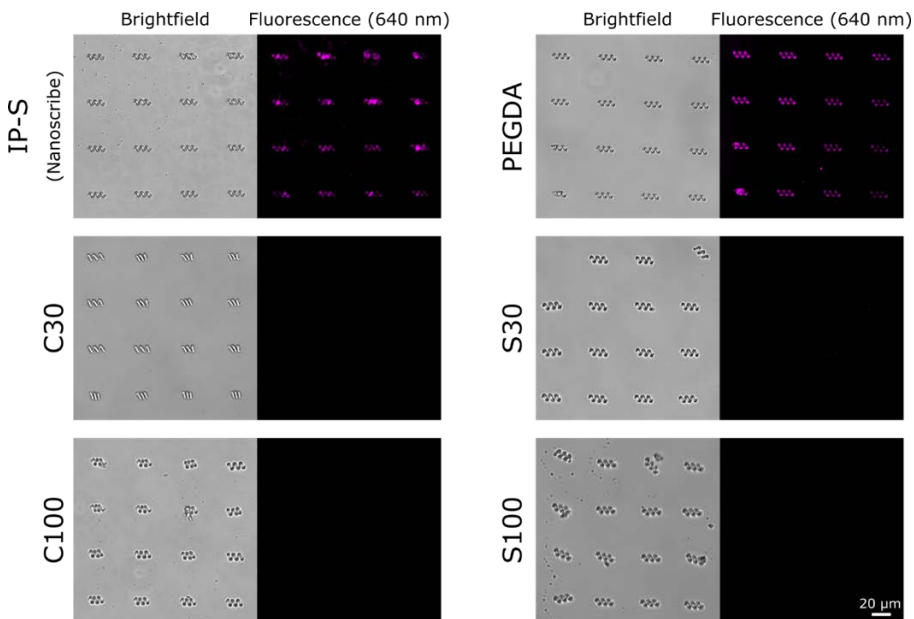


Figure 4.8 Fluorescence microscope images of the different microrobots incubated with Cy5-BSA.

These two results proved that the zwitterionic photoresists developed in this chapter outperformed the current commercial photoresist for biological applications, as well as the “gold standard” in terms of antifouling. Thus, they confirmed the advantages of working with our zwitterionic photoresists over the currently used ones.

4.2.4. Zwitterionic non-immunogenic microrobots

To characterize the interaction between the zwitterionic microrobots and the immune system, we started analyzing the response of macrophages to the zwitterionic materials. They are the main component of the mononuclear phagocyte system (MPS), which belongs to the innate immune system (non-specific), and is responsible for the recognition and clearance of the foreign materials from the body [21,180,201,202]. Macrophages are present in almost all body tissues and especially in lungs, liver and spleen. They are activated when they detect a material as a foreign body, mainly through the identification of adsorbed proteins on the material surface [9,203] and proceed to eliminate the foreign material by phagocytosis. They also perform two additional functions when they recognize and phagocytose a foreign body: the secretion of cytokines (regulators of the immune system) and the presentation of antigens (small peptides of the phagocytosed material that will be used by the adaptive immune system to generate an immune memory). For these reasons, there have been many efforts to characterize and modulate the interaction between macrophages and biomaterials [8,180,186,203–209], and also why we firstly focused in them.

We cultured macrophages with the zwitterionic and control microrobots, and monitored their interaction using microscopy (**Figure 4.9, Movie S2**). PEG-based microrobots (current anti-biofouling benchmark) were immediately recognized and phagocytosed as soon as the macrophages came in contact with them. In contrast, zwitterionic stealth microrobots were not phagocytosed after exhaustive inspection (cells probe, manipulate, and move the robots) and they were released back (**Figure 4.9 and Figure 4.9b**). To have a more quantitative result, we printed different matrix of microrobots and monitored all the microrobot-cell interaction, determining if this interaction led to a capture and phagocytosis or a release (**Figure 4.9c**). PEG microrobots showed ~100% phagocytosis rate, meaning that every time that a cell detected a robot, it ended phagocytizing it. In contrast, of all the interactions between the macrophages and the S30, S100 and C30 microrobots only < 2% ended in phagocytosis, while the big majority of the microrobots were released (**Figure 4.9d**). C100 zwitterionic microrobots showed some phagocytosis rate ~20%. A different behavior of C100 samples was also observed in the cell adhesion experiments, results that could also be related with these ones. Although this fact, the C100 microrobots still outperformed the current state-of-the-art antifouling and biocompatible material (PEG).

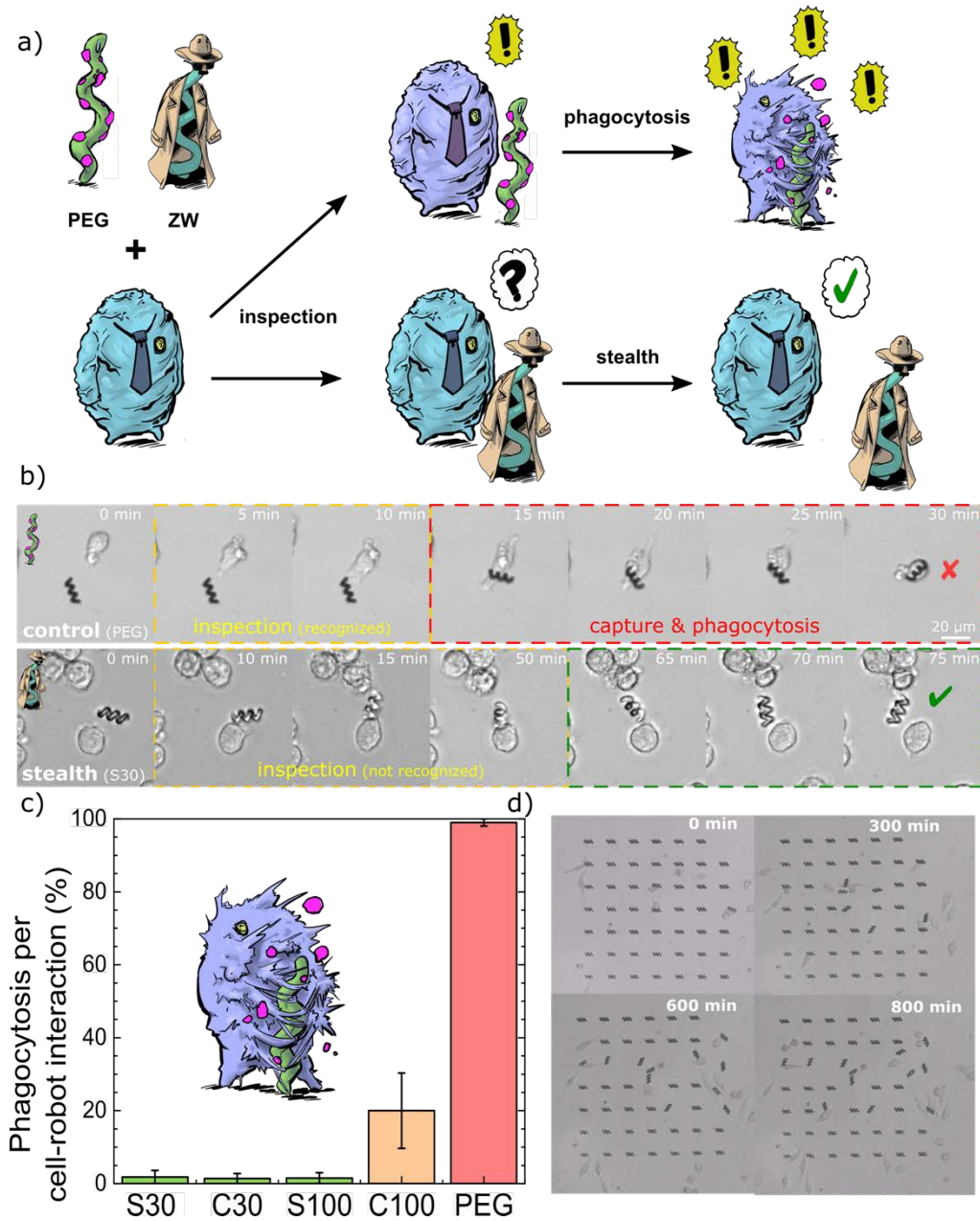


Figure 4.9 Zwitterionic Stealth Microrobots. (a) Schematic of cell-robot interaction. (b) Cell-robot interaction for PEG microrobots and S30 microrobots. (c) Phagocytosis rate for different types of microrobots (normalized by cell-robot interactions). (d) Time-lapse of a 7x7 S30 microrobots matrix in contact with macrophages.

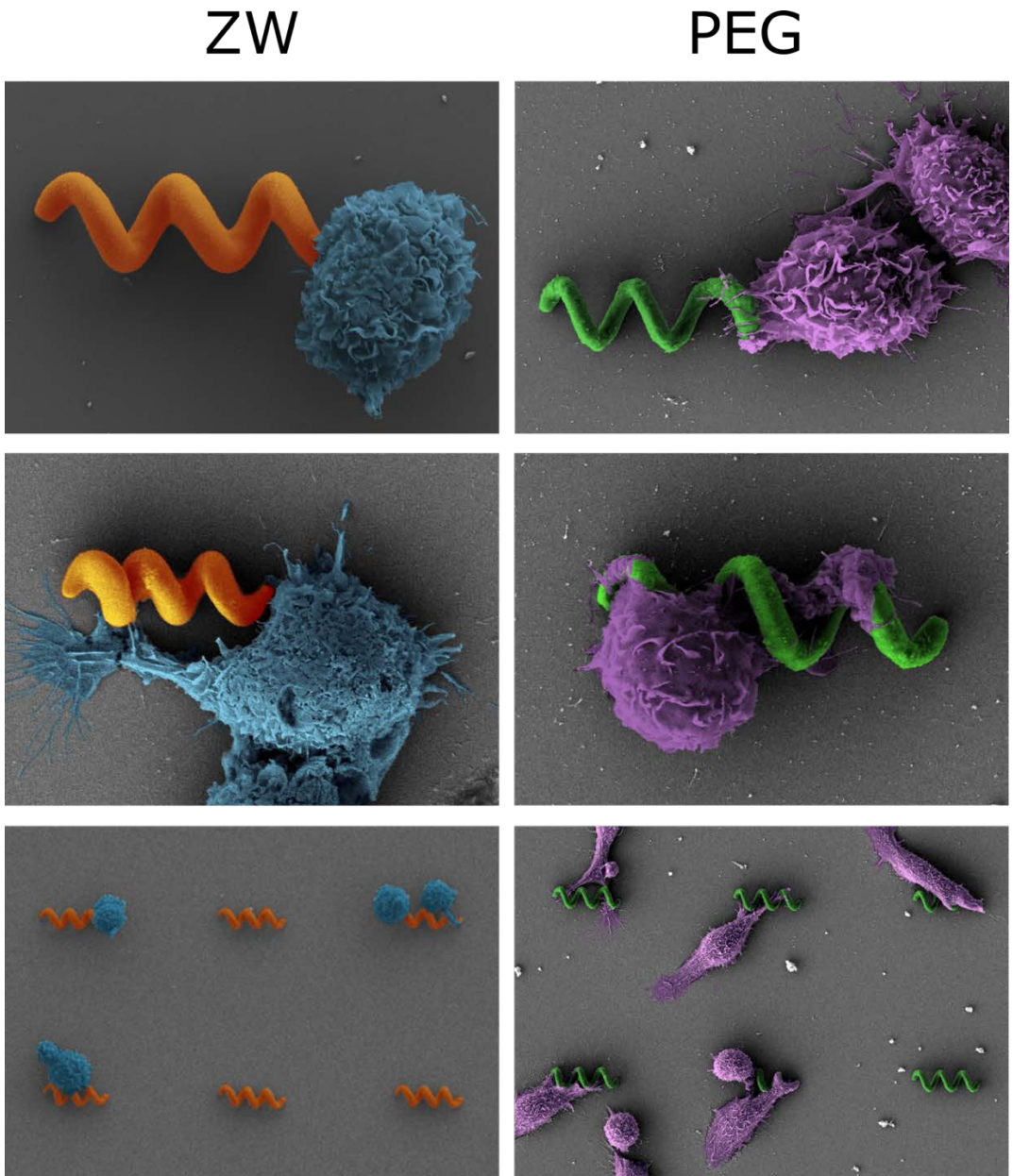


Figure 4.10 SEM images of the interaction between macrophages and the S30 and PEG microrobots.

For a critical evaluation of immunogenicity, these experiments were performed on free-floating robots for several reasons: (i) cells can freely probe and move the robots for intensive inspection, (ii) free-floating robots are most vulnerable to capture by immune cells (as opposed to constrained robots, which can block phagocytosis due to adhesion to the

substrate), and (iii) non-actuated robots (for example, static robots when they have reached their target destination) represent the most vulnerable scenario for capture (as opposed to fast-swimming robots, which can be faster than migrating macrophages). As can be observed in **Figure 4.9d**, zwitterionic microrobots could be detached from the surface by the microrobots, moving them freely. We observed that PEG microrobots could not be detached from the glass surface by macrophages. Therefore, we physically detached them before performing the phagocytosis experiment.

We further investigated the non-immunogenic properties by analyzing the morphology of macrophages interacting with non-stealth PEG microrobots and stealth zwitterionic microrobots at the early stages of inspection (**Figure 4.10**). Macrophages inspecting PEG microrobots exhibited a more aggressive morphology, suggested by distinct surface features (extension of filopodia towards the microrobot and presentation of dorsal ruffles on the cell surface, typically observed in activated macrophages, **Figure 4.11a**) [210]. In contrast, macrophages inspecting zwitterionic microrobots presented smoother cell surfaces with few or no filopodia trying to engulf the robot. This morphology was more similar to the one of unstimulated macrophages (**Figure 4.11b**).

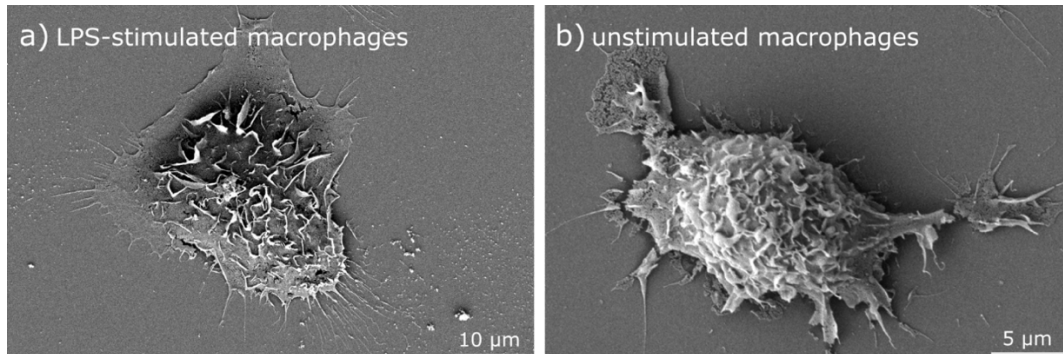


Figure 4.11 SEM images of (a) LPS-stimulated macrophages and (b) non-stimulated macrophages.

Both phagocytosis analysis (**Figure 4.9**) and morphology analysis (**Figure 4.10**) showed clearly the stealth behavior of the zwitterionic robots. Moreover, the zwitterionic robots outperformed the current “gold standard” of antifouling polymers (PEG). The almost 0% phagocytosis rate observed for zwitterionic microrobots, together with the unstimulated morphology of the macrophages in contact with them proved that macrophages are not

activated or aggressive towards zwitterionic microrobots, as they are not recognized as a foreign threat.

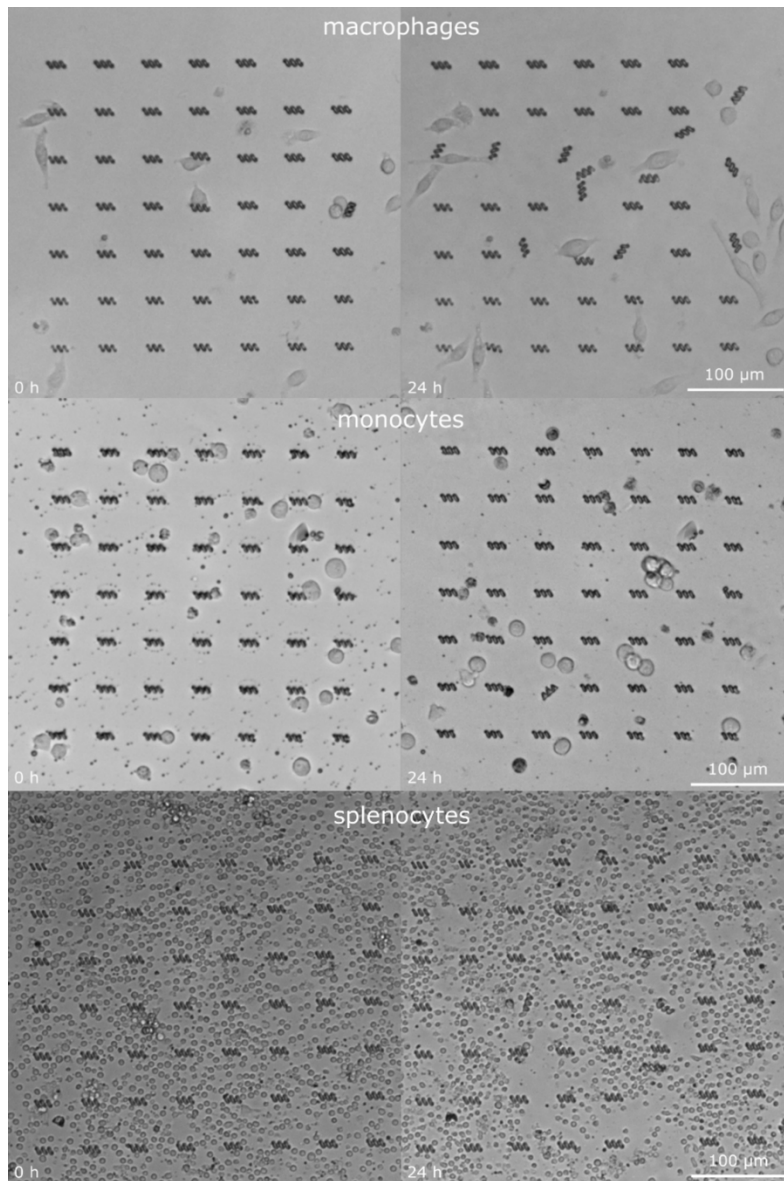


Figure 4.12 S30 microrobot arrays co-cultured with macrophages, monocytes and splenocytes for 24h.

To provide a more comprehensive analysis of the stealth properties and to better evaluate the non-immunogenicity of our microrobots, we also analyzed the response of other type of

immune cells towards our microrobots. As has been previously commented, macrophages are the main cell type responsible to remove the foreign threats by phagocytosis. But there are other cells in the immune systems that can phagocytize foreign materials. Other than macrophages, we used monocytes (macrophage precursors that are found in the bloodstream) and splenocytes, which consist of a diverse collection of immune cells present in the spleen, including T-lymphocytes, B-lymphocytes, dendritic cells, and macrophages (**Figure 4.12, Movie S2**).

After exhaustive inspection, robots were probed and moved around by cells, but we did not observe phagocytosis: stealth robots were released and remained free after inspection. Therefore, the zwitterionic microrobots proved their anti-immunogenicity against the different immune system cells. The stealth behavior was consistent after numerous cell-robot interactions (even with multiple cells repeatedly inspecting the same robot) for prolonged times (up to 90 hours). Therefore, zwitterionic photoresists offer a versatile platform for microfabrication to overcome limitations in microrobot design without compromising stealth functionalities. We observed that C30, S30, and S100 microrobots presented similar stealth behavior, indicating that both CB-based and SB-based photoresists are effective against macrophage recognition even with different mechanical properties (low and high crosslinking ratios). Overall, these results highlight the biocompatibility, anti-biofouling, and stealth properties of our custom zwitterionic photoresists, which outperform state-of-the-art materials for microrobot fabrication including commercially available photoresists and PEG-based materials, the current “gold standard” in terms of anti-biofouling and stealth behavior.

4.2.5. Magnetically actuated zwitterionic microrobots

Other than their anti-biofouling and stealth behavior, the zwitterionic microhydrogels printed with the zwitterionic photoresist presented multiple opportunities for functionalization, both pre-printing and post-printing.

We firstly focused on the introduction of magnetic materials before the printing step in order to remote control the printed structures. We mixed Small Paramagnetic Iron Oxide Nanoparticles (SPIONs) with the zwitterionic photoresists to create a nanocomposite photoresist that created magnetic zwitterionic microhydrogels with a single 3D-printing step (**Figure 4.13a**). We printed the helical microrobot structure out of the nanocomposite using

the 2PP 3D-printing. The printing was not affected by the introduction of SPIONS in concentrations up to 10 mg/ml. Once printed, we actuated the zwitterionic magnetic microrobots using magnetic torque actuation (more efficient than magnetic gradient pulling at the microscale) [211], which is one of the most common strategies for swimming at the low Reynolds number regime in synthetic microrobots [165,212,213]. We used external rotating magnetic fields (10 mT) at specific frequencies (ω) to induce spinning torque on the microrobots and propel them through an aqueous solution (**Figure 4.13b, Movie S3**).

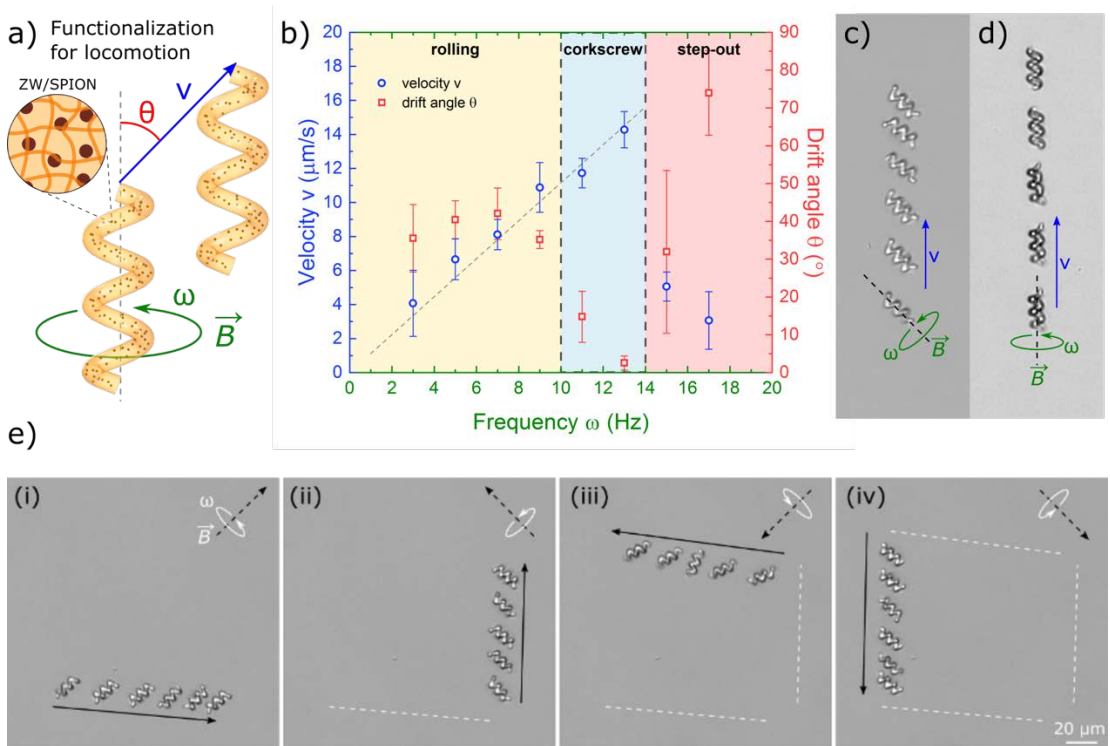


Figure 4.13 Magnetic actuation of the zwitterionic helical microrobots. *a) Addition of SPIONS in the zwitterionic photoresist to achieve magnetic actuation. b) Velocity and drift angle as a function of spinning frequency showed rolling, corkscrew, and step-out regimes. c) Rolling locomotion of microrobots ($\omega = 3$ Hz). d) Corkscrew locomotion of microrobots ($\omega = 13$ Hz). e) Microrobot rolling locomotion along a programmed square trajectory.*

At lower frequencies ($\omega < 10$ Hz), we observed rolling-type locomotion increasing linearly with actuation frequency and at a drift angle $\theta \sim 45^\circ$ (between magnetic actuation axis and microrobot locomotion axis) caused by friction with the substrate (wall effect) (**Figure 4.13c**).

At the optimum frequency range $10 < \omega < 13$ Hz, the magnetic torque overcomes the substrate friction and we achieved corkscrew-type locomotion through the fluid with zero drift (**Figure 4.13d**). At higher frequencies ($\omega > 14$ Hz, step-out frequency), the microrobot cannot catch up with the actuation frequency and the locomotion was defective (low velocity and moving in random directions). We achieved maximum velocities of 14.3 ± 1.1 $\mu\text{m/s}$ (0.8 ± 0.1 body lengths per second), which is an acceptable swimming performance for a soft magnetic composite microrobot[166,213,214]. Better performance for specific tasks could be achieved by increasing the concentration of magnetic particles in the photoresist, which involves colloidal stability problems, aligning the particles to create anisotropy, or using stronger magnetic materials. SPIONs are biocompatible, but other stronger magnetic nanomaterials typically present toxicity problems[215]. However, the current approach already demonstrates the compatibility of our zwitterionic materials with state-of-the-art methods of microscale robot actuation, allowing for locomotion through pre-programmed trajectories (**Figure 4.13e**), and provides with a new biocompatible, non-immunogenic material platform for magnetic microrobot designs.

4.2.6. Biomolecule encapsulation

After proving that inorganic magnetic nanoparticles could be introduced in the zwitterionic 3D printed structures, we evaluated their capacity to encapsulate small molecules and biomolecules. As above-mentioned, the zwitterionic photoresists developed were water-based due to the outstanding water solubility of the zwitterionic monomers and crosslinkers (up to 70% w/w). This property made the zwitterionic photoresists suitable for introduction of a wide range of biomolecules and small molecules that are only soluble/stable in water (**Figure 4.14a**).

We entrapped BSA (protein model) and Doxorubicin (DOX, small molecule drug model) into the zwitterionic photoresists, proving their capacity to encapsulate both big biomolecule and small molecule (**Figure 4.14b**). Furthermore, we proved that the encapsulated molecules remained entrapped into the microhydrogel matrix over long periods of time (24h) without the observation of any leakage (**Figure 4.14b**). Current water-soluble resists derived from natural polymers, as their low degree of methacrylation results in porous materials that cannot trap biomolecules. In contrast, we can control the methacrylation degree of the

zwitterionic microhydrogels by changing their crosslink percentage (**Figure 4.3**), being able to modulate the entrapment of such molecules.

This versatile approach for encapsulation of biomolecules makes zwitterionic photoresists attractive for a wide range of biomedical applications for 3D-printed microrobotics, such as targeted drug/gene delivery, imaging, biosensing, enzyme therapy, *etc.* Moreover, it makes them suitable for incorporating biomolecules for other types of locomotion such as chemical locomotion or enzyme propelled locomotion.

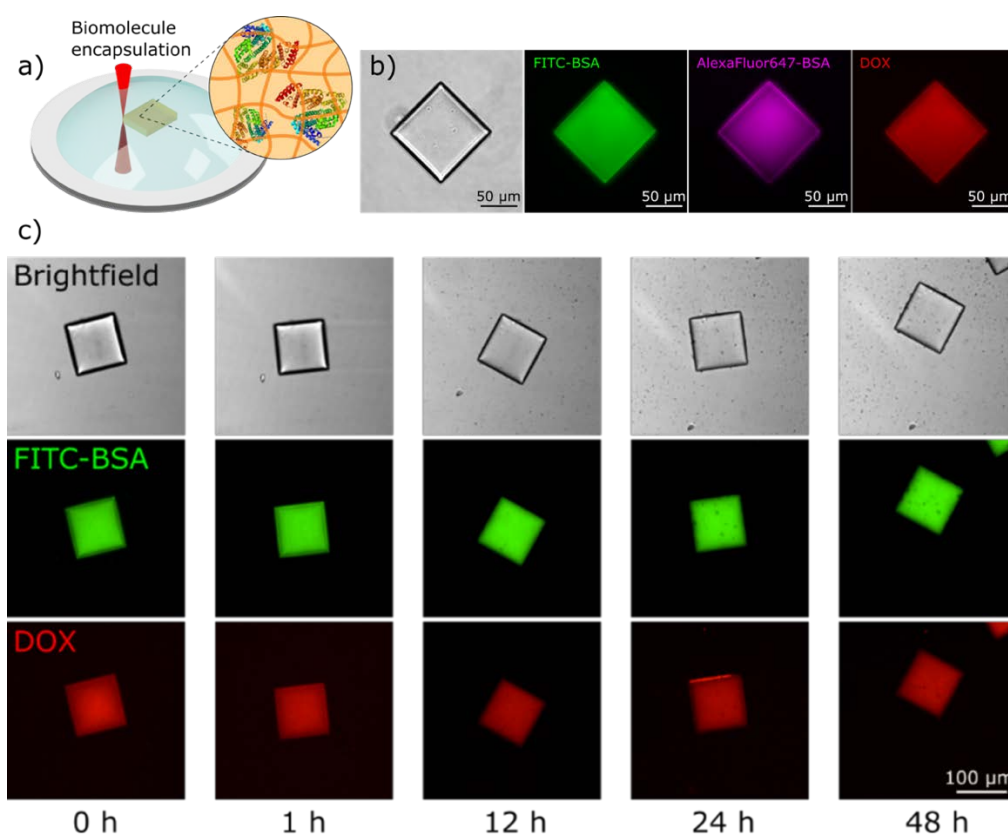


Figure 4.14 Drug and biomolecule encapsulation in zwitterionic 3D printed microhydrogels. *a)* Biomolecules were encapsulated by adding them before the printing step. *b)* Encapsulation of BSA and Doxorubicin (DOX). *c)* BSA and DOX remained encapsulated after 24 hours of incubation in aqueous media.

4.2.7. Surface functionalization of the zwitterionic microrobots

Finally, in order to introduce more functionalities to the zwitterionic microrobots, we explored the possibility to modify their surface. As commented in other chapters, one of the advantages of the use of zwitterionic polymers over other type of antifouling polymers such as PEG is the presence of modifiable groups in some of the zwitterion types (carboxybetaines).

We modified microrobots printed with the carboxybetaine resist using the EDC/NHS coupling chemistry to create an amide bond between the carboxylic acid of the carboxybetaine moiety with any free amine in the media. In first place, and to prove the possibility to perform this type of chemistry, we used a fluorescent probe (**Figure 4.15**). Images from fluorescence microscopy proved the surface modification of the C30 microrobots, confirming the possibility to perform this type of chemistry to include any aminated molecule.

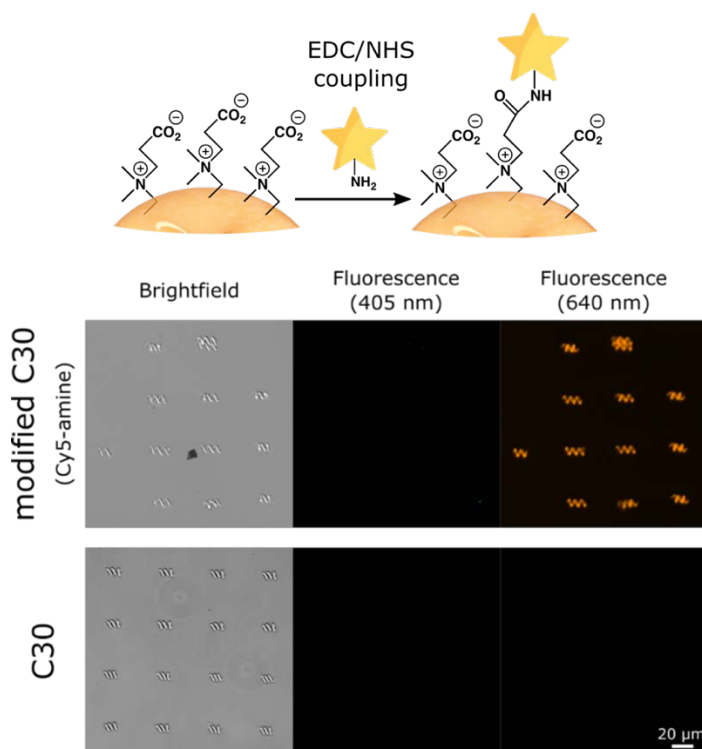


Figure 4.15 Fluorescence microscope images of Cy5-amine modified C30 microrobots and bare C30 microrobots.

We then decided to use this feature of the carboxybetaine microrobots to introduce an on-demand delivery of Doxorubicin through a photo-cleavable linker [166]. Briefly, we bonded a diamine to the carboxylic acid group *via* EDC/NHS coupling, added a photocleavable linker (*o*-nitrobenzyl group with terminal amine-reactive and alkyne groups), and terminated with azide-modified DOX *via* click chemistry (azide-alkyne click reaction) (**Figure 4.16a**).

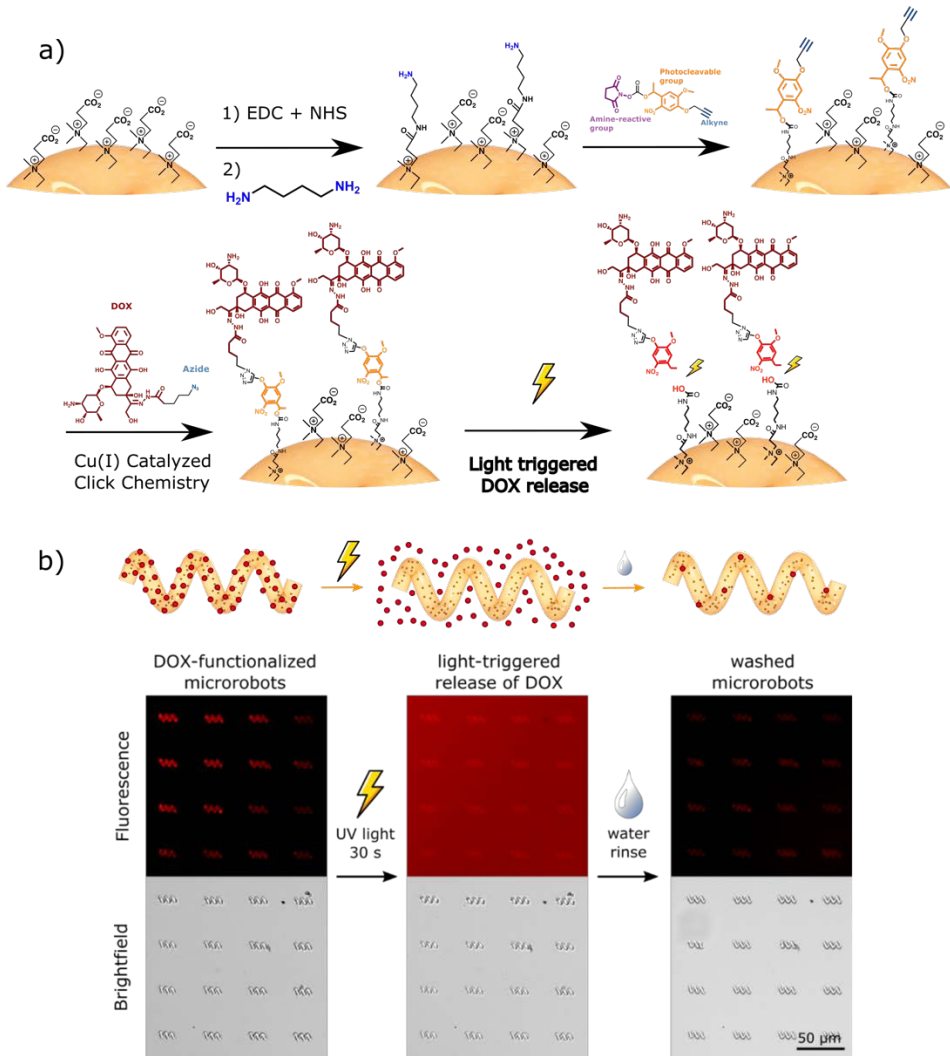


Figure 4.16 On-demand light-triggered release of Doxorubicin. *a)* schematic of the surface modification. *b)* Fluorescence microscopy of the Dox-functionalized microrobots before and after light triggered cleavage of the photo-cleavable linker.

DOX-functionalized microrobots showed stable fluorescence over time, but upon exposure to 365 nm light, the DOX molecules were released to the media due to the photocleavage of the linker molecules (**Figure 4.16b**). This functionalization strategy is particularly useful for on-demand light-triggered drug delivery, however, UV light poses challenges in direct translation into biomedical applications due to limited skin/blood/tissue penetration. Recent advances in optical upconversion of NIR to UV light could be used to enhance penetration depth [216], or the linker could be replaced by other photo-cleavable molecules that are responsive to different wavelengths.

One could argue that extreme functionalization of the microrobot surface might come at the cost of reducing the zwitterionic properties. Since this modification can only be performed in carboxybetaine but not sulfobetaine groups, photoresist formulations with tunable SB/CB composition can be designed to control the surface chemistry and introduce surface modification while preserving a sulfobetaine-dominated zwitterionic surface.

The versatile surface functionalization of zwitterionic microrobots can easily be extended to other drugs, antibodies, signaling moieties, or biomolecules for chemical sensing. Moreover, the anti-biofouling properties of zwitterionic surfaces avoid non-specific adsorption of proteins, which improves the efficiency of targeting, signaling, or sensing of the attached biomolecules [67], making zwitterionic microrobots very attractive for targeted therapy and biosensing applications. Other than microrobotics, other fields could also benefit from these properties. The capacity of having anti-fouling surfaces in the microscale with the capacity to modify their structure to introduce desired molecules would be of high interest for fields such as tissue engineering, diagnosis, among others.

4.3. Concluding Remarks

In this Chapter we have addressed a critical roadblock that is preventing microrobots to reach the clinics. We have developed a zwitterionic photoresist that has been printed using 2-photon polymerization, being the first time that zwitterionic materials have been printed using this high-precision micro-manufacturing. We have printed zwitterionic microrobots that have been proved to resist macrophage detection after exhaustive inspection (>90h), which has not been previously described in any microrobotics system. By avoiding macrophage detection, this microrobots can avoid their neutralization by the immune-system and, therefore, operate in the human body without triggering an immune response. Furthermore, the zwitterionic materials developed here outperform state-of-the-art and commercially available photoresists, and offer broad tailoring and functionalization for robot locomotion, imaging, and drug release strategies.

Although there are still many challenges in the path of the microrobots to the clinics, such as faster robots for locomotion in non-Newtonian biofluids, synthesis of dynamic photoresists for controlled degradation, and *in vivo* demonstrations, this work overcome a challenge that necessarily had to be bypassed but had not been exhaustively addressed before. Therefore, we envision the zwitterionic photoresists developed as an antifouling material toolbox for the design of future microrobots (with other locomotion, control and functions) performing medical functions.

Moreover, the high-resolution microstructures provided with the proved antifouling properties, together with their multifunctionality, can be useful in a wide variety of fields in which the unique properties of zwitterionic polymers are needed in the microscale.

Chapter 5: Conclusions

Chapter 5: Conclusions

In this thesis, we have focused on develop zwitterionic materials for the applications of drug delivery and microrobotics. Regarding the objective to create a platform of zwitterionic amphiphilic block copolymers that can self-assemble in zwitterionic nanoparticles, we have concluded that:

- RAFT polymerization followed by post-polymerization modification is an effective manufacturing method for the synthesis of zwitterionic amphiphilic copolymers. The resulting zwitterionic amphiphilic copolymers have shown to self-assemble in zwitterionic nanoparticles depending on the zwitterion type and the hydrophilic/hydrophobic ratio.
- Amphiphilic block copolymers containing poly(sulfobetaine methacrylate) as zwitterionic block present a salt-dependent self-assembly in water due to the antipolyelectrolyte effect. This problem can be solved by adding a voluminous morpholino group to the quaternary amine of the sulfobetaine, that sterically prevents the interaction between the opposite charges of the moiety. On the other hand, polymers containing poly(carboxybetaine) instead of poly(sulfobetaine) do not present problems in the self-assembly in water. These polymers present a pH-dependent protonation of the carboxylic acid that can be interesting for different applications.

Then, evaluating their antifouling properties and their capacity to become an oral drug delivery system against malaria and cancer, we have concluded that:

- Sulfobetaine nanoparticles have better performance than carboxybetaine nanoparticles in diffusing through the mucus. They are also effective in internalizing in gastrointestinal Caco-2 cell model, indicating their potential to pass through the mucus and crossing the gastrointestinal epithelium, the two barriers that block the oral administration of drug delivery systems.

- All zwitterionic nanoparticles except sulfobetaine ones (due to the anti-polyelectrolyte effect) have proved high levels of curcumin (antimalarial) and paclitaxel (anticancer) drug loading, up to 10 mg/ml. The drug-loaded nanoparticles have been proved to be effective in malarial and cancer *in vitro* models. This is an important feature of the zwitterionic nanoparticles that make them attractive for the drug delivery of hydrophobic drugs.
- Sulfobetaine nanoparticles passively target *Plasmodium* infected erythrocytes, possibly to their disruption when they enter in the *Plasmodium* parasite. This property is interesting, since few drug delivery systems can enter into the parasite. Although *in vivo* experiments with infected mice have not shown increase in survival, the presence of fluorescently marked polymer in the mice bloodstream indicate the oral absorption of zwitterionic nanoparticles and, therefore, their potential to become an oral antimalarial treatment.

Finally, in respect of the objective of developing a zwitterionic photoresist for microfabrication of zwitterionic microrobots, we have concluded that:

- Zwitterionic photoresists formulated with the synthesized zwitterionic monomers and crosslinkers can be microprinted using 2-photon polymerization at high concentrations. The physical properties of the resulting microhydrogels can be tuned by changing the monomer/crosslink ratio. This zwitterionic microscopical structures can be useful in multiple fields such as biosensing or microrobotics.
- Zwitterionic printed structures show antifouling effect when tested against BSA and avoid the adherence of cells. Zwitterionic microrobots outperform current robots in terms of immune-system avoidance, remaining undetected over more than 90 hours of exhaustive examination by macrophages. SEM images of macrophages in contact with zwitterionic microrobots and PEG microrobots (current “state of the art” antifouling polymer) show a difference in the morphology of the cells. While, in contact with PEG microrobots, macrophages show a more aggressive morphology, when in contact with zwitterionic microrobots they present a passive morphology.

- The easy functionalization of microrobots surface, as well as their capacity to encapsulate different biomolecules, provide to zwitterionic photoresists a great versatility to be used in multiple microrobots with different control, actuation and function strategies.

Chapter 6: Materials and Methods

Chapter 6: Materials and Methods

6.1. Methods of Chapter 2

6.1.1. Synthesis of Poly(Butyl methacrylate-*b*-sulfobetaine methacrylate) (PBMA-*b*-SBMA)

Polymers were prepared by RAFT polymerization followed by post-polymerization modification of PDMAEMA. Briefly, to produce PBMA₂₅-SBMA₃₅, BMA (1.0 g; 7.03 mmol) was added to the chain transfer agent (CTA) 2-cyano-2-propyl dodecyl trithiocarbonate (97.2 mg; 0.28 mmol) followed by AIBN (4.6 mg; 0.028 mmol), resulting in a molar ratio BMA:CTA:AIBN of 25:1:0.1. 1 ml of dioxane was further added to the reaction. Oxygen in the solution was removed by three freezing/vacuum/thawing cycles, finally introducing an argon atmosphere. The solution was stirred at 70 °C and terminated after 16 h by exposing it to the room atmosphere. The resulting PBMA was precipitated in methanol and dried over vacuum, obtaining a yellow polymer. Then, DMAEMA (397 mg; 2.52 mmol) was added to PBMA₂₅-CTA (394 mg; 0.10 mmol) followed by AIBN (4.9 mg; 0.03 mmol) and 1 ml of dioxane for a molar proportion DMAEMA:PBMA₂₅-CTA:AIBN of 35:1:0.3. Oxygen was removed by three freezing/vacuum/thawing cycles and after 16 h an argon atmosphere was applied. The solution was stirred at 70 °C and terminated by exposing it to the room atmosphere. The resulting PBMA₂₅-DMAEMA₃₅ was precipitated in hexane and dried over vacuum, obtaining a pale yellow polymer. In the case of PBMA₁₂-DMAEMA₁₈, the precipitation was done with methanol/H₂O 80:20. For the sulfobetainization, PBMA₂₅-DMAEMA₃₅ (292 mg; 0.032 mmol) was dissolved in 5 ml of tetrahydrofuran (THF) and 1,3-propanesultone (5.1 mg; 0.038 mmol) was added. The reaction was stirred for 16 h at room temperature to obtain a gel. The product was washed with cold THF and dried over vacuum to obtain PBMA-SBMA as a powder.

6.1.2. Synthesis of Poly(Butyl methacrylate-*b*-sulfobetainized morpholinoethyl methacrylate) (PBMA-*b*-MESBMA)

The same synthesis as that used in PBMA-DMAEMA was performed to produce PBMA-MEMA. Sulfobetainization was performed using a 2:1 ratio of propanesultone/MEMA in THF

for 7 days in reflux and was washed with cold THF to obtain PBMA-MESBMA, whose aspect depended on the length of the blocks.

6.1.3. Synthesis of Poly(Butyl methacrylate-*b*-carboxybetaine methacrylate) (PBMA-*b*-CBMA)

Production of PBMA-DMAEMA was performed as described previously. Derivatization of DMAEMA was performed with Acrylic Acid. Briefly, PBMA₄₀-DMAEMA₂₀ (500 mg; 0.057 mmol) was dissolved in 5 ml of tetrahydrofuran (THF). Acrylic Acid (11.2 mg; 0.11 mmol) was added and the solution was stirred at room temperature for 16 hours. Solvent was removed using rotary evaporation and solid precipitate was cleaned with Hexane and Ethyl ether to remove the unreacted acrylic acid.

6.1.4. Formation of zwitterionic nanoparticles

Nanoparticles were formed by direct dissolution of the amphiphilic nanoparticles in aqueous media and stirring for 16 h. Concentrations up to 0.8 mg/ml in PBS and NaCl 1M were used for PBMA-*b*-SBMA polymers. Concentrations up to 20 mg/ml in MiliQ water and PBS were used for the rest of the zwitterionic ABCs.

For PBMA-*b*-SBMA polymers, an extrusion processes using Miniextruder® (Avanti Polar Lipids, Inc.; Alabaster, IL, USA) was needed. Briefly, nanoparticles were passed through a 200 nm filter 21 times.

For PBMA-*b*-MESBMA and PBMA-*b*-CBMA polymers, nanoparticles were directly formed without the need of further processes.

6.1.5. DLS Characterization

Hydrodynamical size and Zeta potential were measured using Dynamic Light Scattering (Malvern Zetasizer NanoZS instrument; Malvern Instruments, UK). Nanoparticle concentration was adjusted for each experiment in order to obtain good quality results (concentrations from 0.5 mg/ml to 10 mg/ml). For the Zeta-potential analysis, same equipment was used. pH of samples was adjusted using HCl 0.1M and NaOH 0.1M.

6.1.6. Cryogenic Transmission Electron Microscopy (Cryo-TEM) analysis

The preparation of frozen samples was performed in a EM-CPC vitrification system with controlled environment (Leica Microsystems, Germany). A 4 μl sample drop was placed on a copper grid coated with a perforated polymer film. The sample excess was removed by blotting with filter paper. Right after this, the grid was plunged into liquid ethane held at a temperature just above its freezing point (94 °K). The vitrified sample was transferred to the microscope for analysis. The images were obtained with a JEOL JEM-2011 microscopy (JEOL LTD, Tokio, Japan) operating at 120 kV. To prevent sample perturbation and the formation of crystals, the specimens were kept cool (77 °K) during the transfer and the viewing procedure. Histograms were performed by counting a population of 100 nanoparticles using ImageJ software.

6.2. Methods of Chapter 3

6.2.1. Differential Scanning Calorimetry (DSC) analysis

DSC analysis was performed using Malvern MicroCal VP-DSC equipment (Malvern Instruments, UK). C1 nanoparticles at a concentration of 1 mg/ml in PBS were incubated with 10 mg/ml of BSA for 1 h at 37 °C. After the incubation, the samples were introduced in the DSC cell and analyzed by performing three temperatures cycles between 25 and 98 °C. The baseline was obtained subtracting each third cycle from the respective first one using Origin® software.

6.2.2. Modification of Zwitterionic polymers with Cy3

Cy3-maleimide (1.13 mg) was dissolved in 1 ml of THF and added to a solution of 13.2 mg of PBMA25-DMAEMA35 dissolved in 1 ml of THF in a sealed vial. The resulting solution was degassed with a N₂ stream. Cyclohexylamine (8.5 μl) was then added to the vial. The reaction was stirred in the dark for 16 h under N₂ atmosphere. Then, THF was evaporated with a N₂ flow and, to remove cyclohexylamine, the product was washed twice with cold hexane to obtain a red precipitate, which was dissolved with 200 μl of THF before adding a solution of

12 mg of 1,3-propanesultone in 200 μ l of THF. The reaction was stirred for 16 h at room temperature. The reaction turned into a red gel that was washed 3 times with cold THF, and the product was finally dried under vacuum to obtain the final PBMA25-SBMA35-Cy3 with a yield of 37.5 % (7.7 mg). For the synthesis of PBMA25-MESBMA35-Cy3, the same procedure was carried out.

6.2.3. Caco-2 cell culture

Caco-2 cells were purchased from ATCC (Manassas, VA). Cells were seeded at $4.5 \cdot 10^3$ cells/cm² and subcultured at 50% of confluence ($5.4 \cdot 10^4$ cells/cm²) for 10 passages, changing the medium (complete DMEM medium containing 10% heat inactivated Fetal Bovine Serum, 100 units/ml penicillin, 100 μ g/mL streptomycin, 0.1 mM MEM Non-Essential Amino Acids (NEAA), 2 mM L-glutamine (Gibco)) every two days. A large stock of LD cells was produced and stored at -150 °C. Cells were routinely maintained at 37 C in a 5% CO₂ atmosphere in complete medium.

6.2.4. Caco-2 internalization experiment

Caco-2 aliquots were thawed and subcultured for 2 passages in complete DMEM medium. To perform the experiment, cells were seeded at 20% confluence and nanoparticles were added when they reached 60% confluence. Fluorescence images of the samples were taken using a fluorescence microscope (Zeiss Axiovert 200M) with the 488 nm laser line 24 hours after the addition of the nanoparticles.

6.2.5. Multiple particle tracking (MPT) analysis

NP diffusion through intestinal mucus was assessed by MPT technique using previously described mathematical approaches [107,217]. Samples (0.5 g) of porcine intestinal mucus were incubated in glass-bottom MatTek imaging dishes at 37 C. The fluorescently labelled NPs were inoculated into each 0.5 g mucus sample in a 25 μ l aliquot at a suspension concentration of 0.002% NPs, a dilution confirmed to reproducibly avoid particle aggregation at the point of inoculation into the mucus sample. To ensure effective particle distribution following inoculation within the mucus a 2 h period of equilibration was adopted prior to beginning video microscopy capture of NP movements. Video capture involved 2-

dimensional imaging on a Leica DM IRB wide-field epifluorescence microscope (63 magnification oil immersion lens) using a high speed camera (Allied Vision Technologies, UK) running at a frame rate of 33 ms i.e. capturing 30 frames s⁻¹; each completed video film comprised 300 frames. For each 0.5 g mucus sample approximately 120 NPs were simultaneously tracked and their movements captured. For any distinct NP species, e.g. a particular polyelectrolyte mass ratio, a minimum of three distinct mucus samples were analysed, i.e. minimum of 360 individual NP trajectories assessed. The tracking (over a maximum of 10 s) of fully intact discrete particles was confirmed by microscopic criteria, and particle size and zeta potential stability over 2 h. Videos were imported into Fiji ImageJ software to convert the movement of each NP into individual NP trajectories across the full duration of the 10 s videos. However, for the analysis of particle diffusion only a 30 frame video period (1 s) was used, with the criterion that any individual particle tracked must display a continuous presence in the X–Y plane throughout the respective 30 sequential frames. Limiting the period of analysis to 30 frames minimized the impact of mucin movement upon the particle diffusion calculations. The individual particle trajectories were converted into numeric pixel data (Mosaic Particle Tracker within Fiji ImageJ) which, based on the microscope and video capture settings, were converted into metric distance. The distances moved by every individual particle over a selected time interval (Δt) in the X–Y trajectory were then expressed as a squared displacement (SD). The mean square displacement (MSD) of any single particle (n) represents the geometric mean of that particle's squared displacements throughout its entire 30-frame trajectory.

MSD was determined as follows [218]:

$$\text{MSD}_{(n)} = (X_{\Delta t})^2 + (Y_{\Delta t})^2$$

In any single mucus sample experiment an MSD was calculated for at least each of 120 individual particles (i.e. 120 MSD calculations) with the experiment replicated a further two times for any particle type, i.e. at least 360 particles studied in total. For each NP type under study, an “ensemble mean square displacement” (defined by $\langle \text{MSD} \rangle$) was then determined for each of the three replicate studies. The Effective Diffusion Coefficient ($\langle \text{Deff} \rangle$) for a particular NP type was then calculated by:

$$\langle \text{Deff} \rangle = \langle \text{MSD} \rangle / (4 * \Delta t)$$

where 4 is a constant relating to the 2-dimensional mode of video capture and Δt is the selected time interval.

Heterogeneity in particle diffusion: Profiling the diffusive properties of each particle within an entire population provides information on the heterogeneity of particle movement and the presence of outlier sub-populations that may follow distinct pathways of diffusion through the matrix. Here the Effective Diffusion Coefficient for each individual particle (Deff) was calculated at the time interval (Δt) of 1 s, and for any NP type all 360 $\text{Deff}_{\Delta t=1s}$ were then ranked to allow comparison of the highest (90th) and lowest (10th) percentiles, where for example the 90th percentile is the Deff value below which 90% of the Deff observations may be found.

6.2.6. Curcumin encapsulation

The encapsulation of curcumin in PBMA-SBMA nanoparticles was performed by adding different volumes of a solution of curcumin (50 mg/ml) in DMSO before the extrusion step, with an incubation time of 30 min. In the case of PBMA-PMESBMA and PBMA-PCBMA nanoparticles, the loading was performed by adding curcumin directly to the micelles and vortexing until the solution became transparent again. Finally, the samples were centrifuged (7,400 $\times g$, 5 min) to remove any unloaded curcumin. Maximum loading of curcumin was determined as the maximum concentration added into the system that did not present any pellet after the centrifugation (indicating full solubilization of the hydrophobic molecule).

6.2.7. *P. falciparum* cultures and in vitro growth inhibition assays

P. falciparum 3D7 was grown in vitro in human RBCs of blood group type B prepared as described elsewhere [219], using previously established conditions [220]. Briefly, parasites (thawed from glycerol stocks) were cultured at 37 °C in T25 flasks (SPL Life Sciences) in Roswell Park Memorial Institute (RPMI) complete medium (containing 5 g/l Albumax II and supplemented with 2 mM glutamine) under a gas mixture of 92% N₂, 5% CO₂, and 3% O₂. Synchronized ring stage cultures were obtained by 5% sorbitol lysis [221], and the medium was changed every 2 days maintaining 3% hematocrit. For culture maintenance, parasitemia

was kept below 5% late forms by dilution with RBCs. These Plasmodium cultures (200 μ l) were plated in 96-well plates and incubated for 48 h at 37 °C in the presence of free curcumin and polymer-curcumin conjugates dissolved in RPMI. Parasitemia was determined by microscopic counting of blood smears or by flow cytometry as previously described [222].

6.2.8. Targeting analysis

Living *P. falciparum* cultures were incubated in complete RPMI at 37 °C for 90 min with gentle stirring in the presence of 0.6 mg/ml (or 0.15 mg/ml for time-lapse microscopy) of Cy3-labeled PBMA-PSBMA and PBMA-PMESBMA polymers. After 80 min, Hoechst 33342 nuclear stain was added at a final concentration of 2 μ g/ml and cells were further incubated for another 10 min. For fluorescence microscopy, cells were washed twice with RPMI, diluted 20 times in RPMI to reach 0.15% hematocrit and transferred into a Lab-Tek®II chambered coverglass (Nunc, Thermo Fisher Scientific; catalog number 155409). Preparations were then analyzed by laser scanning confocal microscopy in either a Leica TCS SP5 microscope (63 \times immersion oil objective with 1.4 numerical aperture), or a ZEISS LSM 800 microscope (100 \times immersion oil objective). Hoechst 33342 and Cy3 were detected by excitation with 405 nm and 514 or 561 nm lasers, respectively. Emission was collected between 415 nm and 500 nm for Hoechst 33342, and between 580 nm and 680 nm for Cy3. Time-lapse images were taken every 8 s during 55 min. For flow cytometry, cells were either washed twice with RPMI or left without washing before being diluted with PBS to reach a final hematocrit of 0.03%. Preparations were then analyzed using a LSRFortessa™ flow cytometer instrument (BD Biosciences) set up with the 5 lasers, 20 parameters standard configuration. The single-cell population was selected on a forward-side scatter scattergram. Cy3 was excited using a yellow-green laser (561 nm), and its fluorescence collected through a 610/20-600 nm LP filter. Hoechst 33342 was excited with a UV laser (350 nm), and its fluorescence collected using a 450/50 nm filter.

6.2.9. Body weight loss analysis

Six-week old BALB/c mice were separated in 5 groups (n = 4) and administered intravenously with the different nanoparticle preparations in PBS. The weight of each mouse was determined every day, and they were observed carefully for signs of toxicity. Mice were euthanized at day 3 of the nanoparticle treatment.

6.2.10. Hemolysis tests

Mice blood samples were collected from six-week old BALB/c mice and collected in heparinized tubes (1000 U heparin/ml). The fresh blood samples were centrifuged at $867 \times g$ for 10 min at 4 °C and supernatant was discarded. The pellet was washed in PBS and centrifuged again to remove traces of plasma, and finally taken up in PBS and cell concentration was determined with a hemocytometer to adjust RBC concentration at 8×10^9 cells/ml. 10 μ l of this erythrocyte suspension was added to 100 μ l of each polymer sample in PBS and incubated for 10 min at 37 °C. Samples were then centrifuged, the supernatant was collected, and its absorbance was measured at 540 nm with a Tecan Infinity M Plex microplate reader (Tecan Group Ltd., Switzerland). Milli-Q® water and PBS were used as positive and negative controls respectively.

6.2.11. In vivo antimalarial assays

To test the antimalarial activity of free and encapsulated curcumin, a 4-day blood suppressive test was performed as previously described [223]. Briefly, BALB/c mice were inoculated 2×10^7 red blood cells from *Plasmodium yoelii yoelii* 17XL-infected mice by intraperitoneal injection and the survival of mice was assayed for 16 days. In order to test the prophylactic activity of curcumin, treatment started 1 day before infection (day -1), and consisted of a dose of $100 \text{ mg kg}^{-1} \text{ day}^{-1}$ curcumin administered by oral delivery of 200 μ l of a 10 mg/ml curcumin solution (in free form or incorporated in PBMA-PMESBMA nanoparticles) followed by identical dose administration for the next 3 days. The samples were prepared at appropriate concentrations in water and the control groups received PBS.

6.2.12. In vivo determination of polymers in pRBCs after oral administration

A BALB/c mouse was inoculated intraperitoneally with 100 μ l of a *P. yoelii yoelii* 17XL (PyL) MRA-267 frozen stock, and after 4 days blood was extracted from the tail and the parasitemia was checked by Giemsa staining. The infected mouse was anesthetized and total blood was obtained with an intracardiac puncture in the presence of ca. 10% EDTA (w/v). Blood was washed (sterile PBS, $500 \times g$, 10 min), reconstituted in PBS, and 100 μ l of this

reconstituted blood were used to inoculate intraperitoneally BALB/c mice with ca. 2×10^6 RBCs from the infected mouse. Five days post-infection, 200 μ l of 1.5 mg/ml Cy3-PBMA-SBMA or 10 mg/ml Cy3-PBMA-MESBMA polymers (dissolved in PBS and Milli-Q[®] H₂O, respectively) were administered by oral gavage, and blood samples were taken from the tail 20 min and 1, 2, and 4 h post-administration. A control blood sample was also removed just before administration. Samples were preserved at 4 °C in sterile PBS containing 1% EDTA (w/v) until their microscopic analysis, for which they were diluted 1:40 in 1 \times PBS containing 2 μ g/ml Hoechst 33342. Images were collected with a Leica TCS SP5 fluorescence confocal microscope (Mannheim, Germany) using a 63 \times oil immersion objective. Cy3 was excited with a 514 nm line of an Argon laser and Hoechst 33342 with a 405 nm line of a diode laser. To avoid crosstalk between the different fluorescence signals, a sequential scanning was performed.

6.2.13. Paclitaxel (PTX) encapsulation

PTX was encapsulated in PBMA-PMESBMA and PBMA-PCBMA nanoparticles using the same procedure used for curcumin. A 50 mg/ml PTX solution was prepared in DMSO and added directly to the micelle solution. The samples were vortexed until the solutions became transparent. Finally, the samples were centrifuged (7,400 \times g, 5 min) to remove any unloaded PTX. Maximum PTX concentration was determined as the concentration in which pellet was not observed after centrifugation.

6.2.14. HeLa cell line culture

HeLa cells were purchased from ATCC (Manassas, VA). Cells were seeded at 20% confluence and passages were performed when confluence reached 80%. Medium (complete DMEM medium containing 10% heat inactivated Fetal Bovine Serum, 100 units/ml penicillin, 100 μ g/mL streptomycin, 0.1 mM MEM Non-Essential Amino Acids (NEAA), 2 mM L-glutamine (Gibco)) was changed every two days.

6.2.15. Incucyte[®] live-cell analysis

HeLa cells were seeded at 30 % confluence in complete medium. After 24 hours, the different samples were added to the cells and they were incubated in the Incucyte[®] live-cell

analysis incubator (Sartorius, Germany). Images of cells were taken with a frequency of 1 hour. The images were analyzed using Incucyte® live analysis software to determine the % confluence at each time-point.

6.2.16. MTT toxicity assay

PTX loaded PBMA-PMESBMA and PBMA-CBMA nanoparticles antitumoral activity was measured using MTT assay (Sigma-Aldrich) at 24 hours after incubation. MTT assay measures the activity of living cells via mitochondrial dehydrogenase activity. Briefly, MTT stock solution (5 mg/mL) was added to each culture well, being assayed to equal one-tenth of the original culture volume and incubated for 3 h. After that, DMSO was added in an amount equal to the original culture volume. Finally, the cell viability was determined by measuring the absorbance at 570 nm using a microplate reader (Elx808 Biotek Instrument Ltd, USA). Cell viability was expressed as a relative percentage compared with untreated cells.

6.2.17. Introduction of S12 targetting peptide

We used EDC/NHS coupling to modify nanoparticle surface of C1. To a solution of C1 nanoparticles 10/mg/ml in MES buffer 20 mM (pH=5.4), there were added 2 µl of a 1 µg/ml solution of NHS in water and 3.6 µl of a 1 µg/ml solution of EDC in water. The samples were incubated during 6 hours at room temperature. Then, PBS 10X was added to the solution to change the pH to 7.8. 5.8 µl of a 1 µg/ml solution of N-(2-aminoethyl) maleimide trifluoroacetate salt in water was added to the sample, that was incubated during 2 hours. Finally, Cys-terminated S12 peptide was added to the solution in a concentration of 2.9 µg/ml and incubated for 16 hours. The modified samples were used directly after this step.

6.2.18. U87 cell culture

U87 glioblastoma cells were purchased from ATCC (Manassas, VA). Cells were seeded at 20% confluence and passages were performed when confluence reached 80%. Medium (complete DMEM medium containing 10% heat inactivated Fetal Bovine Serum, 100 units/ml penicillin, 100 ug/mL streptomycin, 0.1 mM MEM Non-Essential Amino Acids (NEAA), 2 mM L-glutamine (Gibco)) was changed every two days.

6.2.19. S12 targeting evaluation

Coumarin-6 was used as a fluorescent probe to determine nanoparticle internalization. 20 μ l of a solution of coumarin in ethanol (0.5 mg/ml) was added to the previous prepared samples. U87 cells were seeded at 30% confluence and, after incubating 24 hours, the different samples were added to the cells. Medium was changed 6 hours after the addition of the samples and the fluorescence of coumarin was determined using a fluorescence microscope (Zeiss Axiovert 200M) with the 405 nm laser line.

6.3. Methods of Chapter 4

6.3.1. Synthesis of carboxybetaine methacrylate (CB)

The synthesis of carboxybetaine methacrylate (CB) was adapted from elsewhere[188]. Briefly, 140 mL of acrylic acid (AA) were added to 170 mL of N,N-dimethyl(aminoethyl) methacrylate (DMAEMA) in an ice bath. The solution was stirred for 30 min at 0 °C and 4 hours at room temperature. 100 mL of ethanol were added to the reaction and the solution was stirred at room temperature for 12 hours. Ethanol was removed at reduced pressure and the resulting liquid was added to a 1 L solution of diethyl ether/trimethylamine (8:2). A white solid precipitated, it was filtered and then cleaned with ethyl ether. The resulting white solid was dried under vacuum (85 g, 35% yield).

6.3.2. Synthesis of sulfobetaine methacrylate (SB)

50 mL of DMAEMA were added to 250 mL of tetrahydrofuran (THF). 44 g of propanesultone were dissolved in 250 mL of THF and then were added to the solution in an ice bath. The solution was stirred overnight. A white solid precipitated from the reaction, it was filtered, cleaned with THF, and dried under vacuum (56 g, 73% yield).

6.3.3. Synthesis of carboxybetaine dimethacrylate (CBX)

The synthesis of carboxybetaine dimethacrylate (CBX) was adapted from a protocol developed in Jiang's lab [224] in which they synthesized a carboxybetaine moiety with two methacrylate groups. First, 11.9 g of N-methyldiethanolamine, 100 mL of toluene, 21.5 g of

methacrylic acid and 2 g of hydroquinone were added to a 500 mL reaction flask fitted with a stirrer, condenser, and Dean-Star trap. 14.4 g of methanesulfonic acid were added and the mixture was heated to reflux. After 6 hours, the solution was cooled to room temperature. The mixture was neutralized with aqueous sodium hydroxide and the aqueous phase was removed in a decantation funnel. The organic phase was washed with 10% brine solution and it was dried with anhydrous magnesium sulphate. Alumina free base was added to the solution and filtered. Toluene was removed under vacuum to obtain *N*-methyl-diethanolamine dimethacrylate (**Figure S3**) as a colorless liquid with a yield of 65% (16.5 g). Next, 16.5 g of *N*-methyl-diethanolamine dimethacrylate were dissolved in 150 mL of acetonitrile in a 500 mL round flask. The solution was purged with nitrogen for 20 min and 15.2 g of *t*-butyl bromoacetate were added to the solution. The solution was purged again with nitrogen during 10 min and the solution was stirred during 48 h at 60 °C. The solvent was removed under vacuum and the resulting liquid was added to 500 mL of diethyl ether, in which a white solid precipitates. This solid (*N*-Methyl-*N*-di(2-methacryloyloxy-ethyl)-*N*-1-(*t*-butyloxycarbonylmethyl) is cleaned with 250 mL of diethyl ether and dried under vacuum. The yield of this step is 86% (25.0 g). Finally, the *tert*-butyl protecting group was removed by adding 60 mL of trifluoroacetic acid and 240 mL of dichloromethane to 20 g of *N*-Methyl-*N*-di(2-methacryloyloxy-ethyl)-*N*-1-(*t*-butyloxycarbonylmethyl). The reaction was stirred for 40 hours at room temperature and then the solvent was evaporated under vacuum. 200 mL of acetonitrile were added to the remaining liquid and Amberlite® IRN 78 free base was added to the solution to neutralize it. Acetonitrile was removed under vacuum and the resulting liquid was precipitated in diethyl ether to obtain a white solid. This solid (**Figure S5**) was cleaned with diethyl ether and was dried in vacuum. The yield of this step was 51% (7.1 g).

6.3.4. Synthesis of sulfobetaine dimethacrylate (SBX)

The synthesis of SBX was adapted from elsewhere [189], starting from *N*-methyl-diethanolamine dimethacrylate, a mid-product of CBX synthesis. 10 g of *N*-methyl-diethanolamine dimethacrylate were dissolved in 50 mL of anhydrous acetone. 5.75 g of propanesultone were dissolved in 25 mL of anhydrous acetone and were added to the previous solution. The reaction was stirred for 5 hours at 60 °C, and a white solid appeared. The solid was filtered, cleaned with anhydrous acetone, and dried in vacuum. The yield was 64% (10.0 g).

6.3.5. UV photopolymerization of zwitterionic photoresists

Photoresists formulations of CB/CBX and SB/SBX in deionized water with concentrations of 10%, 17%, 40%, and 60% (w/w) and variable crosslinking ratio were prepared and investigated. Lithium phenyl-2,4,6-trimethylbenzoylphosphinate (LAP) photoinitiator was added to the formulation to a 4.3% (w/w) to monomer content. *In situ* photopolymerization was analyzed in a TA Instruments Discovery HR-2 rheometer with a photorheology accessory and an external UV light source (Omniculture series 2000 UV lamp, broadband 320–500 nm). Photorheology measurements were performed at 0.1% strain and a frequency of 10 rad/s.

6.3.6. 3D microprinting (two-photon polymerization)

Helical microrobots (single helix, 20 μm long, 5 μm in diameter, 2 μm in thread diameter, 7 μm in pitch) were designed in Solidworks, and CAD files were prepared for printing using Describe software (Nanoscribe GmbH). Water-based zwitterionic photoresists were prepared at the desired crosslinking ratio and concentration, with 4.3 % (w/w) LAP photoinitiator. For example, C100 at 60 % (w/w) photoresists were prepared by dissolving 30 mg of CBX and 1.35 mg of LAP in 20 μL of deionized water and sonicated for 5 min. The photoresist was then placed on a glass slide and transferred for 3D-printing via two-photon polymerization in a Photonic Professional system (Nanoscribe GmbH) with a 63x oil-immersion objective (NA 1.4). For better printing results, printing parameters were optimized to a laser power of 20 mW and scanning speed of $10^4 \mu\text{m/s}$. The photoresist concentration and crosslinking ratio were optimized for optimal resolution, reproducibility, and microstructure stability. The approximated printing time for a single helical microrobot was 20 seconds. To print magnetic microrobots, dextran-coated 50 nm iron oxide magnetic nanoparticles (Chemicell GmbH) were added to the photoresist formulation prior to printing at a concentration of 12.5 mg/mL and were printed using the same parameters. PEG-based microrobots were printed with poly(ethylene glycol) diacrylate (PEGDA, $M_n \approx 250$) containing 3% (w/v) Irgacure 369 photoinitiator. 27.5 mW laser power and scanning speed of $1.16 \cdot 10^4 \mu\text{m/s}$ were used for all printings. The overall printing rate was measured as approximately 10 s for a single helical microrobot.

6.3.7. J774A.1 and THP-1 cell culture conditions

All cell culture was performed in sterile conditions under or within a biosafety cabinet. The cell culture medium used for each cell line was prepared as DMEM (Dulbecco's Essential Medium) (Gibco) supplemented with 10% HI-FBS (heat-inactivated Fetal Bovine Serum) (Gibco) with 1% Penicillin & Streptomycin (Gibco). All cells were stored under standard cell culture conditions, 5% CO₂, 80% humidity, and 37°C.

6.3.8. J774A.1 Cell Culture

Murine macrophage cells (J774A.1) were purchased from ATCC. The cells were characterized by surface markers (CD11b, CD80, CD206), morphology, and ability to phagocyte. The cells were thawed from cryopreservation at passage 3. The cellular passages for the experiments was between passages 5 up to passage 25. J774A cells were allowed to reach ~80% confluence, observed by microscopy. The cellular removal procedure was performed by rinsing with DPBS without Ca²⁺ and Mg²⁺ for 5 min. After aspiration of DPBS, a fresh addition of medium was added. The cells were then removed from the flask by cell scraper and counted with a hemocytometer. A cell suspension of 5·10⁴ cells per mL was created.

6.3.9. THP-1 Cell Culture

Human monocyte non-adherent cell line THP-1 cells were purchased from ATCC. The cell culture medium was also DMEM. The cells were thawed from cryopreservation at passage 2. Due to the non-adherent nature of the THP-1 cells, the passage procedure is centrifugation at 400 × g for 5 min. Then the cells were resuspended to a density of 5·10⁴ cells per mL in DMEM. The final volume of media and cells added to microrobots was 1·10⁶ cells in 2 mL of DMEM.

6.3.10. Murine Spleen Isolation/Harvest

Mouse spleen was provided by the Facility for Animal Welfare, Veterinary Service and Laboratory Animal Science at the Eberhard Karls Universität Tübingen. Immediately after sacrificing, the spleen was removed and kept in PBS without Ca²⁺/Mg²⁺ at 4°C. The time between harvest and isolation step was ~2 hours. The spleen was passed through a 70 µm cell

strainer (Corning®) containing Roswell Park Memorial Institute (RPMI) 1640 medium in a 50 mL conical tube. This suspension was centrifuged at $800 \times g$ for 5 min. The supernatant was aspirated off and the pellet of cells was resuspended in 1 mL of (ACK) Ammonium-Chloride-Potassium Lysing Buffer for the lysis of red blood cells. This suspension was kept at room temperature for 5 min. The cell suspension was then diluted with 9 mL of RPMI 1640 and centrifuged again. The cells were then resuspended with fresh RPMI 1640 and counted. The cell density was calculated and prepared as a 1 million cell suspension in 2 mL of RPMI 1640 which was added to the microrobots.

6.3.11. Cell viability of ZW hydrogels

J774A.1 cells were allowed to reach ~80% confluence. The cellular removal procedure was performed by rinsing with Dulbecco's phosphate-buffered saline (DPBS) without Ca^+ and Mg^+ for 5 min. After aspiration of DPBS a fresh addition of medium was added. The cells were then removed from the flask by cell scraper and counted by hemocytometer. A cell suspension of $5 \cdot 10^4$ cells per mL was created. The samples were placed within trans-well inserts of 6.5 mm diameter with 8.0 μm pore size. After mixing, the cell suspension was added to the wells of the plate containing samples at $5 \cdot 10^4$ per well. After attachment, the media was aspirated and replaced with 800 μL of media placed into the bottom of the well, 200 μL of media placed into the top compartment of the trans-well insert already containing the sample. The plates were placed into standard culture conditions and incubated for 24 hours of exposure time. Following the 24 hours exposure time, the plates were removed and visually observed. The media was collected and stored at 4°C until analyzed for other markers. A batch of 10% water-soluble tetrazolium salt (WST-8) into cell culture media was prepared. Approximately 200 μL of the WST-8 dilution was placed into the wells containing cells. This was incubated at standard culture conditions for ~1 hour before the media was removed and placed into a 96-well plate. This was measured at 450 nm on a spectrophotometer. After the removal of the WST-8 the wells were rinsed with DPBS and a Live/Dead stain was added to the well. This Live/Dead stain was incubated at room temperature for 20 min before being observed by a fluorescence microscope (Nikon Eclipse Ti-E, Tokyo, Japan). The live cells were imaged at 494/518 nm, while the dead cells were imaged at 528/617 nm. Images were analyzed with Fiji software (ImageJ version 1.52g).

6.3.12. Cell adhesion on ZW hydrogels

J774A.1 cell suspension of $5 \cdot 10^4$ cells per mL was prepared as described above and added to the 24-well cell culture plates containing samples at $5 \cdot 10^4$ per well. After a 24 hour exposure time the plates were removed and observed by microscopy. The initial 24 hour images were then taken at 10x magnification at the bottom of the plate and the surface of the samples. A subsequent 24 hours were allowed to pass and the samples were immersed in DPBS and moved gently to ensure a full rinse. The samples were then placed into fresh medium. The final images were taken at 48 h post cell culture addition and after DPBS rinsing.

6.3.13. Protein adsorption on ZW microrobots

Microrobot arrays were printed from PEGDA, IP-S (commercial photoresist, Nanoscribe GmbH), S30, C30, S100, and C100 photoresists. Microrobots were immersed in $10 \mu\text{g/mL}$ albumin from bovine serum (BSA), Alexa Fluor® 647 conjugate in PBS for 2 hours, and were then rinsed with DI water.

6.3.14. Cell inspection of microrobots

Cell suspensions were prepared as described above for each cell type. Cell suspension were added to a petri dish containing 3D-printed microrobots. The samples cultured with J774A.1 were kept at standard culture conditions for 1 hour to allow attachment. Then the samples were moved to the incubation chamber of the Nikon Spinning Disk microscope and a time-lapse recording was initiated with images taken every 5 min. The samples cultured with THP-1 or splenocytes were moved to microscope enclosure at standard culture conditions immediately following seeding. The interaction between microrobots and immune cells was monitored, analyzing every contact interaction and whether the microrobots were detected and phagocytosed or not detected and released. Arrays of 7×7 microrobots were analyzed in triplicates (at least 147 microrobots for every material formulation). As a representative figure of merit, the number of phagocytosed robots was normalized by the number of contact interactions.

6.3.15. Scanning Electron Microscopy

Samples with cells were fixed with 2.5% (v/v) glutaraldehyde in 1x PBS for 30 min at 4°C and then rinsed 3 times with 1x PBS. After that, they were dehydrated in a series of increasing aqueous ethanol concentrations (20%, 40%, 60%, 80%, and 100%) for 3 min in each solution. Then, the samples were dried using a CO₂ critical point dryer (Leica EM CPD300, Leica Microsystems, Wetzlar, Germany) and coated with 10 nm gold using a spin coater (Leica EM ACE600, Leica Microsystems, Wetzlar, Germany). Finally, they were examined with a Zeiss Ultra 550 Gemini scanning electron microscope (Carl Zeiss Inc., Oberkochen, Germany) using an accelerating voltage of 5 keV.

6.3.16. Magnetic actuation of microrobots

Although the magnetic nanoparticles in the photoresist were homogeneously distributed, the microrobots were actuated via magnetic torque due to the anisotropic geometry of the microstructures. Magnetic microrobots were actuated using a custom-built five-electromagnetic coil system (5-coil setup: 4 x-y coils and 1 z coil, each 1.6 cm in diameter and 3.5 cm long) mounted on an inverted microscope that generated variable magnetic fields (5x5x1 mm³ of workspace, field range of 0-10 mT, and current range of +/- 10 A). Electric currents through the coils were calculated to minimize magnetic field spatial gradients. Rotating 10 mT magnetic fields at variable frequency and orientation were used to induce torque to propel and steer the microrobots along programmable trajectories.

6.3.17. Biomolecule encapsulation in 3D-printed zwitterionic microstructures

FITC-labeled BSA (Sigma Aldrich), AlexaFluor[®]647-labeled BSA (AlexaFluor), and DOX (LifeTein LLC) were simultaneously added to the photoresist formulation to a concentration of 1 mg/mL each. The photoresists were directly transferred to printing with the previous printing parameters without any additional step. The printed microstructures were thoroughly rinsed to remove non-polymerized photoresist and were imaged in a Nikon Ti-E fluorescence microscope.

6.3.18. Microrobot functionalization for light-triggered controlled drug release

Microrobots were printed with CB30 (i.e., 70 % CB, 30 % CBX) and further functionalized with DOX molecules through a photocleavable linker. First, free amine groups were introduced to the surface of microrobots via EDC/NHS coupling to the carboxybetaine carboxylic groups. Microrobots were incubated for 4 hours in 10 mM of 1-ethyl-3-(3-dimethylaminopropyl)carbodiimide and 20 mM of N-hydroxysuccinimide in a 0.1 M MES buffer (pH=5.5). Microrobots were then rinsed with PBS and incubated in 0.1 M of butyldiamine in PBS overnight, and were then rinsed with DI water and dimethyl sulfoxide. Next, microrobots were incubated in a solution containing 2.5 mM of 1-(5-methoxy-2-nitro-4-prop-2-ynyloxyphenyl)ethyl N-succinimidyl carbonate (a photocleavable o-nitrobenzyl linker, LifeTein LLC, Somerset, NJ) for 3 hours, and then rinsed with DMSO. Last, copper (I) catalyzed azide-alkyne click chemistry was performed to bond an azide-modified DOX (LifeTein LLC) with the alkyne end of the photocleavable linker. A 50 mM of azide-DOX, 100 μ M CuSO₄, 5 mM sodium ascorbate, and 500 μ M tris(3-hydroxypropyltriazolylmethyl)amine solution was prepared and microrobots were incubated in it during 2 hours. Samples were rinsed with DI water to remove excess DOX. Light-triggered DOX release from the functionalized microrobots was performed using a 365 nm UV external light source (55 mW/cm²) source. Drug release from the microswimmers was measured using an inverted fluorescence microscope (Nikon Eclipse Ti-E, Tokyo, Japan).

Chapter 7: Bibliography

Chapter 7: Bibliography

- [1] N. Huebsch, D.J. Mooney, Inspiration and application in the evolution of biomaterials, *Nature*. 462 (2009) 426–432. <https://doi.org/10.1038/nature08601>.
- [2] B.D. Ratner, S.J. Bryant, Biomaterials: Where We Have Been and Where We Are Going, *Annu. Rev. Biomed. Eng.* 6 (2004) 41–75. <https://doi.org/10.1146/annurev.bioeng.6.040803.140027>.
- [3] B.D. Ratner, Biomaterials: Been There, Done That, and Evolving into the Future, *Annu. Rev. Biomed. Eng.* 21 (2019) 171–191. <https://doi.org/10.1146/annurev-bioeng-062117-120940>.
- [4] P.A. Sharp, R. Langer, Promoting convergence in biomedical science, *Science* (80-.). 333 (2011) 527. <https://doi.org/10.1126/science.1205008>.
- [5] B.D. Ratner, A.S. Hoffman, F.J. Schoen, J.E. Lemons, *Biomaterials Science: An Introduction to Materials: Third Edition*, 2013. <https://doi.org/10.1016/B978-0-08-087780-8.00148-0>.
- [6] S. Barua, S. Mitragotri, Challenges associated with penetration of nanoparticles across cell and tissue barriers: A review of current status and future prospects, *Nano Today*. 9 (2014) 223–243. <https://doi.org/10.1016/j.nantod.2014.04.008>.
- [7] E. Mariani, G. Lisignoli, R.M. Borzì, L. Pulsatelli, Biomaterials: Foreign Bodies or Tuners for the Immune Response?, *Int. J. Mol. Sci.* 20 (2019) 636. <https://doi.org/10.3390/ijms20030636>.
- [8] J.M. Anderson, A. Rodriguez, D.T. Chang, Foreign body reaction to biomaterials, *Semin. Immunol.* 20 (2008) 86–100. <https://doi.org/10.1016/j.smim.2007.11.004>.
- [9] Z.J. Deng, M. Liang, M. Monteiro, I. Toth, R.F. Minchin, Nanoparticle-induced unfolding of fibrinogen promotes Mac-1 receptor activation and inflammation, *Nat. Nanotechnol.* 6 (2011) 39–44. <https://doi.org/10.1038/nnano.2010.250>.
- [10] G. Caracciolo, O.C. Farokhzad, M. Mahmoudi, Biological Identity of Nanoparticles In Vivo : Clinical Implications of the Protein Corona, *Trends Biotechnol.* 35 (2017) 257–264. <https://doi.org/10.1016/j.tibtech.2016.08.011>.
- [11] D. Campoccia, L. Montanaro, C.R. Arciola, A review of the biomaterials technologies for infection-resistant surfaces, *Biomaterials.* 34 (2013) 8533–8554. <https://doi.org/10.1016/j.biomaterials.2013.07.089>.
- [12] E. Ostuni, R.G. Chapman, M.N. Liang, G. Meluleni, G. Pier, D.E. Ingber, G.M. Whitesides, Self-Assembled Monolayers That Resist the Adsorption of Proteins and the Adhesion of Bacterial and Mammalian Cells, *Langmuir.* 17 (2001) 6336–6343. <https://doi.org/10.1021/la010552a>.
- [13] C.F. Wertz, M.M. Santore, Adsorption and Relaxation Kinetics of Albumin and

- Fibrinogen on Hydrophobic Surfaces: Single-Species and Competitive Behavior, *Langmuir*. 15 (1999) 8884–8894. <https://doi.org/10.1021/la990089q>.
- [14] Y. Chen, S. Thayumanavan, Amphiphilicity in Homopolymer Surfaces Reduces Nonspecific Protein Adsorption †, *Langmuir*. 25 (2009) 13795–13799. <https://doi.org/10.1021/la901692a>.
- [15] E.W. Merrill, E.W. Salzman, Polyethylene oxide as a biomaterial, *ASAIO J.* (1983).
- [16] S. Nagaoka, Y. Mori, H. Takiuchi, K. Yokota, H. Tanzawa, S. Nishiumi, INTERACTION BETWEEN BLOOD COMPONENTS AND HYDROGELS WITH (OXYETHYLENE) CHAINS., in: 1984. https://doi.org/10.1007/978-1-4613-2433-1_26.
- [17] M.S. Hershfield, PEG-ADA replacement therapy for adenosine deaminase deficiency: An update after 8.5 years, *Clin. Immunol. Immunopathol.* (1995). [https://doi.org/10.1016/S0090-1229\(95\)90306-2](https://doi.org/10.1016/S0090-1229(95)90306-2).
- [18] A. Hamilton, L. Biganzoli, R. Coleman, L. Mauriac, P. Hennebert, A. Awada, M. Nooij, L. Beex, M. Piccart, I. Van Hoorebeeck, P. Bruning, D. de Valeriola, EORTC 10968: A phase I clinical and pharmacokinetic study of polyethylene glycol liposomal doxorubicin (Caelyx®, Doxil®) at a 6-week interval in patients with metastatic breast cancer, *Ann. Oncol.* 13 (2002) 910–918. <https://doi.org/10.1093/annonc/mdf157>.
- [19] L. Huang, S. Guo, Nanoparticles escaping RES and endosome: Challenges for siRNA delivery for cancer therapy, *J. Nanomater.* 2011 (2011). <https://doi.org/10.1155/2011/742895>.
- [20] K. Knop, R. Hoogenboom, D. Fischer, U.S. Schubert, Poly(ethylene glycol) in Drug Delivery: Pros and Cons as Well as Potential Alternatives, *Angew. Chemie Int. Ed.* 49 (2010) 6288–6308. <https://doi.org/10.1002/anie.200902672>.
- [21] E. Blanco, H. Shen, M. Ferrari, Principles of nanoparticle design for overcoming biological barriers to drug delivery, *Nat. Biotechnol.* 33 (2015) 941–951. <https://doi.org/10.1038/nbt.3330>.
- [22] J.M. Harris, R.B. Chess, Effect of pegylation on pharmaceuticals, *Nat. Rev. Drug Discov.* 2 (2003) 214–221. <https://doi.org/10.1038/nrd1033>.
- [23] L. Li, S. Chen, J. Zheng, B.D. Ratner, S. Jiang, Protein Adsorption on Oligo(ethylene glycol)-Terminated Alkanethiolate Self-Assembled Monolayers: The Molecular Basis for Nonfouling Behavior, *J. Phys. Chem. B.* 109 (2005) 2934–2941. <https://doi.org/10.1021/jp0473321>.
- [24] M.C. Parrott, J.M. DeSimone, Relieving PEGylation, *Nat. Chem.* 4 (2012) 13–14. <https://doi.org/10.1038/nchem.1230>.
- [25] P. Zhang, F. Sun, S. Liu, S. Jiang, Anti-PEG antibodies in the clinic: Current issues and beyond PEGylation, *J. Control. Release.* 244 (2016) 184–193. <https://doi.org/10.1016/j.jconrel.2016.06.040>.

- [26] Q. Yang, S.K. Lai, Anti-PEG immunity: emergence, characteristics, and unaddressed questions, *Wiley Interdiscip. Rev. Nanomedicine Nanobiotechnology*. 7 (2015) 655–677. <https://doi.org/10.1002/wnan.1339>.
- [27] M.D. McSweeney, Z.C. Versfeld, D.M. Carpenter, S.K. Lai, Physician Awareness of Immune Responses to Polyethylene Glycol-Drug Conjugates, *Clin. Transl. Sci.* 11 (2018) 162–165. <https://doi.org/10.1111/cts.12537>.
- [28] Y. Liu, C.A. Smith, J.C. Panetta, W. Yang, L.E. Thompson, J.P. Counts, A.R. Molinelli, D. Pei, N.M. Kornegay, K.R. Crews, H. Swanson, C. Cheng, S.E. Karol, W.E. Evans, H. Inaba, C.-H. Pui, S. Jeha, M. V. Relling, Antibodies Predict Pegaspargase Allergic Reactions and Failure of Rechallenge, *J. Clin. Oncol.* 37 (2019) 2051–2061. <https://doi.org/10.1200/JCO.18.02439>.
- [29] Z. Cao, S. Jiang, Super-hydrophilic zwitterionic poly(carboxybetaine) and amphiphilic non-ionic poly(ethylene glycol) for stealth nanoparticles, *Nano Today*. 7 (2012) 404–413. <https://doi.org/10.1016/j.nantod.2012.08.001>.
- [30] F.M. Veronese, Peptide and protein PEGylation, *Biomaterials*. 22 (2001) 405–417. [https://doi.org/10.1016/S0142-9612\(00\)00193-9](https://doi.org/10.1016/S0142-9612(00)00193-9).
- [31] F.M. Muggia, J.D. Hainsworth, S. Jeffers, P. Miller, S. Groshen, M. Tan, L. Roman, B. Uziely, L. Muderspach, A. Garcia, A. Burnett, F.A. Greco, C.P. Morrow, L.J. Paradiso, L.J. Liang, Phase II study of liposomal doxorubicin in refractory ovarian cancer: Antitumor activity and toxicity modification by liposomal encapsulation, *J. Clin. Oncol.* (1997). <https://doi.org/10.1200/JCO.1997.15.3.987>.
- [32] L. Zheng, H.S. Sundaram, Z. Wei, C. Li, Z. Yuan, Applications of zwitterionic polymers, *React. Funct. Polym.* 118 (2017) 51–61. <https://doi.org/10.1016/j.reactfunctpolym.2017.07.006>.
- [33] J. Wu, W. Lin, Z. Wang, S. Chen, Y. Chang, Investigation of the Hydration of Nonfouling Material Poly(sulfobetaine methacrylate) by Low-Field Nuclear Magnetic Resonance, *Langmuir*. 28 (2012) 7436–7441. <https://doi.org/10.1021/la300394c>.
- [34] J. Wu, S. Chen, Investigation of the Hydration of Nonfouling Material Poly(ethylene glycol) by Low-Field Nuclear Magnetic Resonance, *Langmuir*. 28 (2012) 2137–2144. <https://doi.org/10.1021/la203827h>.
- [35] D.R. Canchi, A.E. García, Cosolvent Effects on Protein Stability, *Annu. Rev. Phys. Chem.* 64 (2013) 273–293. <https://doi.org/10.1146/annurev-physchem-040412-110156>.
- [36] E.J. Guinn, L.M. Pegram, M.W. Capp, M.N. Pollock, M.T. Record, Quantifying why urea is a protein denaturant, whereas glycine betaine is a protein stabilizer, *Proc. Natl. Acad. Sci.* 108 (2011) 16932–16937. <https://doi.org/10.1073/pnas.1109372108>.
- [37] Q. Zou, B.J. Bennion, V. Daggett, K.P. Murphy, The molecular mechanism of stabilization of proteins by TMAO and its ability to counteract the effects of urea, *J. Am. Chem. Soc.* 124 (2002) 1192–1202. <https://doi.org/10.1021/ja004206b>.

- [38] A.D. White, A.K. Nowinski, W. Huang, A.J. Keefe, F. Sun, S. Jiang, Decoding nonspecific interactions from nature, *Chem. Sci.* 3 (2012) 3488. <https://doi.org/10.1039/c2sc21135a>.
- [39] A.J. Keefe, K.B. Caldwell, A.K. Nowinski, A.D. White, A. Thakkar, S. Jiang, Screening nonspecific interactions of peptides without background interference, *Biomaterials*. 34 (2013) 1871–1877. <https://doi.org/10.1016/j.biomaterials.2012.11.014>.
- [40] J. Ladd, Z. Zhang, S. Chen, J.C. Hower, S. Jiang, Zwitterionic Polymers Exhibiting High Resistance to Nonspecific Protein Adsorption from Human Serum and Plasma, *Biomacromolecules*. 9 (2008) 1357–1361. <https://doi.org/10.1021/bm701301s>.
- [41] Z. Cao, L. Zhang, S. Jiang, Superhydrophilic zwitterionic polymers stabilize liposomes, *Langmuir*. 28 (2012) 11625–11632. <https://doi.org/10.1021/la302433a>.
- [42] H. Vaisocherová, W. Yang, Z. Zhang, Z. Cao, G. Cheng, M. Pilarik, J. Homola, S. Jiang, Ultralow Fouling and Functionalizable Surface Chemistry Based on a Zwitterionic Polymer Enabling Sensitive and Specific Protein Detection in Undiluted Blood Plasma, *Anal. Chem.* 80 (2008) 7894–7901. <https://doi.org/10.1021/ac8015888>.
- [43] R. Rajan, K. Matsumura, Inhibition of protein aggregation by zwitterionic polymer-based core-shell nanogels, *Sci. Rep.* 7 (2017) 45777. <https://doi.org/10.1038/srep45777>.
- [44] B. Li, J. Xie, Z. Yuan, P. Jain, X. Lin, K. Wu, S. Jiang, Mitigation of Inflammatory Immune Responses with Hydrophilic Nanoparticles, *Angew. Chemie - Int. Ed.* 57 (2018) 4527–4531. <https://doi.org/10.1002/anie.201710068>.
- [45] Y. Kadoma, N. Nakabayashi, E. Masuhara, J. Yamauchi, Synthesis and hemolysis test of the polymer containing phosphorylcholine groups, *KOBUNSHI RONBUNSHU*. (1978). <https://doi.org/10.1295/koron.35.423>.
- [46] K. Ishihara, T. Ueda, N. Nakabayashi, Preparation of phospholipid polymers and their properties as polymer hydrogel membranes, *Polym. J.* (1990). <https://doi.org/10.1295/polymj.22.355>.
- [47] K. Ishihara, Revolutionary advances in 2-methacryloyloxyethyl phosphorylcholine polymers as biomaterials, *J. Biomed. Mater. Res. Part A*. 107 (2019) 933–943. <https://doi.org/10.1002/jbm.a.36635>.
- [48] A. Laschewsky, Structures and synthesis of zwitterionic polymers, *Polymers (Basel)*. 6 (2014) 1544–1601. <https://doi.org/10.3390/polym6051544>.
- [49] B. Li, P. Jain, J. Ma, J.K. Smith, Z. Yuan, H.-C. Hung, Y. He, X. Lin, K. Wu, J. Pfaendtner, S. Jiang, Trimethylamine N -oxide-derived zwitterionic polymers: A new class of ultralow fouling bioinspired materials, *Sci. Adv.* 5 (2019) eaaw9562. <https://doi.org/10.1126/sciadv.aaw9562>.
- [50] L.D. Blackman, P.A. Gunatillake, P. Cass, K.E.S. Locock, An introduction to zwitterionic polymer behavior and applications in solution and at surfaces, *Chem.*

- Soc. Rev. 48 (2019) 757–770. <https://doi.org/10.1039/C8CS00508G>.
- [51] K. Letchford, H. Burt, A review of the formation and classification of amphiphilic block copolymer nanoparticulate structures: micelles, nanospheres, nanocapsules and polymersomes, *Eur J Pharm Biopharm.* 65 (2007) 259–269. <https://doi.org/10.1016/j.ejpb.2006.11.009>.
- [52] P. Alexandridis, Amphiphilic copolymers and their applications, *Curr. Opin. Colloid Interface Sci.* 1 (n.d.) 490–501. [https://doi.org/10.1016/S1359-0294\(96\)80118-X](https://doi.org/10.1016/S1359-0294(96)80118-X).
- [53] A. V Kabanov, E. V Batrakova, V.Y. Alakhov, Pluronic (R) block copolymers as novel polymer therapeutics for drug and gene delivery, *J. Control. Release.* 82 (2002) 189–212. [https://doi.org/10.1016/s0168-3659\(02\)00009-3](https://doi.org/10.1016/s0168-3659(02)00009-3).
- [54] A. Rösler, G.W.. M. Vandermeulen, H.-A.A. Klok, Advanced drug delivery devices via self-assembly of amphiphilic block copolymers, *Adv. Drug Deliv. Rev.* 53 (2001) 95–108. [https://doi.org/10.1016/S0169-409X\(01\)00222-8](https://doi.org/10.1016/S0169-409X(01)00222-8).
- [55] G.S. Kwon, K. Kataoka, Block copolymer micelles as long-circulating drug vehicles, *Adv. Drug Deliv. Rev.* 16 (1995) 295–309. [https://doi.org/10.1016/0169-409X\(95\)00031-2](https://doi.org/10.1016/0169-409X(95)00031-2).
- [56] D.E. Discher, F. Ahmed, POLYMERSOMES, *Annu. Rev. Biomed. Eng.* 8 (2006) 323–341. <https://doi.org/10.1146/annurev.bioeng.8.061505.095838>.
- [57] J.S. Lee, J. Feijen, Polymersomes for drug delivery: Design, formation and characterization, *J. Control. Release.* 161 (2012) 473–483. <https://doi.org/10.1016/j.jconrel.2011.10.005>.
- [58] S. Panja, G. Dey, R. Bharti, K. Kumari, T.K. Maiti, M. Mandal, S. Chattopadhyay, Tailor-Made Temperature-Sensitive Micelle for Targeted and On-Demand Release of Anticancer Drugs, *ACS Appl. Mater. Interfaces.* (2016). <https://doi.org/10.1021/acsami.6b03820>.
- [59] C. Chen, J. Zhao, M. Gao, X. Meng, A. Fan, Z. Wang, Y. Zhao, Photo-triggered micelles: Simultaneous activation and release of microtubule inhibitors for on-demand chemotherapy, *Biomater. Sci.* (2018). <https://doi.org/10.1039/c7bm01053b>.
- [60] Y. Liu, W. Wang, J. Yang, C. Zhou, J. Sun, pH-sensitive polymeric micelles triggered drug release for extracellular and intracellular drug targeting delivery, *Asian J. Pharm. Sci.* (2013). <https://doi.org/10.1016/j.ajps.2013.07.021>.
- [61] J. Ahn, Y. Miura, N. Yamada, T. Chida, X. Liu, A. Kim, R. Sato, R. Tsumura, Y. Koga, M. Yasunaga, N. Nishiyama, Y. Matsumura, H. Cabral, K. Kataoka, Antibody fragment-conjugated polymeric micelles incorporating platinum drugs for targeted therapy of pancreatic cancer, *Biomaterials.* (2015). <https://doi.org/10.1016/j.biomaterials.2014.10.069>.
- [62] V.P. Torchilin, Targeted polymeric micelles for delivery of poorly soluble drugs, *Cell.*

- Mol. Life Sci. (2004). <https://doi.org/10.1007/s00018-004-4153-5>.
- [63] H. Maeda, J. Wu, T. Sawa, Y. Matsumura, K. Hori, Tumor vascular permeability and the EPR effect in macromolecular therapeutics: A review, *J. Control. Release.* (2000). [https://doi.org/10.1016/S0168-3659\(99\)00248-5](https://doi.org/10.1016/S0168-3659(99)00248-5).
- [64] S.K. Golombek, J.-N. May, B. Theek, L. Appold, N. Drude, F. Kiessling, T. Lammers, Tumor targeting via EPR: Strategies to enhance patient responses, *Adv. Drug Deliv. Rev.* 130 (2018) 17–38. <https://doi.org/10.1016/j.addr.2018.07.007>.
- [65] L. Leibler, H. Orland, J.C. Wheeler, Theory of critical micelle concentration for solutions of block copolymers, *J. Chem. Phys.* 79 (1983) 3550–3557. <https://doi.org/10.1063/1.446209>.
- [66] S.M. Moghimi, A.C. Hunter, J.C. Murray, Long-circulating and target-specific nanoparticles: theory to practice., *Pharmacol. Rev.* 53 (2001) 283–318. <http://www.ncbi.nlm.nih.gov/pubmed/11356986>.
- [67] F. Alexis, E. Pridgen, L.K. Molnar, O.C. Farokhzad, Factors Affecting the Clearance and Biodistribution of Polymeric Nanoparticles, *Mol. Pharm.* 5 (2008) 505–515. <https://doi.org/10.1021/mp800051m>.
- [68] S. Tenzer, D. Docter, J. Kuharev, A. Musyanovych, V. Fetz, R. Hecht, F. Schlenk, D. Fischer, K. Kiouptsi, C. Reinhardt, K. Landfester, H. Schild, M. Maskos, S.K. Knauer, R.H. Stauber, Rapid formation of plasma protein corona critically affects nanoparticle pathophysiology, *Nat. Nanotechnol.* 8 (2013) 772–781. <https://doi.org/10.1038/nnano.2013.181>.
- [69] A.V. V. Kabanov, V.P.P. Chekhonin, V.Y.Y. Alakhov, E.V. V. Batrakova, A.S.S. Lebedev, N.S.S. Melik-Nubarov, S.A.A. Arzhakov, A.V. V. Levashov, G.V. V. Morozov, E.S.S. Severin, V.A.A. Kabanov, The neuroleptic activity of haloperidol increases after its solubilization in surfactant micelles, *FEBS Lett.* 258 (1989) 343–345. [https://doi.org/10.1016/0014-5793\(89\)81689-8](https://doi.org/10.1016/0014-5793(89)81689-8).
- [70] J.S. Suk, Q. Xu, N. Kim, J. Hanes, L.M. Ensign, PEGylation as a strategy for improving nanoparticle-based drug and gene delivery, *Adv. Drug Deliv. Rev.* 99 (2016) 28–51. <https://doi.org/10.1016/j.addr.2015.09.012>.
- [71] S.C. Owen, D.P.Y. Chan, M.S. Shoichet, Polymeric micelle stability, *Nano Today.* 7 (2012) 53–65. <https://doi.org/10.1016/j.nantod.2012.01.002>.
- [72] R. Luxenhofer, A. Schulz, C. Roques, S. Li, T.K. Bronich, E. V. Batrakova, R. Jordan, A. V. Kabanov, Doubly amphiphilic poly(2-oxazoline)s as high-capacity delivery systems for hydrophobic drugs, *Biomaterials.* 31 (2010) 4972–4979. <https://doi.org/10.1016/j.biomaterials.2010.02.057>.
- [73] Z. He, X. Wan, A. Schulz, H. Bludau, M.A. Dobrovolskaia, S.T. Stern, S.A. Montgomery, H. Yuan, Z. Li, D. Alakhova, M. Sokolsky, D.B. Darr, C.M. Perou, R. Jordan, R. Luxenhofer, A. V. Kabanov, A high capacity polymeric micelle of paclitaxel:

- Implication of high dose drug therapy to safety and in vivo anti-cancer activity, *Biomaterials*. 101 (2016) 296–309. <https://doi.org/10.1016/j.biomaterials.2016.06.002>.
- [74] M. Talelli, C.J.F. Rijcken, C.F. van Nostrum, G. Storm, W.E. Hennink, Micelles based on HPMA copolymers, *Adv. Drug Deliv. Rev.* 62 (2010) 231–239. <https://doi.org/10.1016/j.addr.2009.11.029>.
- [75] W.A. Braunecker, K. Matyjaszewski, Controlled/living radical polymerization: Features, developments, and perspectives, *Prog. Polym. Sci.* 32 (2007) 93–146. <https://doi.org/10.1016/j.progpolymsci.2006.11.002>.
- [76] G. Moad, E. Rizzardo, S.H. Thang, Living Radical Polymerization by the RAFT Process - A Second Update, *Aust. J. Chem.* 62 (2009) 1402–1472. <https://doi.org/10.1071/CH09311>.
- [77] G. Moad, E. Rizzardo, S.H. Thang, Reversible Addition Fragmentation Chain Transfer (RAFT) Polymerization, *Mater. Matters*. 5 (2010) 2–8.
- [78] A.W. York, S.E. Kirkland, C.L. McCormick, Advances in the synthesis of amphiphilic block copolymers via RAFT polymerization: Stimuli-responsive drug and gene delivery ☆, 60 (2008) 1018–1036. <https://doi.org/10.1016/j.addr.2008.02.006>.
- [79] P.J. Roth, D. Kessler, R. Zentel, P. Theato, A Method for Obtaining Defined End Groups of Polymethacrylates Prepared by the RAFT Process during Aminolysis, *Macromolecules*. 41 (2008) 8316–8319. <https://doi.org/10.1021/ma801869z>.
- [80] J. Zhou, H. Yao, J. Ma, Recent advances in RAFT-mediated surfactant-free emulsion polymerization, *Polym. Chem.* 9 (2018) 2532–2561. <https://doi.org/10.1039/C8PY00065D>.
- [81] E. Sprong, J.S.K. Leswin, D.J. Lamb, C.J. Ferguson, B.S. Hawket, B.T.T. Pham, D. Nguyen, C.H. Such, A.K. Serelis, R.G. Gilbert, Molecular Watchmaking: ab initio Emulsion Polymerization by RAFT-controlled Self-assembly, *Macromol. Symp.* 231 (2005) 84–93. <https://doi.org/10.1002/masy.200590028>.
- [82] Y. Zhu, J.M. Noy, A.B. Lowe, P.J. Roth, The synthesis and aqueous solution properties of sulfobutylbetaine (co)polymers: Comparison of synthetic routes and tuneable upper critical solution temperatures, *Polym. Chem.* 6 (2015) 5705–5718. <https://doi.org/10.1039/c5py00160a>.
- [83] C.-C. Chang, R. Letteri, R.C. Hayward, T. Emrick, Functional Sulfobetaine Polymers: Synthesis and Salt-Responsive Stabilization of Oil-in-Water Droplets, *Macromolecules*. 48 (2015) 7843–7850. <https://doi.org/10.1021/acs.macromol.5b01861>.
- [84] H. Dautzenberg, Polyelectrolyte Complex Formation in Highly Aggregating Systems. 1. Effect of Salt: Polyelectrolyte Complex Formation in the Presence of NaCl, *Macromolecules*. 30 (1997) 7810–7815. <https://doi.org/10.1021/ma970803f>.
- [85] V. Hildebrand, A. Laschewsky, M. Pach, P. Muller-Buschbaum, C.M. Papadakis,

- Effect of the zwitterion structure on the thermo-responsive behaviour of poly(sulfobetaine methacrylates), *Polym. Chem.* 8 (2017) 310–322. <https://doi.org/10.1039/C6PY01220E>.
- [86] F. Wang, J. Yang, J. Zhao, Understanding anti-polyelectrolyte behavior of a well-defined polyzwitterion at the single-chain level, *Polym. Int.* 64 (2015) 999–1005. <https://doi.org/10.1002/pi.4907>.
- [87] G.S. Georgiev, E.B. Kamenska, E.D. Vassileva, I.P. Kamenova, V.T. Georgieva, S.B. Iliev, I.A. Ivanov, Self-assembly, antipolyelectrolyte effect, and nonbiofouling properties of polyzwitterions, *Biomacromolecules.* 7 (2006) 1329–1334. <https://doi.org/10.1021/bm050938q>.
- [88] Z. Li, B. Hao, Y. Tang, H. Li, T.-C. Lee, A. Feng, L. Zhang, S.H. Thang, Effect of end-groups on sulfobetaine homopolymers with the tunable upper critical solution temperature (UCST), *Eur. Polym. J.* 132 (2020) 109704. <https://doi.org/10.1016/j.eurpolymj.2020.109704>.
- [89] K.E.B. Doncom, H. Willcock, R.K. O'Reilly, The direct synthesis of sulfobetaine-containing amphiphilic block copolymers and their self-assembly behavior, *Eur. Polym. J.* 87 (2017) 497–507. <https://doi.org/10.1016/j.eurpolymj.2016.09.002>.
- [90] M. Cai, M. Leng, A. Lu, L. He, X. Xie, L. Huang, Y. Ma, J. Cao, Y. Chen, X. Luo, Synthesis of amphiphilic copolymers containing zwitterionic sulfobetaine as pH and redox responsive drug carriers, *Colloids Surfaces B Biointerfaces.* 126 (2015) 1–9. <https://doi.org/http://dx.doi.org/10.1016/j.colsurfb.2014.12.005>.
- [91] H. Bermudez, A.K. Brannan, D.A. Hammer, F.S. Bates, D.E. Discher, Molecular Weight Dependence of Polymersome Membrane Structure, Elasticity, and Stability, *Macromolecules.* 35 (2002) 8203–8208. <https://doi.org/10.1021/ma020669l>.
- [92] V. Bütün, S.P. Armes, N.C. Billingham, Synthesis and aqueous solution properties of near-monodisperse tertiary amine methacrylate homopolymers and diblock copolymers, *Polymer (Guildf).* 42 (2001) 5993–6008. [https://doi.org/10.1016/S0032-3861\(01\)00066-0](https://doi.org/10.1016/S0032-3861(01)00066-0).
- [93] S. Bhattacharjee, DLS and zeta potential – What they are and what they are not?, *J. Control. Release.* 235 (2016) 337–351. <https://doi.org/10.1016/j.jconrel.2016.06.017>.
- [94] J.D. Clogston, A.K. Patri, Zeta potential measurement., *Methods Mol. Biol.* (2011). https://doi.org/10.1007/978-1-60327-198-1_6.
- [95] Z. Cao, Q. Yu, H. Xue, G. Cheng, S. Jiang, Nanoparticles for Drug Delivery Prepared from Amphiphilic PLGA Zwitterionic Block Copolymers with Sharp Contrast in Polarity between Two Blocks, *Angew. Chemie Int. Ed.* 49 (2010) 3771–3776. <https://doi.org/10.1002/anie.200907079>.
- [96] W. Wang, Y. Lu, Z. Yue, W. Liu, Z. Cao, Ultrastable core-shell structured nanoparticles directly made from zwitterionic polymers, *Chem. Commun.* 50 (2014)

- 15030–15033. <https://doi.org/10.1039/C4CC06558A>.
- [97] T.J. Kindt, R.A. Goldsby, B.A. Osborne, Kuby immunology, Sixth edition, in: *Immunology*, 2007.
- [98] M.A. Dobrovolskaia, P. Aggarwal, J.B. Hall, S.E. McNeil, Preclinical Studies To Understand Nanoparticle Interaction with the Immune System and Its Potential Effects on Nanoparticle Biodistribution, *Mol. Pharm.* 5 (2008) 487–495. <https://doi.org/10.1021/mp800032f>.
- [99] R. Gref, Y. Minamitake, M. Peracchia, V. Trubetskoy, V. Torchilin, R. Langer, Biodegradable long-circulating polymeric nanospheres, *Science* (80-.). 263 (1994) 1600–1603. <https://doi.org/10.1126/science.8128245>.
- [100] S. Liu, S. Jiang, Zwitterionic polymer-protein conjugates reduce polymer-specific antibody response, *Nano Today*. 11 (2016) 285–291. <https://doi.org/10.1016/j.nantod.2016.05.006>.
- [101] C.W. Pouton, Formulation of poorly water-soluble drugs for oral administration: Physicochemical and physiological issues and the lipid formulation classification system, *Eur. J. Pharm. Sci.* 29 (2006) 278–287. <https://doi.org/10.1016/j.ejps.2006.04.016>.
- [102] A. Banerjee, J. Qi, R. Gogoi, J. Wong, S. Mitragotri, Role of nanoparticle size, shape and surface chemistry in oral drug delivery, *J Control Release*. 238 (2016) 176–185. <https://doi.org/10.1016/j.jconrel.2016.07.051>.
- [103] A.Z. Fu, Y. Qiu, L. Radican, Impact of fear of insulin or fear of injection on treatment outcomes of patients with diabetes, 25 (2009) 1413–1420. <https://doi.org/10.1185/03007990902905724>.
- [104] S.V. Sastry, J.R. Nyshadham, J.A. Fix, Nyshadham, Fix, Recent technological advances in oral drug delivery - a review, *Pharm Sci Technolo Today*. 3 (2000) 138–145.
- [105] R.A. Cone, Barrier properties of mucus, *Adv Drug Deliv Rev.* 61 (2009) 75–85. <https://doi.org/10.1016/j.addr.2008.09.008>.
- [106] B.C. Tang, M. Dawson, S.K. Lai, Y.-Y. Wang, J.S. Suk, M. Yang, P. Zeitlin, M.P. Boyle, J. Fu, J. Hanes, Biodegradable polymer nanoparticles that rapidly penetrate the human mucus barrier, *Proc. Natl. Acad. Sci.* 106 (2009) 19268–19273. <https://doi.org/10.1073/pnas.0905998106>.
- [107] S.K. Lai, D.E. O’Hanlon, S. Harrold, S.T. Man, Y.-Y. Wang, R. Cone, J. Hanes, Rapid transport of large polymeric nanoparticles in fresh undiluted human mucus, *Proc Natl Acad Sci U S A*. 104 (2007) 1482–1487. <https://doi.org/10.1073/pnas.0608611104>.
- [108] Y. Wang, S.K. Lai, A. Pace, R. Cone, Addressing the PEG Mucoadhesivity Paradox to Engineer Nanoparticles that “Slip” through the Human Mucus Barrier, 47 (2009) 9726–9729. <https://doi.org/10.1002/anie.200803526>. Addressing.
- [109] A. Muheem, F. Shakeel, M.A. Jahangir, M. Anwar, N. Mallick, G.K. Jain, M.H. Warsi,

- F.J. Ahmad, A review on the strategies for oral delivery of proteins and peptides and their clinical perspectives, *Saudi Pharm. J.* (2016). <https://doi.org/10.1016/j.jsps.2014.06.004>.
- [110] V. V. Khutoryanskiy, Beyond PEGylation: Alternative surface-modification of nanoparticles with mucus-inert biomaterials, *Adv. Drug Deliv. Rev.* (2017). <https://doi.org/10.1016/j.addr.2017.07.015>.
- [111] S.S. Olmsted, J.L. Padgett, A.I. Yudin, K.J. Whaley, T.R. Moench, R.A. Cone, Diffusion of macromolecules and virus-like particles in human cervical mucus, *Biophys J.* 81 (2001) 1930–1937. [https://doi.org/10.1016/S0006-3495\(01\)75844-4](https://doi.org/10.1016/S0006-3495(01)75844-4).
- [112] W.M. Saltzman, M.L. Radomsky, K.J. Whaley, R.A. Cone, Antibody diffusion in human cervical mucus, *Biophys. J.* 66 (1994) 508–515. [https://doi.org/10.1016/S0006-3495\(94\)80802-1](https://doi.org/10.1016/S0006-3495(94)80802-1).
- [113] X. Han, Y. Lu, J. Xie, E. Zhang, H. Zhu, H. Du, K. Wang, B. Song, C. Yang, Y. Shi, Z. Cao, Zwitterionic micelles efficiently deliver oral insulin without opening tight junctions, *Nat. Nanotechnol.* 15 (2020) 605–614. <https://doi.org/10.1038/s41565-020-0693-6>.
- [114] A. Kumar, S.K. Sahoo, K. Padhee, P. Pal, S. Kochar, A. Satapathy, N. Pathak, Review on Solubility Enhancement Techniques for Hydrophobic Drugs, *Pharm. Glob.* 2011 (2011) 3–03.
- [115] N. Desai, Challenges in Development of Nanoparticle-Based Therapeutics, *AAPS J.* 14 (2012) 282–295. <https://doi.org/10.1208/s12248-012-9339-4>.
- [116] G.S. Kwon, T. Okano, Polymeric micelles as new drug carriers, *Adv. Drug Deliv. Rev.* 21 (1996) 107–116. [https://doi.org/10.1016/S0169-409X\(96\)00401-2](https://doi.org/10.1016/S0169-409X(96)00401-2).
- [117] G.S. Kwon, M. Naito, K. Kataoka, M. Yokoyama, Y. Sakurai, T. Okano, Block copolymer micelles as vehicles for hydrophobic drugs, *Colloids Surfaces B Biointerfaces.* 2 (1994) 429–434. [https://doi.org/10.1016/0927-7765\(94\)80007-3](https://doi.org/10.1016/0927-7765(94)80007-3).
- [118] K. Kataoka, A. Harada, Y. Nagasaki, Block copolymer micelles for drug delivery: Design, characterization and biological significance, *Adv. Drug Deliv. Rev.* 64 (2012) 37–48. <https://doi.org/10.1016/j.addr.2012.09.013>.
- [119] N.T. Southall, K.A. Dill, A.D.J. Haymet, A View of the Hydrophobic Effect, *J. Phys. Chem. B.* 106 (2002) 521–533. <https://doi.org/10.1021/jp015514e>.
- [120] G.M. Mortimer, N.J. Butcher, A.W. Musumeci, Z.J. Deng, D.J. Martin, R.F. Minchin, Cryptic Epitopes of Albumin Determine Mononuclear Phagocyte System Clearance of Nanomaterials, *ACS Nano.* 8 (2014) 3357–3366. <https://doi.org/10.1021/nn405830g>.
- [121] N. Brandes, P.B. Welzel, C. Werner, L.W. Kroh, Adsorption-induced conformational changes of proteins onto ceramic particles: Differential scanning calorimetry and FTIR analysis, *J. Colloid Interface Sci.* (2006). <https://doi.org/10.1016/j.jcis.2006.01.065>.

- [122] P.J. Roth, C. Boyer, A.B. Lowe, T.P. Davis, RAFT polymerization and thiol chemistry: a complementary pairing for implementing modern macromolecular design, *Macromol Rapid Commun.* 32 (2011) 1123–1143.
- [123] Y. Sambuy, I. De Angelis, G. Ranaldi, M.L. Scarino, A. Stammati, F. Zucco, The Caco-2 cell line as a model of the intestinal barrier: Influence of cell and culture-related factors on Caco-2 cell functional characteristics, *Cell Biol. Toxicol.* (2005). <https://doi.org/10.1007/s10565-005-0085-6>.
- [124] J. Suh, M. Dawson, J. Hanes, Real-time multiple-particle tracking: Applications to drug and gene delivery, *Adv. Drug Deliv. Rev.* (2005). <https://doi.org/10.1016/j.addr.2004.06.001>.
- [125] WHO Global, World malaria report 2019, 2019.
- [126] R. Tuteja, Malaria-An Overview, *FEBS J.* 274 (2007) 4670–4679. <https://doi.org/10.1111/j.1742-4658.2007.05997.x>.
- [127] R.B.M. Partnership, ed., The Global Malaria Action Plan for a Malaria Free World., (2008).
- [128] WHO, The Malaria Eradication Research Agenda (malERA) initiative, (n.d.). <http://www.who.int/malaria/elimination/maleraupdate.pdf>.
- [129] R.J. Maude, W. Pontavornpinyo, S. Saralamba, R. Aguas, S. Yeung, A.M. Dondorp, N.P.J. Day, N.J. White, L.J. White, The last man standing is the most resistant: eliminating artemisinin-resistant malaria in Cambodia, *Malar. J.* 8 (2009) 31. <https://doi.org/10.1186/1475-2875-8-31>.
- [130] malERA Consultative Group on Drugs, malERA C.G. on Drugs, A research agenda for malaria eradication: drugs., *PLoS Med.* 8 (2011) e1000402. <https://doi.org/10.1371/journal.pmed.1000402>.
- [131] R. Kuttan, P. Bhanumathy, K. Nirmala, M.C. George, Potential anticancer activity of turmeric (*Curcuma longa*), *Cancer Lett.* 29 (1985) 197–202. [https://doi.org/10.1016/0304-3835\(85\)90159-4](https://doi.org/10.1016/0304-3835(85)90159-4).
- [132] A. Shehzad, S. Khan, O. Shehzad, Y.S. Lee, Curcumin therapeutic promises and bioavailability in colorectal cancer, *Drugs of Today.* (2010). <https://doi.org/10.1358/dot.2010.46.7.1509560>.
- [133] R.I. Mahran, M.M. Hagra, D. Sun, D.E. Brenner, Bringing Curcumin to the Clinic in Cancer Prevention: a Review of Strategies to Enhance Bioavailability and Efficacy., *AAPS J.* 19 (2017) 54–81. <https://doi.org/10.1208/s12248-016-0003-2>.
- [134] R.C. Reddy, P.G. Vatsala, V.G. Keshamouni, G. Padmanaban, P.N. Rangarajan, Curcumin for malaria therapy, *Biochem. Biophys. Res. Commun.* 326 (2005) 472–474. <https://doi.org/10.1016/j.bbrc.2004.11.051>.
- [135] O.P. Sharma, Antioxidant activity of curcumin and related compounds, *Biochem.*

- Pharmacol. 25 (1976) 1811–1812. [https://doi.org/10.1016/0006-2952\(76\)90421-4](https://doi.org/10.1016/0006-2952(76)90421-4).
- [136] M. Salem, S. Rohani, E.R. Gillies, Curcumin, a promising anti-cancer therapeutic: a review of its chemical properties, bioactivity and approaches to cancer cell delivery, *RSC Adv.* 4 (2014) 10815. <https://doi.org/10.1039/c3ra46396f>.
- [137] W.C. Jordan, C.R. Drew, Curcumin--a natural herb with anti-HIV activity., *J. Natl. Med. Assoc.* 88 (1996) 333. <http://www.pubmedcentral.nih.gov/articlerender.fcgi?artid=2608099&tool=pmcentrez&rendertype=abstract>.
- [138] P. Anand, A.B. Kunnumakkara, R.A. Newman, B.B. Aggarwal, Bioavailability of Curcumin: Problems and Promises, *Mol. Pharm.* 4 (2007) 807–818. <https://doi.org/10.1021/mp700113r>.
- [139] S. Bisht, G. Feldmann, S. Soni, R. Ravi, C. Karikar, A. Maitra, A. Maitra, Polymeric nanoparticle-encapsulated curcumin (“nanocurcumin”): a novel strategy for human cancer therapy, *J. Nanobiotechnology.* 5 (2007) 3. <https://doi.org/10.1186/1477-3155-5-3>.
- [140] J. Duan, Y. Zhang, S. Han, Y. Chen, B. Li, M. Liao, W. Chen, X. Deng, J. Zhao, B. Huang, Synthesis and in vitro/in vivo anti-cancer evaluation of curcumin-loaded chitosan/poly(butyl cyanoacrylate) nanoparticles, *Int J Pharm.* 400 (2010) 211–220. <https://doi.org/10.1016/j.ijpharm.2010.08.033>.
- [141] D. Gromadzki, V. Tzankova, M. Kondeva, C. Gorinova, P. Rychter, M. Libera, G. Momekov, M. Marić, D. Momekova, Amphiphilic core-shell nanoparticles with dimer fatty acid-based aliphatic polyester core and zwitterionic poly(sulfobetaine) shell for controlled delivery of curcumin, *Int. J. Polym. Mater. Polym. Biomater.* 66 (2017) 915–925. <https://doi.org/10.1080/00914037.2016.1278217>.
- [142] S.S. Bansal, M. Goel, F. Aqil, M. V. Vadhanam, R.C. Gupta, Advanced Drug Delivery Systems of Curcumin for Cancer Chemoprevention, *Cancer Prev. Res.* 4 (2011) 1158–1171. <https://doi.org/10.1158/1940-6207.CAPR-10-0006>.
- [143] G. Flora, D. Gupta, A. Tiwari, Nanocurcumin: a promising therapeutic advancement over native curcumin., *Crit. Rev. Ther. Drug Carrier Syst.* 30 (2013) 331–68. <http://www.ncbi.nlm.nih.gov/pubmed/23662605>.
- [144] Y.J. Wang, M.H. Pan, A.L. Cheng, L.I. Lin, Y.S. Ho, C.Y. Hsieh, J.K. Lin, Stability of curcumin in buffer solutions and characterization of its degradation products, *J. Pharm. Biomed. Anal.* (1997). [https://doi.org/10.1016/S0731-7085\(96\)02024-9](https://doi.org/10.1016/S0731-7085(96)02024-9).
- [145] R. Chakrabarti, P.S. Rawat, B.M. Cooke, R.L. Coppel, S. Patankar, Cellular Effects of Curcumin on Plasmodium falciparum Include Disruption of Microtubules, *PLoS One.* (2013). <https://doi.org/10.1371/journal.pone.0057302>.
- [146] M.C. Wani, H.L. Taylor, M.E. Wall, P. Coggon, A.T. McPhail, Plant antitumor agents. VI. Isolation and structure of taxol, a novel antileukemic and antitumor agent from

- Taxus brevifolia, J. Am. Chem. Soc. 93 (1971) 2325–2327. <https://doi.org/10.1021/ja00738a045>.
- [147] P.B. Schiff, J. Fant, S.B. Horwitz, Promotion of microtubule assembly in vitro by taxol [19], Nature. (1979). <https://doi.org/10.1038/277665a0>.
- [148] P.B. Schiff, S.B. Horwitz, Taxol stabilizes microtubules in mouse fibroblast cells, Proc. Natl. Acad. Sci. U. S. A. (1980). <https://doi.org/10.1073/pnas.77.3.1561>.
- [149] K.C. Nicolaou, Z. Yang, J.J. Liu, H. Ueno, P.G. Nantermet, R.K. Guy, C.F. Claiborne, J. Renaud, E.A. Couladouros, K. Paulvannan, E.J. Sorensen, Total synthesis of taxol, Nature. 367 (1994) 630–634. <https://doi.org/10.1038/367630a0>.
- [150] R.A. Holton, C. Somoza, H.B. Kim, F. Liang, R.J. Biediger, P.D. Boatman, M. Shindo, C.C. Smith, S. Kim, First total synthesis of taxol. 1. Functionalization of the B ring, J. Am. Chem. Soc. 116 (1994) 1597–1598. <https://doi.org/10.1021/ja00083a066>.
- [151] R.A. Holton, H.B. Kim, C. Somoza, F. Liang, R.J. Biediger, P.D. Boatman, M. Shindo, C.C. Smith, S. Kim, First total synthesis of taxol. 2. Completion of the C and D rings, J. Am. Chem. Soc. 116 (1994) 1599–1600. <https://doi.org/10.1021/ja00083a067>.
- [152] H. Gelderblom, J. Verweij, K. Nooter, A. Sparreboom, Cremophor EL: the drawbacks and advantages of vehicle selection for drug formulation, Eur. J. Cancer. 37 (2001) 1590–1598. [https://doi.org/10.1016/S0959-8049\(01\)00171-X](https://doi.org/10.1016/S0959-8049(01)00171-X).
- [153] S.S.W. Ng, W.D. Figg, A. Sparreboom, Taxane-Mediated Antiangiogenesis in Vitro: Influence of Formulation Vehicles and Binding Proteins, Cancer Res. (2004). <https://doi.org/10.1158/0008-5472.CAN-03-3391>.
- [154] M.R. Green, G.M. Manikhas, S. Orlov, B. Afanasyev, A.M. Makhson, P. Bhar, M.J. Hawkins, Abraxane®, a novel Cremophor®-free, albumin-bound particle form of paclitaxel for the treatment of advanced non-small-cell lung cancer, Ann. Oncol. (2006). <https://doi.org/10.1093/annonc/mdl104>.
- [155] P. Ma, R.J. Mumper, Paclitaxel nano-delivery systems: A comprehensive review, J. Nanomedicine Nanotechnol. (2013). <https://doi.org/10.4172/2157-7439.1000164>.
- [156] J. Baggerman, M.M.J. Smulders, H. Zuillhof, Romantic Surfaces: A Systematic Overview of Stable, Biospecific, and Antifouling Zwitterionic Surfaces, Langmuir. 35 (2019) 1072–1084. <https://doi.org/10.1021/acs.langmuir.8b03360>.
- [157] H. Alemzadeh, J. Raman, N. Leveson, Z. Kalbarczyk, R.K. Iyer, Adverse events in robotic surgery: A retrospective study of 14 years of fda data, PLoS One. (2016). <https://doi.org/10.1371/journal.pone.0151470>.
- [158] M.J. Mack, Minimally Invasive and Robotic Surgery, JAMA. 285 (2001) 568. <https://doi.org/10.1001/jama.285.5.568>.
- [159] B.J. Nelson, I.K. Kaliakatsos, J.J. Abbott, Microrobots for Minimally Invasive Medicine, Annu. Rev. Biomed. Eng. 12 (2010) 55–85. <https://doi.org/10.1146/annurev-bioeng->

010510-103409.

- [160] B.S. Peters, P.R. Armijo, C. Krause, S.A. Choudhury, D. Oleynikov, Review of emerging surgical robotic technology, *Surg. Endosc.* (2018). <https://doi.org/10.1007/s00464-018-6079-2>.
- [161] S.S. Mapara, V.B. Patravale, Medical capsule robots: A renaissance for diagnostics, drug delivery and surgical treatment, *J. Control. Release.* (2017). <https://doi.org/10.1016/j.jconrel.2017.07.005>.
- [162] J. Li, B.E.F. De Ávila, W. Gao, L. Zhang, J. Wang, Micro/nanorobots for Biomedicine: Delivery, surgery, sensing, and detoxification, *Sci. Robot.* 2 (2017) 1–10. <https://doi.org/10.1126/scirobotics.aam6431>.
- [163] M. Sitti, *Mobile Microrobotics*, MIT Press, Cambridge, MA, 2017.
- [164] J. Wang, W. Gao, Nano/microscale motors: Biomedical opportunities and challenges, *ACS Nano.* (2012). <https://doi.org/10.1021/nn3028997>.
- [165] S. Tottori, L. Zhang, F. Qiu, K.K. Krawczyk, A. Franco-Obregón, B.J. Nelson, Magnetic Helical Micromachines: Fabrication, Controlled Swimming, and Cargo Transport, *Adv. Mater.* 24 (2012) 811–816. <https://doi.org/10.1002/adma.201103818>.
- [166] U. Bozuyuk, O. Yasa, I.C. Yasa, H. Ceylan, S. Kizilel, M. Sitti, Light-Triggered Drug Release from 3D-Printed Magnetic Chitosan Microswimmers, *ACS Nano.* 12 (2018) 9617–9625. <https://doi.org/10.1021/acsnano.8b05997>.
- [167] G.H. Kwon, J.Y. Park, J.Y. Kim, M.L. Frisk, D.J. Beebe, S.-H. Lee, Biomimetic Soft Multifunctional Miniature Aquabots, *Small.* 4 (2008) 2148–2153. <https://doi.org/10.1002/sml.200800315>.
- [168] A. Aghakhani, O. Yasa, P. Wrede, M. Sitti, Acoustically powered surface-slipping mobile microrobots, *Proc. Natl. Acad. Sci.* (2020) 201920099. <https://doi.org/10.1073/pnas.1920099117>.
- [169] D. Ahmed, T. Baasch, B. Jang, S. Pane, J. Dual, B.J. Nelson, Artificial Swimmers Propelled by Acoustically Activated Flagella, *Nano Lett.* 16 (2016) 4968–4974. <https://doi.org/10.1021/acs.nanolett.6b01601>.
- [170] H. Zeng, P. Wasylczyk, C. Parmeggiani, D. Martella, M. Burresti, D.S. Wiersma, Light-fueled microscopic walkers, *Adv. Mater.* 27 (2015) 3883–3887.
- [171] V. Sridhar, B. Park, M. Sitti, Light-driven Janus hollow mesoporous TiO₂-Au microswimmers, *Adv. Funct. Mater.* 28 (2018) 1704902.
- [172] S. Palagi, A.G. Mark, S.Y. Reigh, K. Melde, T. Qiu, H. Zeng, C. Parmeggiani, D. Martella, A. Sanchez-Castillo, N. Kapernaum, F. Giesselmann, D.S. Wiersma, E. Lauga, P. Fischer, Structured light enables biomimetic swimming and versatile locomotion of photoresponsive soft microrobots, *Nat. Mater.* 15 (2016) 647–653. <https://doi.org/10.1038/nmat4569>.

- [173] A. Pena-Francesch, J. Giltinan, M. Sitti, Multifunctional and biodegradable self-propelled protein motors, *Nat. Commun.* 10 (2019) 3188. <https://doi.org/10.1038/s41467-019-11141-9>.
- [174] V. Magdanz, M. Medina-Sánchez, Y. Chen, M. Guix, O.G. Schmidt, How to improve spermbot performance, *Adv. Funct. Mater.* (2015). <https://doi.org/10.1002/adfm.201500015>.
- [175] X. Zhao, K. Gentile, F. Mohajerani, A. Sen, Powering Motion with Enzymes, *Acc. Chem. Res.* 51 (2018) 2373–2381. <https://doi.org/10.1021/acs.accounts.8b00286>.
- [176] X. Ma, A.C. Hortelão, T. Patiño, S. Sánchez, Enzyme catalysis to power micro/nanomachines, *ACS Nano.* 10 (2016) 9111–9122.
- [177] J.G.S. Moo, M. Pumera, Chemical Energy Powered Nano/Micro/Macromotors and the Environment, *Chem. - A Eur. J.* 21 (2015) 58–72. <https://doi.org/10.1002/chem.201405011>.
- [178] H. Ceylan, I.C. Yasa, U. Kilic, W. Hu, M. Sitti, Translational prospects of untethered medical microrobots, *Prog. Biomed. Eng.* 1 (2019) 012002. <https://doi.org/10.1088/2516-1091/ab22d5>.
- [179] L. Ilium, S.S. Davis, C.G. Wilson, N.W. Thomas, M. Frier, J.G. Hardy, Blood clearance and organ deposition of intravenously administered colloidal particles. The effects of particle size, nature and shape, *Int. J. Pharm.* 12 (1982) 135–146. [https://doi.org/10.1016/0378-5173\(82\)90113-2](https://doi.org/10.1016/0378-5173(82)90113-2).
- [180] Y. Tabata, Y. Ikada, Phagocytosis of polymer microspheres by macrophages, in: *New Polym. Mater.*, Springer-Verlag, Berlin/Heidelberg, 1990: pp. 107–141. <https://doi.org/10.1007/BFb0043062>.
- [181] S. Schuerle, I.A. Vizcarra, J. Moeller, M.S. Sakar, B. Özkale, A.M. Lindo, F. Mushtaq, I. Schoen, S. Pané, V. Vogel, B.J. Nelson, Robotically controlled microprey to resolve initial attack modes preceding phagocytosis, *Sci. Robot.* 2 (2017) eaah6094. <https://doi.org/10.1126/scirobotics.aah6094>.
- [182] J. Han, J. Zhen, V. Du Nguyen, G. Go, Y. Choi, S.Y. Ko, J.-O. Park, S. Park, Hybrid-Actuating Macrophage-Based Microrobots for Active Cancer Therapy, *Sci. Rep.* 6 (2016) 28717. <https://doi.org/10.1038/srep28717>.
- [183] J.A. Champion, S. Mitragotri, Shape Induced Inhibition of Phagocytosis of Polymer Particles, *Pharm. Res.* 26 (2009) 244–249. <https://doi.org/10.1007/s11095-008-9626-z>.
- [184] J.A. Champion, S. Mitragotri, Role of target geometry in phagocytosis, *Proc. Natl. Acad. Sci. U. S. A.* (2006). <https://doi.org/10.1073/pnas.0600997103>.
- [185] J.A. Champion, A. Walker, S. Mitragotri, Role of particle size in phagocytosis of polymeric microspheres, *Pharm. Res.* (2008). <https://doi.org/10.1007/s11095-008-9562-y>.

- [186] I.C. Yasa, H. Ceylan, U. Bozuyuk, A.-M. Wild, M. Sitti, Elucidating the interaction dynamics between microswimmer body and immune system for medical microrobots, *Sci. Robot.* 5 (2020) eaaz3867. <https://doi.org/10.1126/scirobotics.aaz3867>.
- [187] S. Jiang, Z. Cao, Ultralow-Fouling, Functionalizable, and Hydrolyzable Zwitterionic Materials and Their Derivatives for Biological Applications, *Adv. Mater.* 22 (2010) 920–932. <https://doi.org/10.1002/adma.200901407>.
- [188] Y. Li, H. Xue, Y. Song, PRODUCTION AND PURIFICATION OF CARBOXYLIC BETANE ZWITTERONIC MONOMERS, 2014.
- [189] P. Kasák, Z. Kroneková, I. Krupa, I. Lacík, Zwitterionic hydrogels crosslinked with novel zwitterionic crosslinkers: Synthesis and characterization, *Polymer (Guildf)*. 52 (2011) 3011–3020. <https://doi.org/10.1016/j.polymer.2011.04.056>.
- [190] L.R. Carr, Y. Zhou, J.E. Krause, H. Xue, S. Jiang, Uniform zwitterionic polymer hydrogels with a nonfouling and functionalizable crosslinker using photopolymerization, *Biomaterials.* 32 (2011) 6893–6899. <https://doi.org/10.1016/j.biomaterials.2011.06.006>.
- [191] C. Barner-Kowollik, M. Bastmeyer, E. Blasco, G. Delaittre, P. Müller, B. Richter, M. Wegener, 3D laser micro- and nanoprinting: challenges for chemistry, *Angew. Chemie Int. Ed.* 56 (2017) 15828–15845.
- [192] J. Song, C. Michas, C.S. Chen, A.E. White, M.W. Grinstaff, From Simple to Architecturally Complex Hydrogel Scaffolds for Cell and Tissue Engineering Applications: Opportunities Presented by Two-Photon Polymerization, *Adv. Healthc. Mater.* 9 (2020) 1901217. <https://doi.org/10.1002/adhm.201901217>.
- [193] J.-F. Xing, M.-L. Zheng, X.-M. Duan, Two-photon polymerization microfabrication of hydrogels: an advanced 3D printing technology for tissue engineering and drug delivery, *Chem. Soc. Rev.* 44 (2015) 5031–5039. <https://doi.org/10.1039/C5CS00278H>.
- [194] B.H. Cumpston, S.P. Ananthavel, S. Barlow, D.L. Dyer, J.E. Ehrlich, L.L. Erskine, A.A. Heikal, S.M. Kuebler, I.-Y.S. Lee, D. McCord-Maughon, J. Qin, H. Röckel, M. Rumi, X.-L. Wu, S.R. Marder, J.W. Perry, Two-photon polymerization initiators for three-dimensional optical data storage and microfabrication, *Nature.* 398 (1999) 51–54. <https://doi.org/10.1038/17989>.
- [195] K.-S. Lee, R.H. Kim, D.-Y. Yang, S.H. Park, Advances in 3D nano/microfabrication using two-photon initiated polymerization, *Prog. Polym. Sci.* 33 (2008) 631–681. <https://doi.org/10.1016/j.progpolymsci.2008.01.001>.
- [196] G.S. He, L.-S. Tan, Q. Zheng, P.N. Prasad, Multiphoton Absorbing Materials: Molecular Designs, Characterizations, and Applications, *Chem. Rev.* 108 (2008) 1245–1330. <https://doi.org/10.1021/cr050054x>.
- [197] X. Zhou, Y. Hou, J. Lin, A review on the processing accuracy of two-photon polymerization, *AIP Adv.* 5 (2015) 30701.

- [198] D.J. Bell, S. Leutenegger, K.M. Hammar, L.X. Dong, B.J. Nelson, Flagella-like Propulsion for Microrobots Using a Nanocoil and a Rotating Electromagnetic Field, in: Proc. 2007 IEEE Int. Conf. Robot. Autom., IEEE, 2007: pp. 1128–1133. <https://doi.org/10.1109/ROBOT.2007.363136>.
- [199] K.E. Peyer, L. Zhang, B.J. Nelson, Bio-inspired magnetic swimming microrobots for biomedical applications, *Nanoscale*. 5 (2013) 1259–1272. <https://doi.org/10.1039/C2NR32554C>.
- [200] L. Anderson, N.G. Anderson, High resolution two-dimensional electrophoresis of human plasma proteins, *Proc. Natl. Acad. Sci.* 74 (1977) 5421–5425.
- [201] R.L. Juliano, Factors affecting the clearance kinetics and tissue distribution of liposomes, microspheres and emulsions, *Adv. Drug Deliv. Rev.* 2 (1988) 31–54. [https://doi.org/10.1016/0169-409X\(88\)90004-X](https://doi.org/10.1016/0169-409X(88)90004-X).
- [202] S. Nie, Understanding and overcoming major barriers in cancer nanomedicine, *Nanomedicine*. 5 (2010) 523–528. <https://doi.org/10.2217/nnm.10.23>.
- [203] J.E. Rayahin, R.A. Gemeinhart, *Macrophages*, Springer International Publishing, Cham, 2017. <https://doi.org/10.1007/978-3-319-54090-0>.
- [204] W.J. Kao, Evaluation of protein-modulated macrophage behavior on biomaterials: Designing biomimetic materials for cellular engineering, *Biomaterials*. 20 (1999) 2213–2221. [https://doi.org/10.1016/S0142-9612\(99\)00152-0](https://doi.org/10.1016/S0142-9612(99)00152-0).
- [205] R. Klopfleisch, Macrophage reaction against biomaterials in the mouse model – Phenotypes, functions and markers, *Acta Biomater.* 43 (2016) 3–13. <https://doi.org/10.1016/j.actbio.2016.07.003>.
- [206] J.M. Anderson, K.M. Miller, Biomaterial biocompatibility and the macrophage, in: *Biomater. Silver Jubil. Compend.*, Elsevier, 1984: pp. 21–26. <https://doi.org/10.1016/B978-008045154-1.50004-6>.
- [207] P. Pacheco, D. White, T. Sulchek, Effects of Microparticle Size and Fc Density on Macrophage Phagocytosis, *PLoS One*. 8 (2013) e60989. <https://doi.org/10.1371/journal.pone.0060989>.
- [208] M.E. Ogle, C.E. Segar, S. Sridhar, E.A. Botchwey, Monocytes and macrophages in tissue repair: Implications for immunoregenerative biomaterial design, *Exp. Biol. Med.* 241 (2016) 1084–1097. <https://doi.org/10.1177/1535370216650293>.
- [209] O. Lunov, T. Syrovets, C. Loos, J. Beil, M. Delacher, K. Tron, G.U. Nienhaus, A. Musyanovych, V. Mailänder, K. Landfester, T. Simmet, Differential Uptake of Functionalized Polystyrene Nanoparticles by Human Macrophages and a Monocytic Cell Line, *ACS Nano*. 5 (2011) 1657–1669. <https://doi.org/10.1021/nn2000756>.
- [210] J.L. Stow, N.D. Condon, The cell surface environment for pathogen recognition and entry, *Clin. Transl. Immunol.* 5 (2016) e71.

- [211] X. Chen, B. Jang, D. Ahmed, C. Hu, C. De Marco, M. Hoop, F. Mushtaq, B.J. Nelson, S. Pané, Small-Scale Machines Driven by External Power Sources, *Adv. Mater.* 30 (2018) 1705061.
- [212] A. Ghosh, P. Fischer, Controlled propulsion of artificial magnetic nanostructured propellers, *Nano Lett.* 9 (2009) 2243–2245.
- [213] H. Ceylan, I.C. Yasa, O. Yasa, A.F. Tabak, J. Giltinan, M. Sitti, 3D-Printed Biodegradable Microswimmer for Theranostic Cargo Delivery and Release, *ACS Nano.* 13 (2019) 3353–3362.
- [214] X. Wang, X. Qin, C. Hu, A. Terzopoulou, X. Chen, T. Huang, K. Maniura-Weber, S. Pané, B.J. Nelson, 3D printed enzymatically biodegradable soft helical microswimmers, *Adv. Funct. Mater.* 28 (2018) 1804107.
- [215] M. Mahmoudi, H. Hofmann, B. Rothen-Rutishauser, A. Petri-Fink, Assessing the in vitro and in vivo toxicity of superparamagnetic iron oxide nanoparticles, *Chem. Rev.* 112 (2011) 2323–2338.
- [216] A. Barhoumi, Q. Liu, D.S. Kohane, Ultraviolet light-mediated drug delivery: Principles, applications, and challenges, *J. Control. Release.* 219 (2015) 31–42.
- [217] J.S. Suk, S.K. Lai, N.J. Boylan, M.R. Dawson, M.P. Boyle, J. Hanes, Rapid transport of muco-inert nanoparticles in cystic fibrosis sputum treated with N-acetyl cysteine, *Nanomedicine.* (2011). <https://doi.org/10.2217/nnm.10.123>.
- [218] A. Macierzanka, A.R. Mackie, B.H. Bajka, N.M. Rigby, F. Nau, D. Dupont, Transport of particles in intestinal mucus under simulated infant and adult physiological conditions: Impact of mucus structure and extracellular DNA, *PLoS One.* (2014). <https://doi.org/10.1371/journal.pone.0095274>.
- [219] P. Urbán, J. Estelrich, A. Cortés, X. Fernández-Busquets, A nanovector with complete discrimination for targeted delivery to Plasmodium falciparum-infected versus non-infected red blood cells in vitro, *J. Control. Release.* 151 (2011) 202–211. <https://doi.org/10.1016/j.jconrel.2011.01.001>.
- [220] S.L. Cranmer, C. Magowan, J. Liang, R.L. Coppel, B.M. Cooke, An alternative to serum for cultivation of Plasmodium falciparum in vitro, *Trans. R. Soc. Trop. Med. Hyg.* (1997). [https://doi.org/10.1016/S0035-9203\(97\)90110-3](https://doi.org/10.1016/S0035-9203(97)90110-3).
- [221] C. Lambros, J.P. Vanderberg, Synchronization of Plasmodium falciparum Erythrocytic Stages in Culture, *J. Parasitol.* (1979). <https://doi.org/10.2307/3280287>.
- [222] E. Moles, S. Galiano, A. Gomes, M. Quiliano, C. Teixeira, I. Aldana, P. Gomes, X. Fernández-Busquets, ImmunoPEGliposomes for the targeted delivery of novel lipophilic drugs to red blood cells in a falciparum malaria murine model, *Biomaterials.* (2017). <https://doi.org/10.1016/j.biomaterials.2017.08.020>.
- [223] D.A. Fidock, P.J. Rosenthal, S.L. Croft, R. Brun, S. Nwaka, Antimalarial drug

discovery: Efficacy models for compound screening, *Nat. Rev. Drug Discov.* (2004). <https://doi.org/10.1038/nrd1416>.

- [224] L.R. Carr, H. Xue, S. Jiang, Functionalizable and nonfouling zwitterionic carboxybetaine hydrogels with a carboxybetaine dimethacrylate crosslinker, *Biomaterials*. 32 (2011) 961–968. <https://doi.org/10.1016/j.biomaterials.2010.09.067>.